SEARCH FOR A HEAVY-PHILIC W' BOSON USING PROTON-PROTON COLLISONS AT $s = \sqrt{13}$ TeV USING THE ATLAS DETECTOR

By

Jason Peter Gombas

A DISSERTATION

Submitted to
Michigan State University
in partial fulfillment of the requirements
for the degree of

Physics & Computational Mathematics, Science and Engineering — Dual Doctor of Philosophy

2025

ABSTRACT

SEARCH FOR A HEAVY-PHILIC W' BOSON USING PROTON-PROTON COLLISONS AT $s = \sqrt{13}$ TeV USING THE ATLAS DETECTOR

By

Jason Peter Gombas

This thesis is dedicated to searching for a hypothetical W' that only couples to the third generation of quarks, top and bottom. This W' is produced from proton-proton collisions at the Large Hadron Collider (LHC) primarily via gluon fusion. The final state after the decay is $tbW' \to tbtb$. This search is done with data collected with the ATLAS detector in Run 2 at the LHC looking in the single lepton region with at least 5 jets with at least 3 of them b-tagged. To increase the sensitivity of the search for this very rare process, machine learning techniques were used. A profile likelihood fit on the output variable is done to perform this search.

TABLE OF CONTENTS

Chapter 1

Introduction

Ever since the discovery of the Higgs boson at the LHC by the ATLAS collaboration [1] and the CMS collaboration [2], the Standard Model has been subjected to increasingly rigorous experimental scrutiny. It has been repeatedly confirmed, each time in novel and more precise ways. During Run 2, the ATLAS experiment achieved remarkable milestones: measuring the properties of the Higgs boson [3], advancing our understanding of electroweak and QCD processes and flavor physics [4], exploring the top quark [5], probing for additional scalars and exotic Higgs decays [6], continuing the search for supersymmetry [7], and conducting a wide range of searches for exotic particles [8].

While the Standard Model remains extraordinarily successful at describing known fundamental particles and interactions, compelling evidence suggests it is incomplete. Observations of galactic rotation curves, along with other evidence, point to the presence of non-luminous, non-baryonic matter (dark matter) that cannot be explained by the Standard Model alone [9, 10]. This, along with other open questions in particle physics, motivates the ongoing search for new physics beyond the Standard Model.

It is quite remarkable that, despite living in a universe filled with chaos and destruction, scientists are able to find moments of peace and venture towards discovery and understanding. It should be surprising that the universe is not only governed by order and natural laws, but also it can be understood through natural laws and expressed through mathematical equations. As Einstein famously remarked, "The most incomprehensible thing about the universe is that it is comprehensible" [11]. This sentiment is echoed by Eugene Wigner, who reflected on the deep harmony between mathematics and physics, calling it "the unreasonable effectiveness of mathematics in the natural sciences" [12].

The natural sciences has also sought to uncover the fundamental nature of matter for centuries. At first, scientist observed the macroscopic world through the lens of visible light, uncovering the beauty and complexity of cells, bacteria, and surface patterns with microscopes [13]. With the discovery of the electron [14], scientist pushed further, developing electron microscopes [15] that revealed atoms, molecules, and the intricate structures they form.

However, there are limits to how far visible light and electrons can take us. To look at smaller things, scientists turned to nuclear science, propelling atoms together with particle accelerators to unlock the quantum world [16]. This exploration revealed protons, neutrons, and eventually the quarks [17] and leptons that form part of the Standard Model. Today, we probe even further, seeking to understand not only these fundamental particles, but whether they themselves are composed of something even more elementary or if there are even more particles that we have missed all along.

1.1 Exotic Particle Searches

At the writing of this dissertation, no particle beyond the Standard Model has been discovered. There have been extensive exotic particle searches that have been conducted by the ATLAS [8] and CMS [18] collaborations. The Standard Model has been remarkably successful in describing the known particles and their interactions. However, it is well established that the Standard Model, while highly successful, does not provide a complete description of the fundamental forces and particles in the universe. This motivates ongoing searches for new and exotic physics beyond its framework.

Oftentimes, theories which predict new physics Beyond the Standard Model (BSM theories) involve symmetry breaking at the energy scale reached by the LHC. There are some theories which suggest that there are certain scales which are flavor non-universal [19, 20, 21, 22]. This means the couplings do not adhere to all flavors of quarks and leptons. If this is true, then the first hint of new physics would come from couplings to the third generation of quarks first, then to the second, and then to the first generation of quarks. Each new flavor would be included once one reaches a higher and higher energy scale. Fig. 1.1 shows a diagram representing this schematically.

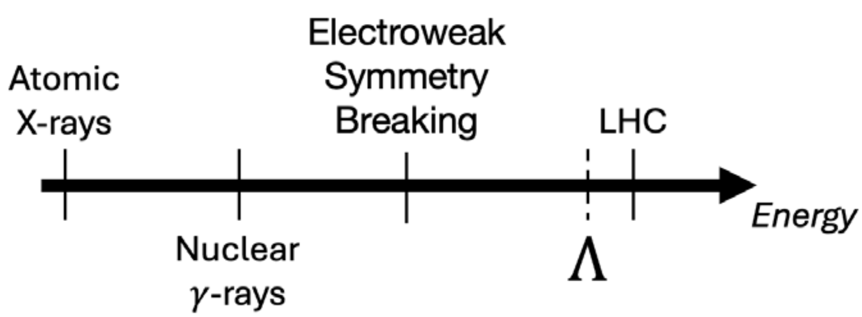

Figure 1.1: A diagram showing the possible separation of energy scales. Starting from the atomic scale with X-rays and increasing through γ-rays, electroweak symmetry breaking where the Higgs and top quarks are probed, to the energy scale of the LHC. At a currently unknown scale, new physics is predicted which would have couplings to the third generation of quarks.

Almost all BSM theories predict the existence of a new gauge boson, usually denoted as W' or Z' boson, arising from mechanisms such as extra dimensions [23], strong dynamics [24, 25], or a composite Higgs [19].

Previous searches for the W' boson have focused on Standard Model-like couplings to all quarks. A recent effort examined a top-philic Z', where couplings to lighter quarks are suppressed, resulting in different kinematic signatures [26]. Building on this idea, this dissertation explores a heavy-philic W' boson, hypothesized to couple exclusively to the third-generation quarks: top and bottom. By turning off the couplings to the first and second generations, the production dynamics shift significantly, relying primarily on gluon-gluon fusion through gluon pair-production rather than quark-gluon interactions.

While there have been numerous studies on the hypothetical W' boson [27, 28, 29], there have been no studies so far that have attempted to turn off the couplings to the first and second generation of quarks. If new physics beyond the Standard Model exists but has remained hidden due to suppression in third-generation production channels, it would represent a significant missed opportunity for discovery. This study aims to address a gap that remains despite the substantial progress made in W' boson and other BSM searches.

1.2 Detecting Particles

Particles are often conceptualized as tiny specks moving through space with well-defined positions. However, Quantum Field Theory (QFT) has a more complex description of nature. In QFT, particles are not discrete objects like billiard balls; rather, they are excitations of underlying quantum fields that permeate space. Particles are described by probability distributions—the modulus squared of their wave functions—representing the likelihood of finding a particle at a given location.

The framework used to model physical phenomena depends on the relevant energy and time scales. At the smallest scales—characterized by the highest energies and shortest time intervals—Quantum Field Theory (QFT) is essential for describing the creation and interactions of fundamental particles within the Standard Model. However, as particles travel away from the collision site, the relevant time and energy scales shift. At this scale, a more simplified model of particle interactions becomes applicable, eliminating the need for the full complexity of QFT while still providing an accurate description of the observed behavior of nature.

1.3 Natural Units

Beam energies at the LHC are in the TeV range, corresponding to extremely high energies. An interesting aspect of using natural units in theoretical calculations is the ability to highlight key insights. In the case of the LHC, the natural units are defined by setting $\hbar = 1$, which simplifies the treatment of quantum phenomena, and $c = 1$, which corresponds to extremely high speeds. By setting $c = 1$, mass and energy both have the same units (MeV, GeV).

Because $\hbar$ (with units of energy $\times$ time) is set to 1, energy and time become directly related, i.e., energy is inversely proportional to time. Additionally, since c (with units of distance/time) is set to 1, distance becomes proportional to time. Therefore higher energies probe smaller distances.

This brief exercise highlights why particles are collided at such high energies: to study the fundamental particles of the universe, which exist at the smallest scales.

1.4 Thesis Structure

This dissertation focuses on a novel search for a particle Beyond the Standard Model (BSM). Chapter 1 provides an introduction to the field of high-energy physics. Chapter 2 contains a brief summary of the Standard Model and Quantum Field Theory (QFT) as the foundation for this work. Chapter 3 describes the Large Hadron Collider (LHC) facility and the ATLAS detector, essential tools for probing the frontiers of particle physics. Chapter 4 outlines the modeling of proton-proton collisions and the reconstruction of events from the data measured by the ATLAS detector. Chapter 5 introduces the heavy-philic W' boson, a theoretical BSM particle and the focus of this dissertation, and discusses the Standard Model background relevant to the phase space of the search. Chapter 6 presents the results of the analysis, including fits and statistical interpretations. Finally, Chapter 7 concludes with a discussion of the findings and potential directions for future research.

Chapter 2

Theory

2.1 Quantum Field Theory

In Lagrangian Field Theory a special quantity exists called the action, S. This quantity is the time integral of the Lagrangian, L. In local field theory, one typically can write the Lagrangian as an integral over the Lagrangian density which is a function of a field $\phi_X(x)$, or fields, and their derivatives $\partial_\mu(x)$. This can be written as the following

$$S = \int L dt = \int \mathcal{L}(\phi_X, \partial_\mu \phi_X) d^4x \tag{2.1}$$

according to [30]. The principal of least action states that configurations will proceed along a path in such a way that minimizes S as time progresses from t_1 to t_2. This statement can be summed up as $0 = \delta S$ since the extremum is normally the minimum. The Euler-Lagrange formula can then be derived by taking the derivative of S as defined in Eq. 2.1, and finding where it vanishes. To do this one must assume that δS is zero at the temporal beginning and end of the integration region. The condition that satisfies these requirements independent of $\partial\phi_X$ is the Euler-Lagrange formula

$$\partial \left(\frac{\partial \mathcal{L}}{\partial(\partial_\mu \phi_X)} \right) - \frac{\partial \mathcal{L}}{\partial \phi_X} = 0 \tag{2.2}$$

this process is independent of the field which means that there exists an Euler-Lagrange equation for each and every field illustrated with the subscript X.

The Lagrangian is then used to derive the quantities of interest. In high-energy physics, the Lorentz-invariant phase space form of Fermi's Golden Rule takes the form of

$$d\Gamma = \frac{(2\pi)^4\delta^4(p_i - p_f)}{2E_1 2E_2}|\mathcal{M}_{fi}|^2 \prod_f \frac{d^3p_f}{(2\pi)^3 2E_f} \tag{2.3}$$

$d\Gamma$ is the differential decay rate, $(2\pi)^4\delta^4(p_i - p_f)$ is a four-dimensional Dirac delta function ensuring that four-momentum is conserved, E_1 and E_2 are the energies of the initial state particles, $|\mathcal{M}_{fi}|^2$ is the squared matrix element that contains all the dynamics of the interaction, $\prod_f \frac{d^3p_f}{(2\pi)^3 2E_f}$ is the phase space volume element for each final-state particle f. Integrating this yields the total decay rate over the allowed final momenta.

Cross section is a quantity that describes the probability of a given interaction occurring between particles. It is the effective area that creates a particular interaction. Convention has been established to use units of barns (1 barn = 10^{-28} m^2). The cross section is central to experimental particle physics since it directly determines the number of events observed in a detector. For the collision of two particles, it can be written as

$$\sigma(X_1X_2 \to Y) = \frac{1}{4E_1E_1|\vec{v}_1 - \vec{v}_2|}\int |\mathcal{M}|^2\, d\Phi \tag{2.4}$$

The differential cross-section is also important, as it tells what kinematic region to expect a flux of particles.

The total number of expected events with final state Y also depends on the luminosity of the colliding beams. This is why the instantaneous luminosity, $I(t)$, is measured. The integrated luminosity, $\mathcal{I}$, is then the total number of incident particles per unit area, and is given by $\mathcal{I} = \int I(t)dt$. The number of observed events N for a particular process that has cross-section σ is therefore given by $N = \mathcal{I} \cdot \sigma$. The total integrated luminosity measured for the ATLAS detector during Run 2 was 140 fb^{-1} [31].

To compute the cross-section along with the kinematic differential distributions, the integral of the matrix element must be taken. Since this integral results in IR divergences due to soft and co-linear gluon emission, the direct calculation is impossible to calculate by hand. Hence, this study uses the Monte Carlo method to produce these distributions.

At small distances, the strong coupling constant is small enough where the modeled process in QCD can be approximated by a finite amount of interactions.

In perturbative QCD, the calculation of hadronic cross-sections requires the separation of short- and long-distance physics. This is achieved through the factorization theorem, which introduces the factorization scale μ_F.

In addition, the renormalization scale μ_R appears through the running of the strong coupling constant $\alpha_S(\mu_R)$, as a consequence of renormalizing ultraviolet divergences in loop calculations. Although physical observables are, in principle, independent of both μ_F and μ_R, fixed-order calculations retain some residual dependence on these scales.

In perturbative QCD, the desired process can be calculated up to a certain order in the strong coupling constant. This is called a fixed order calculation in QCD.

The 4-flavor scheme (4FS) is used, in which top and bottom quarks are excluded from the parton distribution functions (PDFs). The advantages and disadvantages of using the 4-flavor versus the 5-flavor scheme (5FS) are discussed in detail in [32]. While each scheme has its own domain of validity and theoretical motivations, they generally yield consistent results within uncertainties for inclusive observables.

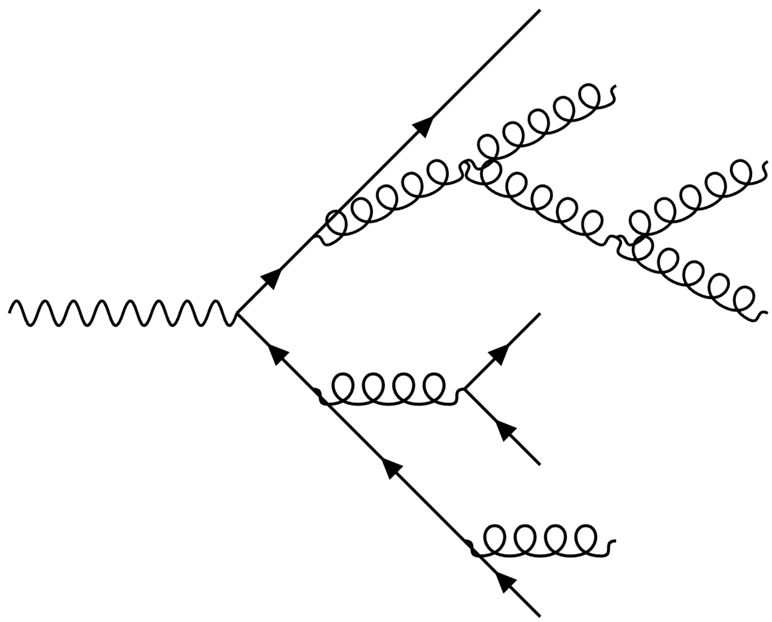

Figure 2.1: A Feynman diagram of a boson decaying into a quark-antiquark pair which produces parton showering where the curly lines represent gluons and the solid lines represent quarks.

When highly energetic quarks or gluons are produced in a collision, they will undergo a phenomenon known as parton showering. This occurs as quarks or gluons travel through space and emit additional gluons or split into quark-antiquark pairs. The emitted gluons can themselves undergo further branching, creating a cascade of partons. This process is a result of the self-interacting nature of gluons, governed by the QCD coupling constant at high energies, such as those at the LHC. As the gluons continue to propagate, they can undergo pair production and split into additional gluons or quark pairs, leading to the creation of thousands of particles in a rapid cascade. This process can be visualized through a Feynman diagram, as shown in Fig. 2.1.

After the phenomenon of parton showering, hadronization of each unstable particles occurs. Due to a phenomenon called quantum confinement, quarks cannot exist on their own. They must be paired with at least 1 other quark after a period of time. Therefore, quarks will immediately hadronize into mesons and hadrons after the parton shower.

2.2 The Standard Model

The Standard Model is a model of all the fundamental particles that are known about and their interactions. Gluons are the force carriers for the strong force, W and Z bosons are the force carriers for the weak force, and photons are the force carriers for the electromagnetic force. Mathematically, the Standard Model is a non-abelian gauge quantum field theory that has the symmetries of SU(3)× SU(2)× U(1) group.

There are 6 quarks in the Standard Model, arranged in 3 generations with 2 quarks in each generation. Each generation has increasing mass and each flavor within the generation share similar properties. The first generation of quarks are the up and down quarks (u,d), the second generation of quarks are charm and strange quarks (c,s), and the third generation of quarks is are the top and bottom quarks (t,b). Each quark has a pair anti-quark that is denoted with an overhead bar (ie $\bar{u}$, $\bar{c}$, $\bar{t}$).

There are 3 leptons, electrons, muons, and tauons (e^-, μ^-, τ^-), and each lepton has a matching neutrino (ν_e, ν_μ, ν_τ), and matching anti-matter ($e^+, \mu^+, \tau^+, \bar{\nu_e}, \bar{\nu_\mu}, \bar{\nu_\tau}$). See Fig. 2.2 for a diagram of all these particles.

In high energy proton-proton collision experiments, most of the energy in the quarks are in the momentum of the particles. Therefore, particles with less mass than the b quark are approximated to be massless in most event simulations. Setting particle masses to 0 GeV despite their mass being non-zero is an approximation, and one that significantly improves computation time with negligible effects on the resulting calculations.

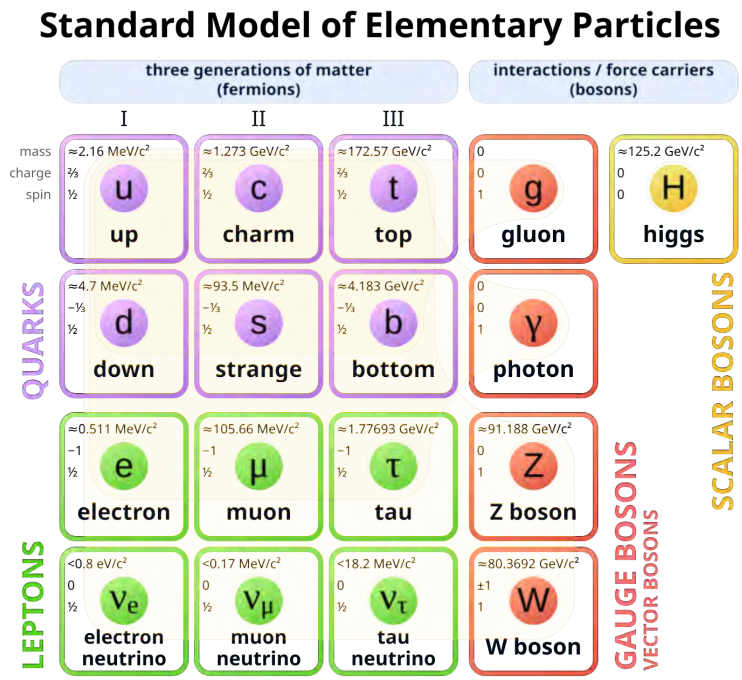

Figure 2.2: Standard Model diagram showing approximate values for masses, and grouping particles according to their symmetries. The Standard Model particle couplings are also shown in the background.

The charged current interaction is included in the overall Lagrangian with the following expression:

$$\mathcal{L}^{\text{eff}} = \frac{g}{2\sqrt{2}} \bar{f}_i \gamma^\mu (1 - \gamma^5)(T^+ W_\mu^+ + T^- W_\mu^-) f_j + \text{h.c.} \tag{2.5}$$

Here g is the weak coupling constant, γ^μ are the Dirac γ-matrices, T^+ and T^- are the weak isospin raising and lowering operators, and $W^\pm$ are the charged weak boson fields.

The full SM Lagrangian after electroweak symmetry breaking that is complete with other interactions can be viewed in [33].

2.3 Top Quark Physics

The top quark is by far the most massive quark in the Standard model with a nominal mass of 172.5 GeV [34]. This large mass gives rise to its extremely short lifetime at about 10^{-25} s [35], which is an order of magnitude shorter than the process of hadronization in QCD which is about 10^{-24} s [36]. This leads to the unusual phenomenon where the top quark decays before it has time to hadronize. Top quark bound states have not been observed yet, however, there is ongoing discussion of how the inclusion of toponium in QCD calculations might improve current QCD calculations [37].

Production of top quarks at the LHC proceeds mainly via gluon-gluon fusion where two gluons collide to produce a top-antitop quark pair. Quark-antiquark fusion also contributes to top quark pair production, but at a much lower rate. The nominal value of the top quark mass for cross-section calculations is taken to be 172.5 GeV.

The LHC produces many top quarks as the current cross-section measurement for inclusive $t\bar{t}$ is 829 pb corresponding to $N = 829$ pb $\times$ 140 fb^{-1} $= 116$ million events within ATLAS during Run 2 [38].

The decay of the top quark almost exclusively decays to a W boson and a bottom quark (99%). The bottom quark undergoes gluon emission and subsequent hadronization forming a conical spray of particles (jet) which will be discussed in Chapter 4. The W boson undergoes decay into either a lepton neutrino pair (32%), or a quark-antiquark pair (68%) [39].

In the case of a quark-antiquark pair decay of the W boson, two additional jets will be produced. In the case of a lepton neutrino pair, a lepton and missing transverse energy will be observed in the detector.

In top quark pair production, then, there are a number of possible final states that can be observed in the detector. If neither W bosons from the top pairs decay into a lepton, the event will be fully hadronic. If one W boson decays leptonically, then one lepton will be observed which is called the semi-leptonic channel. If both W bosons decay leptonically, then two leptons will be observed which is called the dilepton channel in $t\bar{t}$ production. The branching fraction of the top quark decaying leptonically is ≈ 0.326 [33]. A pie chart describing the probability of decaying into each channel is shown in Fig. 2.3.

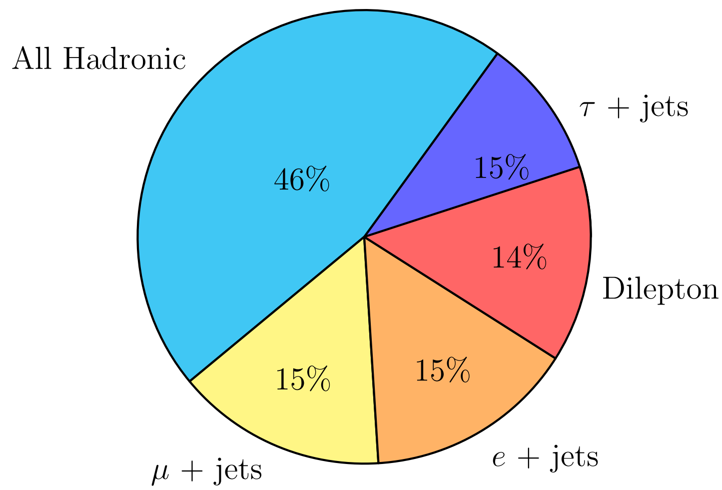

Figure 2.3: Breakdown on $t\bar{t}$ decay channels. μ + jets and e + jets are considered to be the single lepton channel. τ + jets is a very small channel usually considered on its own.

The all-hadronic channel is significantly less precise, but has the possibility to probe highly-boosted top quarks. The all-hadronic channel is dominated by QCD multijet which has high modeling uncertainties. The lepton + jets channel has infinite statistics due to the efficient ATLAS lepton triggers. Lepton + jets channel has single top t-channel, W+jets and some multi-jet backgrounds. The dilepton channel has the most precise results. Although, this channel composes the smallest branching ratio compared to the other 2 channels. The analysis is this work focuses on the single lepton plus jets channel which excludes the all hadronic channel and the dilepton channel.

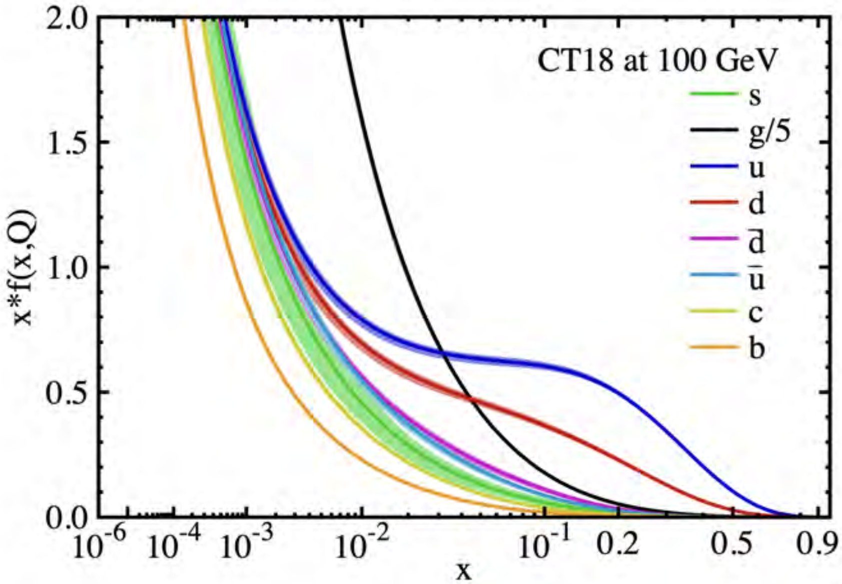

Figure 2.4: CT18 PDF set [42] with $Q^2 = 100$ GeV plotted as the PDF multiplied by the momentum fraction x.

2.4 Proton-Proton Collisions and Parton Distribution Functions

To study the fundamental particles of nature, proton-proton collisions at the Large Hadron Collider (LHC) at CERN are observed. At the LHC, the interacting constituents of protons are typically gluons, which, along with quarks, form the proton's internal structure. The probability of finding a specific parton (quark or gluon) carrying a fraction x of the proton's momentum at a given energy scale Q is described by the parton distribution functions (PDFs). These functions are extracted from experimental data, primarily from deep inelastic scattering, such as those performed at HERA [40]. PDFs also evolve with scale according to the DGLAP equations [41].

PDF distributions are typically plotted as the product of the probability density and momentum fraction to account for steep slopes at small x. The CT18 PDFs are shown in

Fig. 2.4. As seen in the figure, it is most likely to find that the up quark carries most of the momentum fraction of the proton due to it being a valence quark. The down quark carries the next highest momentum fraction, followed by the heavier flavor quarks which tend to carry a small momentum fraction of the proton.

At μ_F, non-perturbative physics is absorbed into the PDFs, while the remaining hard scattering process can be computed perturbatively. PDFs are thus evaluated at μ_F, and their scale dependence is governed by the DGLAP evolution equations.

The leading order QCD prediction cross-section with a final state Y of a collision between two protons therefore takes the form

$$\begin{aligned}\sigma(p(P_1) + p(P_2) \to Y + X) = \int_0^1 dx_1 \int_0^1 dx_2 \sum_f f_f(x_1, \mu_F) f_{\bar{f}}(x_2, \mu_F) \\ \times \sigma(q_f(x_1 P) + q_{\bar{f}}(x_2 P) \to Y, \mu_F, \mu_R),\end{aligned} \tag{2.6}$$

Here the sum runs over every quark flavor and X denotes any hadronic final state. $f_f(x_1, \mu_F)$ and $f_{\bar{f}}(x_2, \mu_F)$ denote the parton distribution functions with quark flavor f and $\bar{f}$. The cross-section is now calculated as a function of momentum fractions. In this computation the cross-section is calculated with quark q_f with momentum $x_1 P$ and quark $q_{\bar{f}}$ with momentum $x_2 P$. The final step of the calculation is then to compute the integral over all momentum fractions x_1 and x_2. More details on PDFs can be found in [16].

2.5 Heavy W' Boson Signal Model

This study defines a specific Beyond the Standard Model (BSM) theory, following the philosophy that, while model-agnostic approaches are valuable for confirming consistency with the

Standard Model, they are limited in specifying new physics, and thus this work focuses on a particular BSM scenario involving a heavy-philic W' boson. This particle has a Lagrangian set up to ensure that the W' boson only couples to the third generation of quarks, and doesn't couple to leptons. The mass is set to an unknown parameter that can be adjusted. When calculating the fixed order QCD calculation of the heavy-philic W' boson, orders up to next-to-leading order (NLO) are performed. This includes up to 3 vertices in the considered interaction diagrams.

There have been several studies that have searched for a W' boson such as [27] where the search is performed with a SM like W' boson which decays into a top and bottom and looking in the 0 lepton and single lepton channel. In [28], the search is conducted on a SM like W' boson that decays into a tau-neutrino pair. However, both assume a SM-like W' boson where the W' boson is produced directly by the proton partons with $u\bar{u}$, $d\bar{d}$, $s\bar{s}$ and $c\bar{c}$.

If the heavy-philic W' boson does not couple to the first two generations of quarks, the production mode of the W' boson changes drastically. Production of the W' boson can no longer occur directly from the proton partons. Primary production comes from gg with small amplitudes coming from a gluon interacting with a quark from the other proton.

In Fig. 2.5, a leading order Feynman diagram of the heavy-philic W' boson in the 4-flavor parton scheme is shown. This diagram includes the effects of two gluons coming together, each splitting into a quark pair where one of them splits into a bottom pair, and the other a top pair. One of the top quarks and one of the bottom quarks then form the W' boson.

This Feynman diagram represents a contribution to the matrix element calculation for the W' process, which determines the probability of producing a bottom quark, a top quark, and a W' boson when two gluons interact.

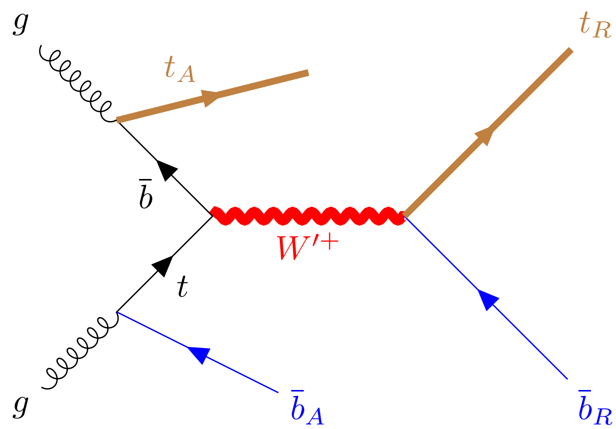

Figure 2.5: Leading order Feynman diagram for heavy-philic W' boson production. This study uses the convention where the spatial dimension is vertical. To produce the heavy-philic W' boson, gluons from the incoming protons undergo pair production of a top pair and bottom pair which can then produce the resonance particle.

The interactions that heavy-philic W' boson has between the Standard Model particles is described by the Lagrangian term:

$$\mathcal{L}^{\text{eff}} = \frac{V_{f_i f_j}}{2\sqrt{2}} g_{W'} \bar{f}_i \gamma_\mu \left[\alpha_R^{f_i f_j}(1+\gamma^5) + \alpha_L^{f_i f_j}(1-\gamma^5) \right] W'^{\mu} f_j + \text{h.c.}, \tag{2.7}$$

where $V_{f_i f_j}$ is the analogue of the Cabibbo-Kobayashi-Maskawa (CKM) matrix if f_i and f_j represent quarks. Specifically, in this heavy-philic W' boson model, the matrix $V_{f_i f_j}$ has values given by

$$V_{f_i f_j} = \begin{bmatrix} V_{ud} & V_{us} & V_{ub} \\ V_{cd} & V_{cs} & V_{cb} \\ V_{td} & V_{ts} & V_{tb} \end{bmatrix} = \begin{bmatrix} 0 & 0 & 0 \\ 0 & 0 & 0 \\ 0 & 0 & 1 \end{bmatrix}$$

While for leptons $V_{f_i f_j}$ is the null matrix. The coupling strength of the W' boson is $g_{W'}$ (aka g'). Two parameters, $\alpha_R^{f_i f_j}$ and $\alpha_L^{f_i f_j}$, are inserted into the modified Lagrangian to be able to regulate the chirality fraction of the modeled W' boson. For samples that are

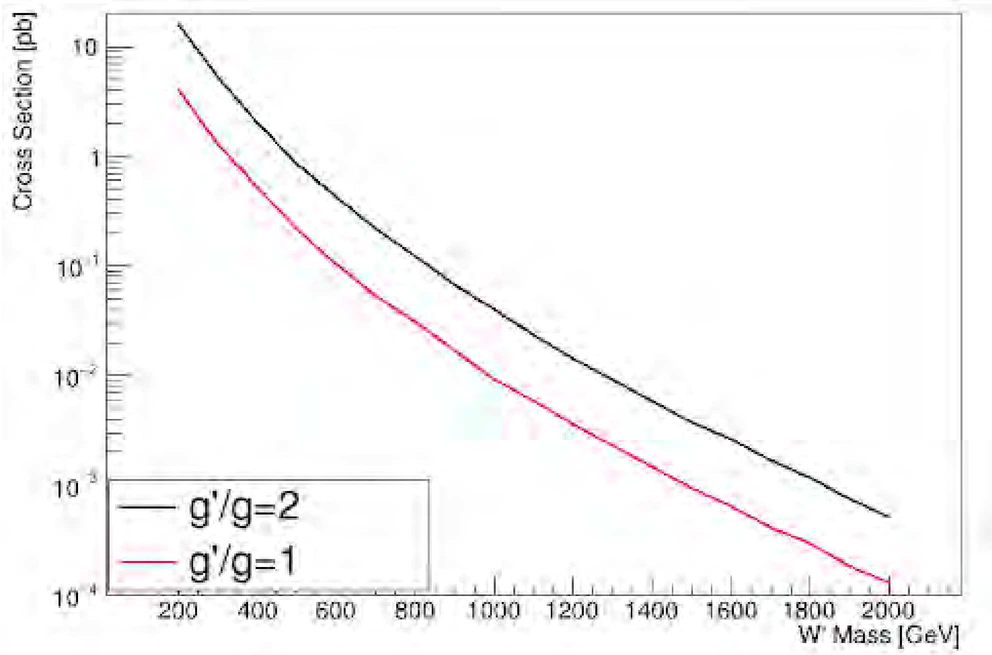

Figure 2.6: Theoretical production cross-section predictions for the LH heavy-philic W' boson as a function of W' mass.

generated for a pure right-handed (RH) W' boson, the coupling parameters are defined as $\alpha_R^{f_i f_j} = 1$ and $\alpha_L^{f_i f_j} = 0$. For samples generated with a purely left-handed (LH) W' boson, the coupling parameters are defined as $\alpha_L^{f_i f_j} = 1$ and $\alpha_R^{f_i f_j} = 0$. The cross section for the heavy-philic W' boson production can be seen in Fig. 2.6.

No significant interference is expected between the heavy-philic W' boson and the SM W boson. This is due to the distinct coupling structure of the W', which couples exclusively to third-generation quarks, and the fact that the relevant initial state, composed of a top and bottom quark, is highly suppressed in the SM. As a result, the SM contribution to this process is small, and any potential interference is negligible.

Chapter 3

The LHC and the ATLAS Detector

3.1 The LHC Facility

The Large Hadron Collider (LHC) [43] is a particle accelerator located on the French-Swiss border near Geneva, Switzerland [44]. It was built by the European Organization for Nuclear Research (CERN). This accelerator was originally designed to be a Higgs boson factory, which had previously been theorized, and then experimentally observed after several years of operation and analysis. The LHC has a synchrotron design which collides two beams of protons that travel in opposite directions at near the speed of light. There are 4 collision centers around the LHC ring. The LHC's 27 km circular tunnel is buried underground to prevent background radiation from interfering with data collection, and to protect personnel from exposure to the high amount of radiation.

The energy of the LHC started at 7 TeV during the first run, which occurred between 2010 and 2011. The energy was then increased to 8 TeV during the next period of data-taking during 2012. Subsequent shutdown of the LHC lasted for 2 years where some equipment was replaced and upgraded. The next period of data taking was called Run-2 which lasted between 2015 and 2018. The center of mass energy was increased to 13 TeV for this period. A total of about 140 fb^{-1} of data was collected at this time.

The next period of data taking then began in 2023 after a long shutdown. This period of data is called Run-3 and collided protons at an center of mass energy of 13.6 TeV. A total of about 31 fb^{-1} of data has been taken at this center of mass energy.

In order to get to the unprecedented CME collision energy, the proton beam goes through several steps that subsequently increase the proton energy. The protons begin by being accelerated through the LINAC 2 linear accelerator. They then enter into the Proton Synchrotron Booster (PSB). At this stage, they have 1.4 GeV. The protons then enter into the Proton Synchrotron (PS), and are accelerated to 450 GeV. Then finally the protons enter into the LHC in bunches composed of about 10^{11} protons. These bunches are separated by 25 ns which gives the possibility to store up to 2500 bunches for each beam.

The LHC then continues to hold these protons in its ring until the beam is dumped. This occurs if the beam becomes unstable, or the beam has lost enough intensity. Protons eventually fall out of the ring over time despite the magnets that are placed to keep them in the ring.

Four collision sites exist at the LHC, and at each of these locations, a unique particle detector measures collisions at its site. The two large detectors are located on opposite sides of the LHC: ATLAS(A Toroidal LHC ApparatuS) and CMS(Compact Muon Solenoid). The two other detectors are ALICE (A Large Ion Collider Experiment) and LHCb (LHC-beauty). ALICE specifically studies the properties of the quark-gluon plasma with proton-lead and lead-lead collisions whereas LHCb studies b-hadron physics. This thesis will focus on experiments within the ATLAS detector.

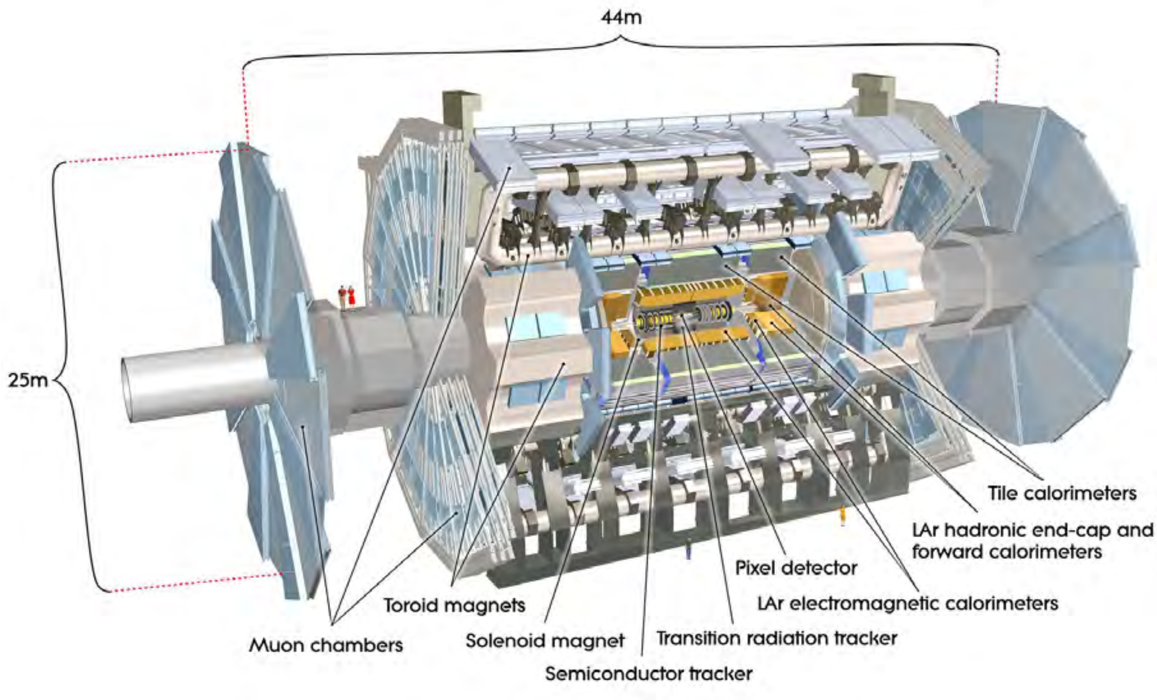

Figure 3.1: A cutout of the ATLAS detector labeling all the significant detector components [46].

3.2 The ATLAS Detector

The ATLAS experiment at the LHC is a multipurpose particle detector with a cylindrically symmetric geometry and a near 4π solid angle coverage [45]. See Fig. 3.1 to reference the locations of all the detector components.

It is approximately 46 meters in length, 25 meters in diameter, and weighs 700 tons. It consists of an inner detector for tracking surrounded by a thin superconducting solenoid which provides a 2 T axial magnetic field, electromagnetic and hadronic calorimeters, and a muon spectrometer. ATLAS uses a right-handed coordinate system with its origin at the nominal interaction point in the center of the detector and its z-axis along the beam pipe. The x-axis points from the interaction point towards the center of the LHC ring, and the y-axis points upwards. Cylindrical coordinates (r, ϕ) are used in the transverse plane, with ϕ being the azimuthal angle around the z-axis. The pseudo-rapidity is defined in terms of the polar angle θ as $\eta = -\ln\tan(\theta/2)$. Angular distance is measured in units of $\Delta R \equiv \sqrt{(\Delta\eta)^2 + (\Delta\phi)^2}$.

Particles created from the proton collisions begin in the center of the cylinder where they are tracked by the inner detector which consists of silicon pixel, silicon microstrip, and transition-radiation tracking detectors. An innermost pixel layer is inserted at a radius of 3.3 cm. Next particles traverse through the Lead/liquid-argon (LAr) sampling calorimeters provide electromagnetic (EM) energy measurements with high granularity. Finally, hadrons traverse through a hadronic calorimeter which covers the central pseudo-rapidity range of $|\eta| < 1.7$. All hadrons are stopped here. Neutrinos have almost no chance of interacting with the detector, and therefore escape without being detected.

Each particle will travel through the detector in different paths. Particles with charge will traverse a curved trajectory due to the strong magnetic field. Photons, and electrons are stopped in the electromagnetic calorimeter. Hadrons are stopped in the hadronic calorimeter. Muons are measured in the muon spectrometer but are likely to escape the detector volume. Neutrinos almost always escape without any interaction within the detector volume.

3.2.1 Calorimetry

The ATLAS calorimeter system covers the range $|\eta| < 4.9$ and is designed to meet the specific needs of obtaining measurements for different physics objects while adapting to its radiation environment. It consists of electromagnetic (EM) and hadronic calorimeters, optimized for measuring electrons, photons, jets, and missing transverse energy (E_T^{miss}).

The EM calorimeter is a liquid argon (LAr) sampling detector with lead absorber plates, divided into a barrel ($|\eta| < 1.475$) and two end-cap components ($1.375 < |\eta| < 3.2$), housed

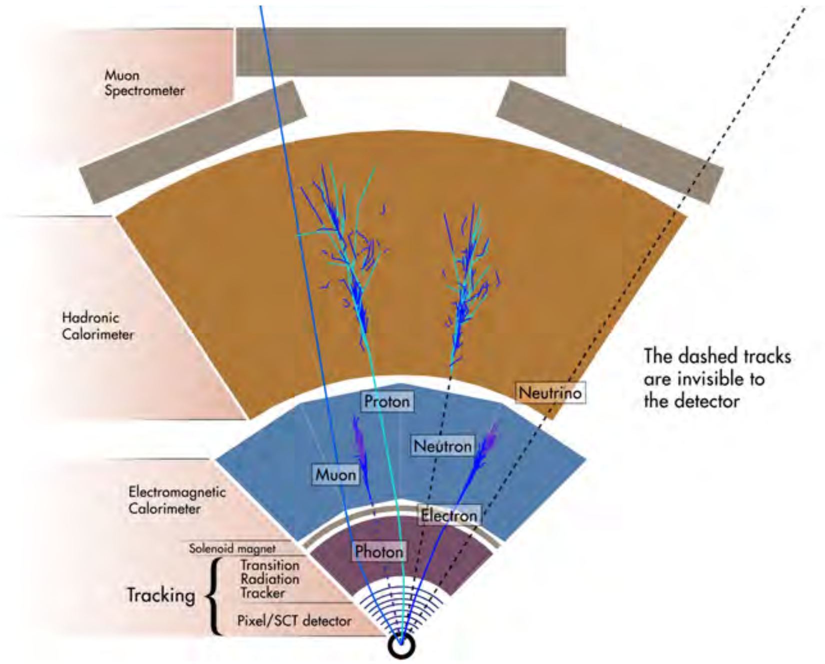

Figure 3.2: A depiction on the different paths particles produced at the collision site within the ATLAS detector traverse. Image from [47]

in separate cryostats. Its accordion geometry ensures uniform energy resolution, while the total thickness exceeds 22 radiation lengths (X_0) in the barrel and 24 X_0 in the end-caps. X_0 is the average distance over which the energy of an electron is reduced by the factor $1/e$ by bremsstrahlung [48]. The EM calorimeter plays a crucial role in electron and photon energy reconstruction.

The hadronic calorimeter comprises three sections: the tile calorimeter [49], LAr hadronic end-caps, and the LAr forward calorimeter [50, 51]. The tile calorimeter ($|\eta| < 1.7$) consists of steel absorber plates and plastic scintillators, segmented into depth layers for precise energy measurements. The LAr hadronic end-caps ($1.5 < |\eta| < 3.2$) share cryostats with the EM end-caps, ensuring seamless energy measurement transitions. The forward calorimeter, integrated into the end-cap cryostats, is designed for high radiation tolerance, with copper and tungsten modules measuring electromagnetic and hadronic interactions, respectively.

The entire system is structured to provide strong containment of electromagnetic and hadronic showers while maintaining high energy resolution, ensuring accurate particle energy measurements crucial for physics analyses at ATLAS.

3.2.2 The Muon Spectrometer

Muons, due to their higher mass and relatively long lifetimes, can traverse the inner detector (ID) and calorimeters without depositing significant energy. To detect and measure muons, the muon spectrometer is employed [52, 53]. This spectrometer, the largest and outermost component of the detector, is surrounded by a system of three toroidal magnetic fields. As muons pass through these fields, they experience the Lorentz force, causing their trajectories to curve. By analyzing this curvature, the momentum of the muons can be determined.

The muon system is divided into two main regions:

- **Barrel Region:** Consists of three cylindrical layers concentric with the beam axis.
- **End-Cap Region:** Features three layers of chambers arranged perpendicular to the beam axis.

The system is composed of both precision tracking and triggering components designed for high-resolution measurements and efficient particle detection across various pseudorapidity regions. The precision tracking subsystem includes Monitored Drift Tubes (MDTs), which provide a fine z-axis spatial resolution of $35\mu m$ and cover the central to forward region of the detector up to $|\eta| < 2.7$. Complementing the MDTs in the forward region are the Cathode Strip Chambers (CSCs), which operate in the range $2.0 < |\eta| < 2.7$ and offer an $R \times \phi$ resolution of $40\,\mu m \times 5\,\mathrm{mm}$. For triggering, the system utilizes Resistive Plate Chambers (RPCs) in the barrel region ($|\eta| < 1.05$), capable of providing 10mm resolution in both the z and ϕ directions. In the end-cap region ($1.05 < |\eta| < 2.7$), Thin Gap Chambers (TGCs) are employed, delivering resolutions between $2-6\,\text{mm}$ in R and $3-7\,\text{mm}$ in ϕ. Together, these components ensure both precise tracking and fast, reliable triggering across the detector.

In addition to tracking, the trigger components contribute independent tracking information in the orthogonal direction of the inner tracking detector. It also provides timing resolution critical for bunch-crossing identification.

Recent upgrades to the ATLAS detector has replaced the MDT with small Muon Drift Tubes (sMDT) that significantly increases the position resolution. Michigan State University fabricated the tubes that were put into chambers at University of Michigan, which were eventually installed in the ATLAS detector. This was the qualification task for my ATLAS authorship, and more is discussed in the Appendix 2.

3.3 Luminosity and the Trigger Systems

The integrated luminosity of all run-2 data is 139 fb^{-1}. This corresponds to a staggering 10^{13} inelastic proton-proton scattering events within the ATLAS detector. Due to limitations in extracting and recording events, it is impossible to record every proton-proton collision event. In order of overcome this problem, a 2-tier trigger system is implemented. One is implemented at the hardware level which cuts the bandwidth information coming from the ATLAS detector. The second is implemented on the software side where cuts are made on the reconstructed objects (more on reconstruction in the next chapter).

The ATLAS trigger system rapidly identifies LHC collision events that meet predefined criteria. It consists of three progressively more selective stages: Level-1 (L1), Level-2 (L2), and the Event Filter (EF). The L1 trigger utilizes muon trigger chambers and coarse-grained calorimeter data to select events containing high-p_T muons, electrons, photons, jets, τ-leptons, and those with significant missing transverse energy (E_T^{miss}). This initial selection reduces the event rate from approximately 40 MHz to 100 kHz [54]. Additionally, the L1 trigger designates regions of interest in η-ϕ space around objects that surpass certain criteria, such as energy thresholds.

The L2 and EF triggers apply further filtering using additional detector information, including data from the tracking detector, within the designated regions of interest. These stages employ stricter selection criteria, such as higher energy thresholds and more precise object definitions, further refining the event selection process. Together, the L2 and EF triggers reduce the event rate from approximately 100 kHz to 1 kHz [55].

Careful measurement of the luminosity is crucial for any measurement because information about the total number of proton-proton collisions per unit area before the trigger system is necessary. Luminosity is measured in several ways to ensure redundancy, consistency and accuracy. The primary luminosity measurement comes from the Luminosity Detector (LUCID) which consists of Cherenkov tubes positioned near the beamline that detect particles from the proton-proton collisions. The inner detector and hadronic calorimeter provide additional cross-checks on these measurements. To calibrate these luminosity measurements, ATLAS periodically performs Van der Meer scans [31]. This involves moving the LHC beams across each other while recording collision rates.

3.4 Data Flow

Due to the large amount of data that is collected from the ATLAS detector, data is transmitted to the "Tier 0" which has the job of processing the raw data, achieving the data to tape, and registering data with the relevant catalogs [56]. The data is then distributed to "Tier 1" clusters for offline processing. Much of the offline processing happens in the 13 Tier 1 computer clusters which are made available 24/7 with support from the CERN Computing GRID. Each is responsible for storing a proportional share of the raw and reconstructed data, performing large-scale reprocessing, and storing the resulting output. "Tier 2" systems are smaller computing sites that offer universities and other scientific institutions sufficient data storage and computing power to further process data and Monte Carlo simulations from the Tier 1 sites. There are about 155 Tier 2 sites around the world.

After the data and simulation has been processed on the cloud computing clusters, further analysis is done locally. Datasets on the order of terabytes are downloaded locally to train machine learning models on local GPUs, perform the final analysis, and the final statistical fit.

Chapter 4

Event Simulation and Reconstruction

The central aim of physics—and the natural sciences more broadly—is to predict the outcome of a given initial condition. In the context of high-energy physics, outcomes follow probability distributions, and many of these distributions cannot be calculated analytically. Therefore, the Monte Carlo method is employed to approximate the theoretical probability distributions. By randomly sampling millions of events, this method approximates the theoretical distributions, with greater accuracy achieved through larger samples.

4.1 Levels of Computation

Several stages of computation have been standardized in the ATLAS collaboration, and similarly in the CMS collaboration. The first level is what is commonly called "truth" level. This is the earliest time frame where Standard Model particles are produced immediately after the proton-proton collision. This is the domain of QFT and perturbative QCD. This level is where the heavy-philic W' boson is produced, the associated top and bottom quarks, and the resulting resonant top and bottom quarks from the W' boson decay. This level is unobservable because the truth level particles decay into more stable particles before they can reach the detector volume.

The generation of truth level events comes out from the high energy tool called Madgraph [57] where the matrix element is integrated over through the use of the Monte Carlo method.

This tool allows one to generate events for a given process of interest. Fig. 2.5 shows a Feynman diagram for W' boson production, which is one of many diagrams Madgraph accounts for during event generation. The output consists of a list of n events with m features for each i particle. There are typically tens of particles at this level and tens of features for each particle such as the 4-momentum, particle ID, decay parents and decay children. There are also other particle-specific features like spin, electromagnetic charge, and QCD color charge. In comparison to the other levels of computation, this step is relatively fast.

After particle generation, particles undergo parton showering and subsequent hadronization. The tool that is used here is Pythia [58] (or Herwig [59]). This level of computation is commonly called the "particle level". At this level of computation, the output consists of a list of n events with j particles and k features. The number of particles at this stage is typically in the thousands, with several features such as 4-momentum, particle ID, and charge. Each particle at this stage is a on-shell particle such as a lepton, neutrino, or hadron. This level of computation obtains the relatively stable particles right before it enters into the detector volume. The particle level is what is used to match the truth level particles to the reconstructed level jets. This increases the accuracy of the matched reconstructed jets to the truth level particles.

The particles that are simulated from the parton showing and hadronization tool are then sent through a detector simulator. ATLAS uses GEANT4 [60] for this. GEANT4 uses the current understanding of how particles interact with matter in each detector module in ATLAS. A virtual ATLAS detector is carefully created to simulate how particles will interact with each sub component.

The results from detector simulation produce signals that can be compared to ATLAS data. However, this is very difficult to do as looking at detector responses is difficult to interpret. For example, a reading from sector 2 of the A detector side, index 5, for the odd sector on the middle barrel MDT is unwieldy. Instead, higher-level objects are created which carry much more interesting physical properties that can be understood. This process is called reconstruction where ATLAS detector responses are used as input, and the output are these higher-level objects which are discussed in the following section.

4.2 Reconstructed Objects and Event Selection

The reconstruction of physics objects in this analysis includes electrons, muons, hadronically decaying taus, jets, b-jets, and missing transverse momentum.

Electrons are reconstructed from energy clusters in the electromagnetic calorimeter matched to tracks in the inner detector (ID). They are required to have $p_T > 27$ GeV and $|\eta| < 2.47$, with candidates in the calorimeter barrel–endcap transition region ($1.37 < |\eta| < 1.52$) excluded. Identification is based on a likelihood discriminant, and electrons must satisfy impact parameter constraints ($|z_0| < 0.5$ mm and $|d_0|/\sigma_{d_0} < 5$), as well as the gradient isolation criteria. More information on electron efficiencies and methods can be found in [61, 62].

Muons are reconstructed from either track segments or full tracks in the muon spectrometer, matched to ID tracks, and re-fitted using information from both detector systems. They must satisfy $p_T > 27$ GeV, $|\eta| < 2.5$, impact parameter constraints ($|z_0| < 0.5$ mm and $|d_0|/\sigma_{d_0} < 3$), and the tight identification and FixedCutTightTrackOnly isolation criteria. More information on muon calibrations and methods can be found in [63].

Hadronically decaying tau leptons (τ_{had}) are identified using track multiplicity and a boosted decision tree incorporating track collimation, jet substructure, and kinematic properties. Candidates must satisfy $p_T > 25$ GeV, $|\eta| < 2.5$, and pass the Medium τ-identification working point. While taus are not directly used in the analysis, they are considered in the overlap removal procedure and event selection.

Jets are reconstructed from topological energy clusters in the calorimeter using the anti-k_t algorithm [64] with a radius parameter of 0.4. Each cluster is first calibrated to the electromagnetic scale response, with additional energy corrections applied using simulation and in situ data. Jets must have $p_T > 25$ GeV, $|\eta| < 2.5$, and pass quality criteria to remove those originating from non-collision sources or detector noise. To mitigate pileup effects, jets with $p_T < 120$ GeV and $|\eta| < 2.4$ are further required to be consistent with the primary vertex using the jet vertex tagger (JVT).

Jets are tagged as coming from the decay products of a b-quark. This tagging is done by using multivariate techniques that incorporate impact parameter information and secondary/tertiary vertex properties. b-tagging in this analysis uses the GN2v01 algorithm at the 77% efficiency working point, trained on simulated $t\bar{t}$ events to distinguish b-jets from light- and c-flavored jets.

The missing transverse momentum (E_T^{miss}) is computed as the negative sum of the p_T of all physics objects in the event, with an additional correction for soft energy unassociated with hard objects. This correction is based on ID tracks matched to the primary vertex to ensure resilience against pileup contamination. Only events with $E_T^{\text{miss}} > 20$ GeV are considered in this analysis.

To prevent multiple detector responses from being counted as separate objects, an overlap removal procedure is applied. Jets within $\Delta R_y = 0.2$ of a selected electron are removed to prevent double-counting of energy deposits. If a jet remains within $\Delta R_y = 0.4$ of an electron, the electron is discarded. Muons are removed if they are within $\Delta R_y < 0.4$ of a jet, unless the jet has fewer than three associated tracks, in which case the muon is retained and the jet is removed. Tau candidates are removed if within $\Delta R_y < 0.2$ of selected electrons or muons. This follows the ATLAS standard overlap removal procedure, except for tau-jet overlap removal, which is not applied to preserve analysis integrity.

Chapter 5

Search for the Heavy-philic W' Boson

5.1 Truth Level Kinematic Properties

This section describes the truth-level kinematic properties of particles involved in the production and decay of the heavy-philic W' boson, focusing on their relevance to signal selection and background rejection.

During heavy-philic W' boson production, two quarks are produced alongside the W' boson. These are referred to as the associated particles: one associated top quark and one associated bottom quark. The heavy-philic W' boson subsequently decays, and since its couplings to all generations other than the third are set to zero, it decays exclusively into a top quark and a bottom quark. These decay products are called the resonant particles. A Feynman diagram of the full process can be seen in Fig. 5.1. Thus, in total, the final state contains a resonant top quark (t_R), a resonant bottom quark (b_R), a associated top quark (t_A), and a associated bottom quark (b_A) to form a final state of $tbtb$.

Since there are two top quarks, there are three main channels; the all-hadronic, single-lepton, and dilepton channel. The branching fractions are identical to $t\bar{t}$ production and the pie chart showing the branching fractions into the different channels can be seen in Fig. 2.3

Since this is the first ever search for a heavy-philic W' boson with couplings exclusively to the third generation of quarks, the 1-lepton channel is selected as it minimizes the background

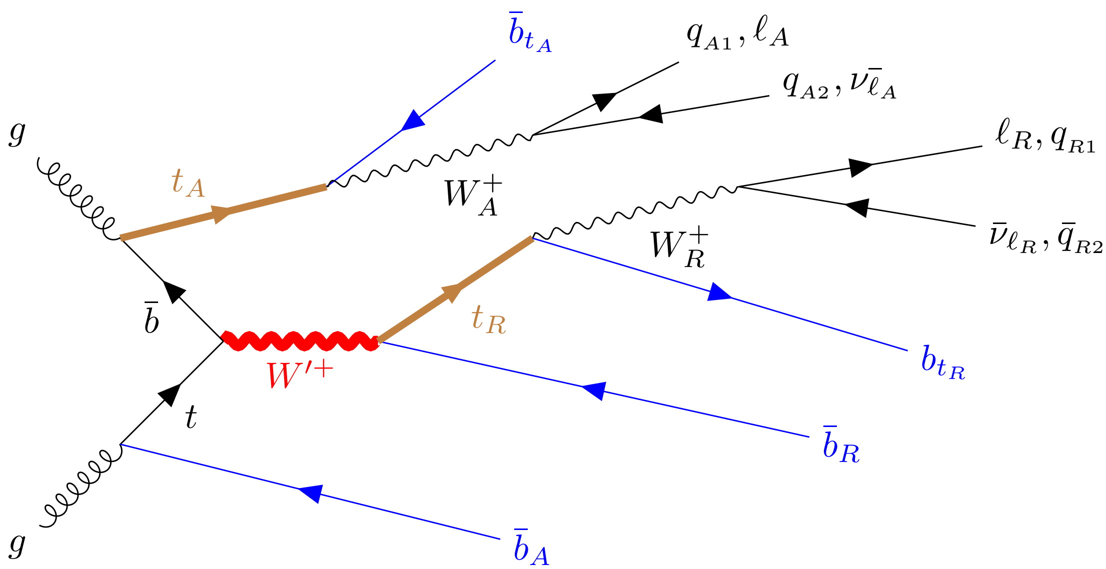

Figure 5.1: A representative Feynman diagram of the full heavy-philic W' boson production and decay into the one-lepton final state. The W' boson is rendered in bold red, the top quarks are rendered in brown, and the bottom quarks are rendered in blue for clarity. Two channels are represented in this diagram as the W bosons from the top quarks can decay leptonically or hadronically. Since this search is conducted in the single lepton channel, the lepton can come from either the t_A or the t_R.

contributions while maintaining a significant number of signal events.

Understanding the kinematic properties of the resonant and associated particles is critical for optimizing the signal region selection and for identifying the dominant Standard Model (SM) backgrounds to reject. Figure 5.2 shows the transverse momentum (p_T) and rapidity (η) distributions of the key particles in this analysis. These distributions reveal that b_R and t_R have high p_T, with the other particles having lower p_T. The b_A have the lowest p_T, and are emitted in a direction closest to the beam line.

5.2 Reconstruction Level Selection

Most of the events measured in the ATLAS detector are irrelevant to this analysis, either lacking a reconstructed electron or muon or containing only a small number of reconstructed

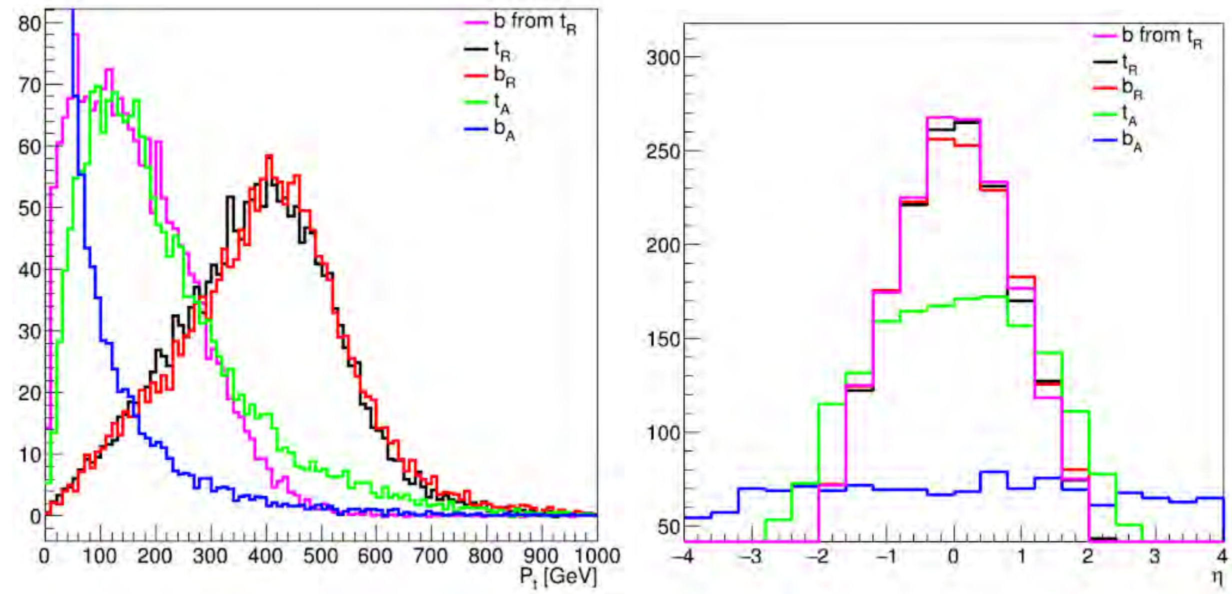

Figure 5.2: Kinematic properties of the truth LH 1 TeV W' production process. The left panel shows the transverse momentum (p_T) distribution for the resonant and associated top and bottom quarks, while the right panel shows their rapidity (η) distributions.

jets. To focus on an enriched signal region and suppress complex backgrounds, a series of selection criteria are applied. These cuts are designed to minimize contributions from complicated SM backgrounds like QCD multijet background while maintaining reasonable signal efficiency.

The signal region is defined by the following criteria:

- At least five jets
- At least two b-tagged jets
- The presence of exactly one electron or one muon

The requirement of one electron or muon helps reject the dominant QCD multijet background, which is both challenging to model and associated with large modeling uncertainties.

Theoretical cross-section predictions for heavy-philic W' boson production as a function of the W' mass are shown in Figure 2.6. These predictions indicate that the cross-section for this process is very small. This low cross-section highlights the need for a precise analysis and stringent event selection to maximize sensitivity.

After pre-selection, events are categorized into different kinematic regions based on the number of b-tagged jets. Each region has 5 or more jets, but separated based on the number of b-tags. A $t\bar{t}$ control region is defined by requiring exactly 2 b-tagged jets with $p_T > 50$ GeV. Signal region 1 (SR1) is defined by requiring exactly 3 jets being b-tagged with $p_T > 50$ GeV. Signal region 2 (SR2) is defined by requiring 4 or more b-tagged jets with $p_T > 50$ GeV.

Another cut designed to further reduce multijet background is implemented. The p_T of the MET must be greater than 20 GeV and MET+M_T^W must be greater than 60 GeV [65]. M_T^W is defined as $M_T^W = \sqrt{2p_T^{\ell}E_T^{\text{miss}}(1 - \cos\Delta\phi)}$. QCD multijet events typically don't have large MET, and typically populate low M_T^W regions.

5.3 Backgrounds

5.3.1 $t\bar{t}$ + jets

The production of $t\bar{t}$ is by far the dominant background in the region of phase space of this search. Since at least 5 jets are required, this automatically rejects many SM processes. For example, the production of two light quarks like an up quark and down quark will not pass this selection. With only two light quarks, these processes will only ever produce 2 jets and in rare cases 3 jets.

In the case where a heavy flavor quark is produced, this will lead to an increased chance of landing in the signal region. Take the example of single top production. In this example, the top quark is produced with a W boson or another quark. Top quarks undergo a decay

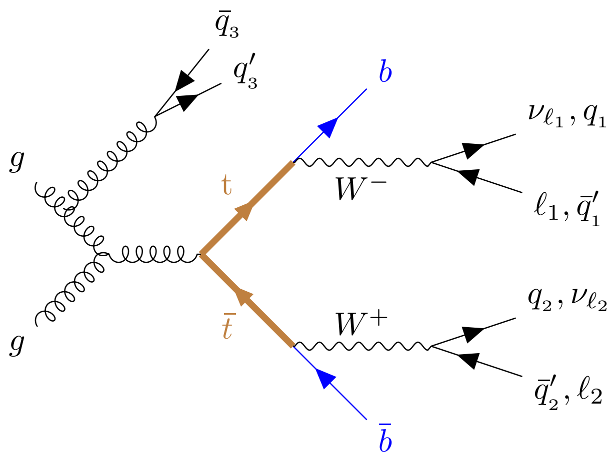

Figure 5.3: Feynman diagram of $t\bar{t}$ production via the more common gluon-gluon production mechanism. The W bosons either decay hadronicaly or leptonically. Depending on these decays, the event will fall into the three main categories (all hadronic, semi-leptonic, and dilepton).

chain that can lead to 3 quarks, and so adding together all of the decay products, 4 jets can be produced. Finally we can get an additional jet from QCD radiation, and we can get 5 jets in certain rare cases. This explains why single top background is much more common than many other Standard Model processes.

However, $t\bar{t}$ production can easily fall within the signal region as can be seen in the Feynman diagram in Fig. 5.3. To fall within the signal region one of them needs to decay hadronically and the other leptonically. Then another jet could come from QCD correction, final state radiation, or additional radiation from the parton showering in order to be put in the selection region for this analysis.

The $t\bar{t}$ cross section is relatively large compared to other Standard Model processes in the analysis region, and its higher acceptance further contributes to its dominance as a background in this phase space.

The production of $t\bar{t}$ events in this analysis is modeled using the PowhegBox v2 generator [66, 67, 68], which provides the matrix element (ME) at NLO in the strong coupling constant (α_S) with the NNPDF3.0NLO PDF set[69] and the h_{damp} parameter set to $1.5m_{top}$. The functional form of μ_f and μ_r is set to the default scale $\sqrt{m_t^2 + p_{T,t}^2}$. The events are showered with Pythia 8.230 [70].

The uncertainty due to initial-state-radiaton (ISR) is estimated using weights in the ME and in the parton shower (PS). To simulate higher parton radiation μ_f and μ_r are varied by a factor of 0.5 in the ME while using the $Var3c$ upward variation from the A14 tune. For lower parton radiation, μ_f and μ_r varied by a factor of 2.0 while using the $Var3c$ downward variation in the PS. The impact of final-state-radiation (FSR) is evaluated using PS weights which vary μ_r, for QCD emission in the FSR by a factor of 0.5 and 2.0, respectively. The impact of the PS and hadronisation model is evaluated by changing the showering of the nominal PowhegBox events from Pythia to Herwig 7.04 [71].

To assess the uncertainty due to the choice of the matching scheme, the Powheg sample is compared to a sample of events generated with MG5.aMC v2.6.0 and the NNPDF3.0NLO PDF set showered with Pythia 8.230. The shower starting scale has the functional form $\mu_q = H_T/2$, where H_T is defined as the scalar sum of all outgoing partons. Choice of μ_f and μ_r is the same as that for the Powheg setup.

5.3.2 $t\bar{t}$ HF Classification

The $t\bar{t}$ + jets background is categorized according to the flavor of additional jets in the event, using the same procedure as described in Ref. [72]. Generator-level particle jets are reconstructed from stable particles (mean lifetime $\tau > 3 \times 10^{-11}$ seconds) using the anti-k_t algorithm with a radius parameter $R = 0.4$, and are required to have $p_T > 15$ GeV and $|\eta| < 2.5$. The flavour of a jet is determined by counting the number of B- or C-hadrons within $\Delta R < 0.4$ of the jet axis. Jets matched to at least one B-hadron with $p_T > 5$ GeV are labeled as B-jets. Similarly, jets matched to at least one C-hadron (and not already identified as a B-jet) are labeled as C-jets. Events that have at least one B-jet, not counting heavy-flavour jets from top-quark or W-boson decays, are labeled as $t\bar{t}+\geq 1b$; those with no B-jets but at least one C-jet are labeled as $t\bar{t}+\geq 1c$. Finally, events not containing any heavy-flavour jets aside from those from top-quark or W-boson decays are labeled as $t\bar{t}+$ light. This classification is used to define the background categories in the likelihood fit.

5.3.3 $t\bar{t}$ Reweighting Technique

The $t\bar{t}$ simulation using the Powheg+Pythia generator does not accurately reproduce data at high jet multiplicities. $t\bar{t}$ mismodeling is a well known problem with high jet multiplicities. To improve the agreement between data and Monte Carlo predictions, data-driven corrections are applied to the MC samples, to aid the convergence of the fit.

Reweighting factors are derived by comparing the data and MC predictions within the $2b$-tagged control region. Since the primary source of mismodelling is assumed to be additional radiation from the parton shower these reweighting factors are also applied in the $3b$ and $\geq 4b$ regions. This is possible because additional radiation from the parton shower is largely independent of the jet flavor. This helps improve data/MC agreement, with any remaining discrepancies expected to be covered by the systematic uncertainties.

The reweighting factors are defined as:

$$R(x) = \frac{\text{Data}(x) - \text{MC}^{\text{non-}t\bar{t}}(x)}{\text{MC}^{t\bar{t}}(x)} \tag{5.1}$$

where x represents the variable misrepresented by the simulation. In this context, $t\bar{t}$ includes $t\bar{t}+>1b$, $t\bar{t}+>1c$, and $t\bar{t}+$ light-flavor jets.

Reweighting is performed sequentially using the number of jets, followed by the neural network (NN) output distribution within the $t\bar{t}$ control region. The neural network architecture and training procedure are described in detail in Section5.4. Figure5.4 shows the original jet multiplicity distribution and the corresponding weight distribution after the first reweighting step. Figure 5.5 displays the NN output distributions before and after the successive reweighting procedures. These two figures only show the $t\bar{t}$ CR.

The $t\bar{t}$ weights are applied to all $t\bar{t}$ events, independent of their heavy flavor classification. Their event weights are based on their jet multiplicity and neural network output values. To perform the neural network reweighting, a functional form combining a hyperbola and a sigmoid, given by:

$$\omega = a + \frac{b}{(x^{\mathrm{NN}} + 10)^c} - \frac{d}{1 + \exp(e - f \cdot (x^{\mathrm{NN}} + 10)}$$

is fitted to the already weighted distributions based on jet multiplicity in $t\bar{t}$ control region (see Figure 5.5). Table 5.1 provides the fitted parameters.

Other kinematic distributions within the $t\bar{t}$ control region are shown in Fig. 5.6. The plots included within this figure show the HT, number of jets, and the leading jet p_T. Perfect agreement between data and MC samples is not expected for HT or leading jet p_T, as these variables are not used in the reweighting. Additionally, discrepancies in the jet multiplicity distribution are also anticipated, since applying weights based on the neural network output slightly alters this distribution. While not shown, all distributions agree within the approximately 25% systematic uncertainty that exists in this region.

Separate histograms are created that include these $t\bar{t}$ weights and another one that doesn't include the weights. This is done to model the systematic uncertainty involved with the $t\bar{t}$

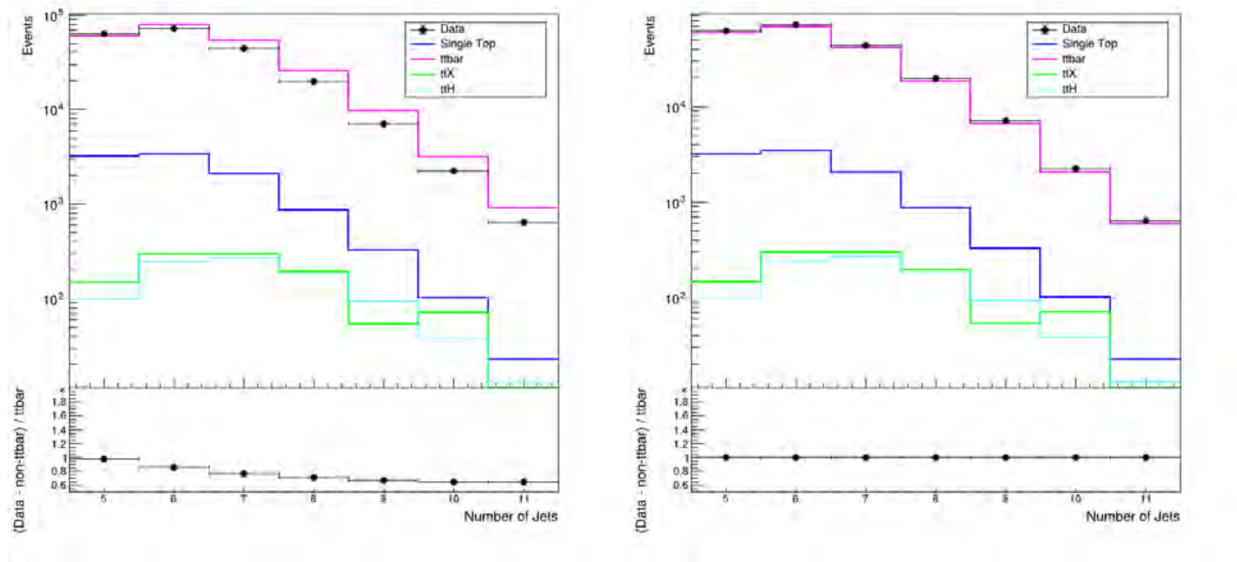

Figure 5.4: The jet multiplicity distribution before any weights are applied is shown on the left. The resulting distribution after weights based on the number of jets is applied is shown on the right.

787 reweighting uncertainty.

Region	a	b	c	d	e	f
$\geq 5j2b$	1.205	-0.2628	0.15926	-0.30738	10.683	0.81727

Table 5.1: The set of fit parameters used to perform $t\bar{t}$ reweighting based on the neural network output score.

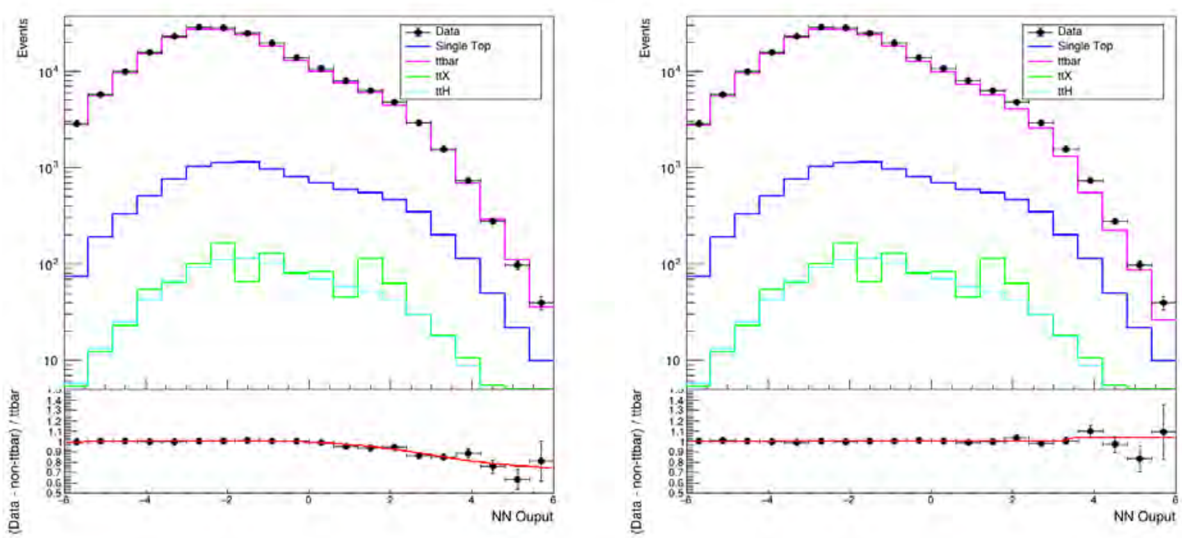

Figure 5.5: The neural network distribution before the reweighting function is applied to it is shown on the left. The neural network distribution after reweighting is shown on the right.

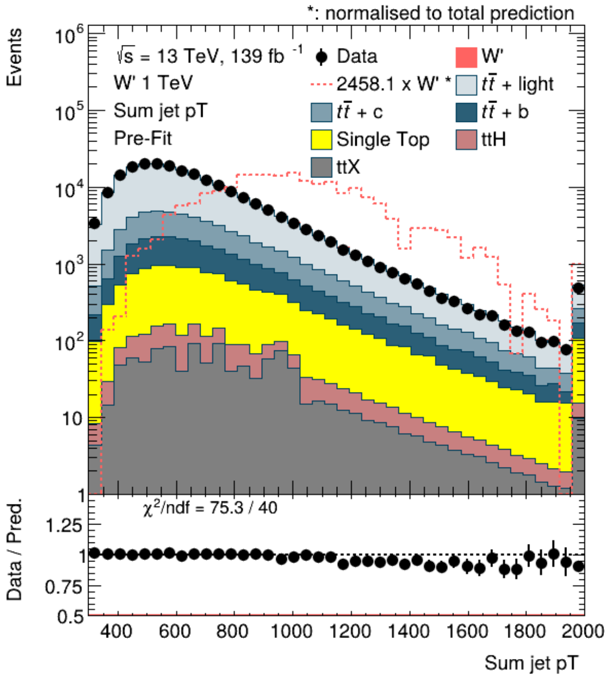

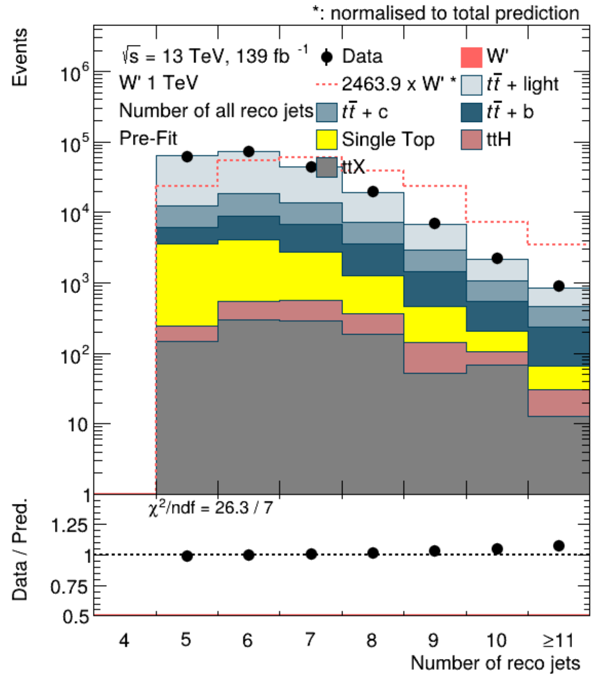

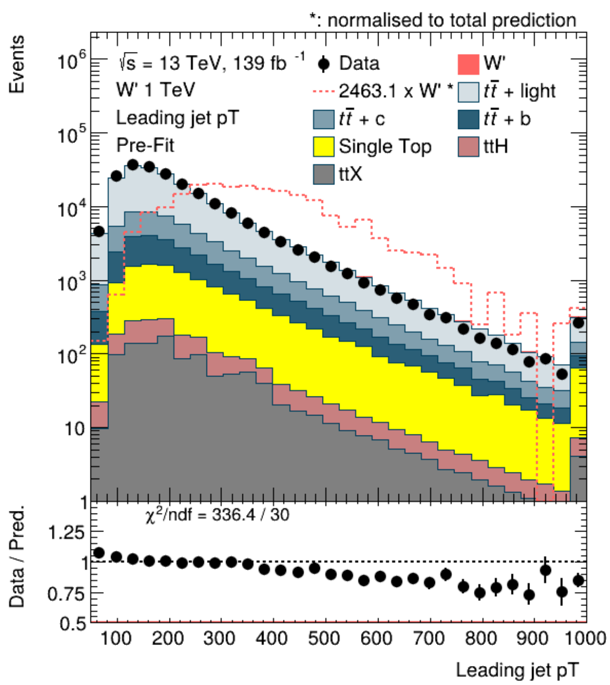

Figure 5.6: Kinematic distributions showing the full SM background distributions within the $t\bar{t}$ CR.

5.3.4 Single Top

Single top quark production is modeled separately for the t-channel, s-channel, and tW associated production modes. For each process, the nominal Monte Carlo (MC) sample is generated at next-to-leading order (NLO) in QCD using the PowhegBox v2 generator, interfaced to Pythia 8.230 for parton showering and hadronisation.

***t*-channel:** The ME is calculated at NLO in the four-flavor scheme (4FS) using the NNPDF3.0NLOnf4 PDF set. The renormalisation and factorisation scales are set to $\sqrt{m_b^2 + p_{T,b}^2}$, as recommended in Ref. [73].

***s*-channel:** The ME is calculated at NLO in the five-flavor scheme (5FS) using the NNPDF3.0NLO PDF set. The renormalisation and factorisation scales are set to the top quark mass.

***tW*-channel:** The ME is calculated at NLO in the 5FS using the NNPDF3.0NLO PDF set, with renormalisation and factorisation scales set to the top quark mass. The PowhegBox v2 generator uses the diagram removal (DR) scheme [74] to handle interference with $t\bar{t}$ production [75].

A 5% uncertainty on the cross section of each of the 3 production modes of single top is assumed in these samples.

5.3.5 $t\bar{t}V$ and $t\bar{t}H$

The production of $t\bar{t}V$ events is modeled using the MG5_aMC v2.3.3 generator [57], which provides the ME at NLO in α_S with the NNPDF3.0NLO PDF set [69]. The functional form of μ_f and μ_r is set to the default scale $0.5 \times \Sigma_i \sqrt{m_i^2 + p_{T_i}^2}$, where the sum runs over all the particles generated from the ME calculation. The events are showered with Pythia 8.210.

A 15% uncertainty in the total cross section for $t\bar{t}V$ is assumed. In this work, the notations $t\bar{t}V$ and $t\bar{t}X$ are used interchangeably.

The production of $t\bar{t}H$ events is modeled in the 5F scheme using the PowhegBox generator [76] at NLO in α_S with the NNPDF3.0NLO PDF set. The h_{damp} parameter is set to $3/4\ \dot{(}m_t + m_{tbar} + m_H) = 352.5$ GeV. The events are showered with Pythia 8.230. A 10% uncertainty in the total cross section for $t\bar{t}H$ is assumed.

5.3.6 Other Rare Backgrounds

The rare top processes that are considered in this analysis are tZq, tZW, 4-top, and diboson events. Once these samples were run through the pre-selection requirements, there were determined to be insignificant ($< 1\%$) and are excluded from the analysis.

5.3.7 Background Composition and Kinematic Properties

In this analysis, we look at the region that includes 1 electron or 1 muon exclusively. At least 5 jets are required, and 2 of them must be b-tagged. In this region, there is still abundant SM background. The biggest contribution is $t\bar{t}+$ jets , but several other processes still exist in this region and the summary of the backgrounds in these regions can be found in Table 5.2.

Several kinematic properties of the reconstructed events are shown in the figures below and include figures for both SR1 and SR2. Fig. 5.8 shows the leading jet p_T and η. Fig. 5.9 shows the second leading jet p_T and η. Fig. 5.10 shows the reconstructed lepton p_T and η. Fig. 5.11 shows HT and MET. Finally, Fig. 5.12 shows the multiplicity of jets.

Table 5.2: Yields of the analysis. Statistical uncertainties are shown in parenthesis.

	CR: 2b	SR1: 3b	SR2: $\geq$ 4b
$t\bar{t}$ + light	152 000(34000)	3400(1000)	19(11)
$t\bar{t}$ + c	29 100(6700)	2090(860)	37.6(120)
$t\bar{t}$ + b	15 000(3500)	8400(2300)	1120(520)
Single Top	10 000(1300)	703(100)	51.2(130)
ttH	945(96)	507(51)	145(15)
ttV	1070(160)	48.0(73)	2.79(44)
1 TeV LH W'	89.8(46)	85.8(46)	26.1(15)
Total	208 000(40000)	15 200(3000)	1400(520)
Data	209 345	18 865	1836

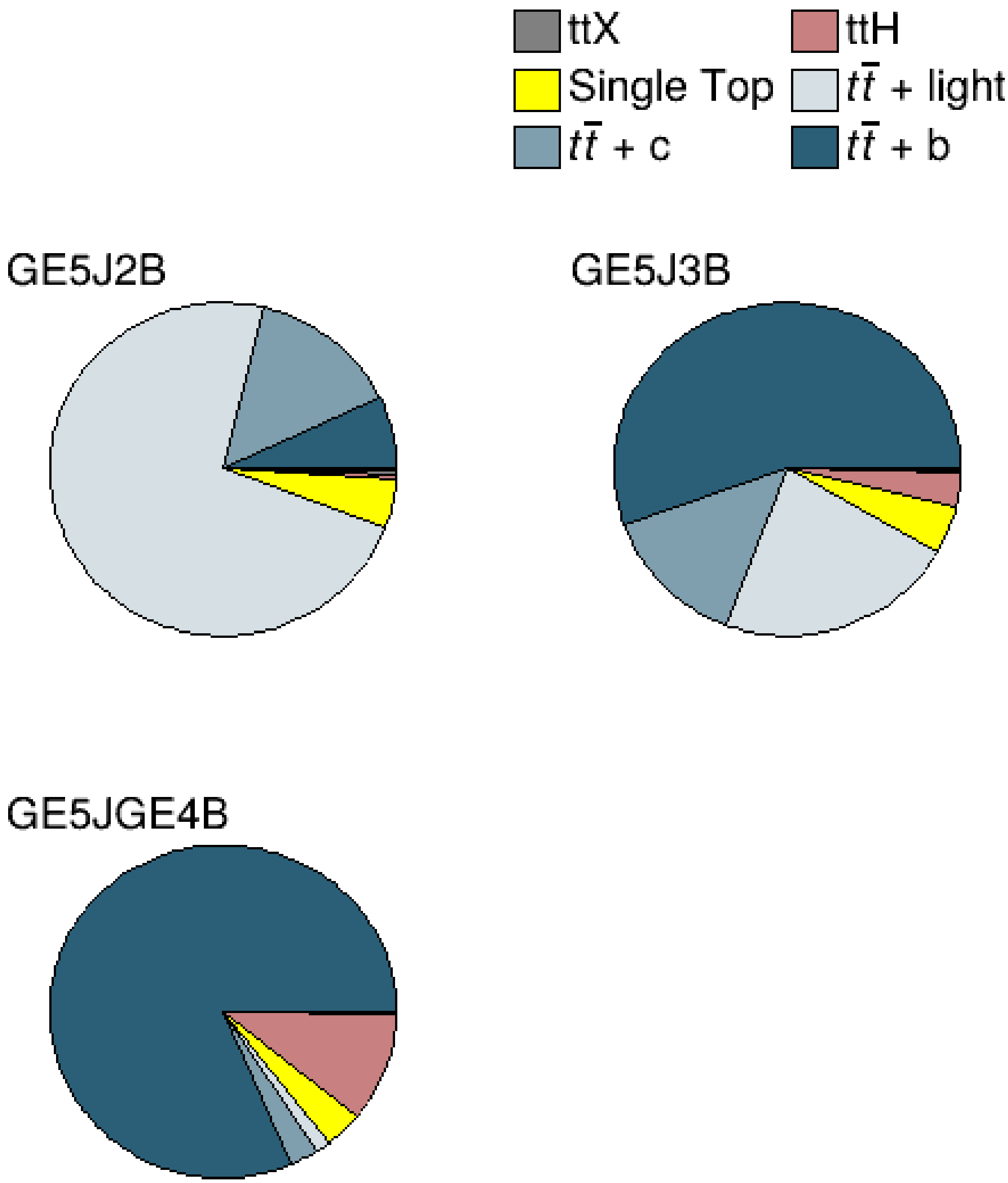

Figure 5.7: A pie chart representing the dominant background contributions in the region for this search.

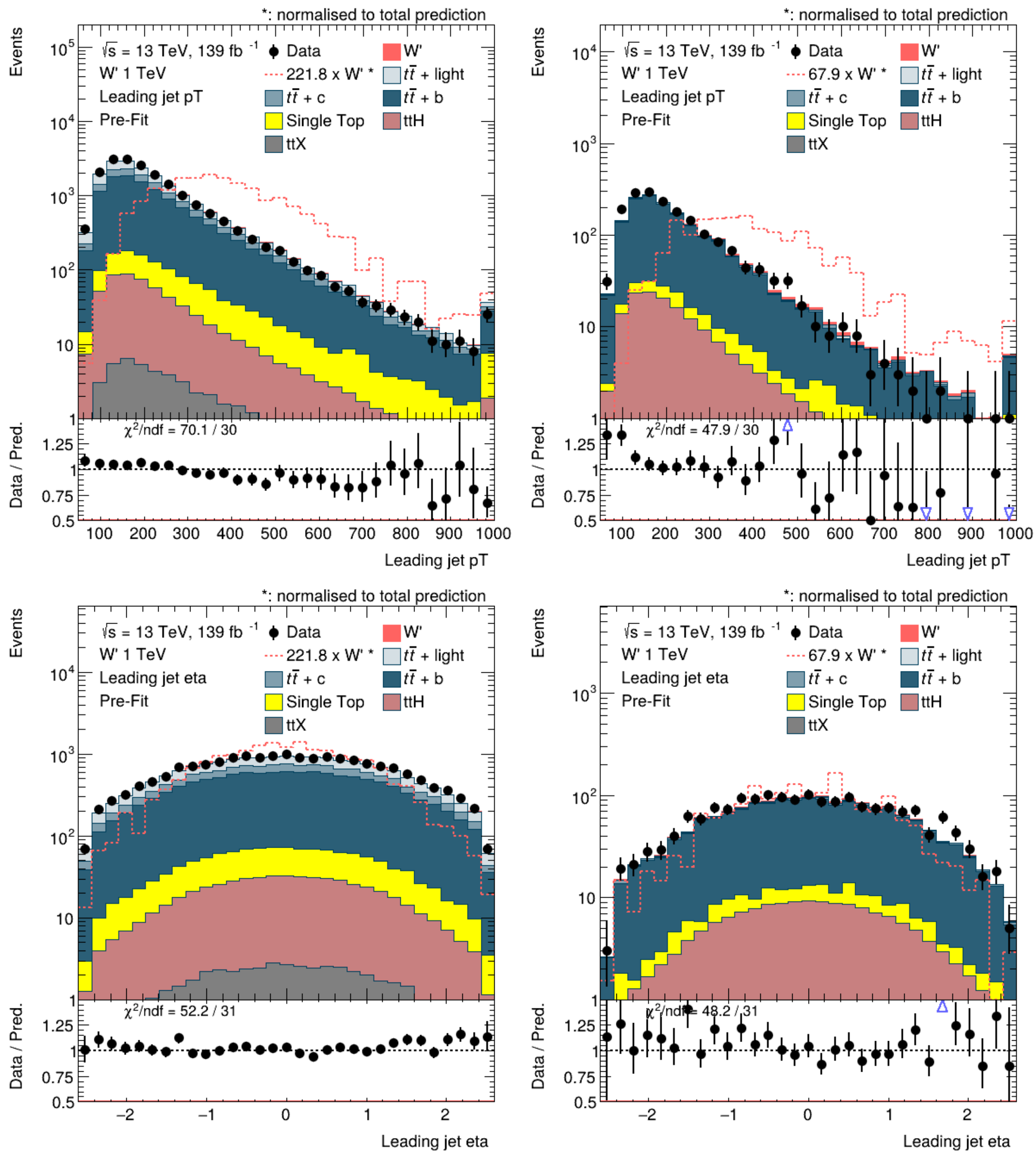

Figure 5.8: Kinematic distributions of background and signal in SR1 (left) and SR2 (right). Each bin in SR1 carries about 15% and in SR2 about 25% systematic uncertainty.

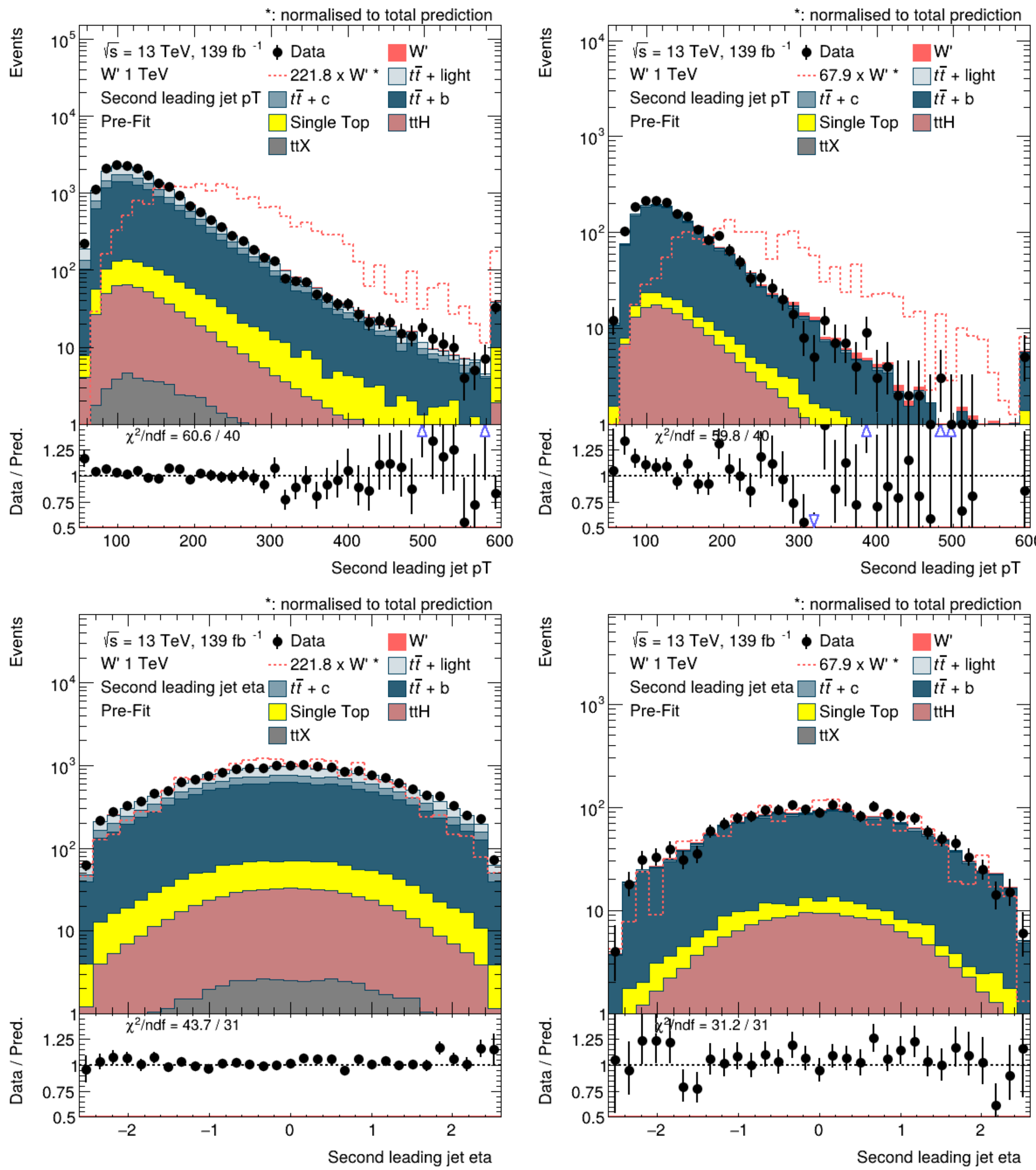

Figure 5.9: Kinematic distributions of background and signal in SR1 (left) and SR2 (right). Each bin in SR1 carries about 15% and in SR2 about 25% systematic uncertainty.

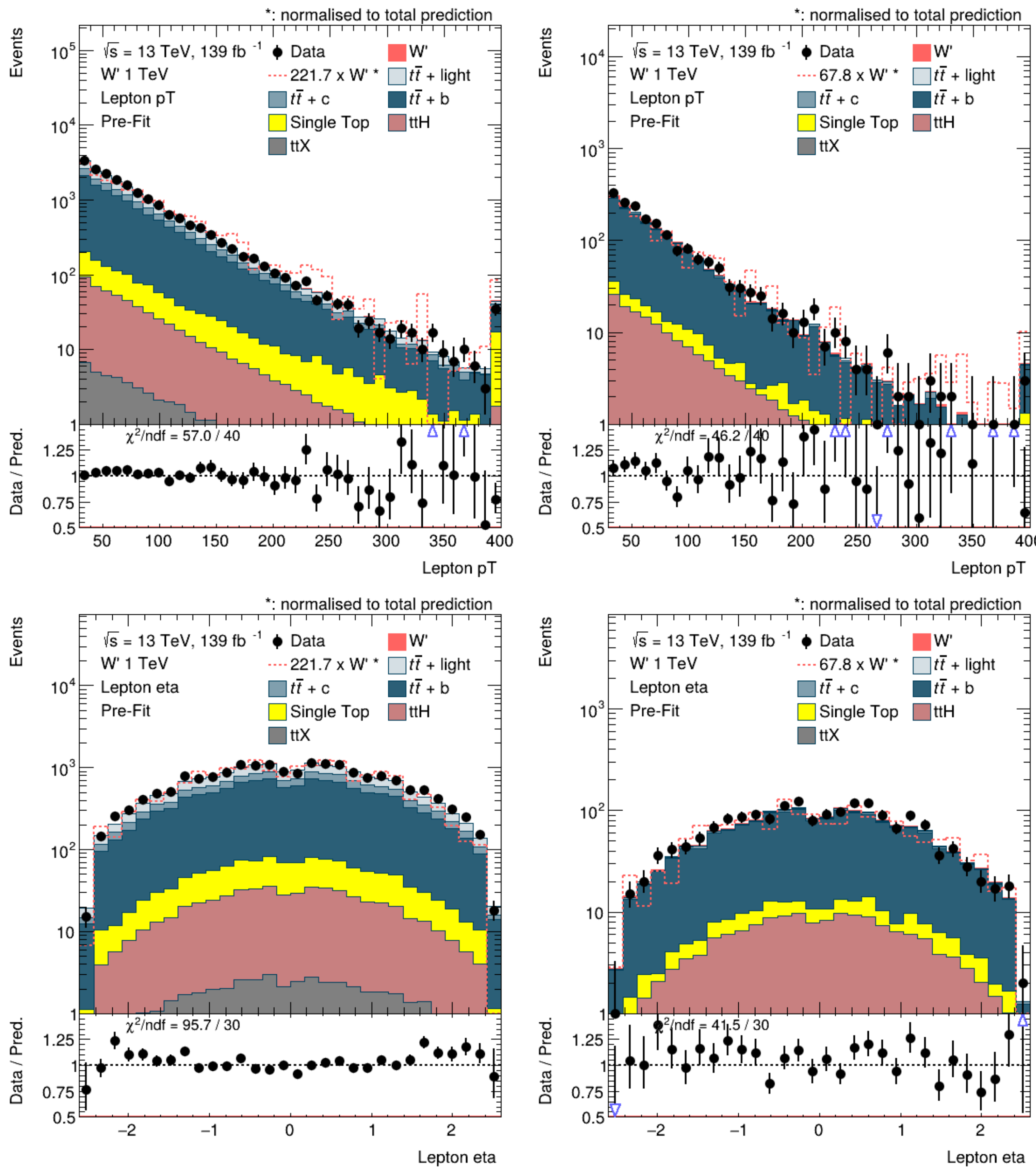

Figure 5.10: Kinematic distributions of background and signal in SR1 (left) and SR2 (right). Each bin in SR1 carries about 15% and in SR2 about 25% systematic uncertainty.

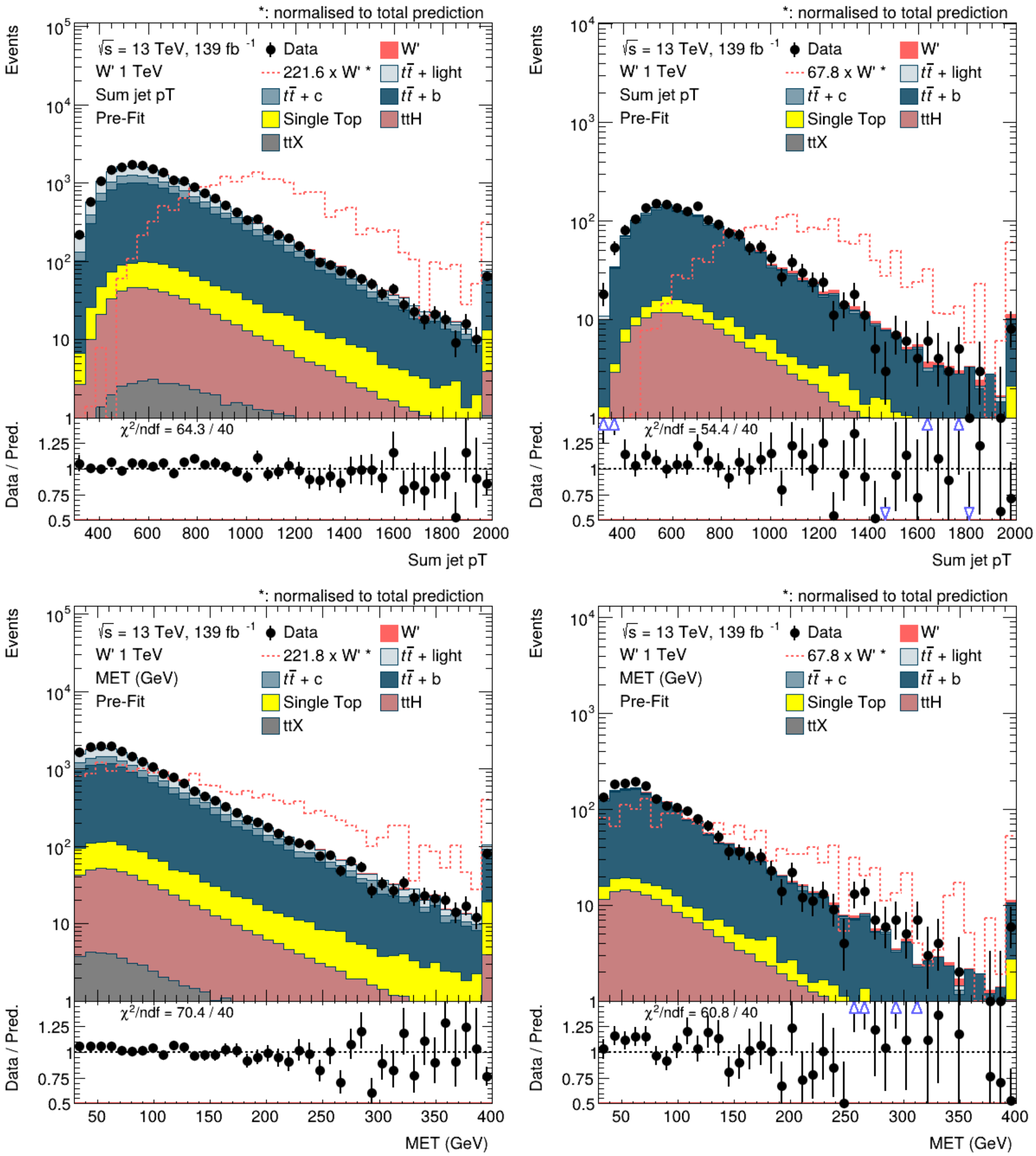

Figure 5.11: Kinematic distributions of background and signal in SR1 (left) and SR2 (right). Each bin in SR1 carries about 15% and in SR2 about 25% systematic uncertainty.

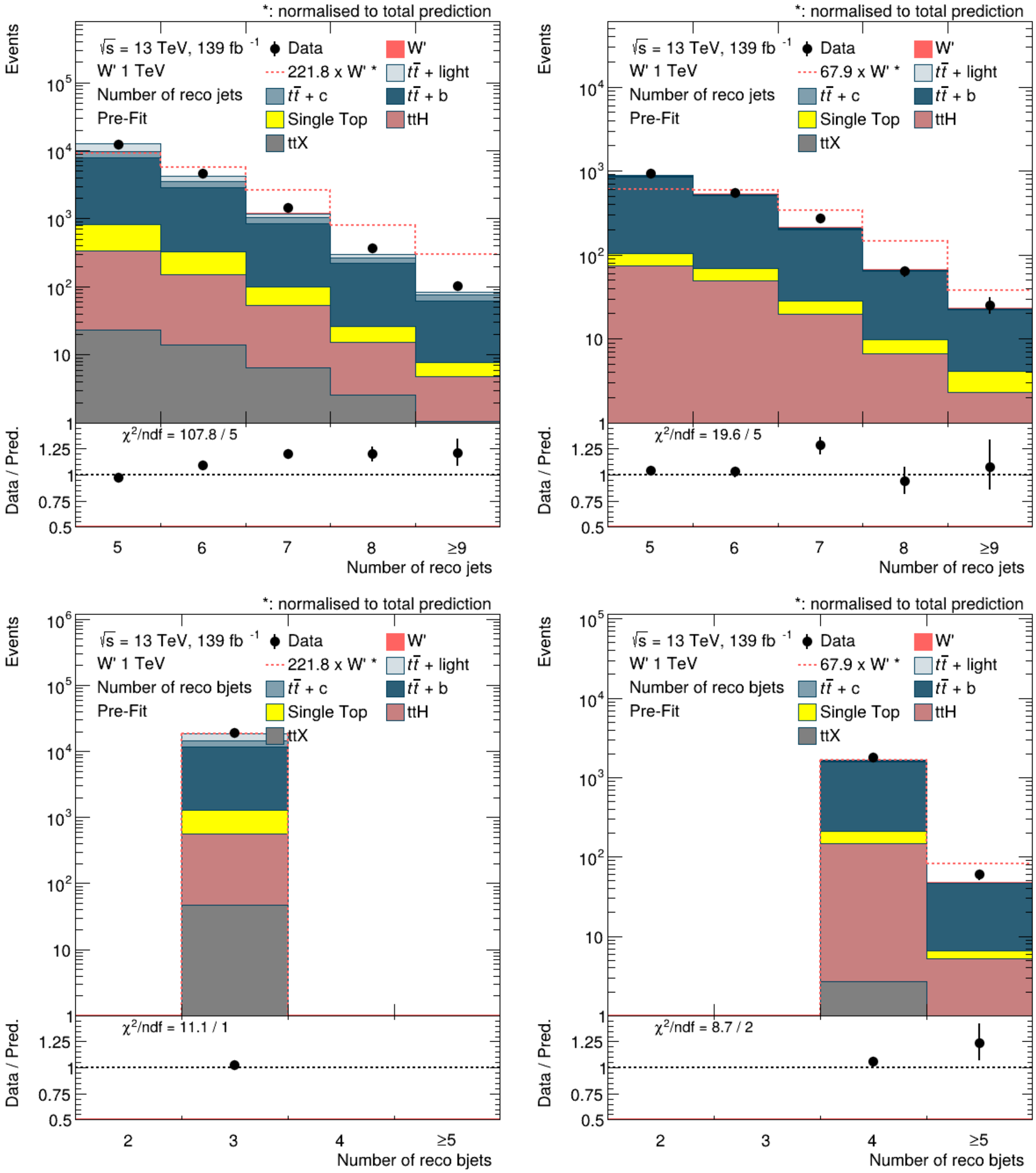

Figure 5.12: Kinematic distributions of background and signal in SR1 (left) and SR2 (right). Each bin in SR1 carries about 15% and in SR2 about 25% systematic uncertainty.

5.4 Neural Network Strategy

In the production of SM-like W' boson with no associated particles, the t_R and b_R can to be reconstructed as in [77]. This method struggles when searching for a heavy-philic W' boson. The heavy-philic W' boson is produced in association with two more particles, a top and bottom quark. Several assumptions, such as the b_R having the highest p_T is no longer a good assumption. Furthermore, figuring out the jet that comes from the decayed t_R is much more complicated.

As seen in the previous section, no kinematic variable has a high enough sensitivity to discriminate between the W' boson signal and SM background. As in many heavy resonance searches, the sum of jet p_T in Fig. 5.10 comes close, but is still not sensitive enough. To perform this search, a more complex analysis needs to be developed.

There are two neural networks that are employed in this analysis to improve the sensitivity the heavy-philic W' boson. The first one is developed within the SPANet framework [78]. This network helps reconstruct the W' boson decay chain which involves using important reconstruction information to predict the jets that come from the b_R and the b from t_R, the decay channel (resonance/associated), and the predicted W' boson mass.

The second neural network is designed to separate the heavy-philic W' boson signal from all the relevant SM backgrounds. This network is a multilayer perceptron (MLP) that predicts a final signal output score (SB discriminator). This score is then used for the final profile likelihood fit.

Figure 5.13 provides a high-level overview of the analysis structure, highlighting where and how the two neural networks are employed. The analysis strategy emphasizes modularity by separating distinct components into interpretable, task-specific blocks rather than treating

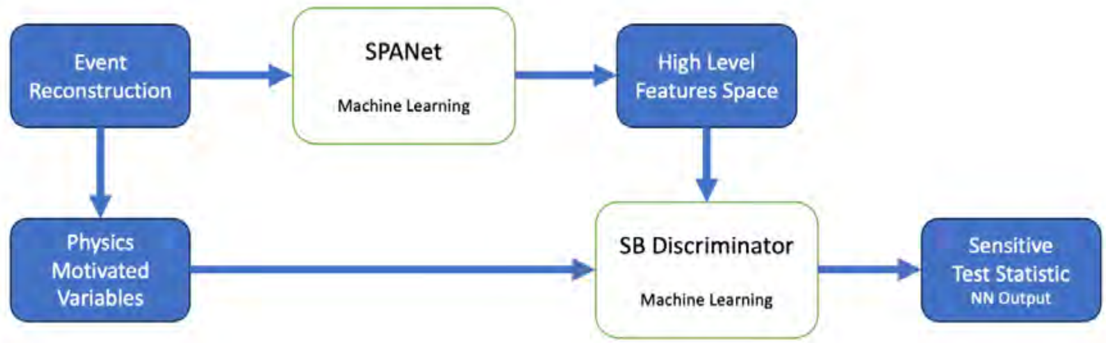

Figure 5.13: This flow chart shows how information is transformed throughout the analysis. The two neural networks are depicted as green blocks, and transformed states of the data and MC samples are depicted in solid blue boxes. This analysis structure combines the power of machine learning and directed by physics-motivated approach.

the workflow as a black box. This design improves the interpretability of each stage and allowing the neural networks to be specialized for their respective objectives.

5.4.1 SPANet and Transformers on W' Boson Signal

The number of jets produced from a proton-proton collision is variable which means that a simple MLP will struggle in this domain. To overcome the problem of variable jet multiplicity in the feature space, transformers [79] are used in a package called SPANet [78]. The high-level architecture of SPANet can be seen in Fig. 5.14.

Each jet which is represented as a vector of fixed length is fed through a position independent embedding which transforms the input feature vector into a more useful embedded latent space representation. Then, each embedding is fed into several transformer encoder layers which process the vectors within the context of the entire event. Transformer encoders follow the central transformer. After the particle transformers, tensor attention layers process

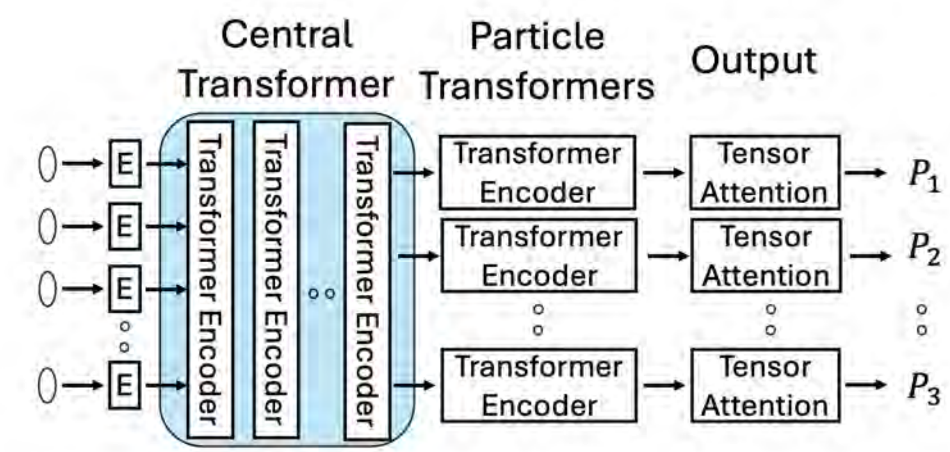

Figure 5.14: A high level diagram of the SPANET architecture [78].

the symmetries of the process which then output the final prediction. The final prediction is a vector of probabilities that are assigned to each jet which are used to match the reconstructed jet to the predicted truth level particle. These are the predictions for assigning each given jet of matching the original b_R , b from t_R , or b from t_A .

A global maximum jet multiplicity of 20 is used in this architecture. Jets are ordered by p_T and low p_T jets are discarded to obtain the maximum of 20 jets per event. When fewer than 20 jets are present, a mask is used to identify how many jets are present in the event.

The output of SPANET consists of probability vectors for each jet. To assign jets to truth particles, the algorithm first selects the jet with the highest probability and removes it from consideration. It then selects the next highest probability from the remaining jets, and repeats this process iteratively. This approach ensures that each jet is uniquely assigned, while maximizing the probability of assignment at each step.

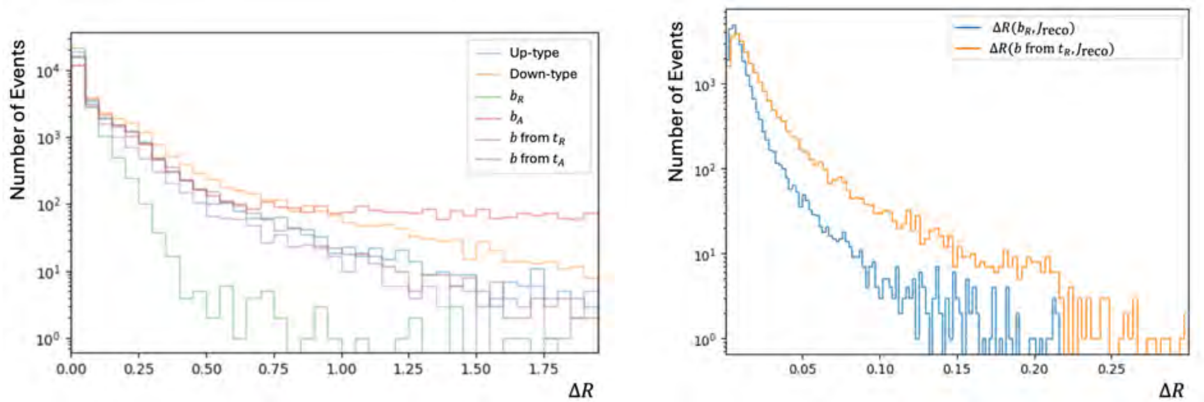

Figure 5.15: This figure shows the ΔR distributions for the 1 TeV left-handed W' boson. On the left, the minimum ΔR between truth-level particles and their matched particle-level jets is shown for the up- and down-type quarks from the hadronic W decay, the W' decay products, and associated particles. On the right, the minimum ΔR between each particle-level jet and its matched reconstructed jet is shown for the two resonance decay products.

5.4.2 SPANet Training

The neural network is trained using supervised machine learning with a labeled dataset. In order to acquire the labeled dataset, reconstructed jets needed to be matched to the original truth particles. This is done in two steps. First the truth particles are matched to their particle level jet (AntiKt4TruthDressedWZJets) by matching the geometrical trajectory of the truth particle to the nearest particle level jet. The second step is to match each particle level jet to a reconstructed jet geometrically again. Truth particles are allowed to be matched to the same jet, and if a match doesn't fall within $\Delta R < 0.3$, then it isn't matched. The distance between truth particles and particle level jets can been seen in Fig. 5.15 as well as the distance between corresponding particle level jets and reconstructed jets.

This matching scheme ensures accurate particle matching. Furthermore, by allowing the truth particles to be unmatched gives rise naturally to a detection probability that SPANet works out. This adds a weight in the final signal-background discriminator to add an element of confidence for a specific jet to be matched to b_R, b from t_R , or b from t_A .

Table 5.3: Different matching efficiencies showing improvement of the new neural network approach over simple algorithms and previous algorithms. The percent correct is calculated based on the number of times the algorithms matches the truth particle to the geometrically matched reconstructed jet.

Algorithm Name	b_R	b from t_R
Random Choice	15%	15%
Algorithm in [77]	29%	24%
Leading Jet	69%	37%
SPANet	65%	50%

During training, a two-fold cross validation method is then used. Even numbered events are used as the training set while the odd numbered events are used for testing and validation. Then, the network is trained again by switching the roles of the odd and even events. This process ensures that the neural network is learning something meaningful, and isn't being over trained. The full dataset is used for the signal and background discriminator (Section 5.4.4) using the properly trained network over the odd and even number Monte Carlo events. Training is performed over 32 epochs using the full W' boson signal dataset, which includes both left-handed and right-handed samples across all mass points. Approximately 4 million events are used for training, with an additional 4 million reserved for validation.

The loss function in SPANet is designed to balance regression of the W' boson mass and W_R kinematic variables, decay channel classification, and truth particle and reconstructed jet matching prediction. Each prediction from SPANet is then utilized by the signal and background discriminator.

5.4.3 Results from SPANet

As part of the analysis, it is desirable to extract important physics variables that characterize the heavy-philic W' boson. There are several variables that are simultaneously regressed from reconstruction level objects from SPANet. One important physics variable is the kinematic 4-vector of the resonance W boson that comes from the t_R. The regression results for these variables are shown in Fig. 5.16.

In addition to the W_R kinematic variables, the mass of the W' boson is also estimated within the SPANet neural network. The distributions of the LH W' boson masses can be seen in Fig. 5.18.

Table 5.3 shows how SPANet compares to different matching algorithms that could be used for selecting matching truth partons to reconstructed jets. The random choice algorithm shows the worst case scenario where the truth particles are matched randomly to the reconstructed jets. The matching algorithm in [77] describes how previous searches for the SM-like W' boson performs when trying to match the heavy-philic W' boson resonance truth particles. This shows that the previous algorithm is far from being optimized for matching the truth particles of the heavy-philic W' boson. The third algorithm is selecting the hightest p_T jet for the b_R and the second highest p_T jet for b from t_R . The neural network approach matches the two jets the best.

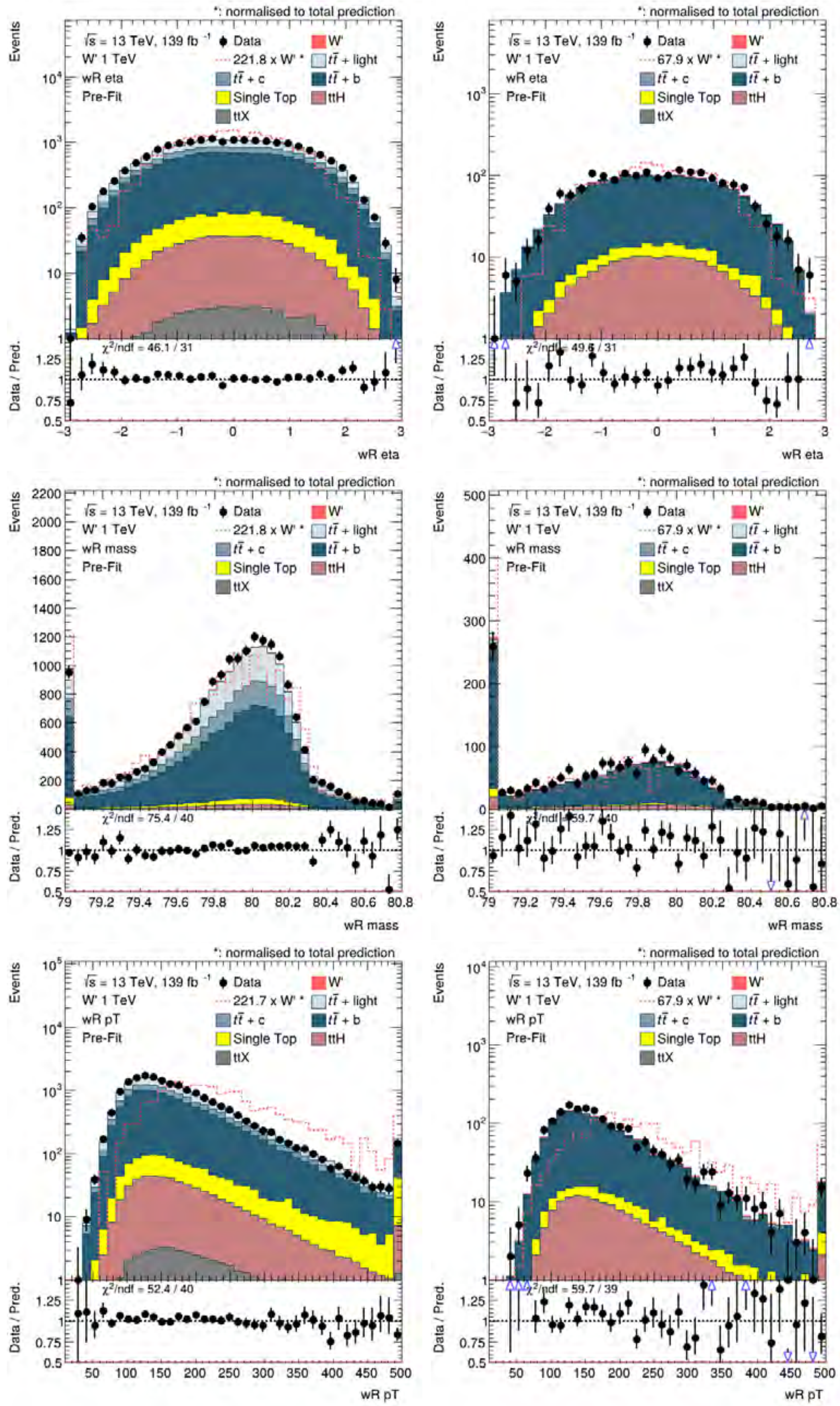

Figure 5.16: SPANet-predicted regression variables in SR1 (left) and SR2 (right), with about 15% and about 25% per-bin systematic uncertainties, respectively.

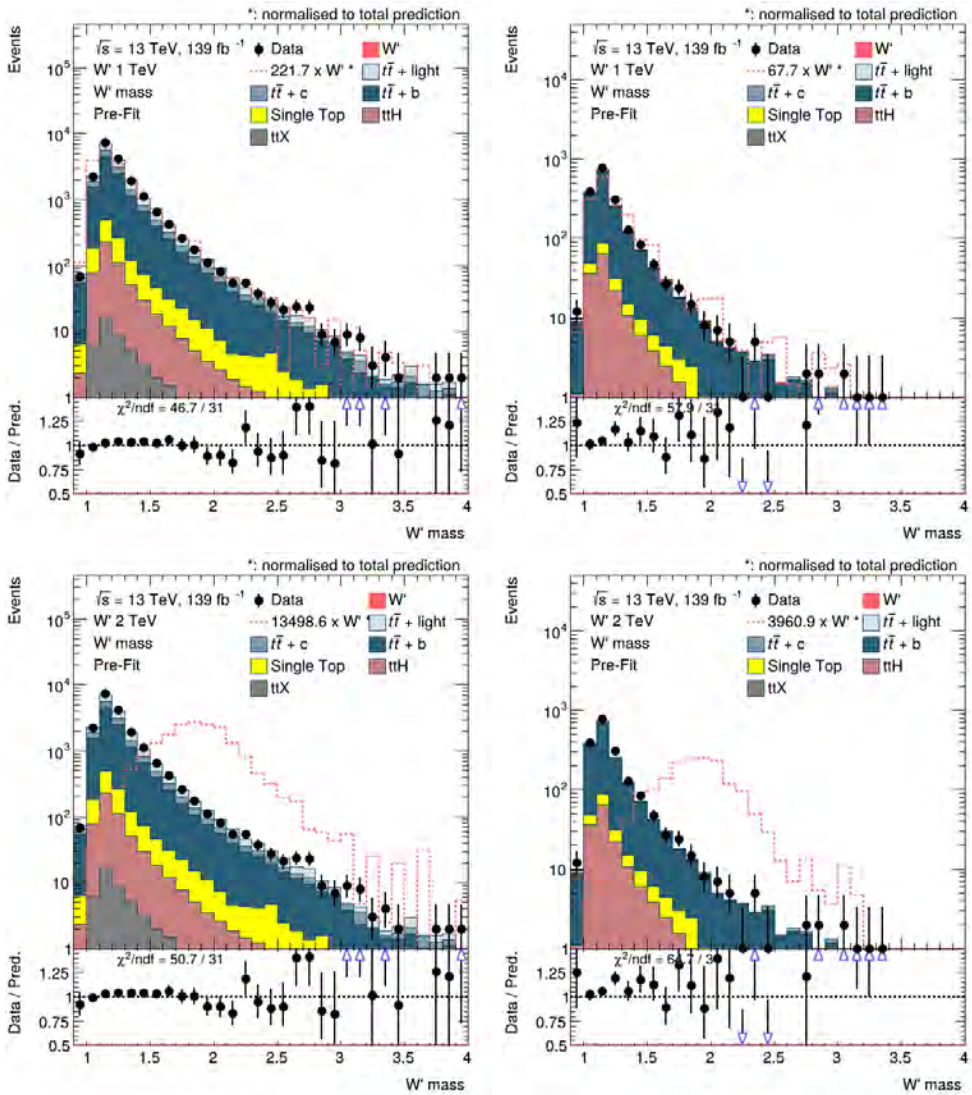

Figure 5.17: W' regression variable that are predicted by the trained SPANet neural network. SR1 variables are on the left and SR2 variables are on the right. The top two depict the regression results for the 1 TeV mass point, and the bottom two depict the regression results for the 2 TeV mass point. The distributions in SR1 have about a 15% systematic uncertainty in each bin while the distributions in SR2 have about a 35% systematic uncertainty in each bin.

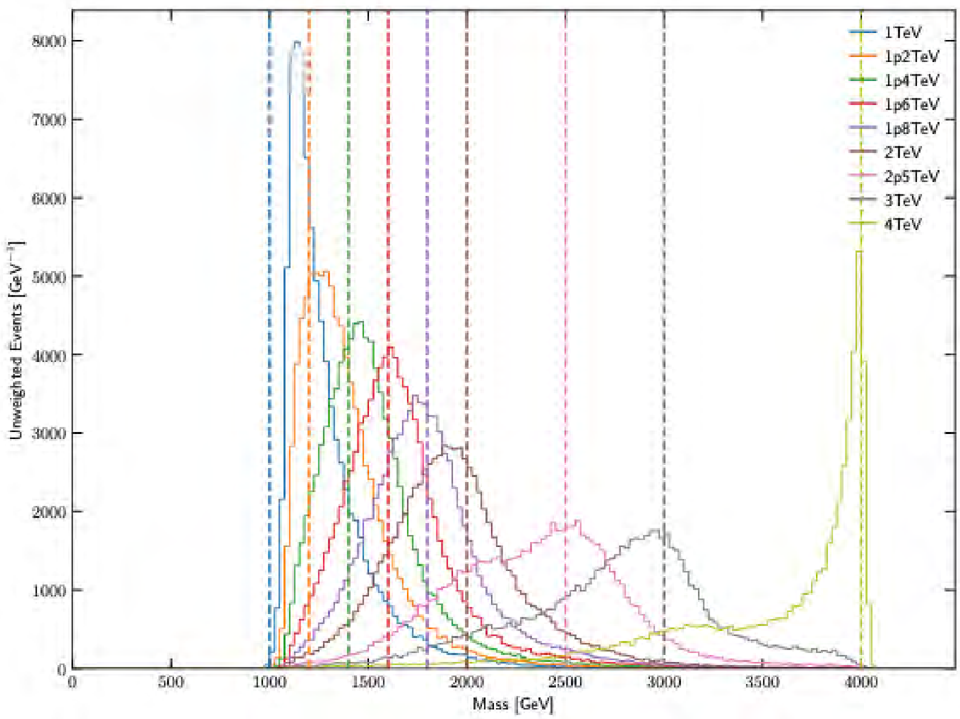

Figure 5.18: The distributions of the predicted W' masses for each sample set for the heavy-philic LH W'. The distributions in SR1 have about a 15% systematic uncertainty in each bin while the distributions in SR2 have about a 35% systematic uncertainty in each bin.

5.4.4 Signal and Background Discriminator

The next phase of the analysis is to discriminate between signal and background. To do this, a multiplayer perceptron (MLP) is used with 5 hidden layers. A dropout layer is added after each layer to ensure that the model wouldn't be over-trained. There are 38 inputs to the model, and each hidden layer has 512 nodes. The activation function that is chosen for these layers are simple rectified linear unit functions. The final layer is a simple linear layer that outputs a float that scores each event as either signal or background. A diagram of the signal-background discriminator can be seen in Fig. 5.19.

One of the key features of this neural network is that it is a mass-parameterized neural network (MP-NN). In order to efficiently train a network that works for each W' boson mass point, one dimension of the neural network is set to the true W' boson mass. This means that in training, the true W' boson mass is input for signal events, and a random number is drawn from the probability density distribution of the W' boson mass distribution of all the samples for the background events. This pools relevant information about a specific mass point into centralized regions of the NN phase space. An alternative would be to train a separate neural network for each mass point. However, this makes inferences between mass points more discrete. With the MP-NN, during evaluation and prediction, this mass parameter is taken to be a random number following the truth level W' boson mass distribution.

To discriminate the dominate backgrounds in this region from the W' boson signal, several high level variables along with some traditional kinematic variables are used as inputs in the multilayer perception. A summary of these inputs can be found in Table 5.4.

Examples of additional output variables from SPANet which is used within the SB discriminator is shown in Fig. 5.20. By themselves, they are not useful to search for signal

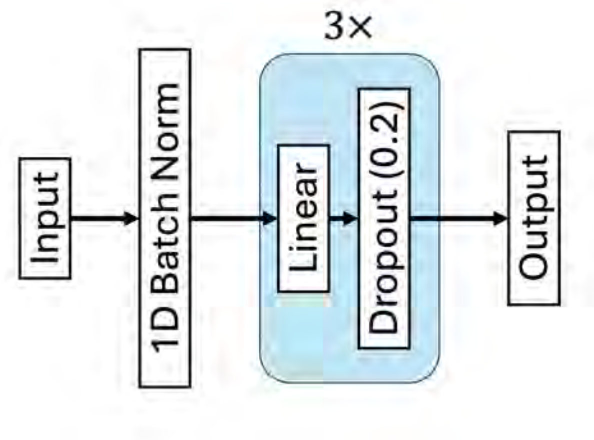

Figure 5.19: A diagram representing the simple MLP design of the signal-background discriminator.

Table 5.4: Summary of input features used in the signal vs. background discriminator neural network. A total of 36 input variables are used in the first layer of the MLP.

Category	**Feature Variables**	**# Variables**
SPANet Variables		
Assignment probabilities	$P(b_R)$, $P(b_{t_A})$, $P(b_{t_R})$	3
Predicted Jet 4-vectors + btag	b_R, b from t_A, b from t_R	$3 \times 5 = 15$
Classification	Resonant channel classification	1
Regression	W' (m), W_R (η, m, ϕ, p_T)	5
Jet kinematic properties		
Next leading jet	btag, η, ϕ, p_T	4
Next-next leading jet	btag, η, ϕ, p_T	4
Jet multiplicity	N_{jets}, N_{btag}	2
Jet p_T sum	Sum of jet p_T	1
W' **Boson Truth Mass Parameter**		1

excess, but the SB discriminator benefits from the addition of these variables as it provides critical information on the kinematics of the W' boson, and the certainty on the assignment of key particles such as the b_R.

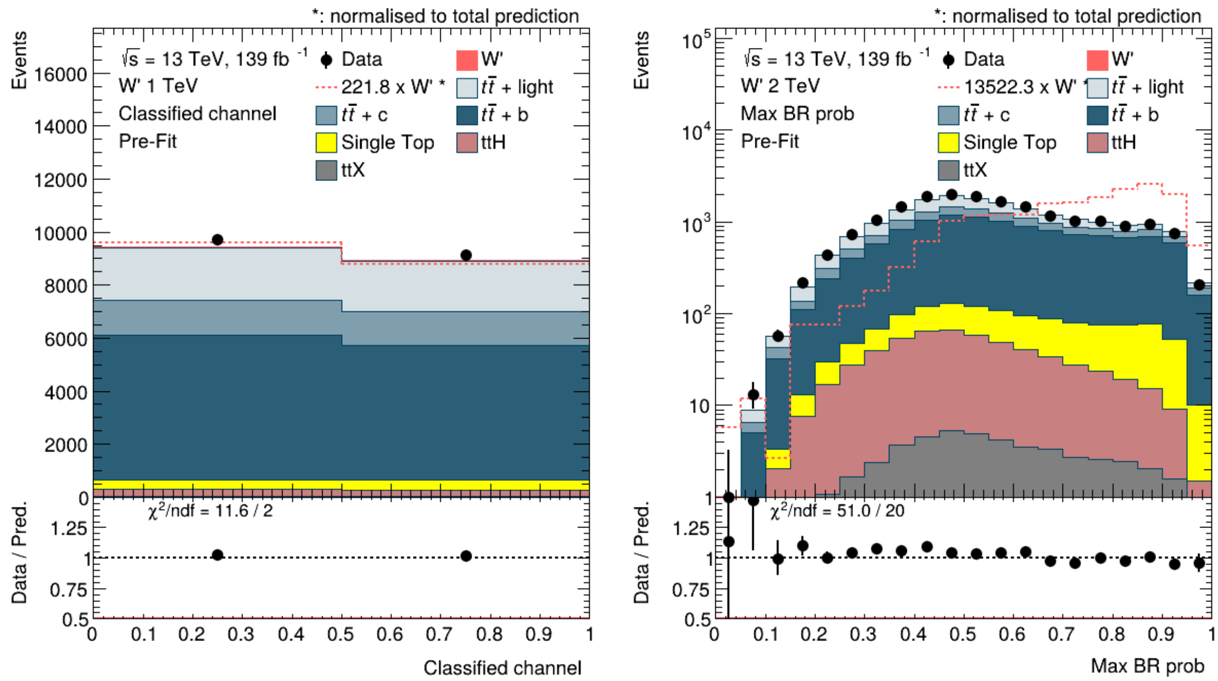

Figure 5.20: The resonance channel classification which comes from the output of SPANET is shown on the left. A hadronically decaying W' is classified as 0, and a leptonically decaying W' boson is classified as 1. The right shows the assignment probability of b_R.

5.4.5 SB Discriminator Training

Training of the signal and background discriminator is done through the use of a two-fold cross validation method similar to the way SPANET is trained. Training occurred over 10 epochs, and is done with unbalanced datasets. There are a significantly larger number of $t\bar{t}$ events compared to other backgrounds and W' boson signal. To utilize the full phase space available for the $t\bar{t}$ dataset, but balance the training, weights are used during the training phase. The cross-section weights for each background event are used, and then the average background weight are used for the W' boson signal. This ensures the network is balanced between signal and background events equally. It also ensures that the different backgrounds are considered with the appropriate weight. Both LH and RH W' boson samples were used in the training of the SB discriminator.

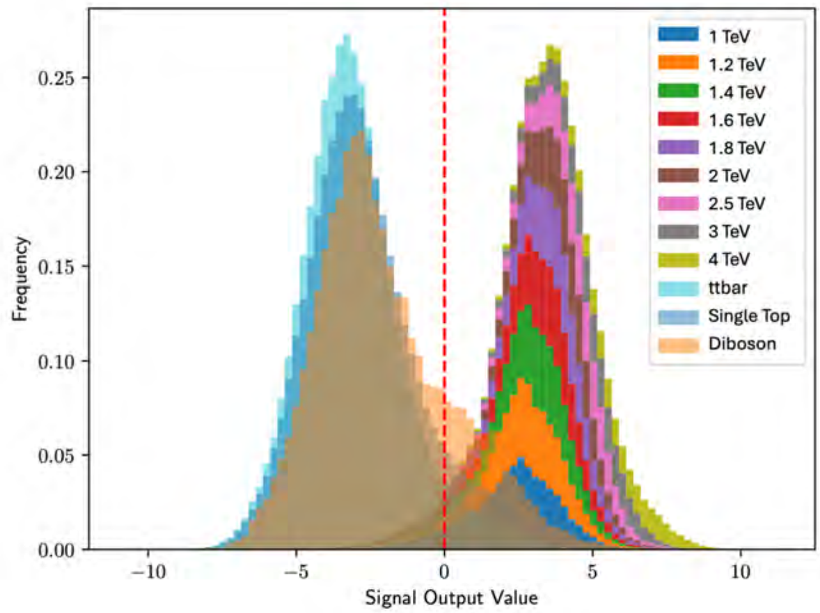

Figure 5.21: Results from the trained neural network showing the output score for each mass stacked on top of each other. The SM backgrounds are normalized, and the sum of the W' boson signal samples are normalized for comparison.

5.4.6 Results from SB Discriminator

The results from training this neural network are shown in Fig. 5.21 and Fig. 5.22. Each W' boson mass point has similar sensitivity, with higher masses having slightly improved discriminating power. This is because the higher the W' boson mass, the easier it is to distinguish from SM $t\bar{t}$ events. The kinematic properties begin to look very different because jets from the resonance particles begin to have even greater transverse momentum. Fig. 5.23 also shows the NN output score in the $t\bar{t}$ CR for each background and compared with the W' boson signal.

The resulting distributions can be found in Fig. 5.24 which compares the samples of the two chiralities in the SR1 and SR2.

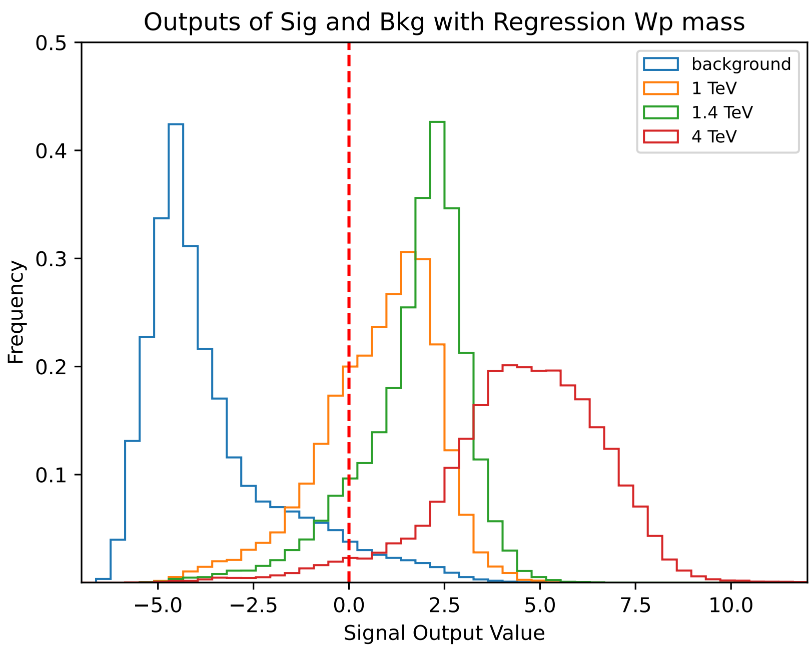

Figure 5.22: The neural network output for the total background is show in comparison to the output score for a couple W' signal samples. The dashed red line is drawn for visibility and isn't a cut on the samples that are made. This output score is binned and a profile likelihood fit is done on this distribution.

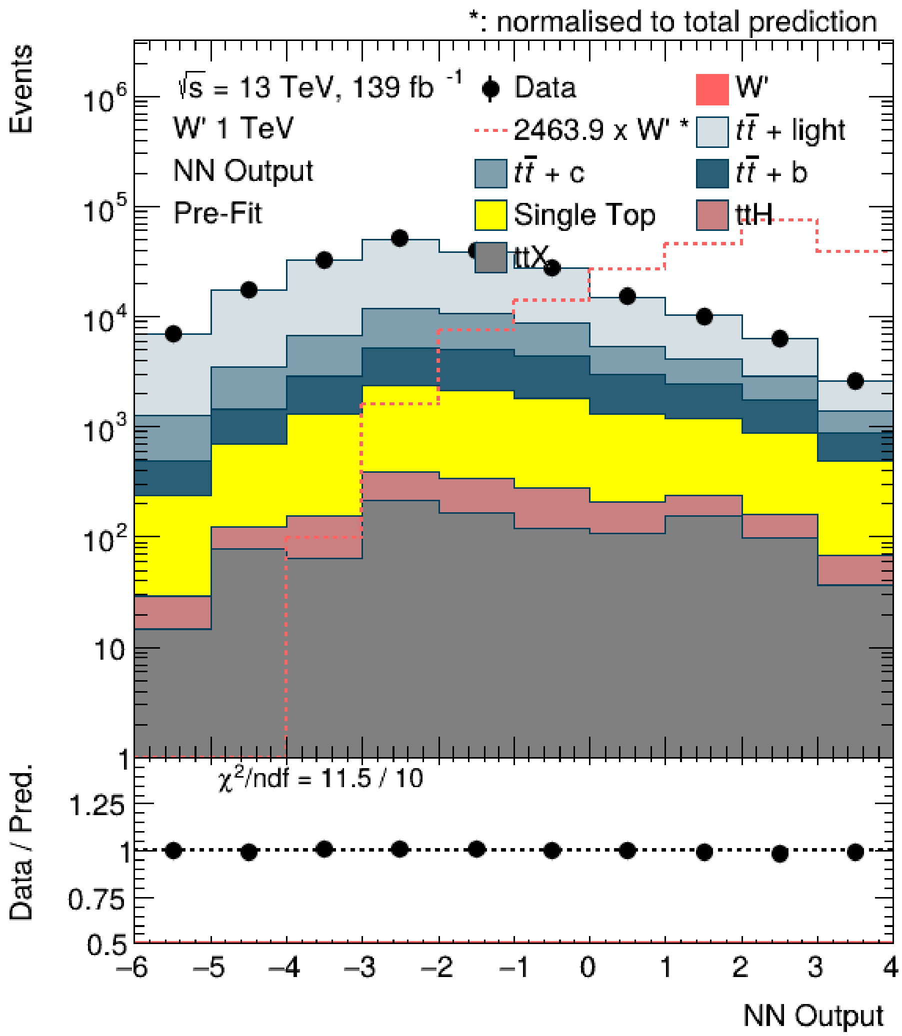

Figure 5.23: The neural network output with all backgrounds in the $t\bar{t}$ CR.

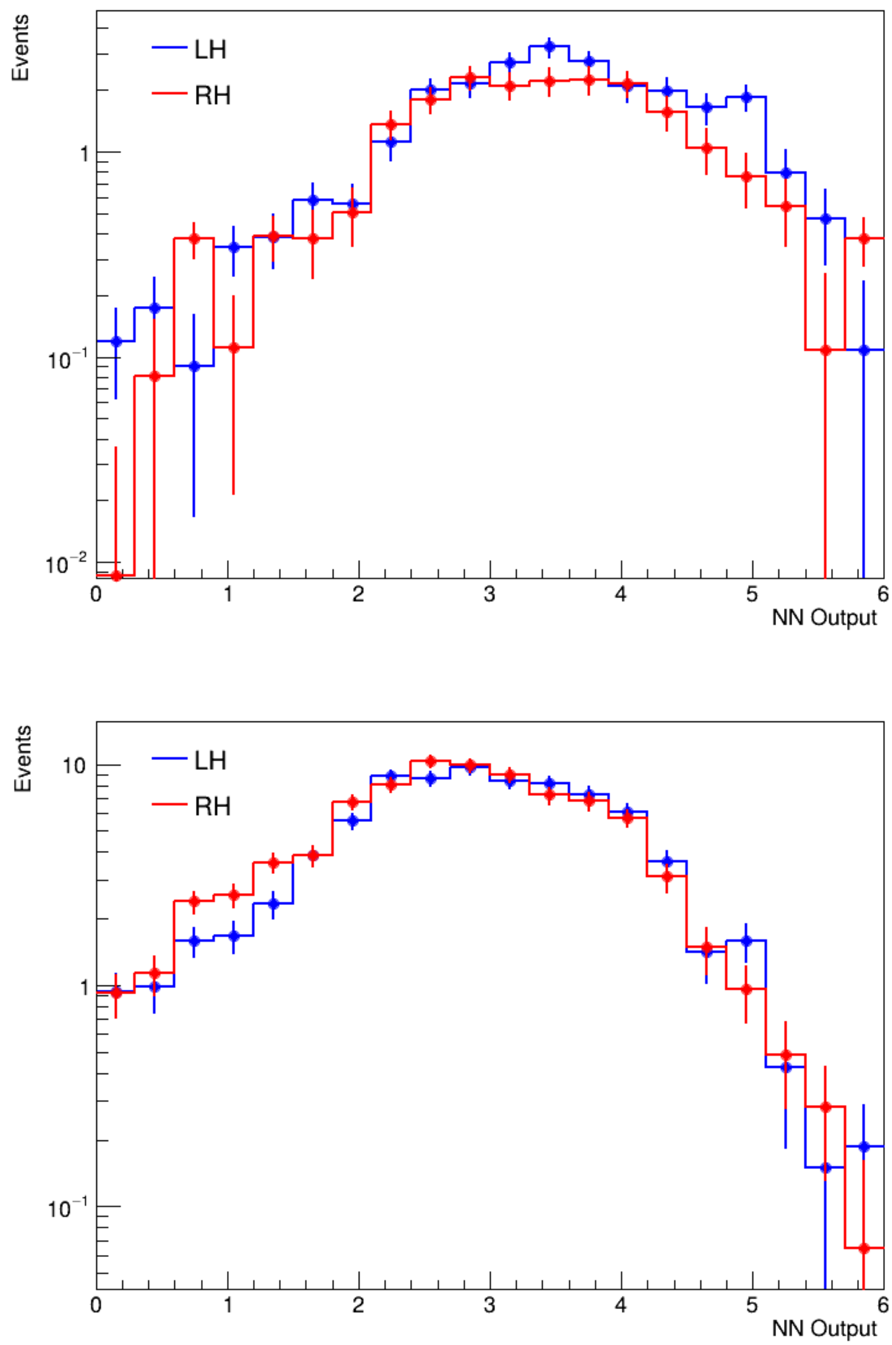

Figure 5.24: Shown is the comparison between purely LH and RH W' boson signal events. The NN output score in SR1 is shown on the top while SR2 is shown on the bottom. This distributions are similar but not identical. The distributions are mostly consistent to within statistical uncertainty.

Chapter 6

Statistical Analysis

The statistical interpretation of the observed data is initiated by evaluating whether there exists a statistically significant excess of events relative to the predicted SM background. In the absence of such an excess, an upper limit is set on the production cross section of the signal process, $\sigma(pp \to tbW')$, using a model-dependent approach based on the modified frequentist method, CL_s [80]. Although exclusion limits are often the final results presented, they are only meaningful once it has been demonstrated that the observed data is consistent with the SM-only hypothesis, i.e., that no significant deviation is observed.

A basic strategy for identifying BSM signals involves a cut-based counting experiment, where events are selected using optimized criteria designed to maximize the signal-to-background ratio. The number of selected events observed in data is then compared to the SM background expectation, which includes both statistical and systematic uncertainties. A significant excess in the observed yield relative to the expected background may indicate potential evidence for new physics. In the absence of such an excess, exclusion limits are placed on the parameter space of the signal model under consideration [44].

However, in the current precision-driven era of particle physics, more sophisticated statistical tools are required to extract the full sensitivity of the data. Rather than relying solely on event counts, analyses typically exploit the shape information of discriminating variables by using binned distributions spanning multiple kinematic regions. In this work, the statistical inference is performed via a binned profile likelihood fit [44] over the signal regions SR1 and SR2, as defined in Chapter 5. This approach enhances the sensitivity of the analysis by incorporating the full distributional information, thereby improving the robustness and reach of the resulting constraints. TRExFitter [81] is the software package that is used to implement the binned, maximum-likelihood fit. The binning algorithm used for binning for SR1 and SR2 is called TransfoD. With the selected options for this analysis, this algorithm merges bins together, but enforces no more than 25% of signal and no more than 20% of total SM background to be in any bin. Details about this algorithm can be found in [82]. The algorithm assists in selecting an optimal binning scheme that avoids the loss of sensitivity associated with overly coarse binning, while also mitigating issues arising from overly fine binning, such as low or negative expected event counts in signal or background distributions.

6.1 Blinding Procedure

A blinding procedure is used in this analysis. The blinding procedure prevents biased results in an analysis while searching for new particles or rare phenomena. The idea is to obscure the final result until all data selection, calibration, and analysis techniques have been finalized. This ensures that methods are not subconsciously tuned to produce a desired outcome.

The technique in this analysis is to do data blinding. The two regions that are sensitive to the heavy-philic W' boson are SR1 and SR2. Therefore, to make sure there is agreement between data and background modeling, the $t\bar{t}$ CR has the data unblinded. This region offers insight into the dominant $t\bar{t}$ background, while minimizing any signal strength. Blinding is crucial in analysis like this because the statistical nature of the experiment makes results susceptible to small biases.

6.2 Profile Likelihood Fit and Nuisance Parameters

To test for the presence of a heavy-philic W' in Run 2 data collected from the ATLAS detector, a binned maximum likelihood fit [44] is performed across all analysis regions simultaneously. The fit is done on the binned distribution of the neural network (NN) output, and conducted separately for each mass hypothesis. Two unconstrained normalization factors are included to estimate the normalizations of the $t\bar{t}+\geq 1b$ and $t\bar{t}+\geq 1c$ backgrounds, and another to estimate the normalization of the $t\bar{t}+$ light background. The parameter of interest is the signal significance, defined as the production cross-section $\sigma(pp \to tbW')$.

To estimate the signal strength, the likelihood function $\mathcal{L}(\mu, \theta)$ is defined as a product of Poisson probability terms, with one term per bin of the neural network (NN) output distribution in each analysis region. The expected event yield in each bin depends on the signal strength μ and a set of nuisance parameters $\theta = (\theta_1, \theta_2, \ldots, \theta_N)$, which encode systematic effects and per-bin statistical uncertainties in the simulated samples. Shape uncertainties are implemented as correlated bin-by-bin distortions of the NN distributions. These uncertainties account for detector calibration, theoretical modeling, and generator-level variations All nuisance parameters are modeled using Gaussian or log-normal probability density functions. The fit includes approximately 150 such parameters, with minor variations across signal hypotheses. Their impact on the signal strength is propagated through the profiling procedure, and their relative influence is assessed via nuisance parameter ranking, defined by the shift in the best-fit signal strength when each parameter is individually fixed to its nominal value.

The negative log-likelihood function is then defined as

$$-\log \mathcal{L}(\hat{\mu}, \hat{\theta}_1, \hat{\theta}_2, \ldots, \hat{\theta}_N) = \min\{-\log \mathcal{L}(\mu; \vec{\theta}) : \mu, \theta_1, \theta_2, \ldots, \theta_N \in \mathbb{R}\}. \tag{6.1}$$

6.3 Exclusion Limit Calculation Using a Test Statistic

To extract the 95% confidence level (CL) exclusion upper limit on $\mu = \sigma(pp \to tbW')$, a likelihood-based test statistic is employed. The test statistic is defined as

$$\tilde{t}_\mu = \begin{cases} -2\ln \frac{\mathcal{L}\left(\mu, \hat{\hat{\theta}}\right)}{\mathcal{L}\left(0, \hat{\hat{\theta}}(0)\right)}, & \text{if } \hat{\mu} < 0 \\ -2\ln \frac{\mathcal{L}\left(\mu, \hat{\hat{\theta}}\right)}{\mathcal{L}(\hat{\mu}, \hat{\theta})}, & \text{if } \hat{\mu} \geq 0 \end{cases} \tag{6.2}$$

where:

- $\mathcal{L}(\mu, \theta)$ is the likelihood function for a given signal strength μ and a set of nuisance parameters θ.

- $\hat{\mu}$ and $\hat{\theta}$ are the values of the signal strength and nuisance parameters that maximize the likelihood function.

- $\hat{\theta}(\mu)$ represents the values of the nuisance parameters that maximize the likelihood function for a fixed value of μ.

- Here $\hat{\hat{\theta}}(0)$ and $\hat{\hat{\theta}}$ refer to the conditional ML estimators of θ given a strength parameter of 0 or μ, respectively. Thus $\hat{\hat{\theta}}(0)$ represents the set of nuisance parameters that maximizes the likelihood function for the background only hypothesis, and $\hat{\hat{\theta}}$ represents the set of nuisance parameters that maximizes the likelihood function for the background plus signal hypothesis given a signal strength μ. By profiling out the nuisance parameters, the method accurately incorporates uncertainties from background normalizations, detector effects, and other systematic sources.

The test statistic $\tilde{t}_\mu$ follows the profile likelihood ratio approach, which quantifies how well a hypothesized signal strength μ agrees with the observed data compared to the best-fit value $\hat{\mu}$. Larger values of $\tilde{t}_\mu$ indicates increasing incompatibility between data and the hypothesized value of μ. The two cases in the definition ensures the proper treatment in the case where $\hat{\mu} < 0$ in models where this is unphysical. If the best-fit signal strength $\hat{\mu}$ is negative, the likelihood ratio is computed relative to the background-only hypothesis ($\mu = 0$). If $\hat{\mu}$ is non-negative, the likelihood ratio is taken relative to the best-fit signal strength, ensuring the most optimal constraint on μ. This approach maximizes over all nuisance parameters for each assumed signal strength, allowing for a comprehensive treatment of systematic uncertainties.

The observed value of $\tilde{t}_\mu$ is compared against the distribution $P(\tilde{t}_\mu)$ to determine the probability, also known as the p-value, of obtaining a test statistic at least as $\tilde{t}_\mu$ can be found in Ref. [83].

The upper limit on μ at 95% CL is determined by finding the largest signal strength μ_{up} such that the probability of obtaining a test statistic more extreme than the observed one in the background-only pseudo-experiments is at most 5%. In other words, μ_{up} satisfies

$$\int_{\tilde{t}_\mu}^{\infty} P(\tilde{t}_\mu|0)d\tilde{t}_\mu = 0.05. \tag{6.3}$$

This ensures that if the true signal strength is equal to μ_{up}, the data would yield a stronger exclusion (larger $\tilde{t}_\mu$) in only 5% of cases, thus setting a limit at the 95% confidence level. This statistical approach provides a well-defined criterion for determining the exclusion limit based on the observed data and expected background fluctuations.

However, there are situations where the p-value may fall below the exclusion threshold, even when neither the signal-plus-background ($s+b$) nor the background-only (b) hypothesis provides a satisfactory fit to the data. A simple example of this occurs when background events are systematically underestimated in a counting experiment, leading to misleading exclusions.

To mitigate this issue, a common refinement is the CL_s method is used which modifies the p-value definition to ensure a more conservative rejection of the $s+b$ hypothesis:

$$p_{s+b} = \frac{p_s}{1 - p_b} < 0.05, \tag{6.4}$$

where p_s represents the p-value for the signal-plus-background hypothesis ($\mu > 0$), and p_b corresponds to the background-only hypothesis ($\mu = 0$). The denominator, $1 - p_b$, quantifies the sensitivity of the statistical test.

6.4 Detector Systematic Uncertainties

Systematic uncertainties exist for the reconstruction of the physics objects used in this analysis which include jets, leptons, and E_T^{miss} . To account for these uncertainties, calibrations in the Monte Carlo samples are adjusted according to the prescribed uncertainty. The variations that follow in the physics objects are then carried throughout the analysis which includes new event selections, rerunning of the neural networks, and resulting in new final NN distributions. It is required to rerun the entire framework. For example, if the rapidity calibration altered then some events which previous passed event selection may not pass with the altered rapidity calibration or vice versa.

After running over detector systematics, the total systematic uncertainty on a bin-by-bin basis, is the sum in quadrature of each uncertainty.

The two main components of systematic uncertainties associated with jets are jet energy scale (JES) and jet energy resolution (JER). The jet energy scale uncertainty reflects the degree to which the calorimeter's response to a particle at a given energy is understood. This uncertainty varies with transverse momentum and pseudorapidity. There are many different sources that comprise of the JES uncertainty such as pseudorapidity calibrations, and flavor response [84]. To reduce the total number of uncertainties, the covariance matrix of these uncertainties are diagonalized and the most important eigenvectors are kept.

The jet energy resolution uncertainty is how precisely energy of the jet is measured. Parts of this uncertainty come from things like electronic noise and pile-up [85]. In much the same way as JES, effective NPs are constructed to model the systematic uncertainties that come from the resolution of each jet.

Systematic uncertainties related to leptons (e and μ) arise from imperfect knowledge of the detector performance and corrections applied to simulation. These uncertainties are primarily associated with the trigger selection, the object reconstruction, identification and isolation criteria, and the lepton momentum scale and resolution, and track-to-vertex association (TTVA). Efficiency scale factors, typically derived from tag-and-probe techniques, are applied to simulated events to match data, and the uncertainties on these scale factors are propagated through the analysis [86, 87]. They account for statistical limitations in control samples, differences between generators, background modeling, and potential mismodeling in specific kinematic regions such as low p_T or high η. In addition, variations related to the combination of inner detector and muon spectrometer information are included. All electron and muon related systematic uncertainties are incorporated as nuisance parameters in the statistical fit, affecting both event yields and shapes, and are treated coherently across control, validation, and signal regions to ensure proper estimation of their impact on the final result.

The E_T^{miss} object is constructed from jets, leptons, as well as the energy not associated with any reconstructed object (soft terms). Therefore, the uncertainty on this object can be divided into two components. One that stems from the physics objects detailed above (leptons and jets), while the other stems from soft terms. These soft terms have uncertainty on their resolution and scale which is included in this analysis [88, 89].

A total of 108 detector-related systematic uncertainties are considered in the final fit. Additional details are provided in Section 6.6, and a summary of the systematics that are pruned prior to inclusion in the fit is shown in Fig. 6.2.

6.5 $t\bar{t}$ Systematic Uncertainties

To account for the various sources of uncertainty on the dominant $t\bar{t}$ background different strategies are employed. A summary of this can be found in Table 6.1.

Systematic uncertainties are extracted by comparing the nominal results to the results of different MC samples with different settings. This is done for each heavy flavor classification separately which allows for the systematic to be profiled. The nominal Powheg+Pythia sample is compared to the Powheg+Herwig sample to assess the effect of the PS and Hadronization models. To account for the effects of varying h_{damp} parameters on the $t\bar{t}$ samples, an additional sample with a modified h_{damp} value is run through the analysis. To account for the modeling uncertainty associated with large jet multiplicity phase space of the $t\bar{t}$ samples, a $t\bar{t}$ reweighting technique similar to [72] is used, and two alternative distributions are used

Uncertainty Source	Description	Components
$t\bar{t}$ Reweighting	Distributions with and without weights	All
PS & Hadronization	Powheg+Herwig	All
h_{damp}	Varying h_{damp} parameter	All
$t\bar{t}+\geq 1b/c$ Normalization	Free-floating	$t\bar{t}+\geq 1b$,$\geq 1c$
$t\bar{t}+$ light Normalization	Free-floating	$t\bar{t}$ light

Table 6.1: Summary of the sources of systematic uncertainty for $t\bar{t}+$ jets modeling.

to create a nuisance parameter. One distribution is the nominal $t\bar{t}$ sample using the weights derived from the reweighting procedure. The other distribution is the nominal $t\bar{t}$ sample without these weights.

6.6 Pruning and smoothing of systematic uncertainties

In the fits, pruning is applied at the 1% level, meaning that if the effect of a nuisance parameter is smaller than 1% (separately for shape and normalization) it does not enter into the fit. This pruning procedure reduces the CPU time and helps the fit to converge. Since the pruning threshold is very small, this has no impact to the final fit results.

A table which summarizes the pruning of the detector systematics is shown in Fig. 6.2. This table only shows the pruning for the majority SM background, and the W' boson signal. Pruning is done separately for each sample in each of the two signal regions.

Table 6.2: A summary table that includes a count on the number of systematics that get pruned before entering into the fit. Only the majority background samples and signal sample are shown. All detector systematics for $t\bar{t}H$ and $t\bar{t}V$ are excluded in both regions.

	W'	$t\bar{t}+>1b$	$t\bar{t}+>1c$	$t\bar{t}+$light
Kept in both regions	9	51	56	57
Shape removed in 1 region	13	52	2	1
Shapes removed in both regions	37	5	50	41
Excluded in 1 region	1	0	0	9
Excluded in both regions	48	0	0	0

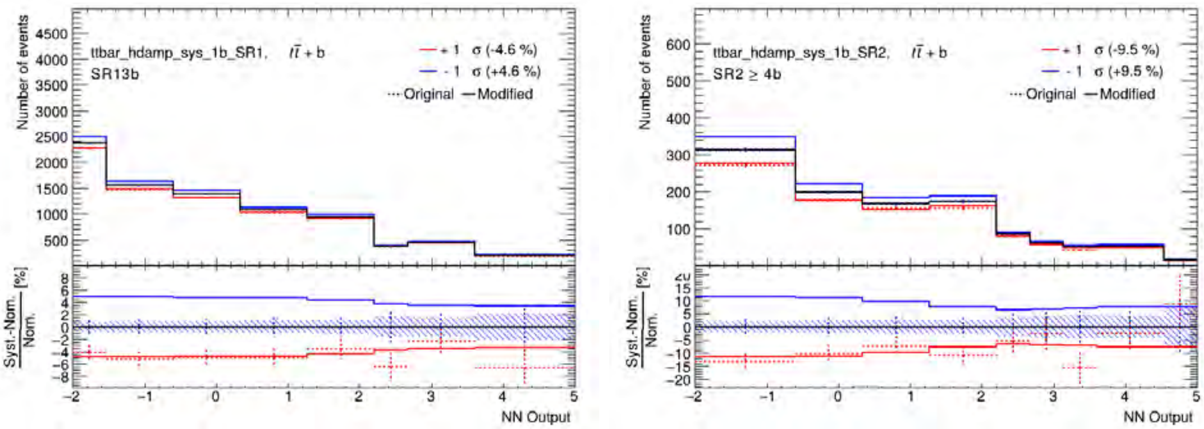

Figure 6.1: Example of systematic smoothing for the $t\bar{t}$ uncertainty associated with the hdamp parameter. The left plot shows the impact in SR1, and the right plot shows the impact in SR2. This uncertainty applies only to the $t\bar{t}+ > 1b$ sample.

Smoothing is applied for systematic uncertainties on $t\bar{t}$ modeling. No smoothing is applied for modeling systematic uncertainties on small backgrounds or for experimental systematics. An example of smoothing is shown in Fig. 6.1 which shows hdamp parameter $t\bar{t}$ systematic uncertainty.

A binning algorithm was used to determine the bins in SR1 and SR2. The algorithm is called TransfoD in TR

6.7 Asimov Fit Results

Below are the results of the fit using Asimov data where pseudo-data is artificially created from only the nominal SM background. This section only shows the results for the fit to the 1 TeV LH W' boson signal. All the other Asimov fits can be seen in Appendix B.

Fig. 6.2 shows the normalization factors that are extracted from the Asimov fit. These normalization factors show that the analysis and statistical fit is sensitive enough to test for the presence of the W' boson signal. The POI, μ, is fitted to 0 as expected, with a low uncertainty and rejects the nominal value of 1.

Figure 6.3 shows the ranking of the most impactful NPs on μ from the Asimov fit. The dominant contributions come from systematic uncertainties associated with the $t\bar{t}$ background, with the most significant NP being the reweighting uncertainty for the $t\bar{t}+>1b$ sample. Following the $t\bar{t}$-related uncertainties, the next most impactful NPs are associated with the JES and JER. This is expected as jet-based kinematic variables are central to variables in this analysis (HT for example). The output of the SB discriminator, which relies on these variables is therefore impacted by these uncertainties which degrade the separation between signal and background, thereby impacting the fit's sensitivity to μ.

Fig. 6.4 shows the pre-fit plots that are determined for this Asimov fit, Fig. 6.5 shows the post-fit plots, and Fig. 6.6 shows the systematic uncertainty pull plots from the NPs.

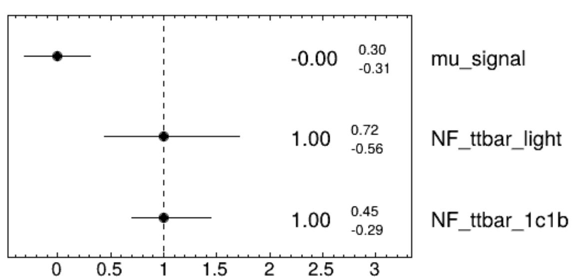

Figure 6.2: Normalization factors determined by the binned maximum likelihood fit for the LH 1 TeV W' boson signal where g'/g=2.

Several of the $t\bar{t}$ NPs are constrained in the Asimov fit. This is primarily because the statistical uncertainties are relatively small, allowing the fit to effectively constrain those parameters. Additionally, some NPs, such as the $t\bar{t}$ reweighting uncertainties, are conservative in their pre-fit estimates. As a result, the fit reduces their uncertainties post-fit, reflecting the fact that the data prefer a smaller variation than initially assumed.

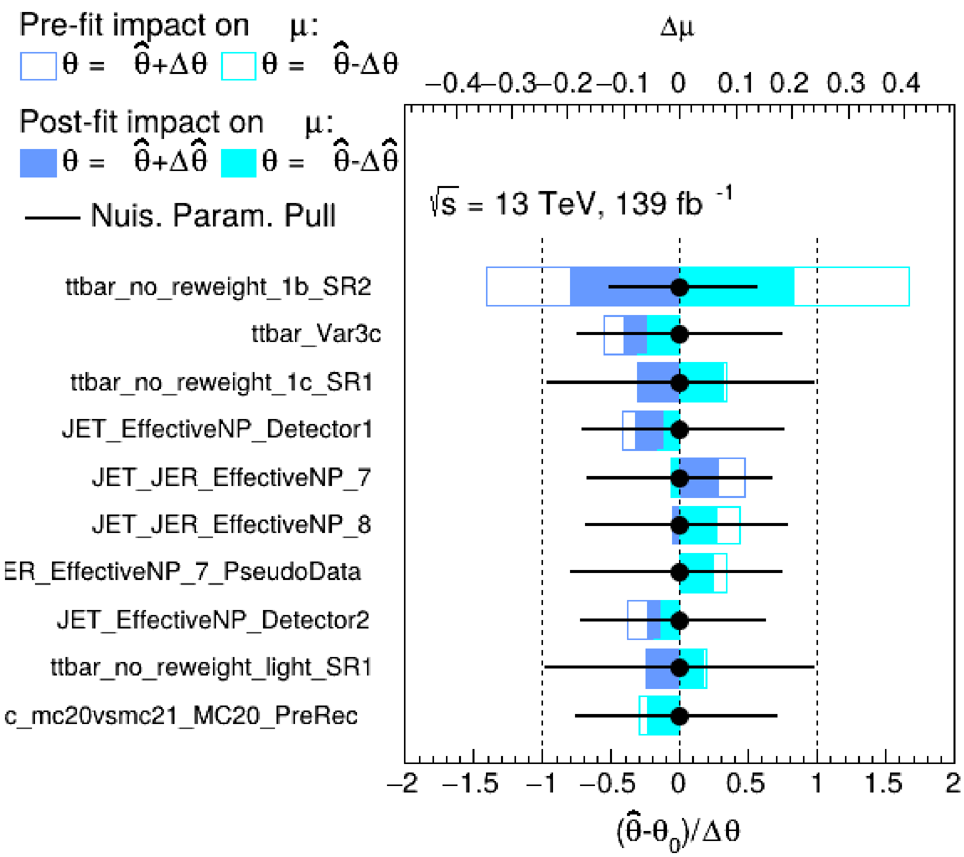

Figure 6.3: Ranking plot of the NPs for μ for the Asimov fit.

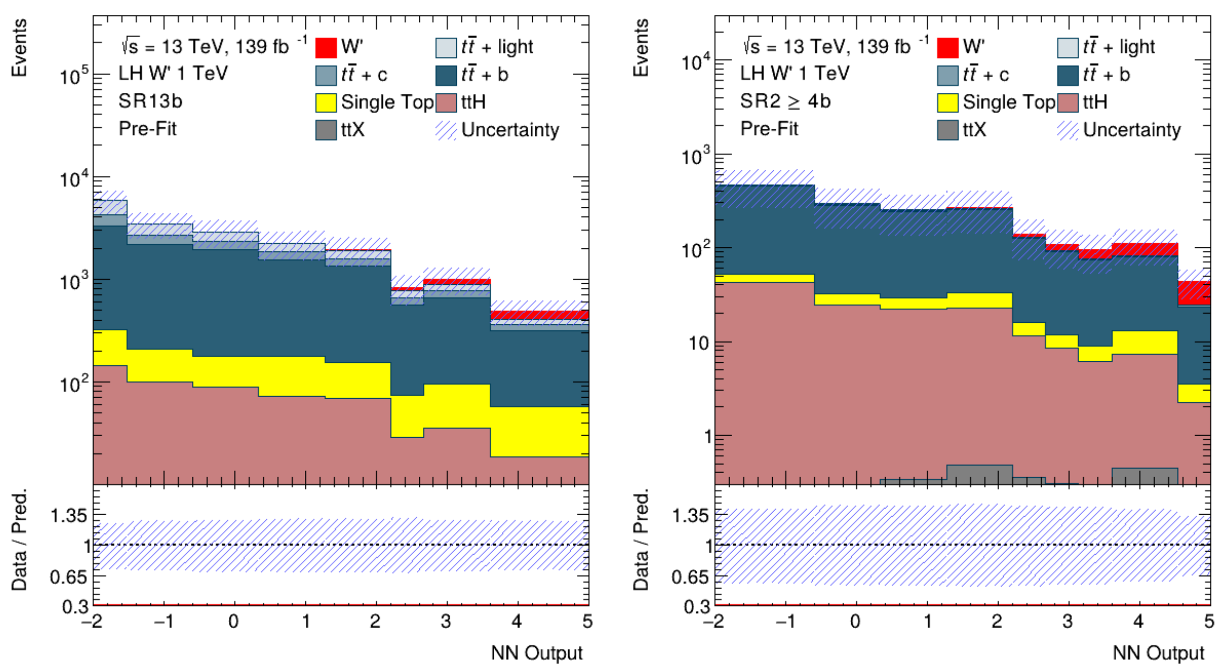

Figure 6.4: Asimov pre-fit plots for LH 1 TeV W' boson signal sample where g'/g=2.

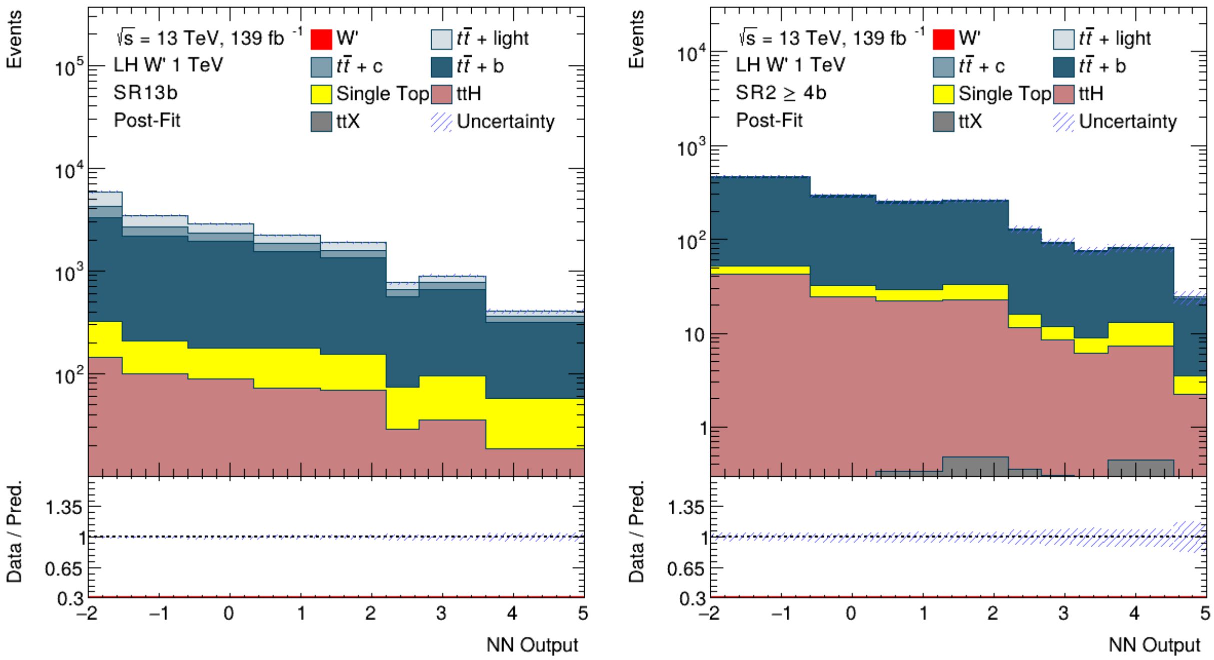

Figure 6.5: Asimov post-fit plots for LH 1 TeV W' boson signal sample where g'/g=2.

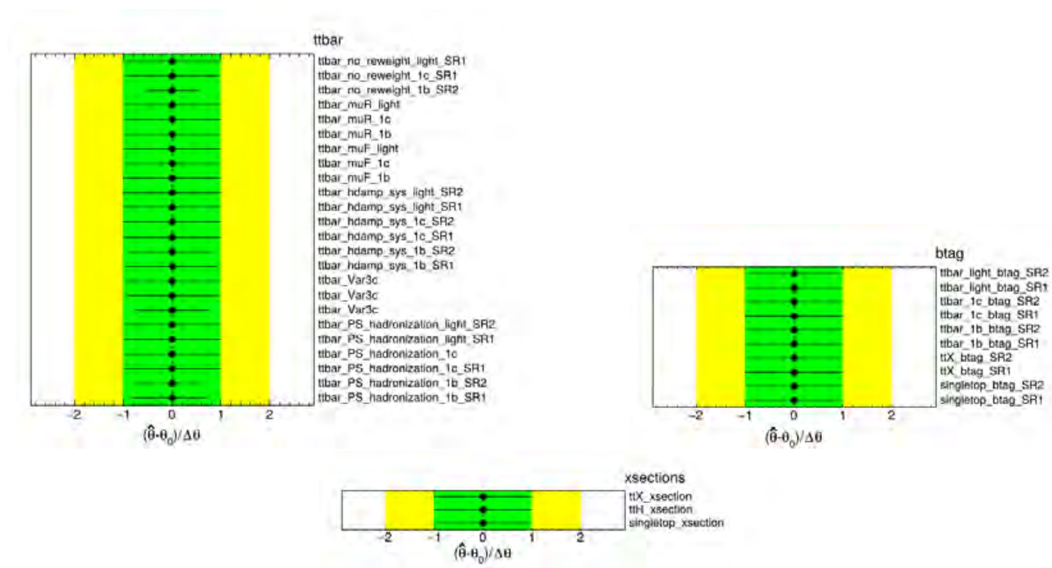

Figure 6.6: Systematic uncertainty pull plot for Asimov fit on LH 1 TeV W' boson sample where g'/g=2. Top left is the $t\bar{t}$ NPs, top right is the btagging NPs, and bottom are the cross-section NPs.

6.8 Fit Results on Data

This section only shows results for the LH 1 TeV W' boson. The other fits to the RH W' boson and all other mass points can be found in Appendix C. Fig. 6.7 shows the normalization factors that are extracted from the fit to data. The fitted signal strength is very close to the results from the Asimov fit, and it is 3σ from the nominal value which shows that the data in this fit is not compatible with the presence of the 1 TeV LH W'. The $t\bar{t}$ normalization factors are adjusted, but as seen in the Asimov fit, the uncertainties on these normalizations are quite high. Both normalization factors are consistent within 1σ from their nominal value.

Fig. 6.8 shows a ranking plot for the most impactful NPs on μ for the fit to data. As expected, the NPs that have the highest effect on μ are the $t\bar{t}$ systematic uncertainties. More specfically, the $t\bar{t}$ reweighting NPs are the top two most important NPs. All NPs are consistent with their nominal value to within 1σ. It also shows, can also be seen in the Asimov fit, that JER is an important NP in this analysis.

Fig. 6.9 shows the resulting pre-fit plots, Fig. 6.10 shows the post-fit plots, and Fig. 6.11 shows the systematic uncertainty pull plots from the $t\bar{t}$ systematics.

The results of the the fit to data reveal some tension. The instrumental NPs are quite

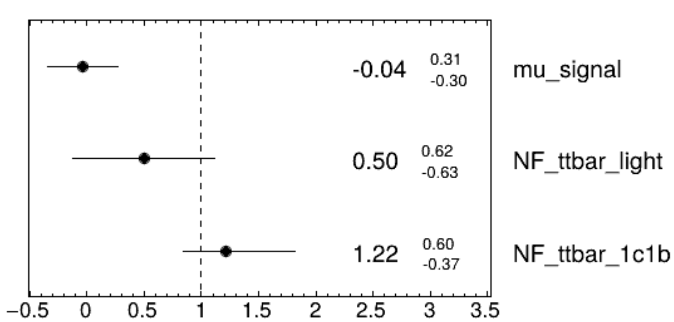

Figure 6.7: Normalization factors determined by the binned maximum likelihood fit for the LH 1 TeV W' boson signal where g'/g=2.

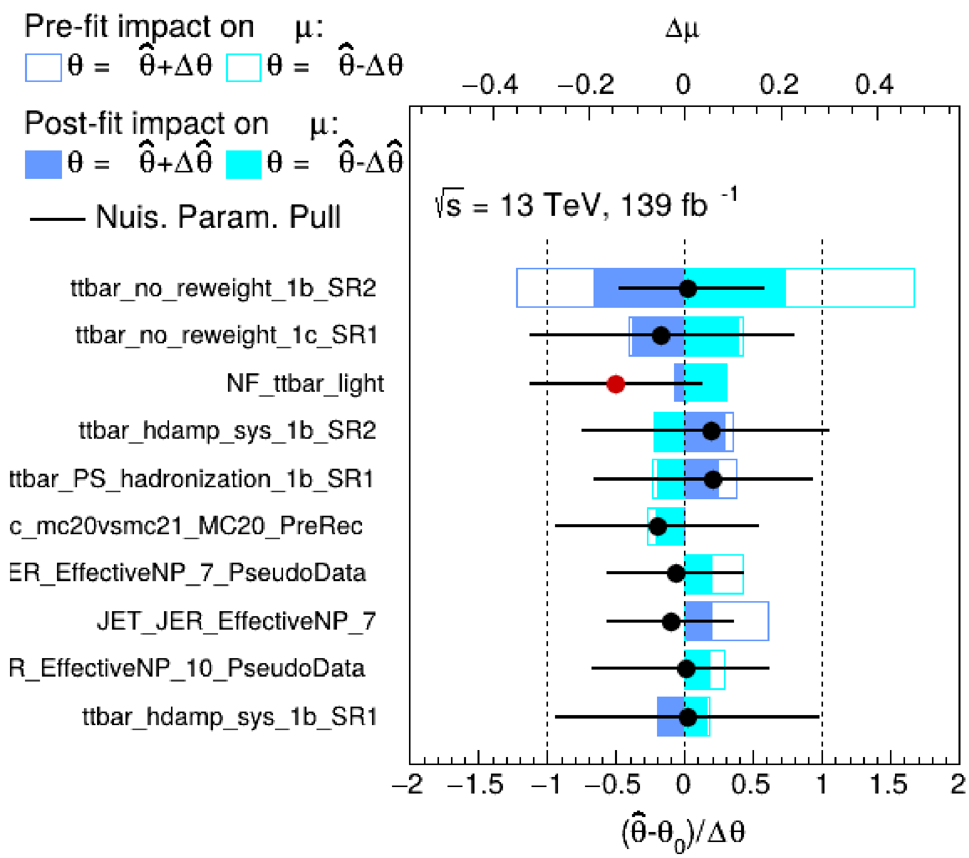

Figure 6.8: Ranking plot of the NPs for μ for the fit to data.

constrained. This can be attributed by poor SM modeling within SR1 and SR2. However, almost all NPs are consistent with their nominal value within 1 standard deviation.

Since no significant excess is observed above the SM background, 95% CL exclusion limits are set on the signal hypotheses.

Figure 6.12 shows the limit plots for the W' boson signal under the $g\prime/g = 2$ hypothesis. The expected limits are obtained using an Asimov dataset, while the observed limits are derived from fits to the actual data. These plots show that the observed upper limit falls withing 1σ of the expected upper limit. The limit curves are quite smooth, with minor fluctuations. The exclusion curve goes down as the W' boson mass increases because the kinematics of a heavier resonance begins to be easier to distinguish from $t\bar{t}$ events. There are also slight differences between the fits to the LH and RH W' boson signal samples. As shown in Fig. 5.24, differences in the neural network output distributions for the two cases lead to variations in the fit results.

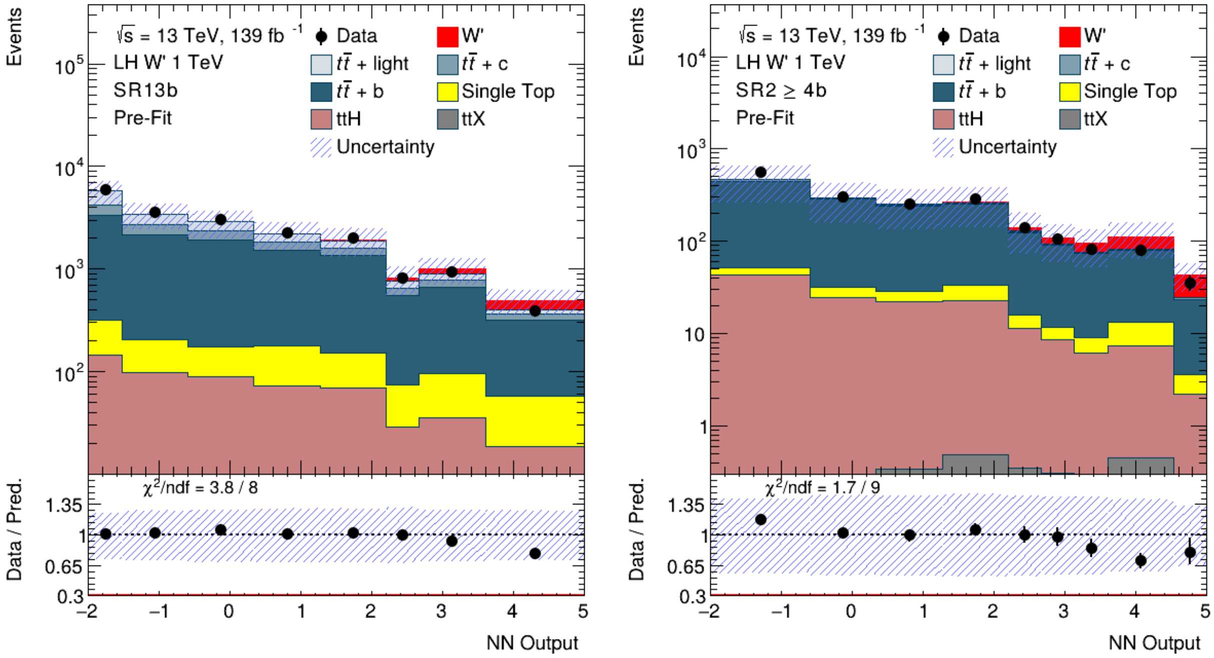

Figure 6.9: Asimov pre-fit plots for LH 1 TeV W' boson signal sample where g'/g=2.

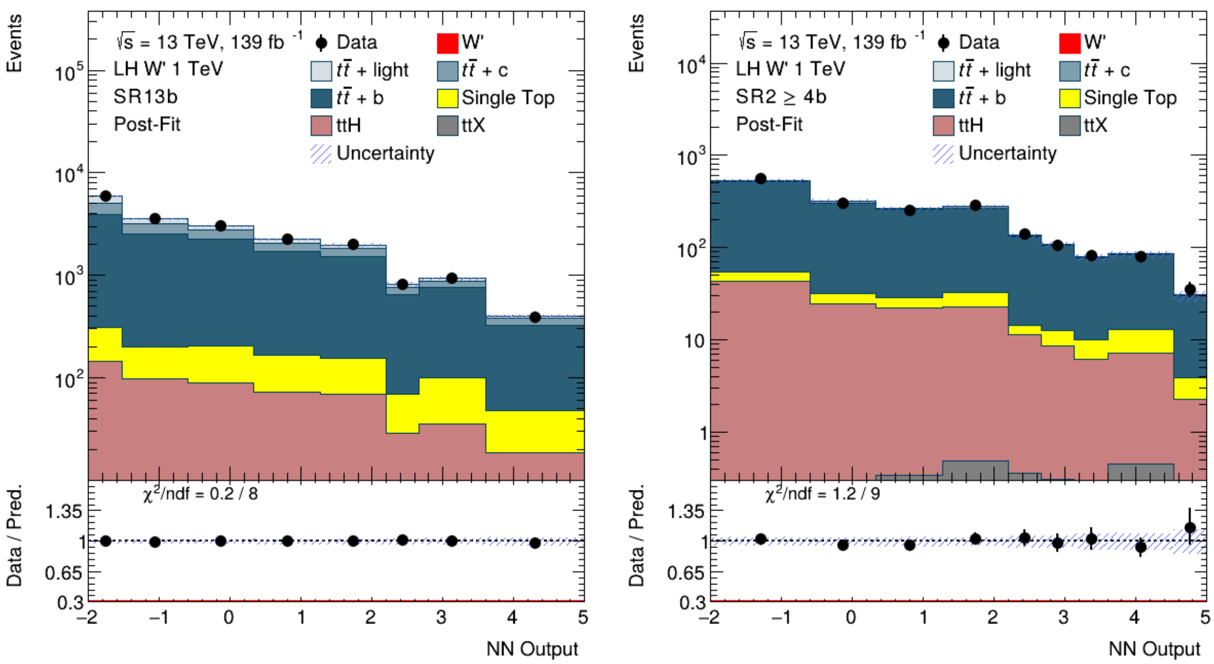

Figure 6.10: Asimov post-fit plots for LH 1 TeV W' boson signal sample where g'/g=2.

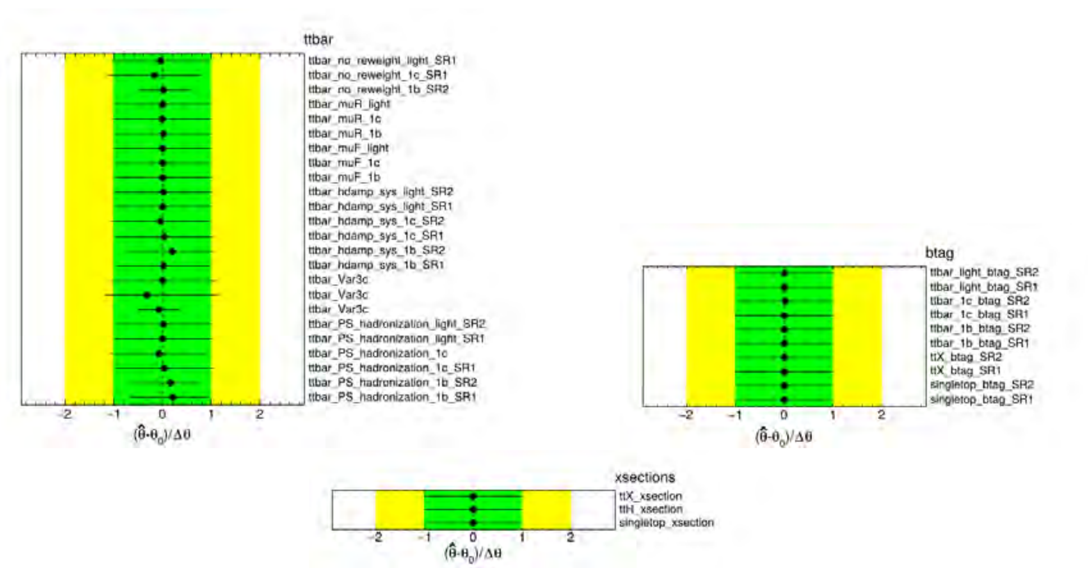

Figure 6.11: $t\bar{t}$ systematic uncertainty pull plot for Asimov fit on LH 1 TeV W' boson sample where g'/g=2.

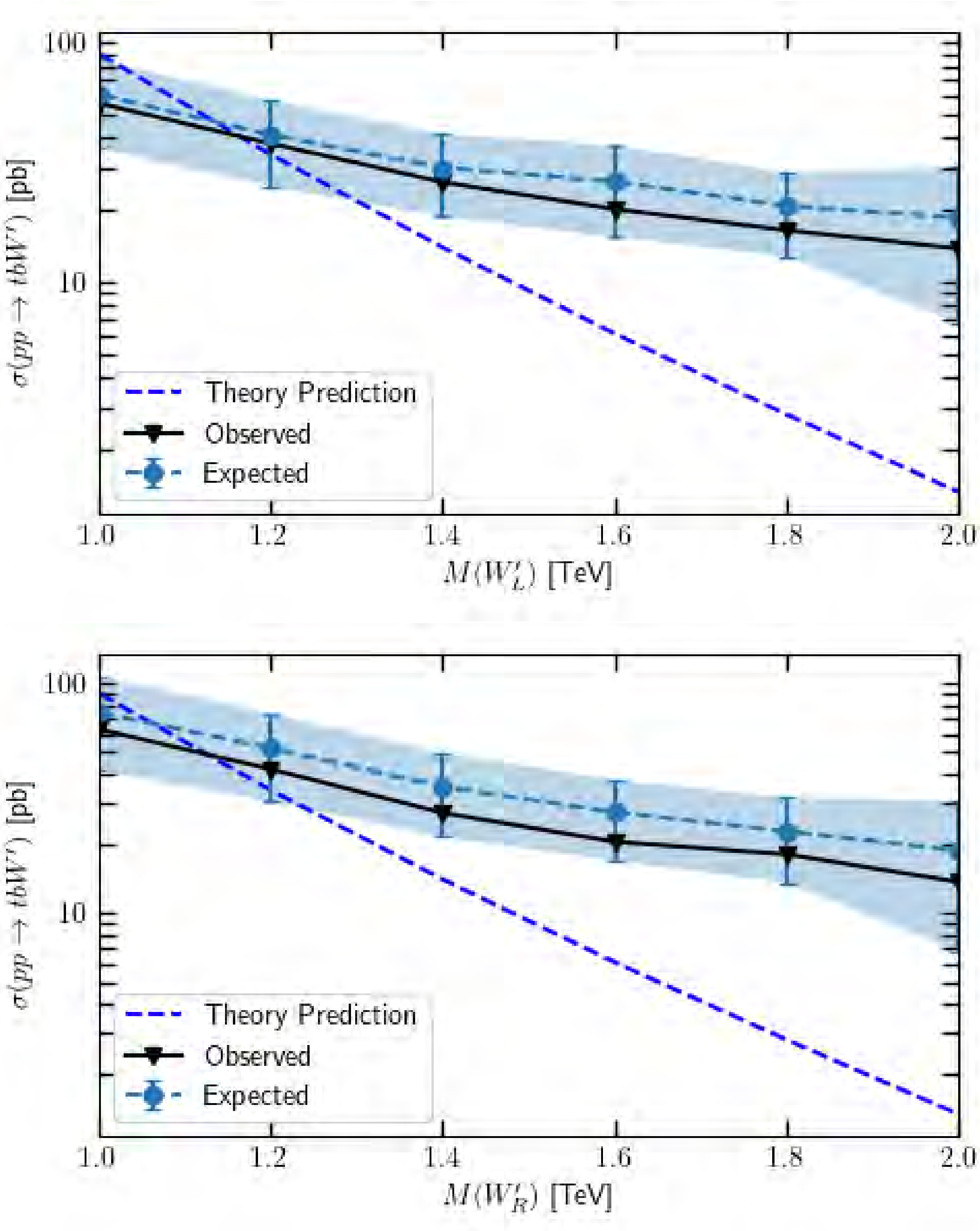

Figure 6.12: Limit plots derived from the 95% CL exclusion upper limit calculation on expected background and data fits. An upper limit on $\sigma(pp \to tbW')$ for the RH W' boson is 1.15 TeV and 1.18 TeV for the LH W' boson where $g'/g = 2$.

Chapter 7

Conclusions

A search for a heavy-philic W' boson with couplings exclusive to the third generation of quarks is performed using data exclusively from ATLAS Run 2 data. This W' boson is produced in association with a top and bottom quark leading to a final state of *tbtb*. The search in this work is done in the single lepton channel and the mass ranges of $1000 < m_{W'} < 2000$ GeV. The kinematic phase-space of this search included events where there are at least 5 jet and >3 of them are b-tagged.

Reconstructing the heavy-philic W' presents a significant challenge due to the complex final state of two top quarks and two bottom quarks. Accurately assigning reconstructed jets to the correct decay products of the W' is nontrivial, given the combinatorial ambiguity and overlapping kinematics. To address this, a machine learning strategy was developed to exploit subtle correlations in the event topology. The analysis uses a unique approach where two neural networks are trained. One neural network extracts high-level physics variables and focuses on fully reconstructing the W'. The other neural network focuses on signal and background discrimination. This architecture allows for physics-motivated interpretation at each stage in the analysis, avoiding the opacity often associated with fully end-to-end machine learning pipelines.

The output of this analysis yielded binned distributions of a final neural network output score with negative values representing SM-like events, and positive values representing events that look like heavy-philic W' boson signal. A binned-maximum likelihood fit was performed on these distributions to test for the presence of the heavy-philic W' boson in the ATLAS Run 2 dataset. The result of this fit show that there isn't any excess above the SM background.

Exclusion limits are set on the possibility of the heavy-philic W' with $g'/g = 2$. Limits of $m_{W'} > 1.18$ TeV for the LH W' boson and $m_{W'} > 1.12$ TeV for the RH W' boson are excluded. The observed upper limit on the cross section can be seen in Fig. 6.12.

This analysis is not able to exclude the scenario of $g'/g = 1$, which had cross-sections that are too low to exclude using the analysis in this work. Further studies would benefit with the addition of jets defined with a larger radius, a more systematic understanding of $t\bar{t}$ theoretical uncertainty, and the measurement of more events in this analysis region.

APPENDICES

Appendix A

PDF Uncertainty Studies

With the upcoming high luminosity large hadron collider (HL-LHC) [90], the next generation of precision measurements will be made. These measurements will be extremely precise, and will require lower theoretical uncertainties. Parton distribution functions (PDFs) are becoming the more dominant theoretical uncertainty in measurements like top quark pair production. However, many other measurements will also require reduced PDF uncertainties [91].

Colliders that will offer useful data that can significantly reduce PDF uncertainty, like the Electron Ion Collider [92], are far in the future. In the meantime, PDF uncertainty can be reduced using HL-LHC data.

Machine learning techniques can be used to pre-process data and distill useful information to reduce uncertainty in specific regions of the parton distribution functions (PDFs) where uncertainties are currently large. Traditional approaches have incorporated one-, two-, or three-dimensional projections of the high-dimensional collider phase space into the global PDF fit [93]. Variables such as the rapidity and longitudinal momentum (p_Z) of the top quark are typical examples, though these do not fully capture the available kinematic information. This appendix shows preliminary results from this ongoing effort.

A sample of $t\bar{t}$ plus one jet events with a center of mass energy of 14 TeV was generated using Madgraph at next-to-leading order (NLO) [57]. A total of 7.5 million events were generated. The PDF set that was selected to study in detail was the CT18NLO PDF set [42]. The study looks at the truth level of $t\bar{t}j$ events without decaying the top quarks. The aim of this study is to constrain the high x region of the gluon PDF. $t\bar{t}j$ has been shown to be a process that has good potential to reduce this region of the PDFs [94].

To test the idea of using machine learning to improve PDF fits, a MLP was developed to separate events with an initial gluon parton that had greater than 2 TeV longitudinal momentum. These $t\bar{t}j$ events were considered signal. Events with less than 2 TeV longitudinal momentum were considered background. The inputs to the MLP were the kinematic 4-vectors of the final state particles ($t\bar{t}j$). Decent separation was achieved which, not surprisingly, indicates that there is information about the initial colliding partons (flavor and initial momentum) in just the kinematics of the final state particles. If the MLP output score was higher than 0.7, it was considered signal and passed the MLP "filter". The MLP output scores can be seen in Fig. A.1.

Two different differential distributions were created to compare how different methods can reduce PDF uncertainty. One histogram was filled if it passed the MLP filter and another which included every event. The rapidity of the top quark was chosen to be the kinematic variable. These differential distributions were then fed into ePump [95] to see how much each could constrain the PDF uncertainty bands. They can be seen in Fig. A.2.

A systematic uncertainty of 1% for the pseudo-data was chosen, and the statistical error was set to zero. This is because with HL-LHC data, the statistical uncertainty is expected to be negligible. This can be confirmed in Fig. A.2 which shows that the PDF uncertainty is larger than the expected statistical uncertainty.

As a best-case-scenario, the gluon PDF is directly fed into ePump with 1% systematic uncertainties. This provides a useful upper limit to how much the gluon PDF uncertainty

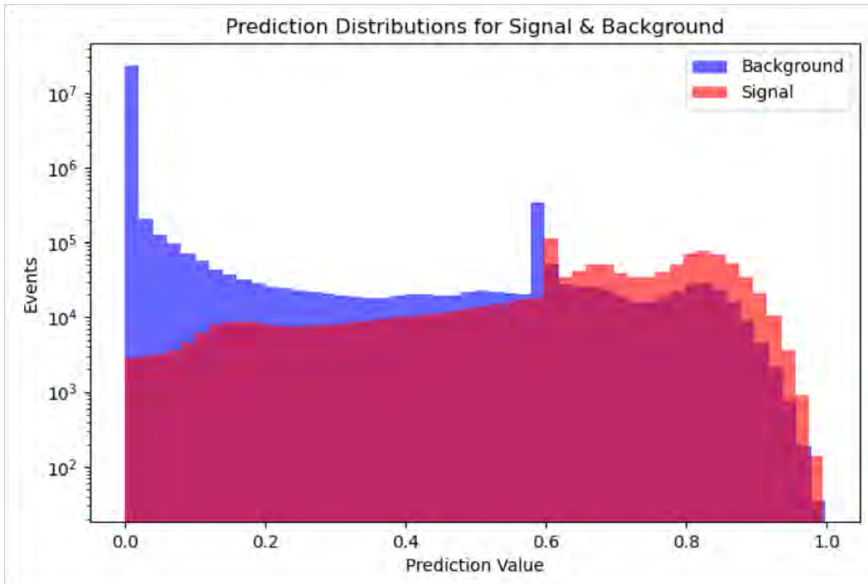

Figure A.1: The MLP output scores for the trained MLP. Events that are closer to 1 are events that the MLP predicts to have an initial gluon parton whose initial momentum is greater than 2 TeV. Events that are closer to 0 are any other event. The inputs to this MLP are the kinematic 4-vectors of the final state $t\bar{t}j$. There are 3 fully connected hidden layers. The peak at about 0.6 is currently not well understood.

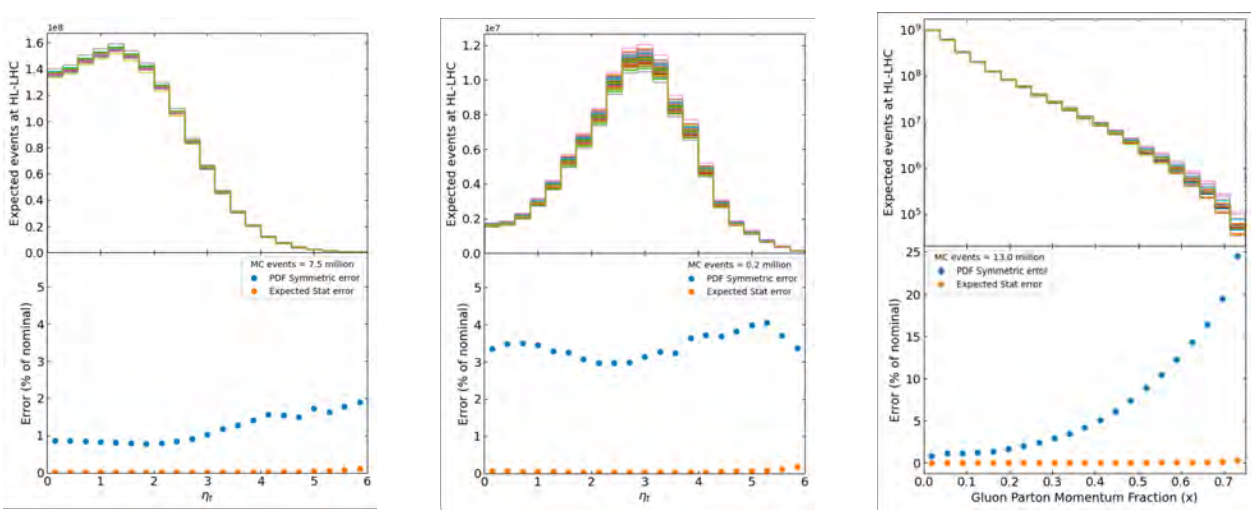

Figure A.2: Differential, pseudo-data distributions that were input into ePump to update the PDF uncertainty.

can be reduced with HL-LHC data.

It can be seen in Fig. A.3 that the uncertainty in the high-x gluon region of the PDF set is heavily reduced when filtering events.

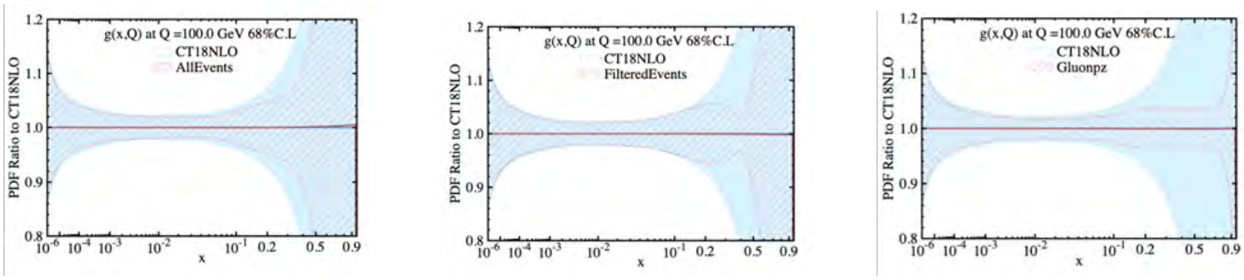

Figure A.3: Updated CT18NLO PDF uncertainty bands before and after ePump updates. Left: Updating with the top rapidity distribution from every event. Center: Updating with the top rapidity distribution with events that pass the MLP filter. Right: Updating with the gluon PDF.

The updated PDF uncertainty band of the best-case-scenario shows quite dramatic improvements in the gluon PDF uncertainty bands as expected. The uncertainty band can be narrowed up to x=0.9. This shows that there is an opportunity to improve the gluon PDF set with HL-LHC data using machine learning techniques up to a very high parton momentum fraction.

Other neural network architectures are currently being explored such as graph neural networks, and different techniques like neural network regression. It is currently not well understood how plausible it is to predict the original gluon parton momentum from final state variables or even from reconstruction level variables. This will be explored in future studies.

This study shows that there is potential to reduce PDF uncertainties by forming variables with machine learning techniques because traditional techniques do not include the full information available for a given process.

Appendix B

Asimov Fit Results

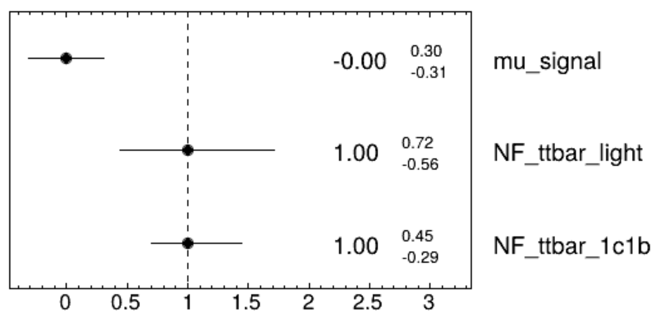

Figure B.1: Normalization factors determined by the binned maximum likelihood fit for the LH 1 TeV W' boson signal where g'/g=2.

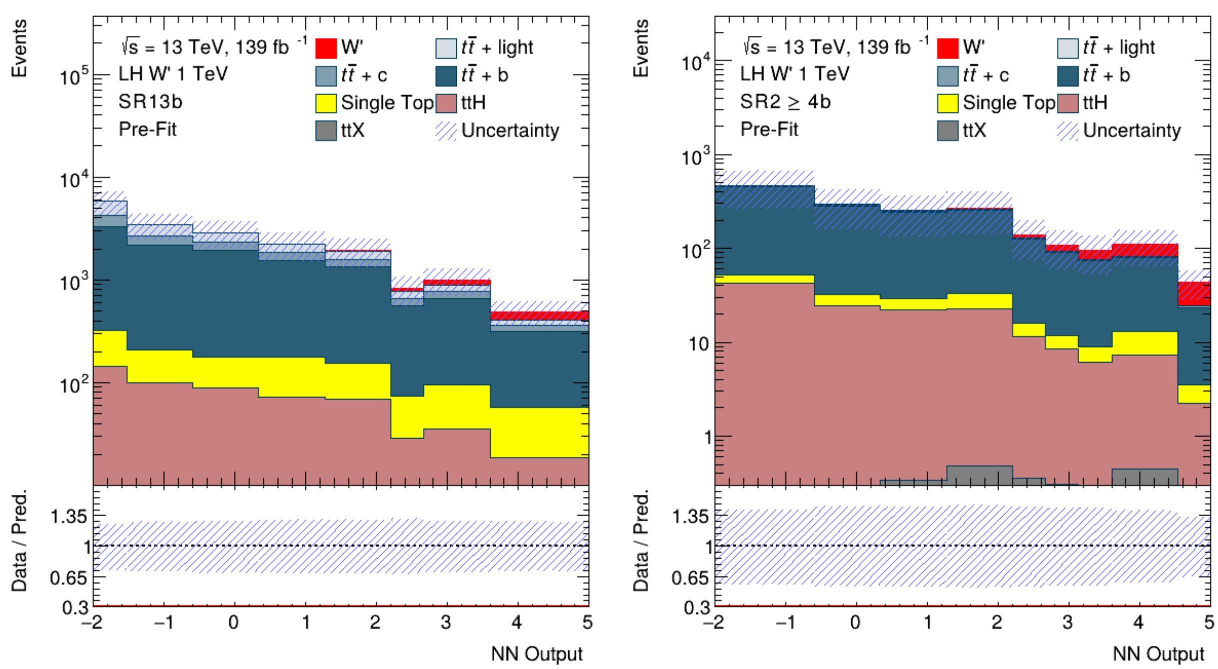

Figure B.2: Asimov pre-fit plots for LH 1 TeV W' boson signal sample where g'/g=2.

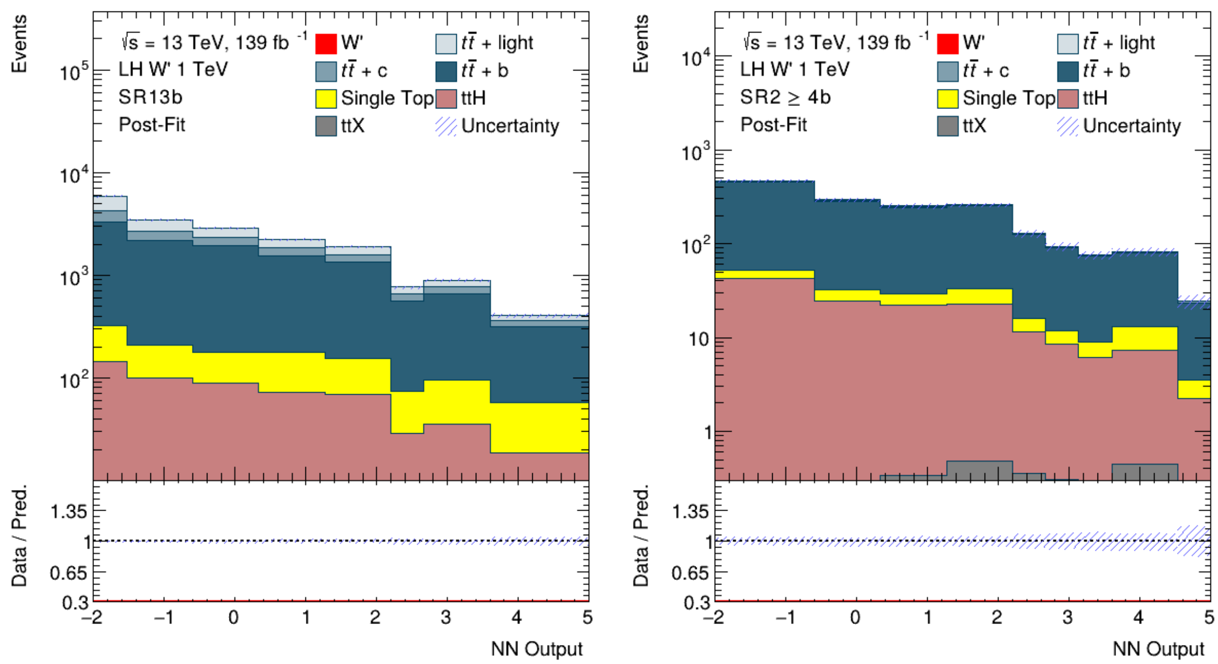

Figure B.3: Asimov post-fit plots for LH 1 TeV W' boson signal sample where g'/g=2.

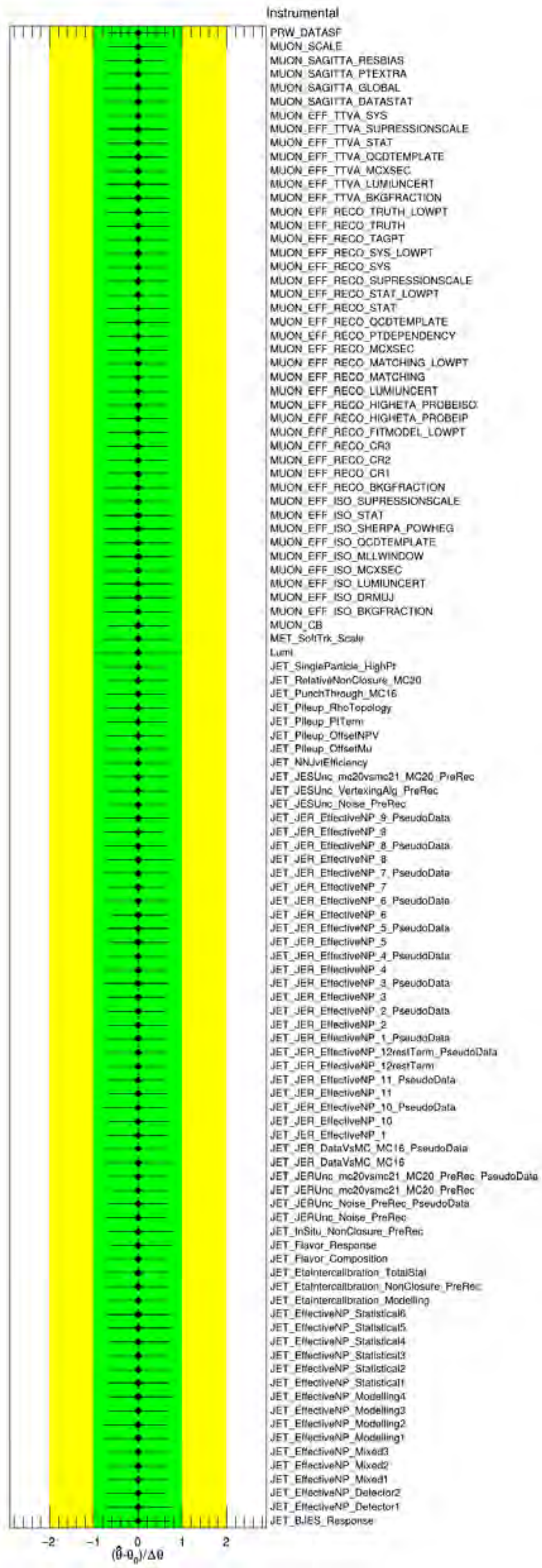

Figure B.4: Detector systematic uncertainty pull plot for Asimov fit on LH 1 TeV W' boson sample where g'/g=2.

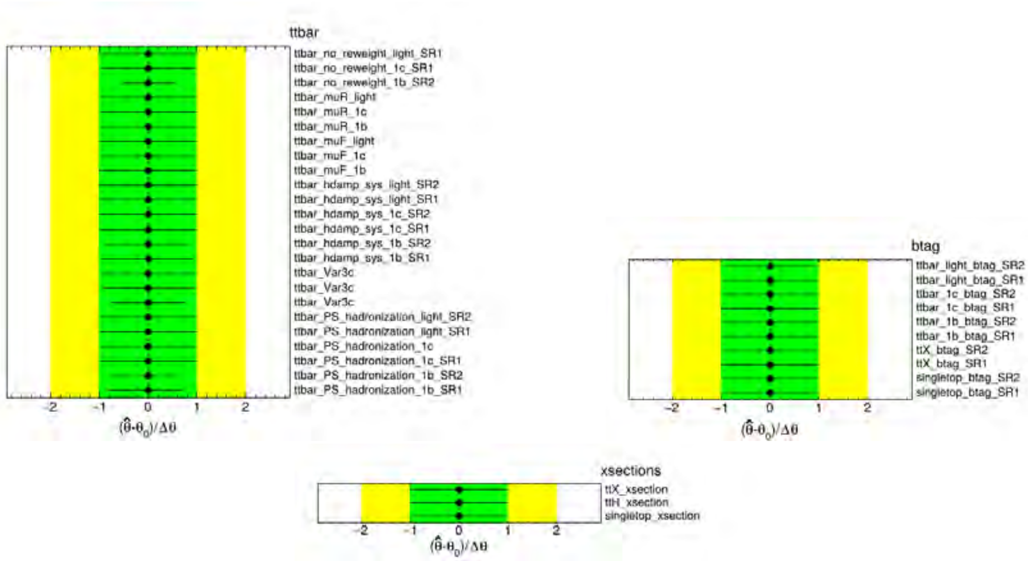

Figure B.5: $t\bar{t}$, b-tagging, and cross-section systematic uncertainty pull plot for Asimov fit on LH 1 TeV W' boson sample where g'/g=2.

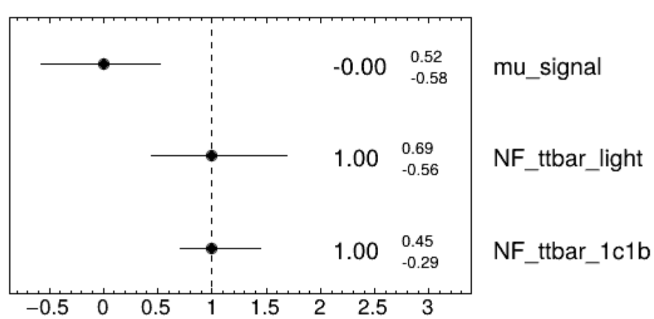

Figure B.6: Normalization factors determined by the binned maximum likelihood fit for the LH 1.2 TeV W' boson signal where $g'/g = 2$.

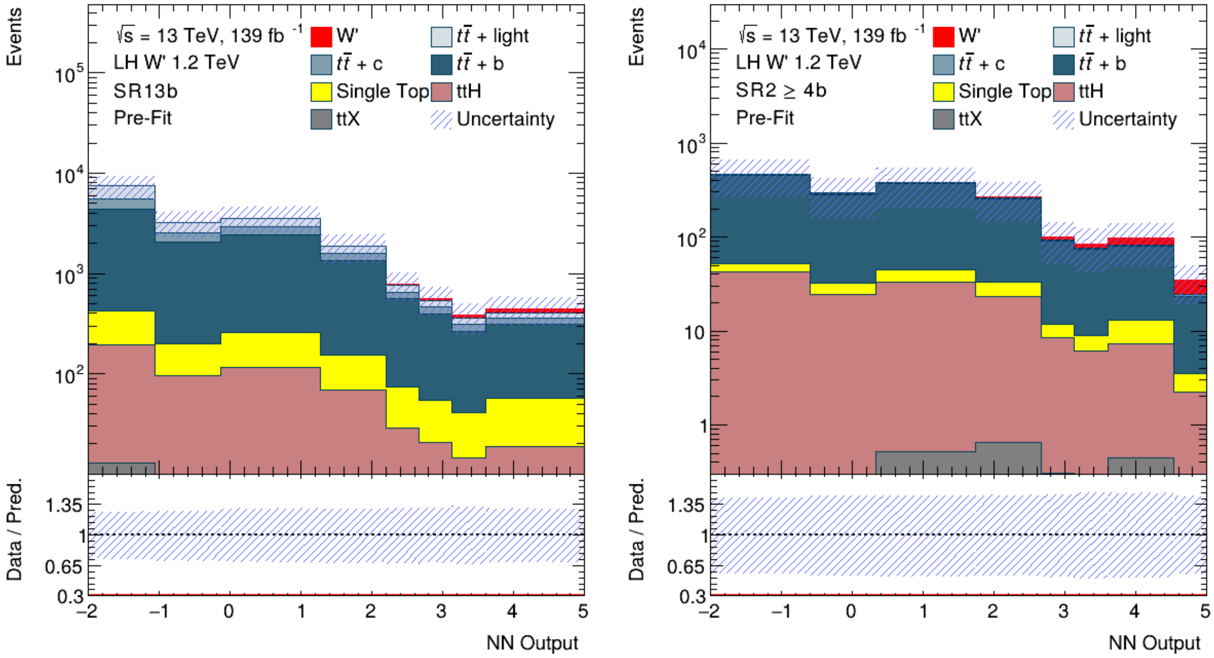

Figure B.7: Asimov pre-fit plots for LH 1.2 TeV W' boson signal sample where $g'/g = 2$.

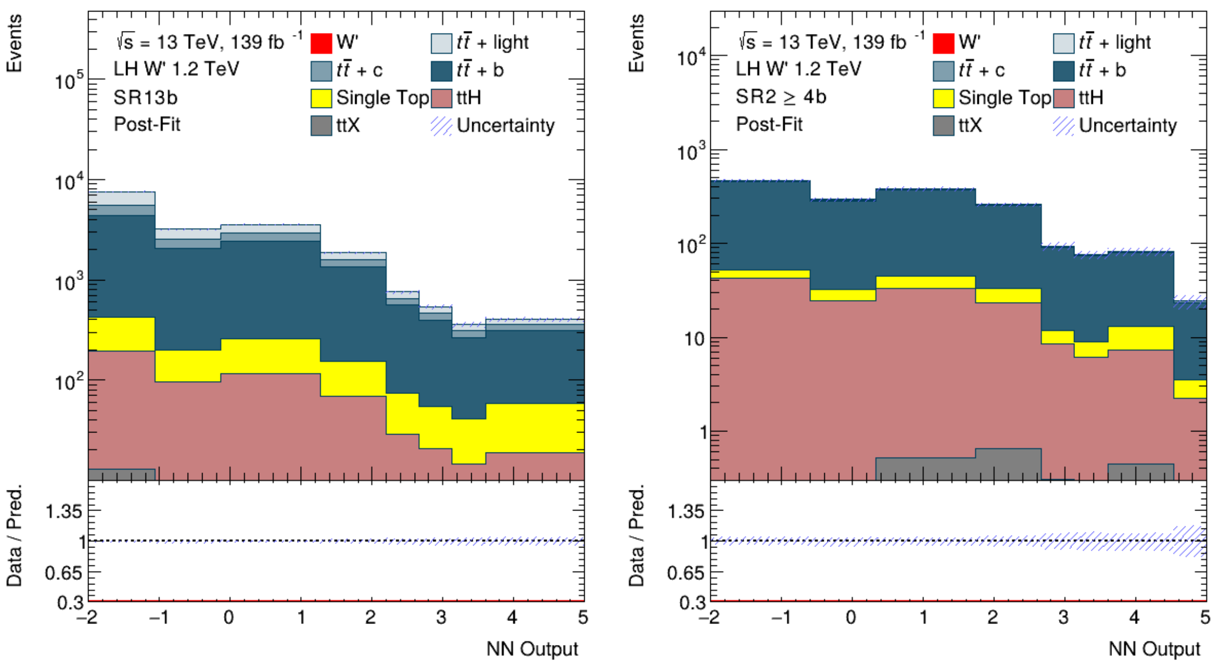

Figure B.8: Asimov post-fit plots for LH 1.2 TeV W' boson signal sample where $g'/g = 2$.

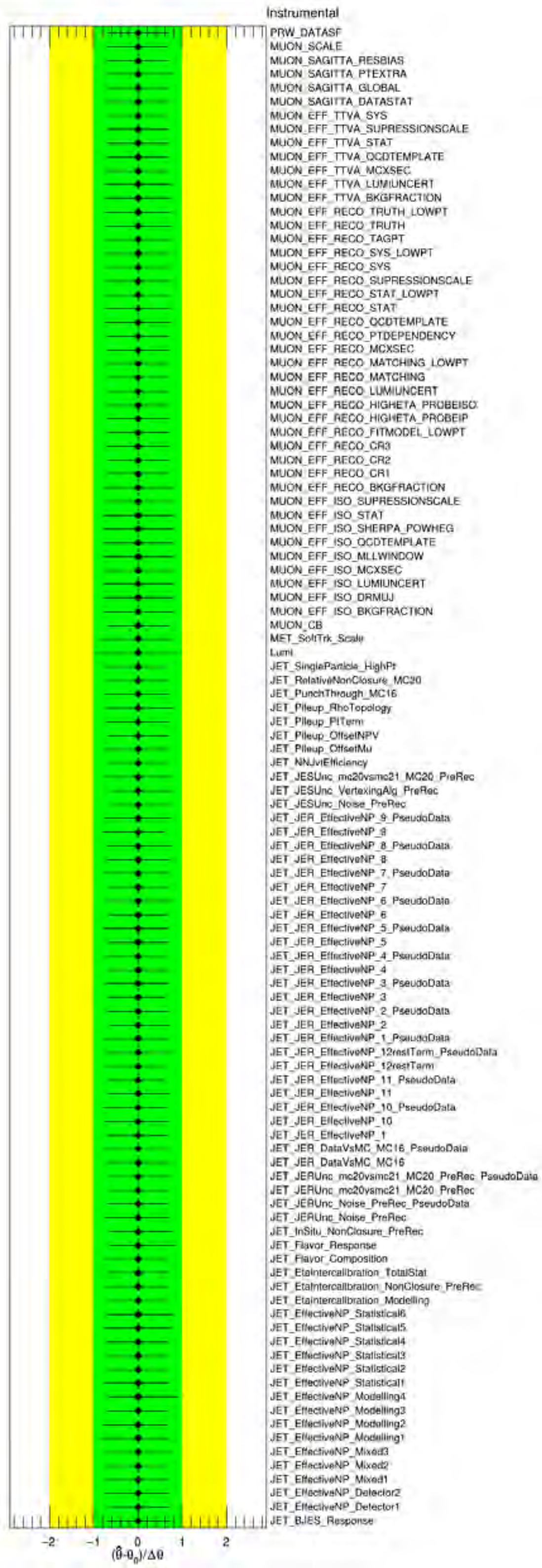

Figure B.9: Detector systematic uncertainty pull plot for Asimov fit on LH 1.2 TeV W' boson sample where $g'/g = 2$.

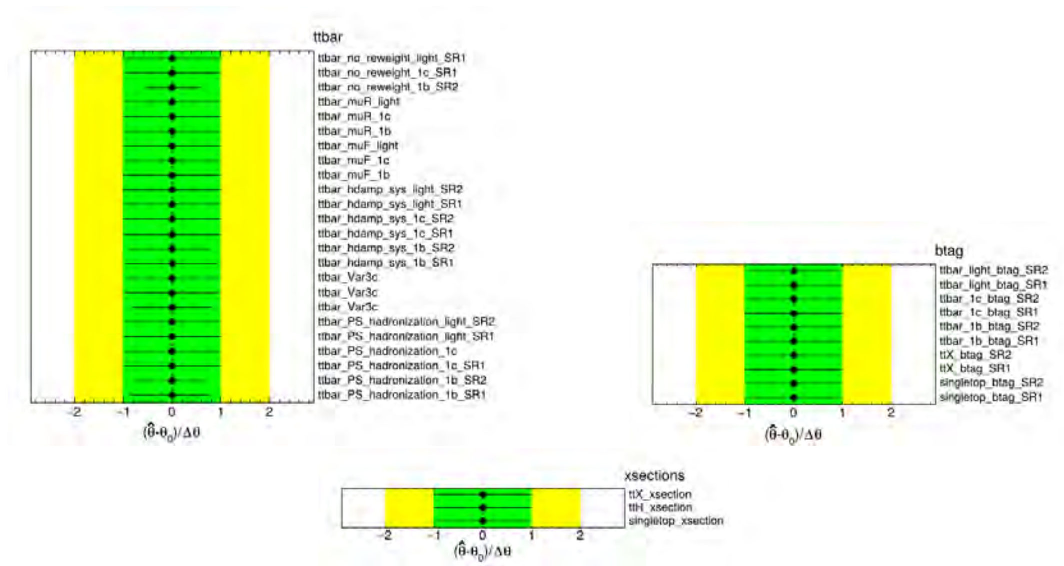

Figure B.10: $t\bar{t}$, b-tagging, and cross-section systematic uncertainty pull plot for Asimov fit on LH 1.2 TeV W' boson sample where $g'/g = 2$.

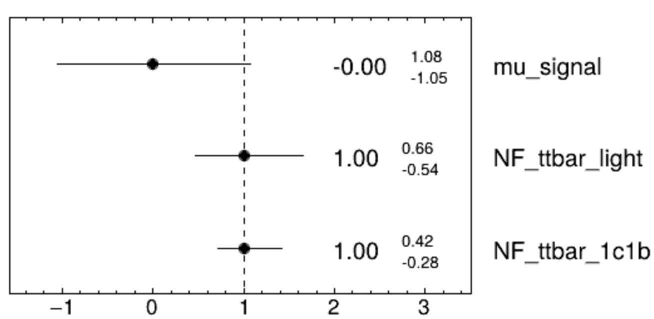

Figure B.11: Normalization factors determined by the binned maximum likelihood fit for the LH 1.4 TeV W' boson signal where $g'/g = 2$.

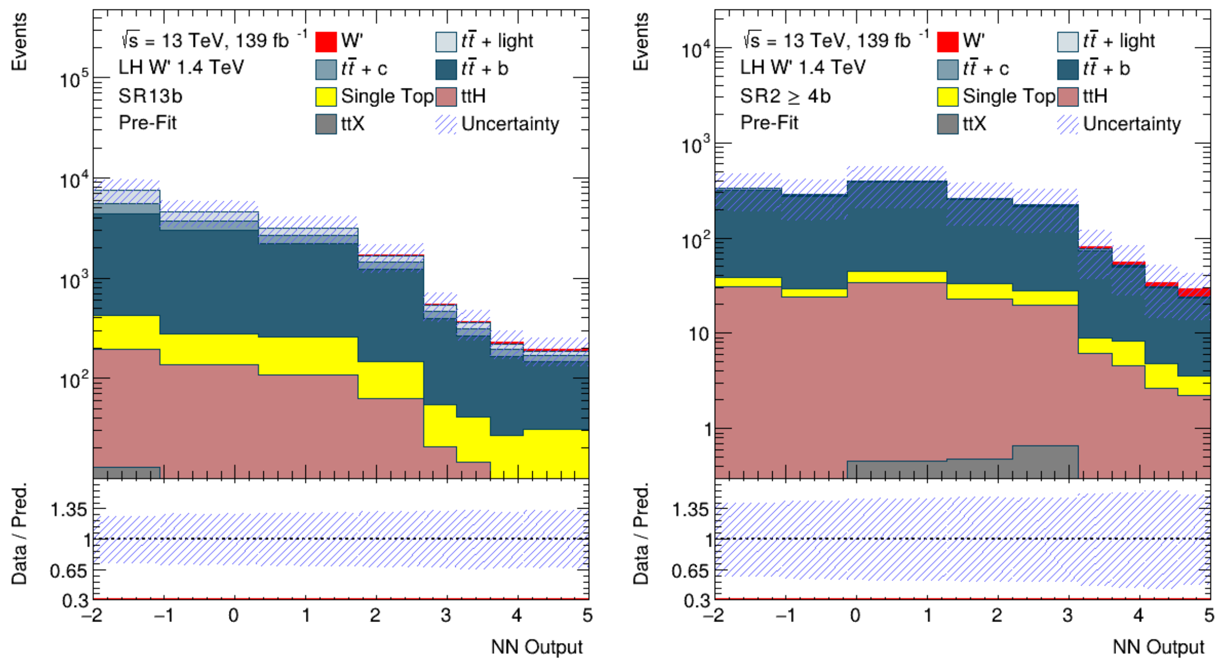

Figure B.12: Asimov pre-fit plots for LH 1.4 TeV W' boson signal sample where $g'/g = 2$.

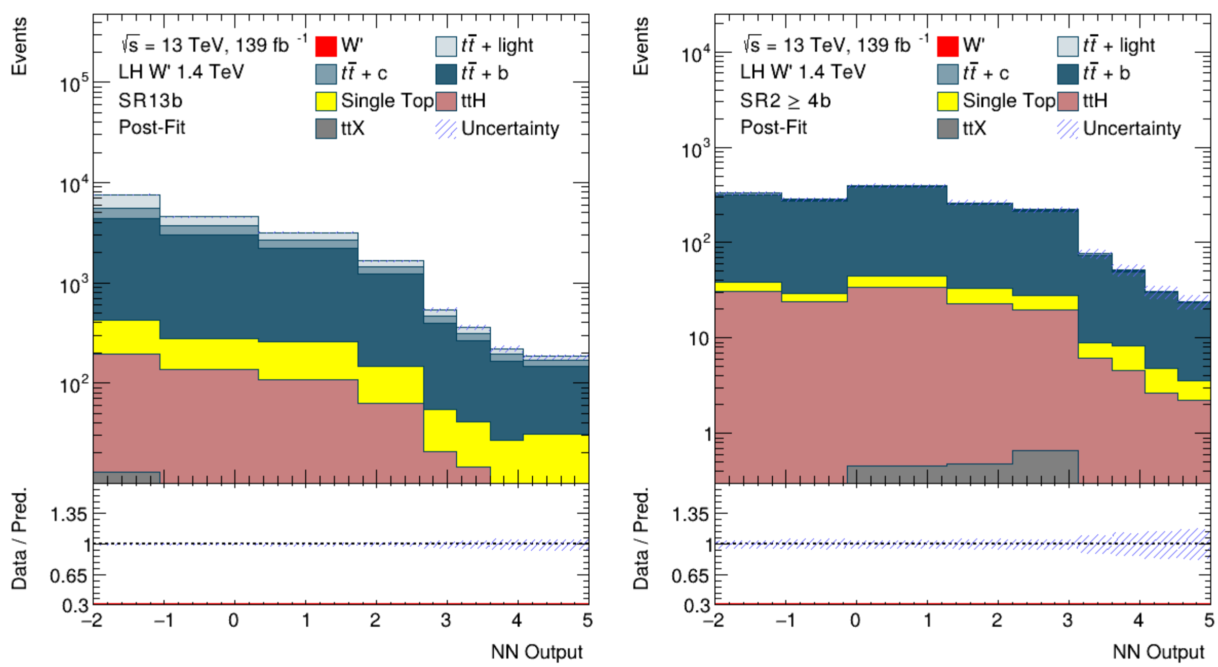

Figure B.13: Asimov post-fit plots for LH 1.4 TeV W' boson signal sample where $g'/g = 2$.

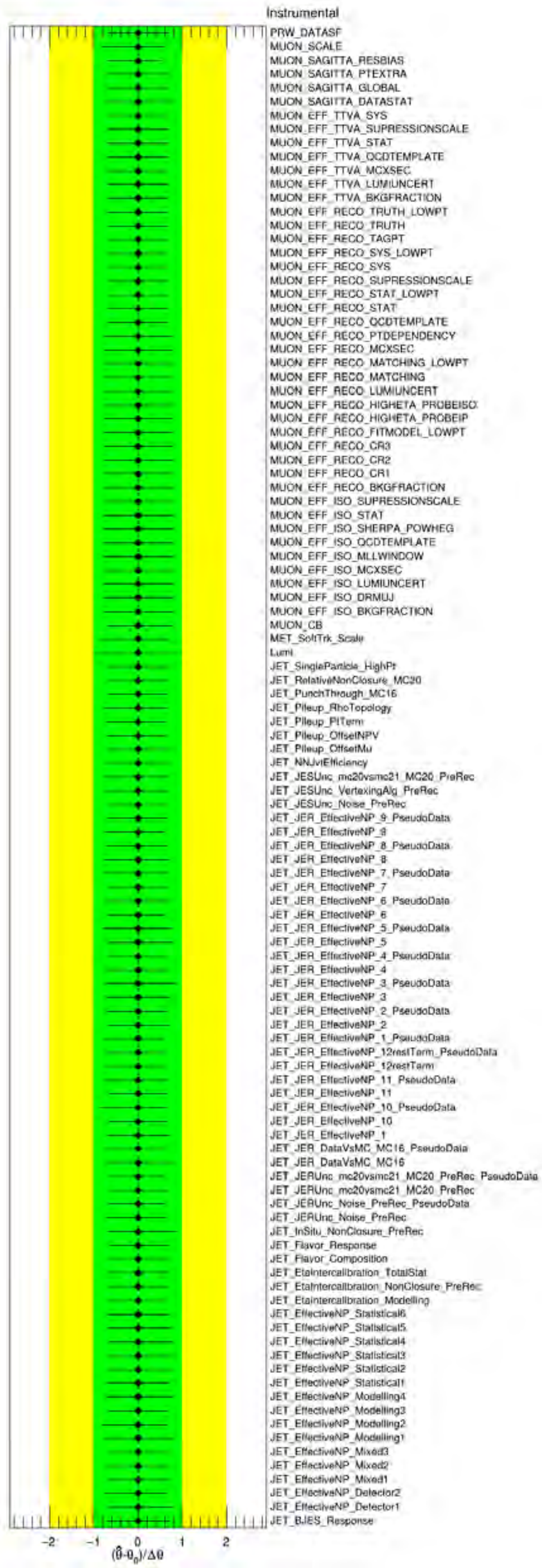

Figure B.14: Detector systematic uncertainty pull plot for Asimov fit on LH 1.4 TeV W' boson sample where $g'/g = 2$.

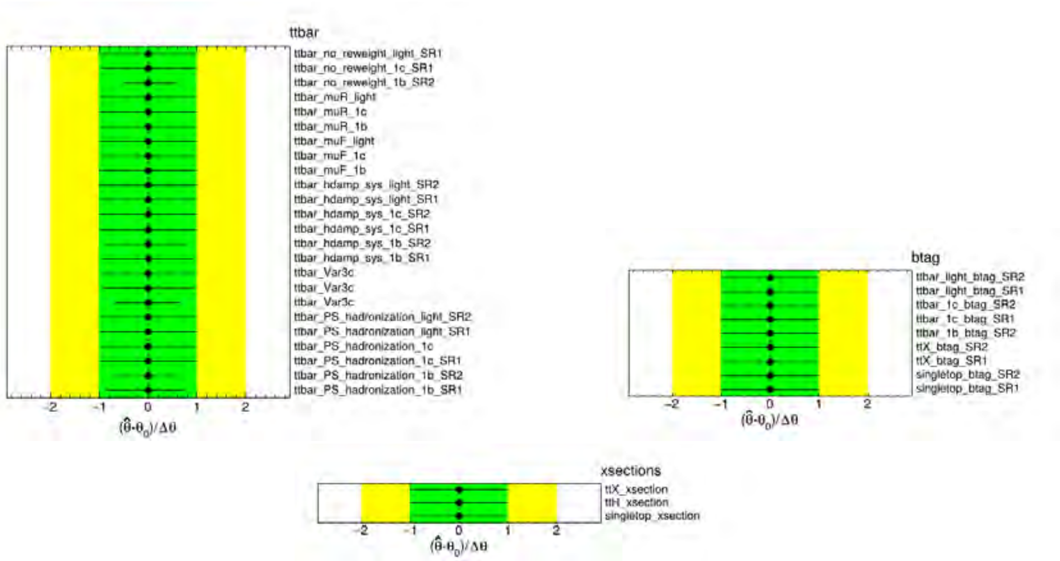

Figure B.15: $t\bar{t}$, b-tagging, and cross-section systematic uncertainty pull plot for Asimov fit on LH 1.4 TeV W' boson sample where $g'/g = 2$.

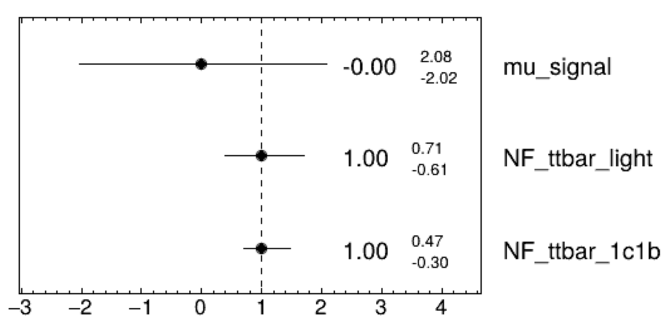

Figure B.16: Normalization factors determined by the binned maximum likelihood fit for the LH 1.6 TeV W' boson signal where $g'/g = 2$.

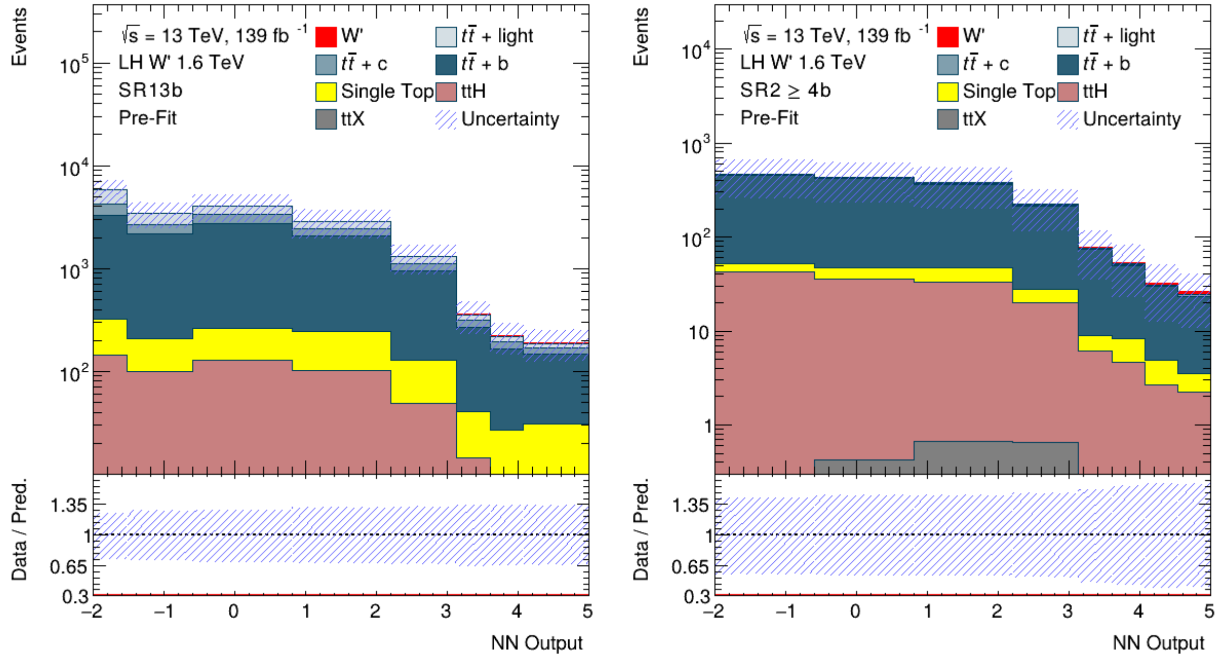

Figure B.17: Asimov pre-fit plots for LH 1.6 TeV W' boson signal sample where $g'/g = 2$.

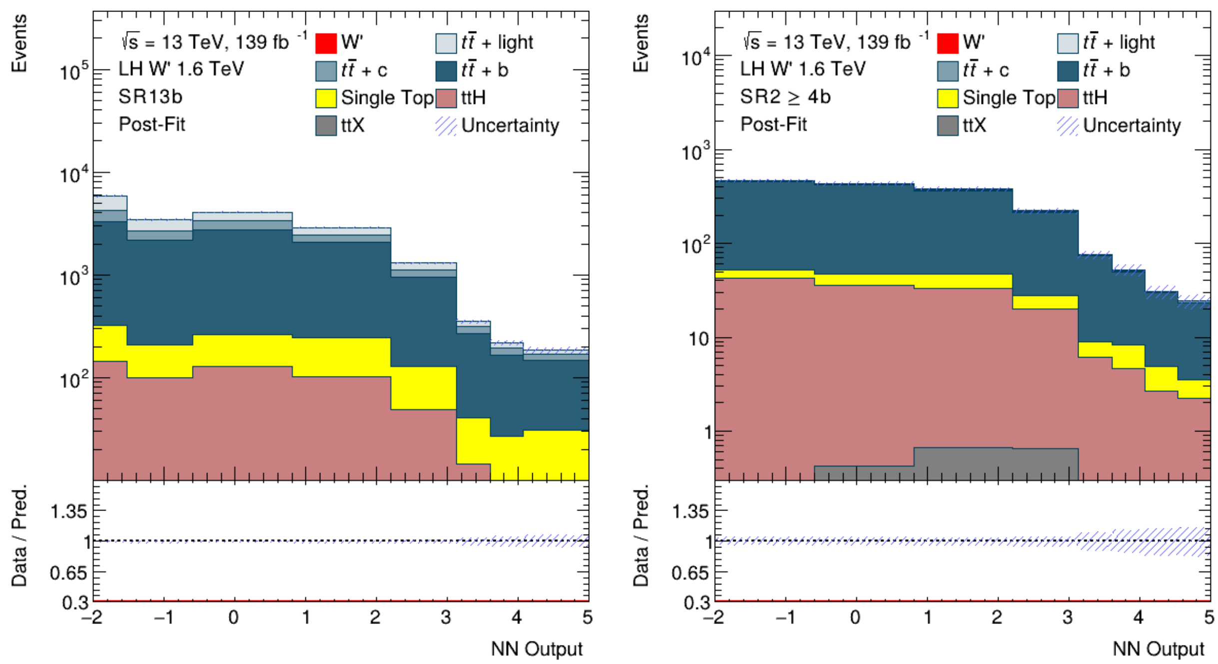

Figure B.18: Asimov post-fit plots for LH 1.6 TeV W' boson signal sample where $g'/g = 2$.

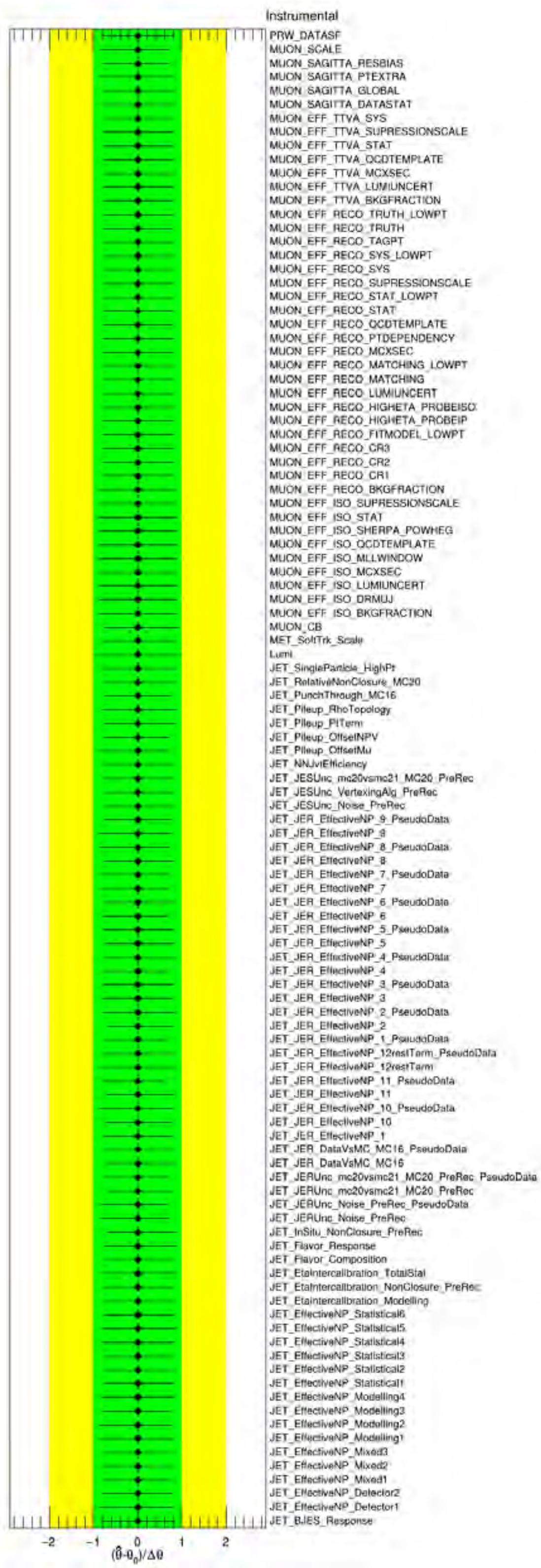

Figure B.19: Detector systematic uncertainty pull plot for Asimov fit on LH 1.6 TeV W' boson sample where $g'/g = 2$.

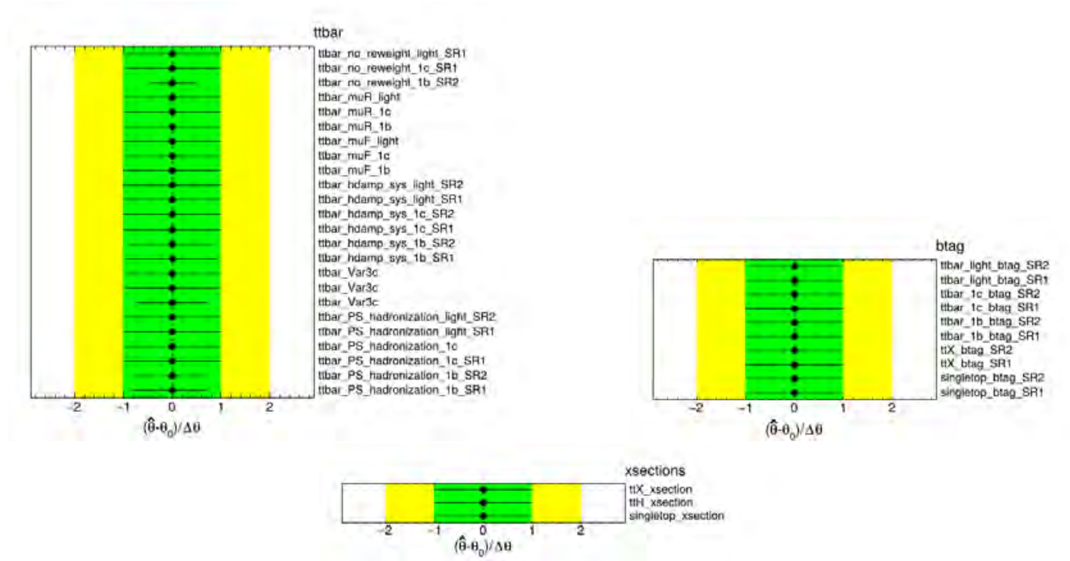

Figure B.20: $t\bar{t}$, b-tagging, and cross-section systematic uncertainty pull plot for Asimov fit on LH 1.6 TeV W' boson sample where $g'/g = 2$.

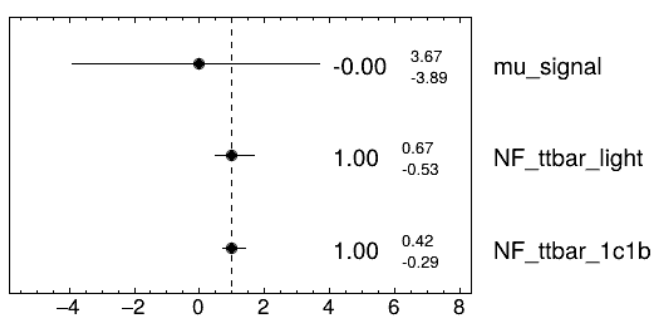

Figure B.21: Normalization factors determined by the binned maximum likelihood fit for the LH 1.8 TeV W' boson signal where $g'/g = 2$.

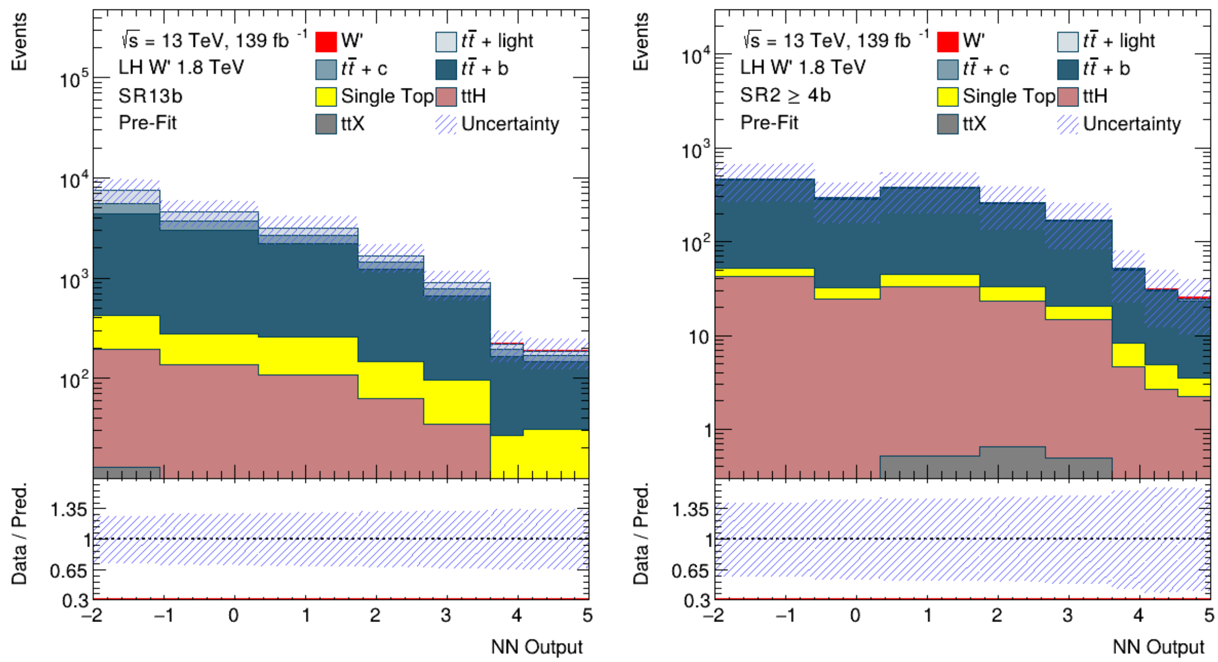

Figure B.22: Asimov pre-fit plots for LH 1.8 TeV W' boson signal sample where $g'/g = 2$.

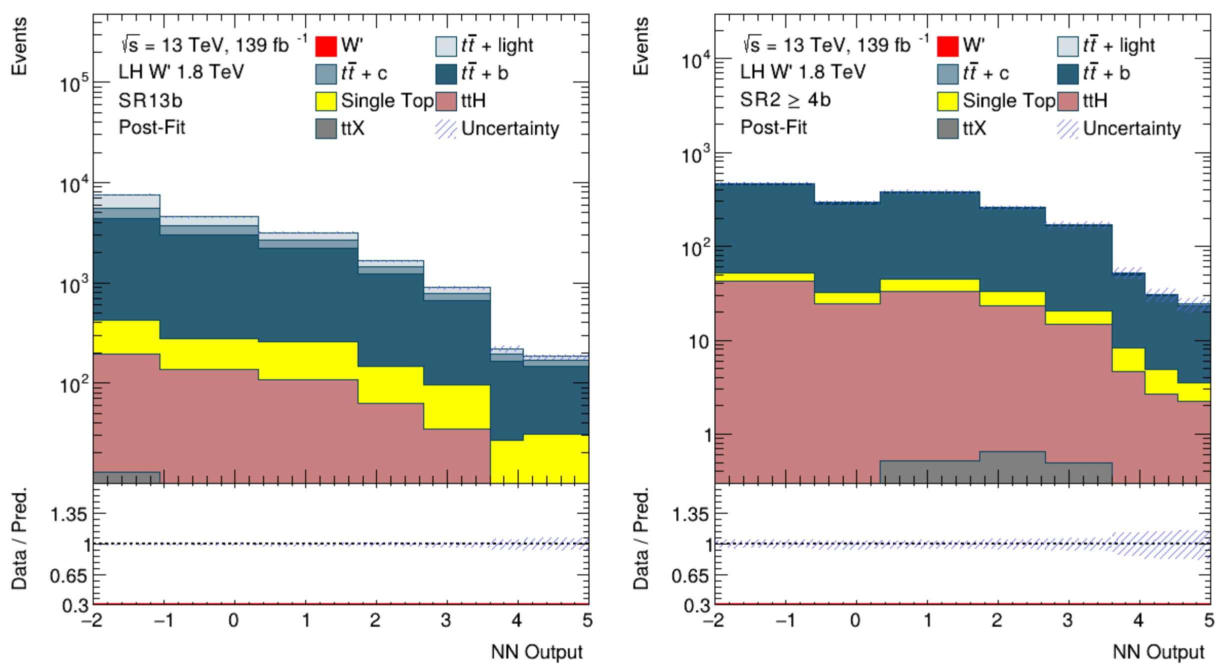

Figure B.23: Asimov post-fit plots for LH 1.8 TeV W' boson signal sample where $g'/g = 2$.

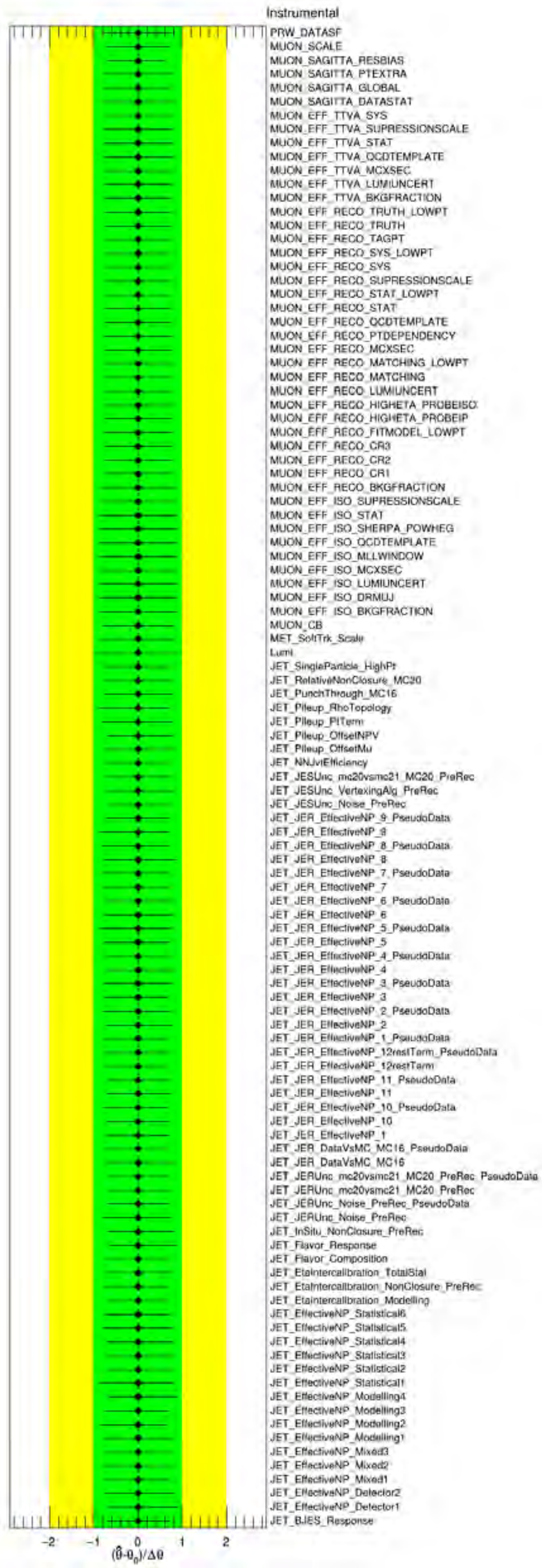

Figure B.24: Detector systematic uncertainty pull plot for Asimov fit on LH 1.8 TeV W' boson sample where $g'/g = 2$.

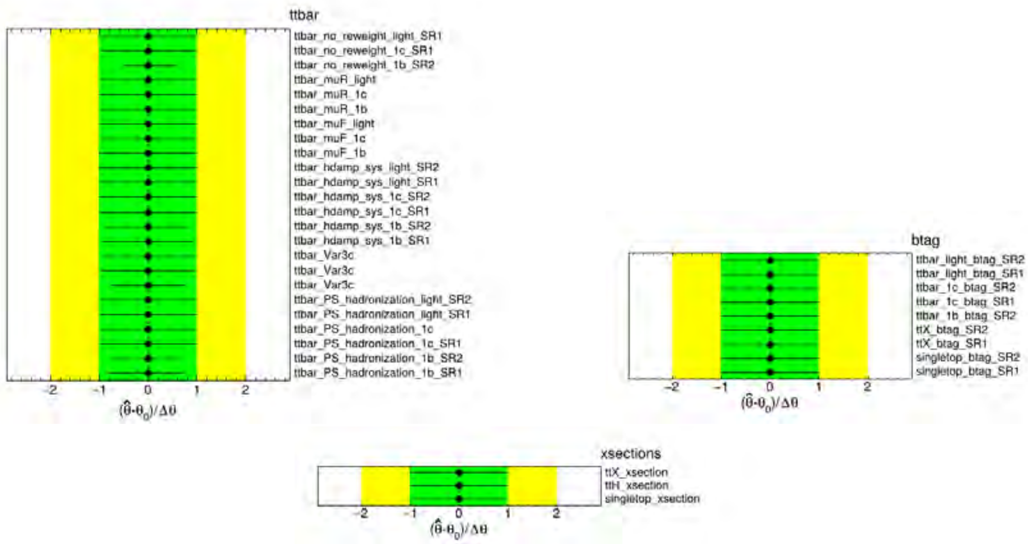

Figure B.25: $t\bar{t}$, b-tagging, and cross-section systematic uncertainty pull plot for Asimov fit on LH 1.8 TeV W' boson sample where $g'/g = 2$.

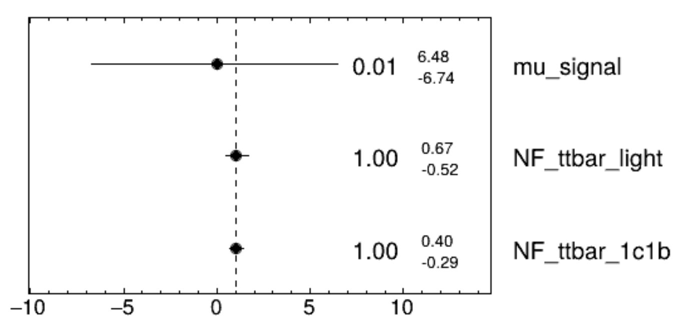

Figure B.26: Normalization factors determined by the binned maximum likelihood fit for the LH 2 TeV W' boson signal where $g'/g = 2$.

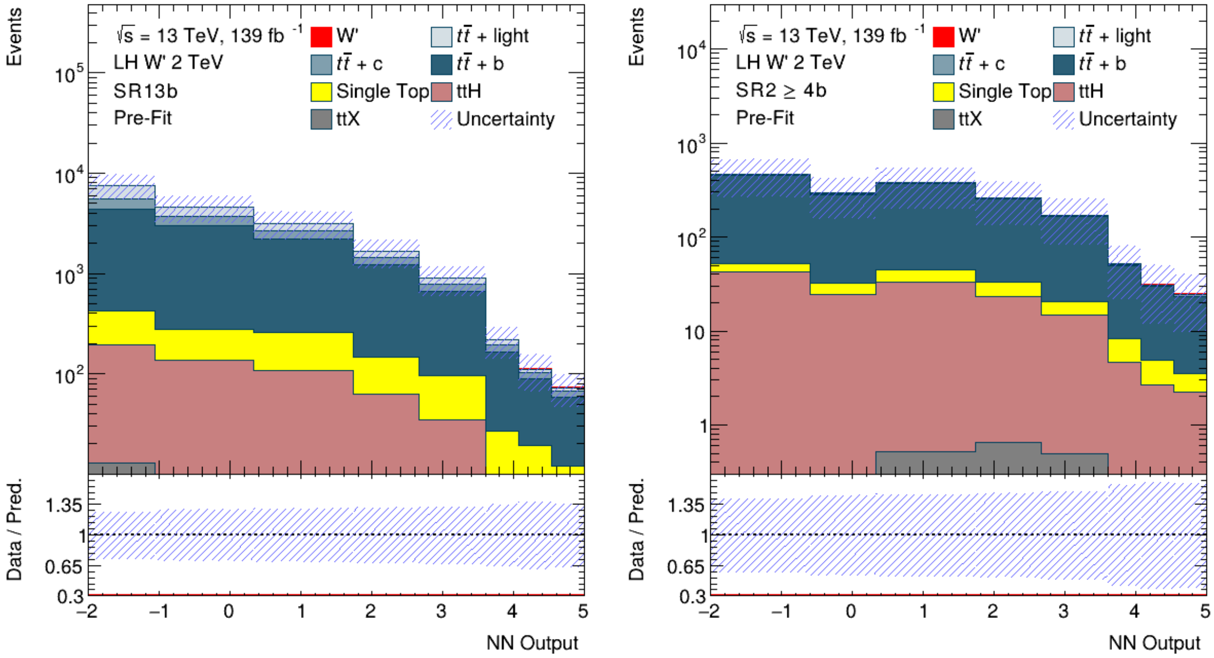

Figure B.27: Asimov pre-fit plots for LH 2 TeV W' boson signal sample where $g'/g = 2$.

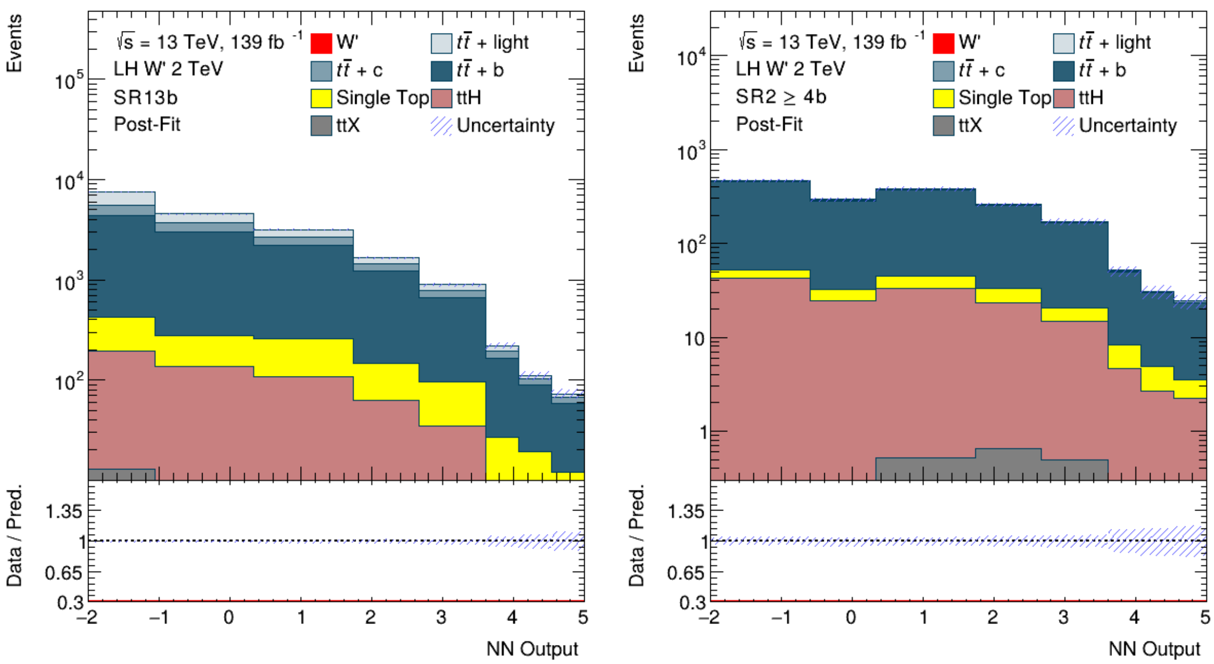

Figure B.28: Asimov post-fit plots for LH 2 TeV W' boson signal sample where $g'/g = 2$.

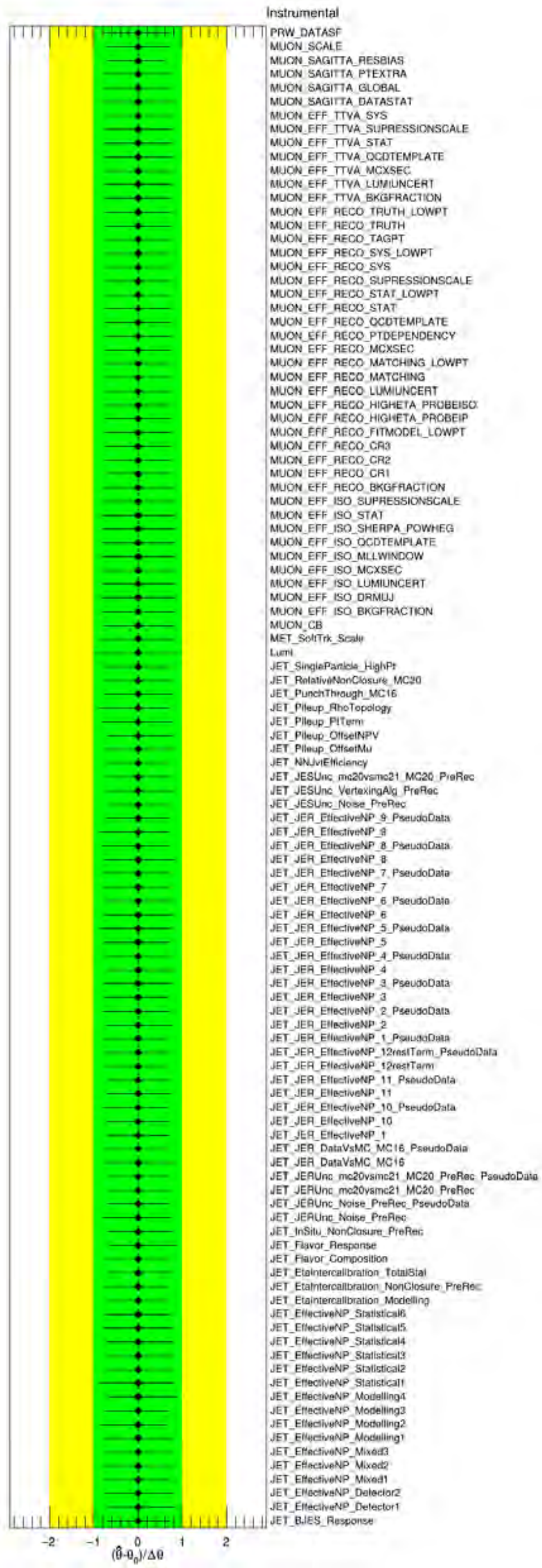

Figure B.29: Detector systematic uncertainty pull plot for Asimov fit on LH 2 TeV W' boson sample where $g'/g = 2$.

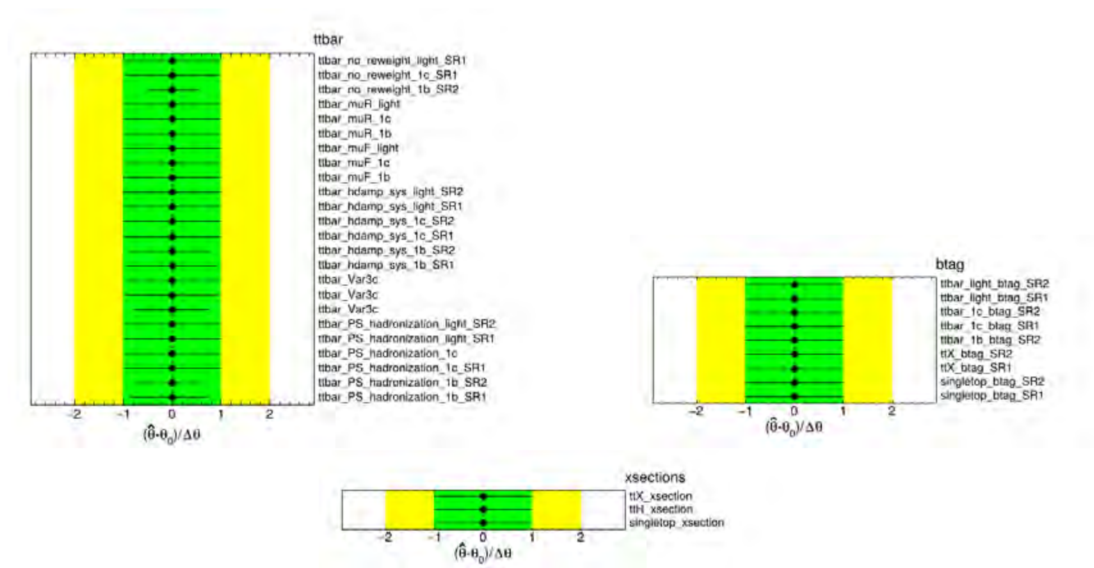

Figure B.30: $t\bar{t}$, b-tagging, and cross-section systematic uncertainty pull plot for Asimov fit on LH 2 TeV W' boson sample where $g'/g = 2$.

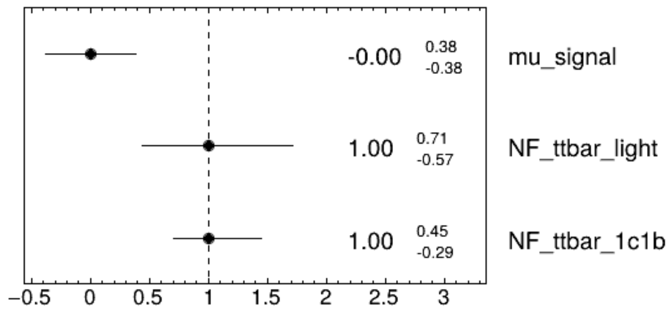

Figure B.31: Normalization factors determined by the binned maximum likelihood fit for the RH 1 TeV W' boson signal where g'/g=2.

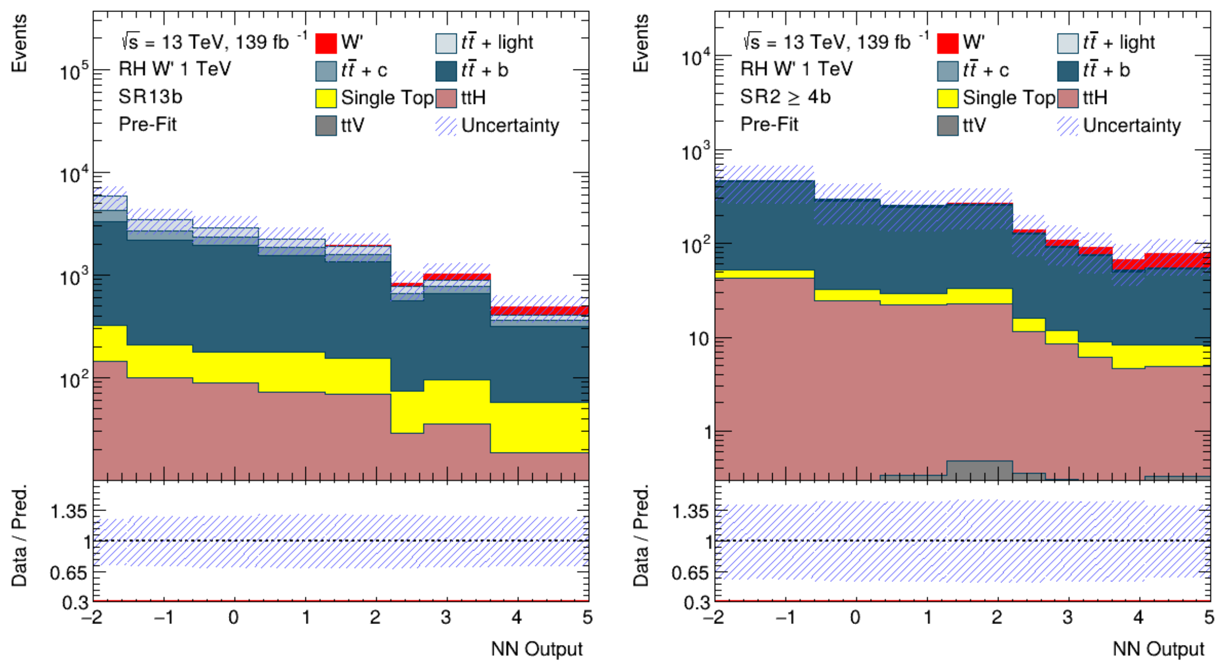

Figure B.32: Asimov pre-fit plots for RH 1 TeV W' boson signal sample where g'/g=2.

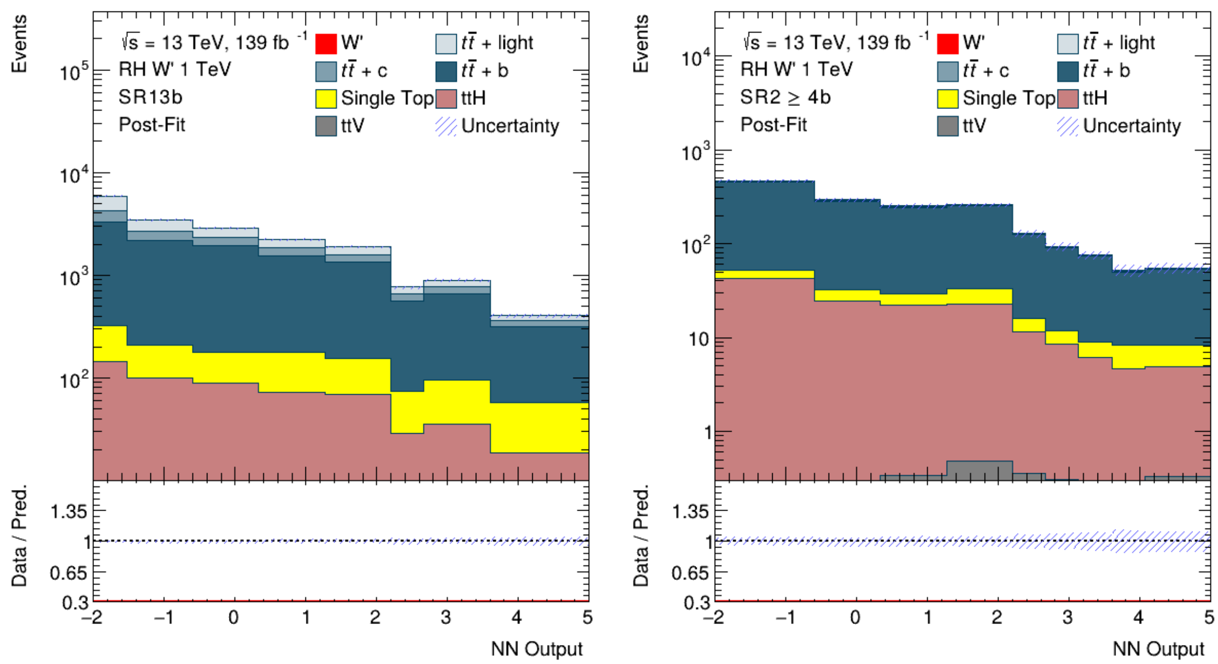

Figure B.33: Asimov post-fit plots for RH 1 TeV W' boson signal sample where g'/g=2.

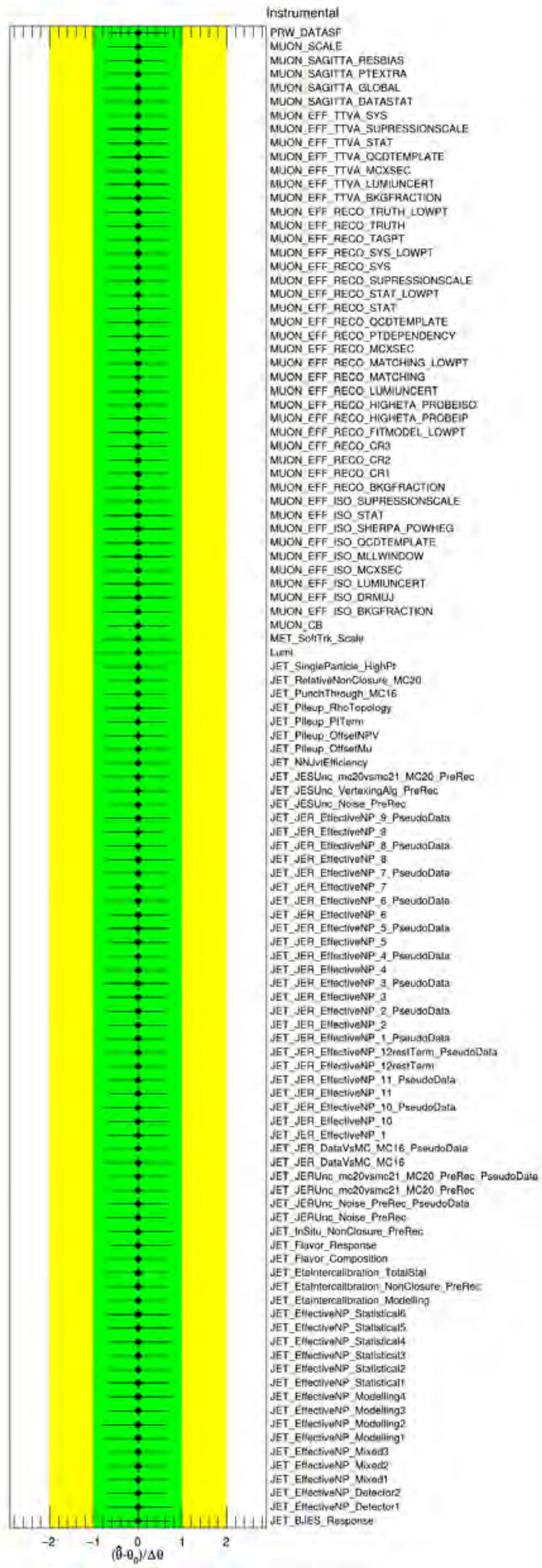

Figure B.34: Detector systematic uncertainty pull plot for Asimov fit on RH 1 TeV W' boson sample where g'/g=2.

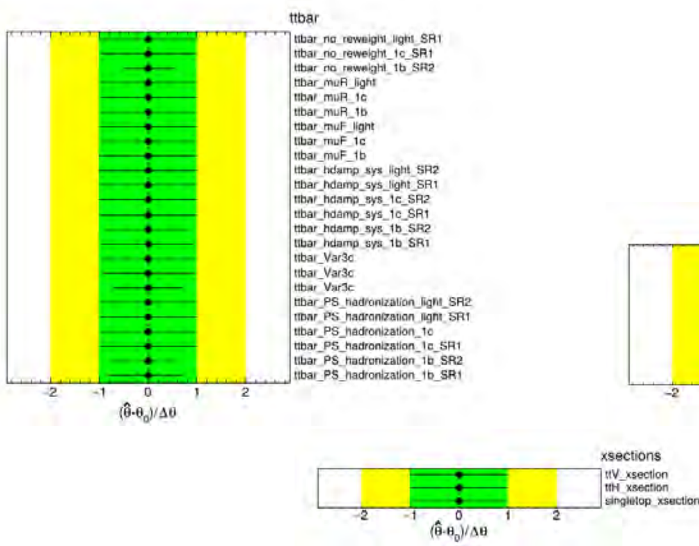

Figure B.35: $t\bar{t}$, b-tagging, and cross-section systematic uncertainty pull plot for Asimov fit on RH 1 TeV W' boson sample where g'/g=2.

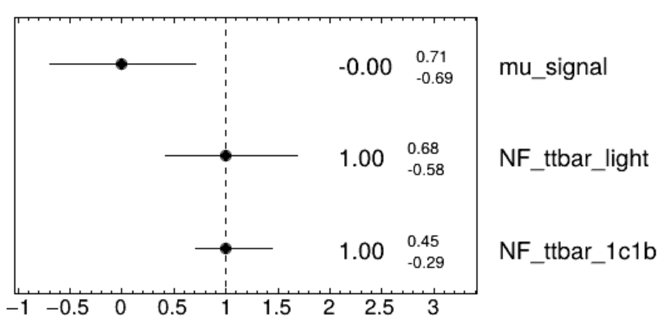

Figure B.36: Normalization factors determined by the binned maximum likelihood fit for the RH 1.2 TeV W' boson signal where $g'/g = 2$.

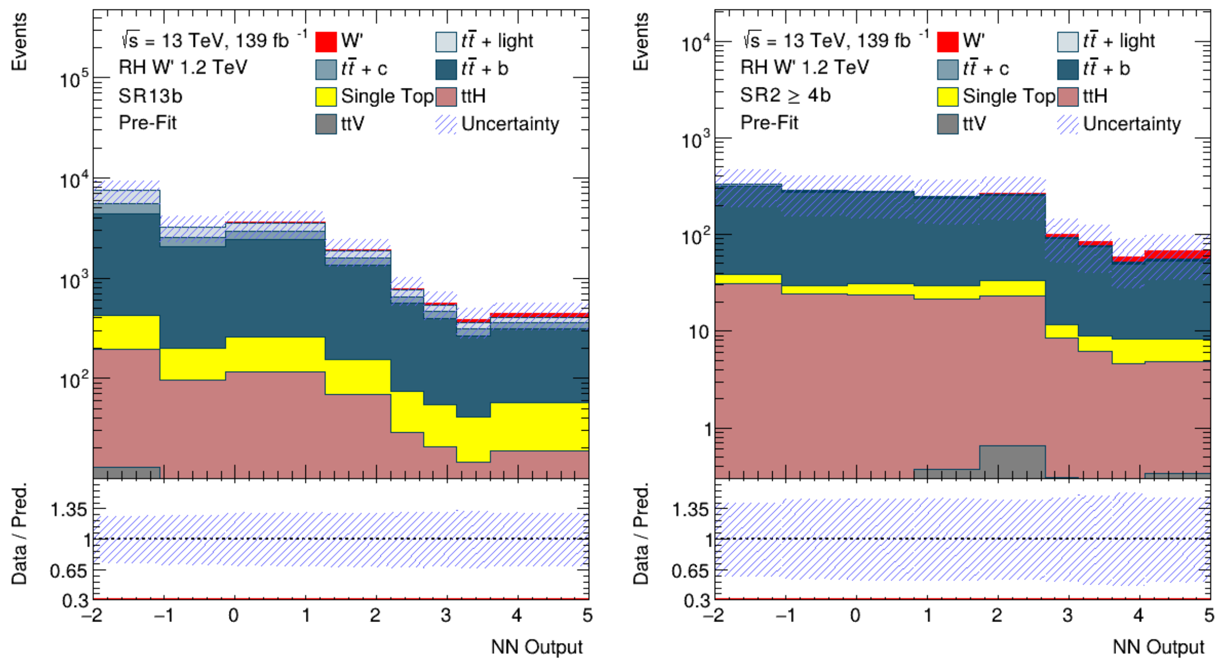

Figure B.37: Asimov pre-fit plots for RH 1.2 TeV W' boson signal sample where $g'/g = 2$.

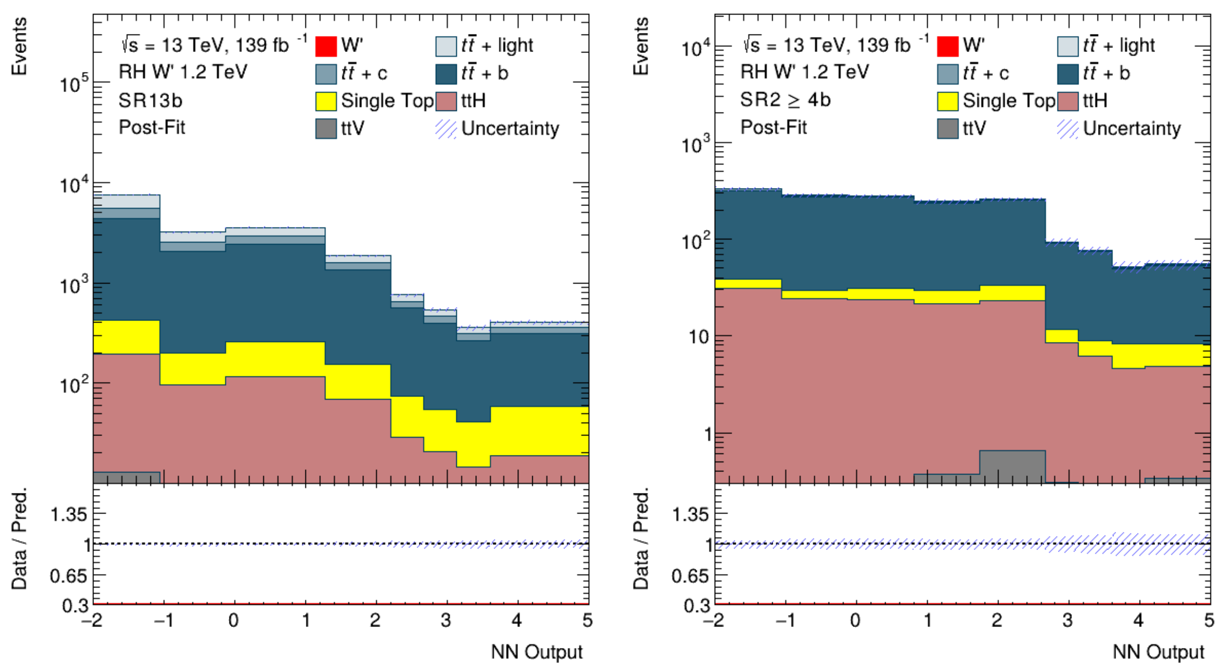

Figure B.38: Asimov post-fit plots for RH 1.2 TeV W' boson signal sample where $g'/g = 2$.

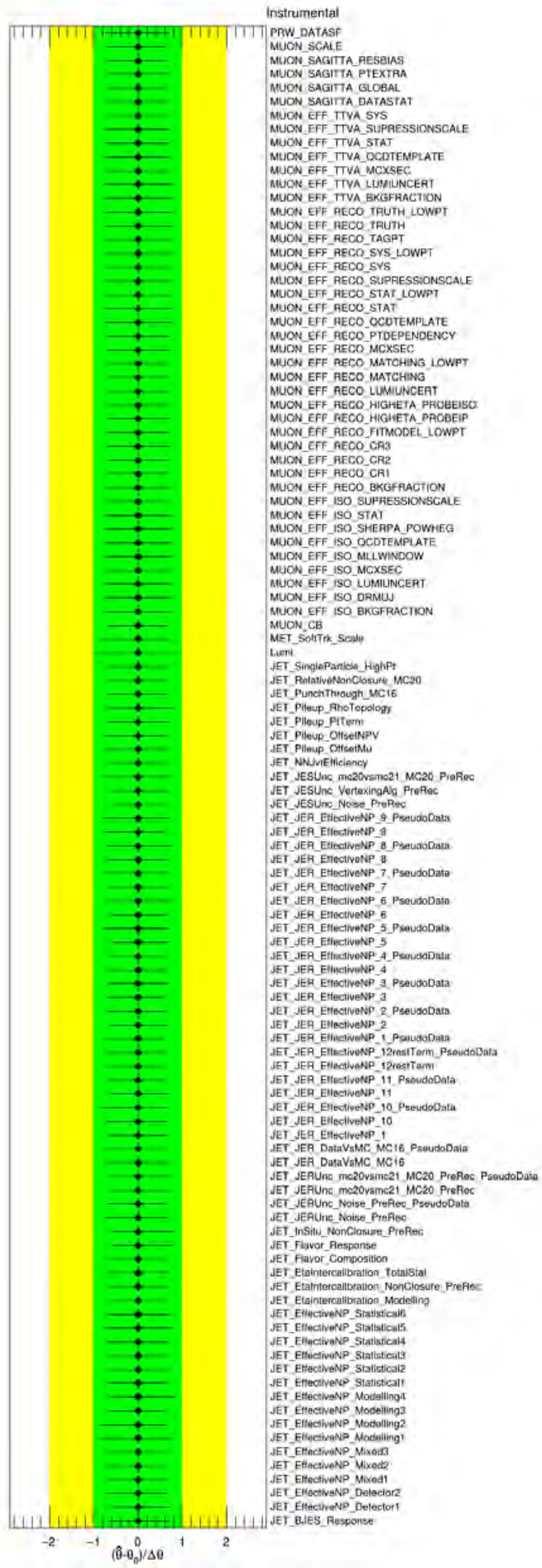

Figure B.39: Detector systematic uncertainty pull plot for Asimov fit on RH 1.2 TeV W' boson sample where $g'/g = 2$.

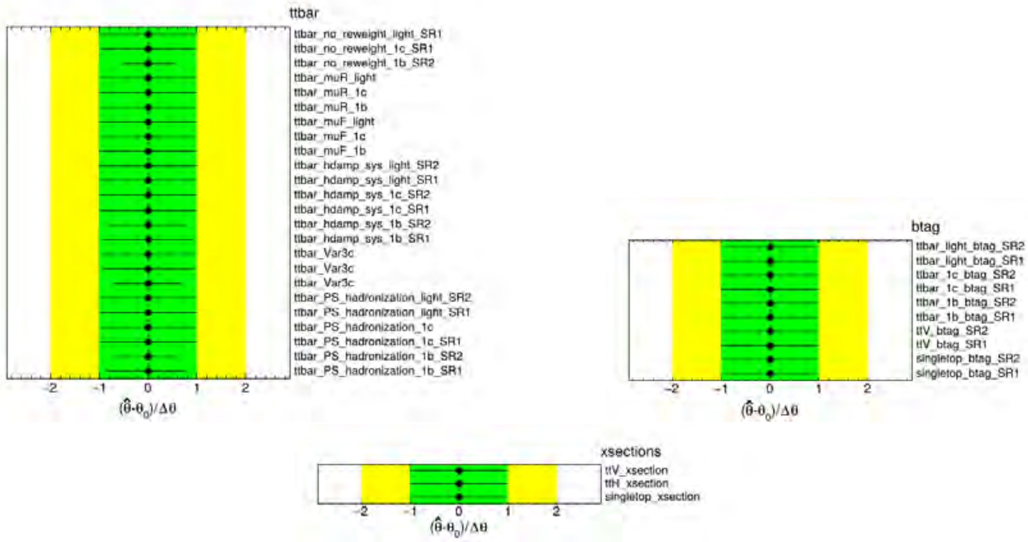

Figure B.40: $t\bar{t}$, b-tagging, and cross-section systematic uncertainty pull plot for Asimov fit on RH 1.2 TeV W' boson sample where $g'/g = 2$.

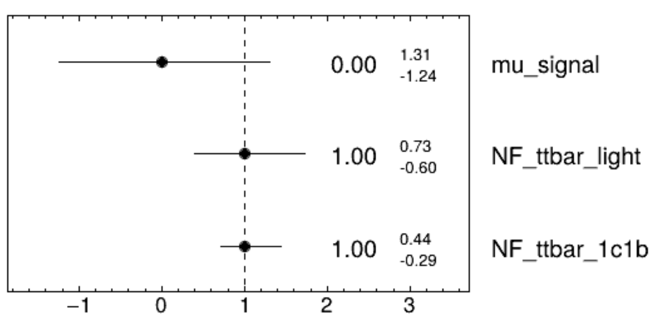

Figure B.41: Normalization factors determined by the binned maximum likelihood fit for the RH 1.4 TeV W' boson signal where $g'/g = 2$.

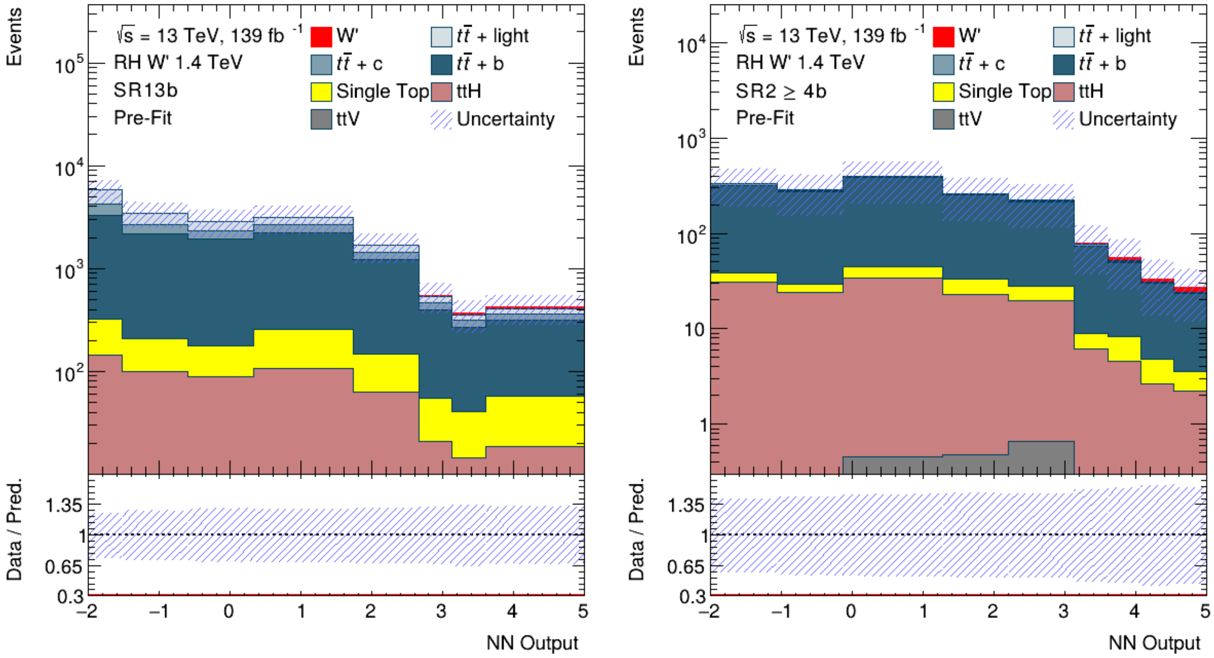

Figure B.42: Asimov pre-fit plots for RH 1.4 TeV W' boson signal sample where $g'/g = 2$.

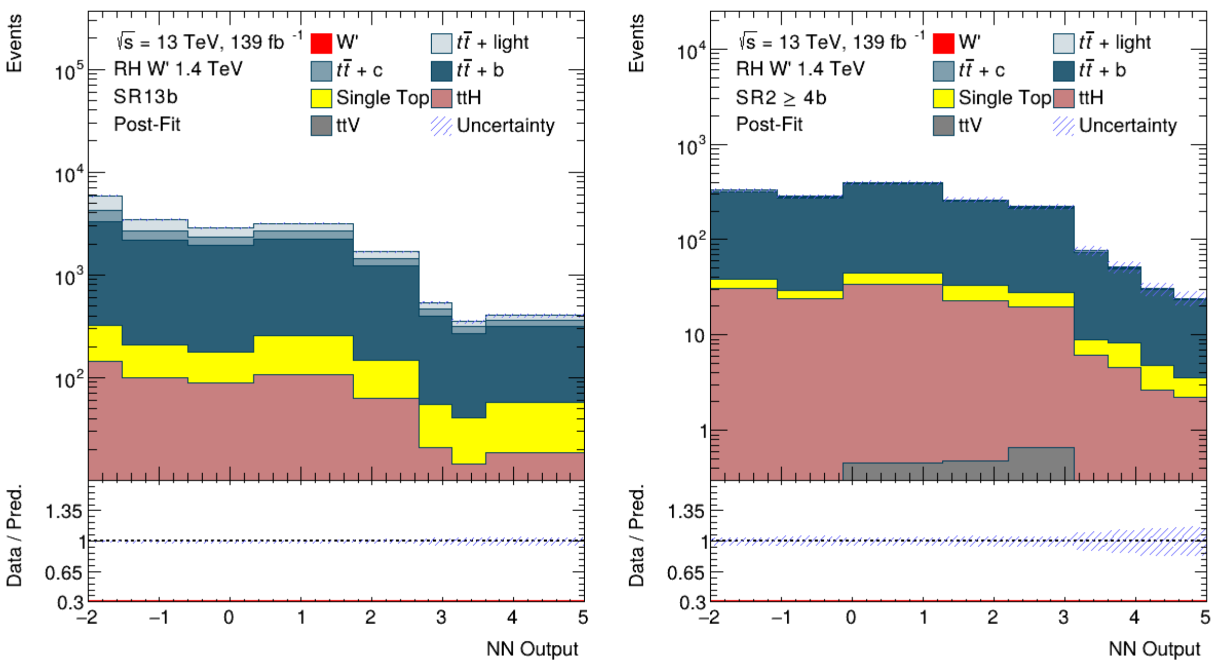

Figure B.43: Asimov post-fit plots for RH 1.4 TeV W' boson signal sample where $g'/g = 2$.

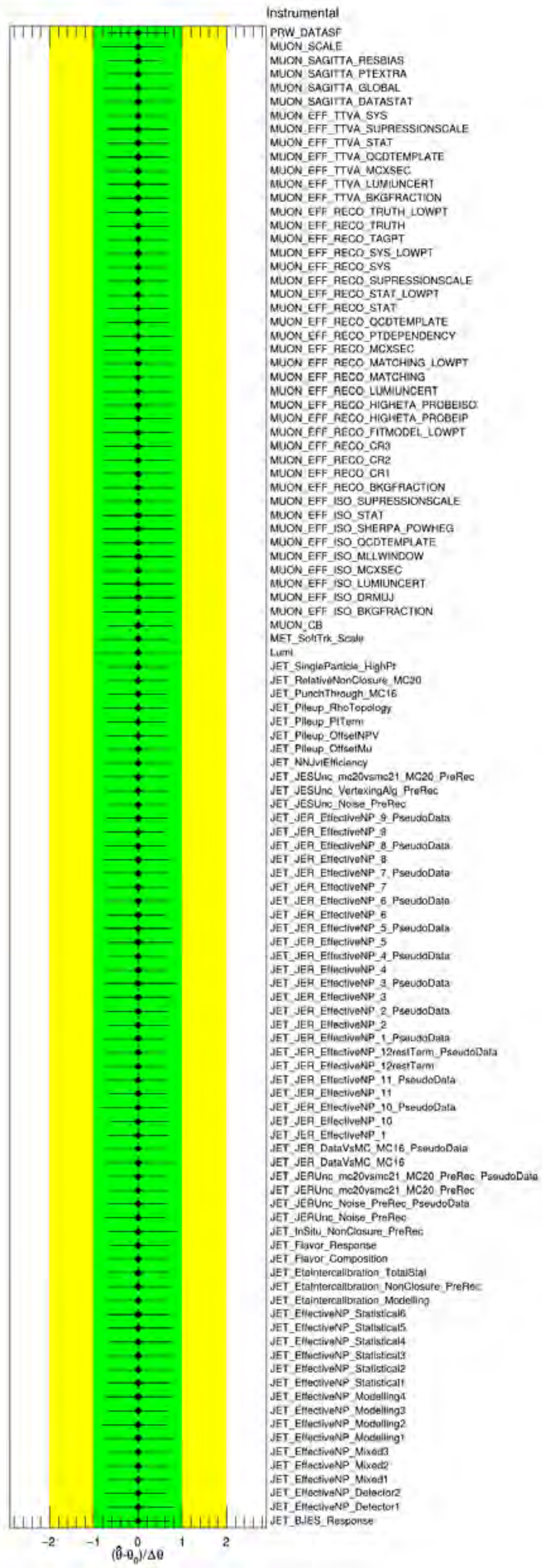

Figure B.44: Detector systematic uncertainty pull plot for Asimov fit on RH 1.4 TeV W' boson sample where $g'/g = 2$.

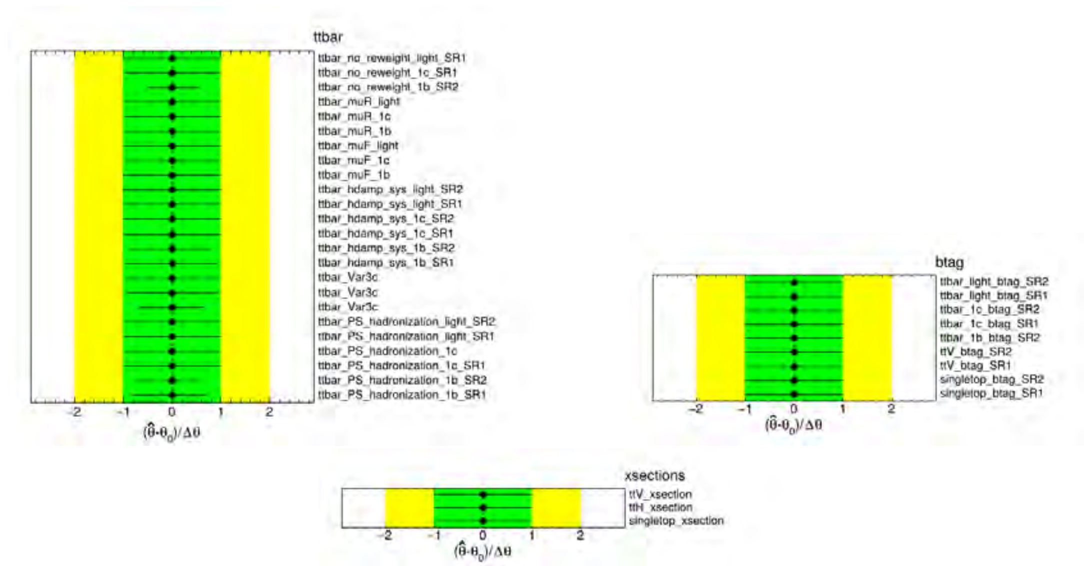

Figure B.45: $t\bar{t}$, b-tagging, and cross-section systematic uncertainty pull plot for Asimov fit on RH 1.4 TeV W' boson sample where $g'/g = 2$.

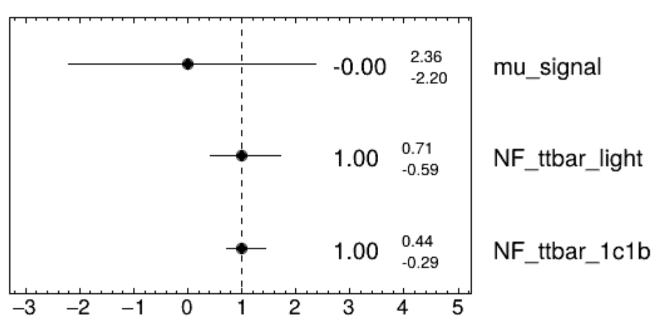

Figure B.46: Normalization factors determined by the binned maximum likelihood fit for the RH 1.6 TeV W' boson signal where $g'/g = 2$.

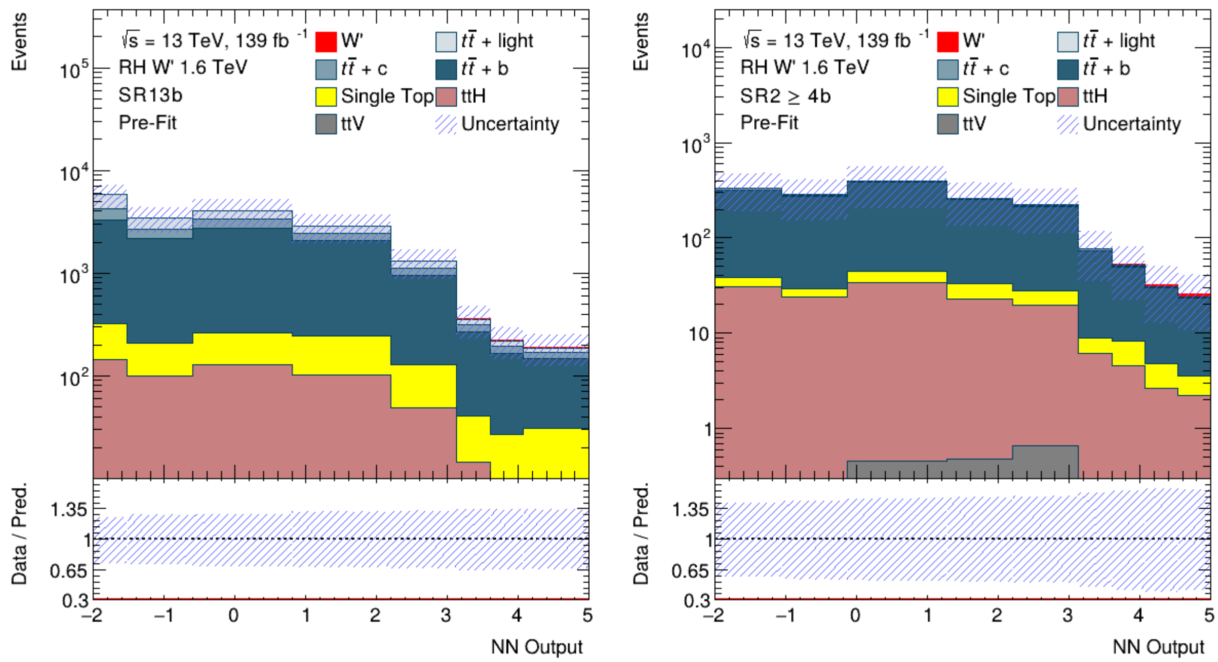

Figure B.47: Asimov pre-fit plots for RH 1.6 TeV W' boson signal sample where $g'/g = 2$.

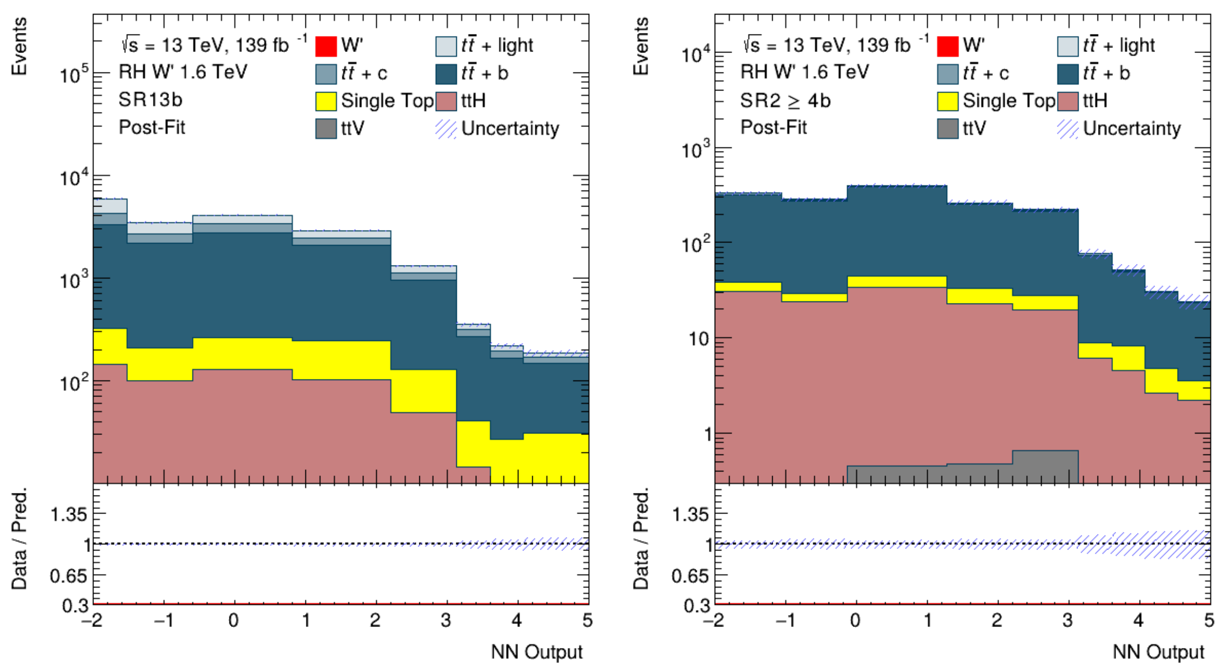

Figure B.48: Asimov post-fit plots for RH 1.6 TeV W' boson signal sample where $g'/g = 2$.

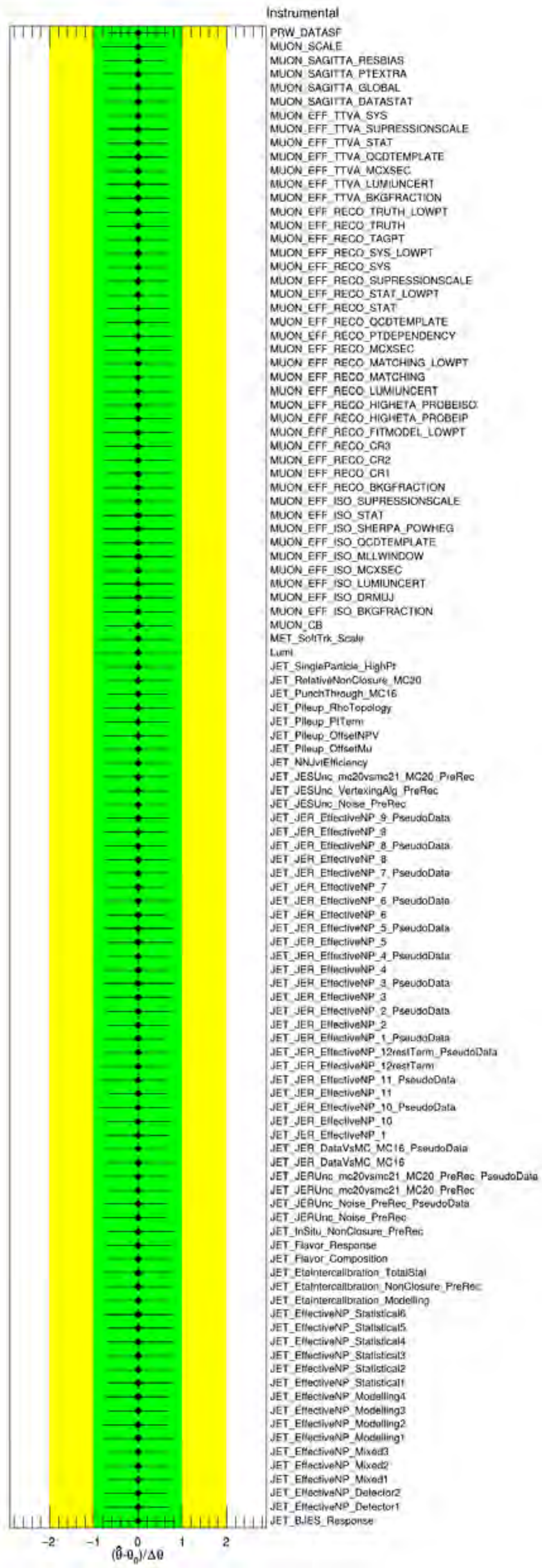

Figure B.49: Detector systematic uncertainty pull plot for Asimov fit on RH 1.6 TeV W' boson sample where $g'/g = 2$.

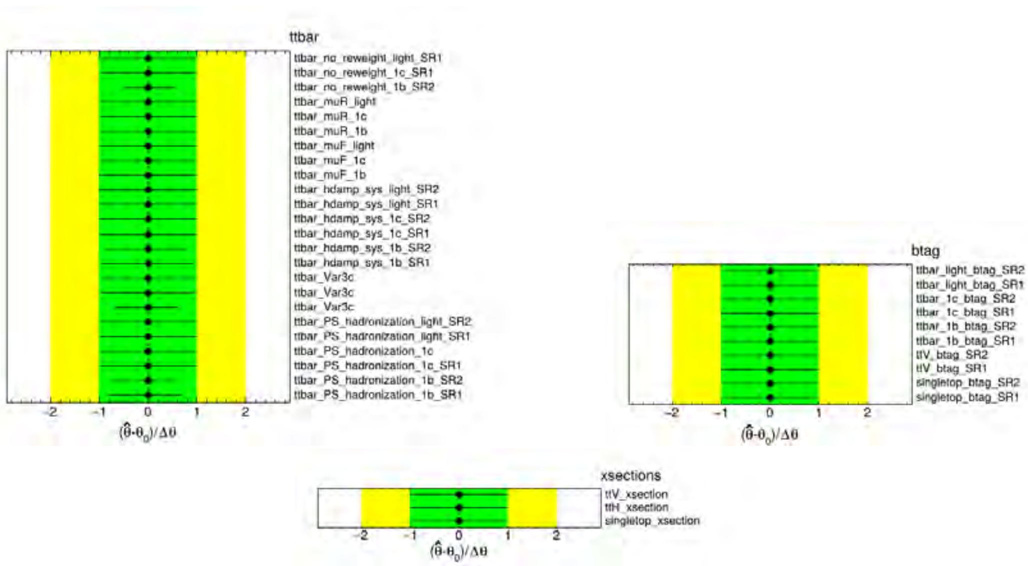

Figure B.50: $t\bar{t}$, b-tagging, and cross-section systematic uncertainty pull plot for Asimov fit on RH 1.6 TeV W' boson sample where $g'/g = 2$.

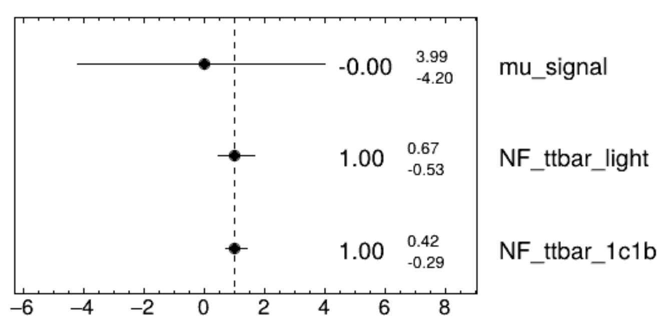

Figure B.51: Normalization factors determined by the binned maximum likelihood fit for the RH 1.8 TeV W' boson signal where $g'/g = 2$.

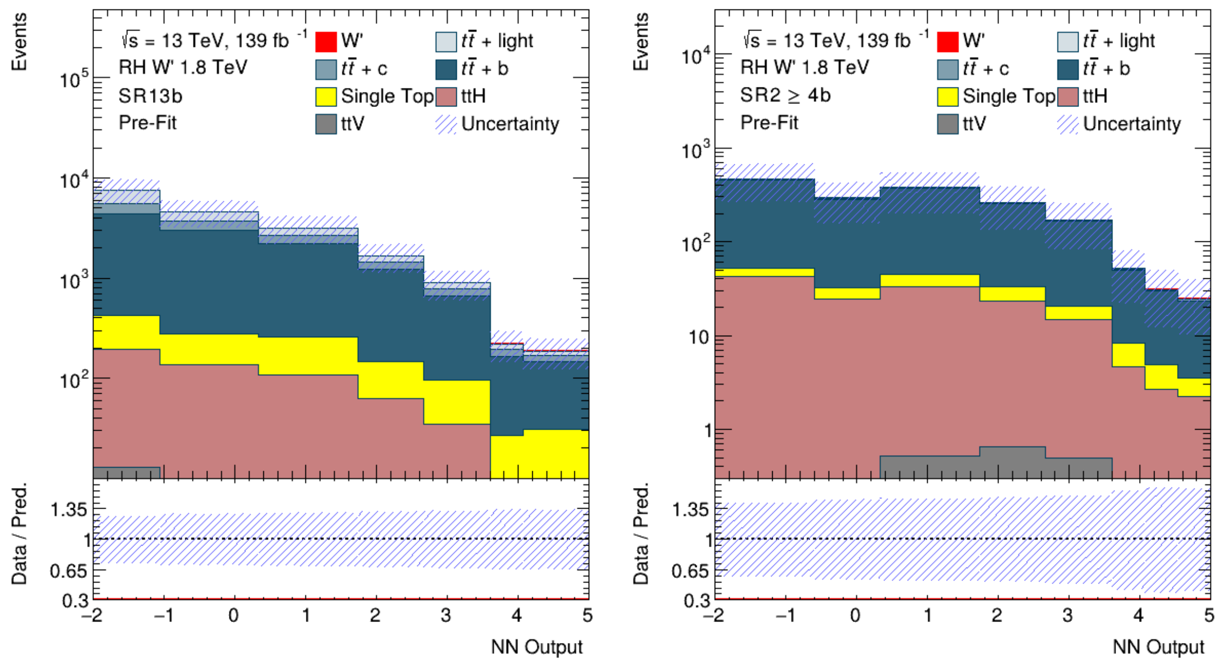

Figure B.52: Asimov pre-fit plots for RH 1.8 TeV W' boson signal sample where $g'/g = 2$.

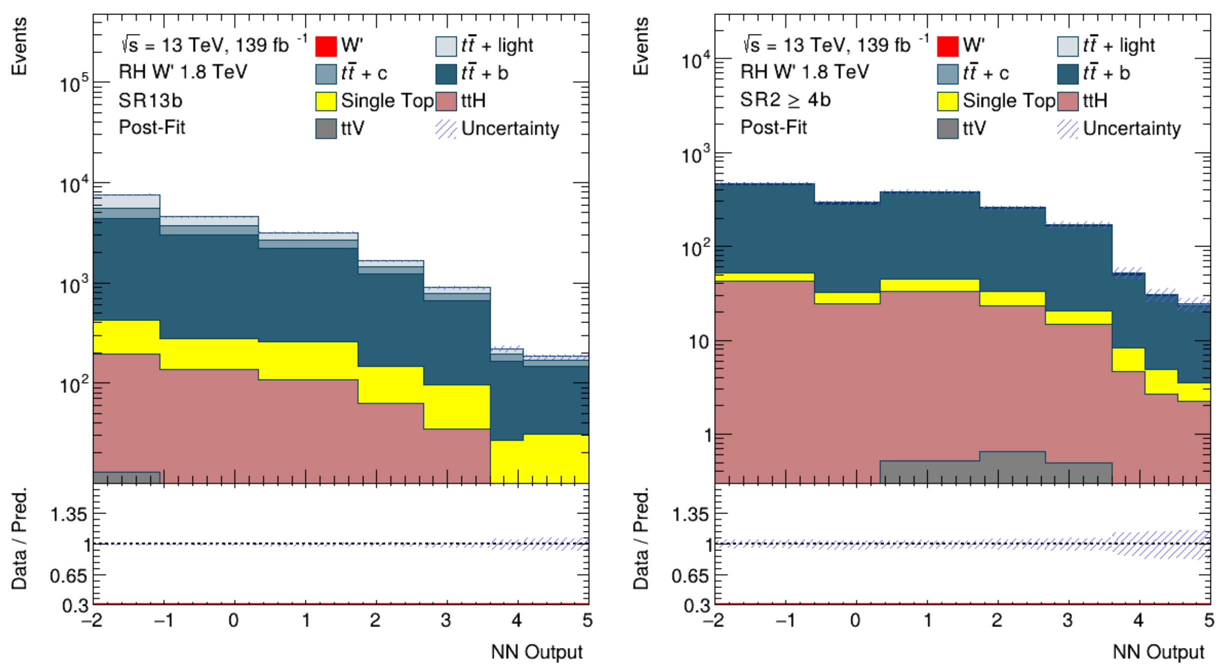

Figure B.53: Asimov post-fit plots for RH 1.8 TeV W' boson signal sample where $g'/g = 2$.

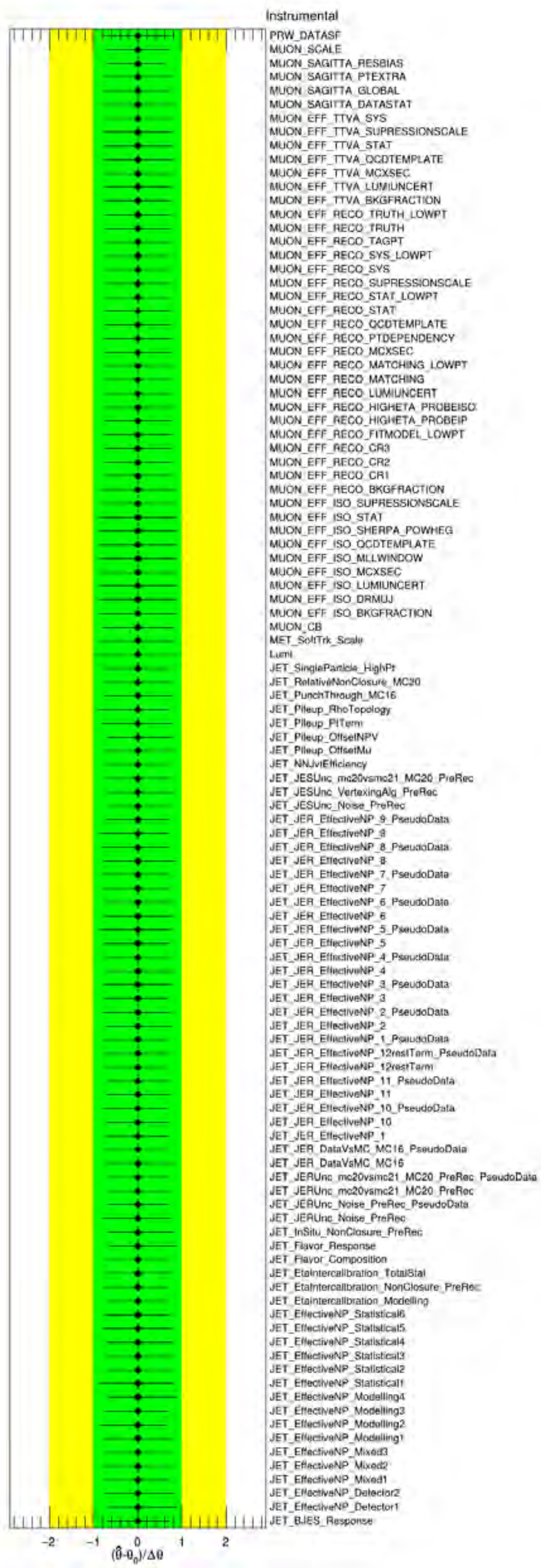

Figure B.54: Detector systematic uncertainty pull plot for Asimov fit on RH 1.8 TeV W' boson sample where $g'/g = 2$.

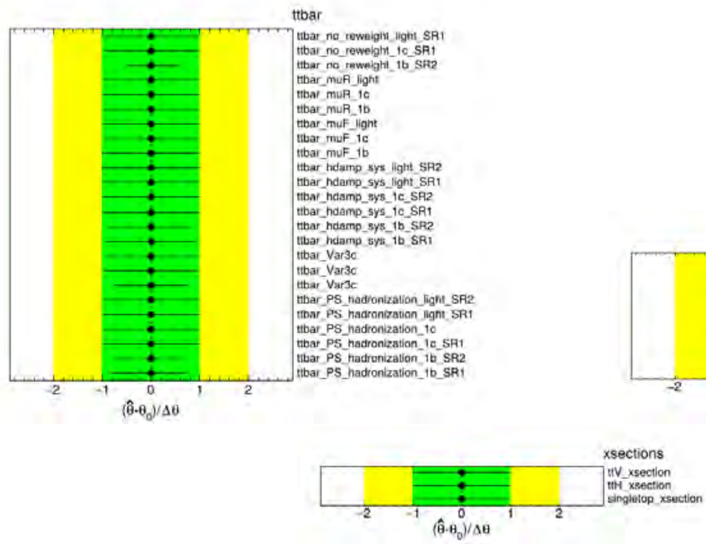

Figure B.55: $t\bar{t}$, b-tagging, and cross-section systematic uncertainty pull plot for Asimov fit on RH 1.8 TeV W' boson sample where $g'/g = 2$.

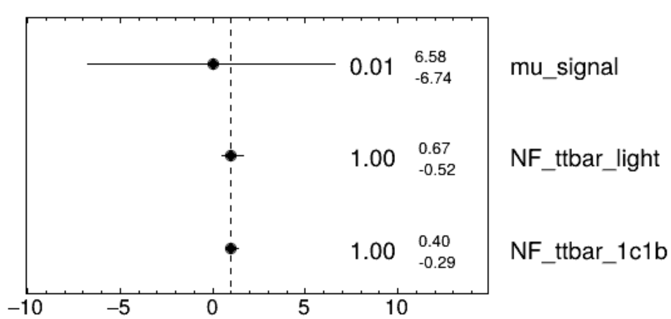

Figure B.56: Normalization factors determined by the binned maximum likelihood fit for the RH 2 TeV W' boson signal where $g'/g = 2$.

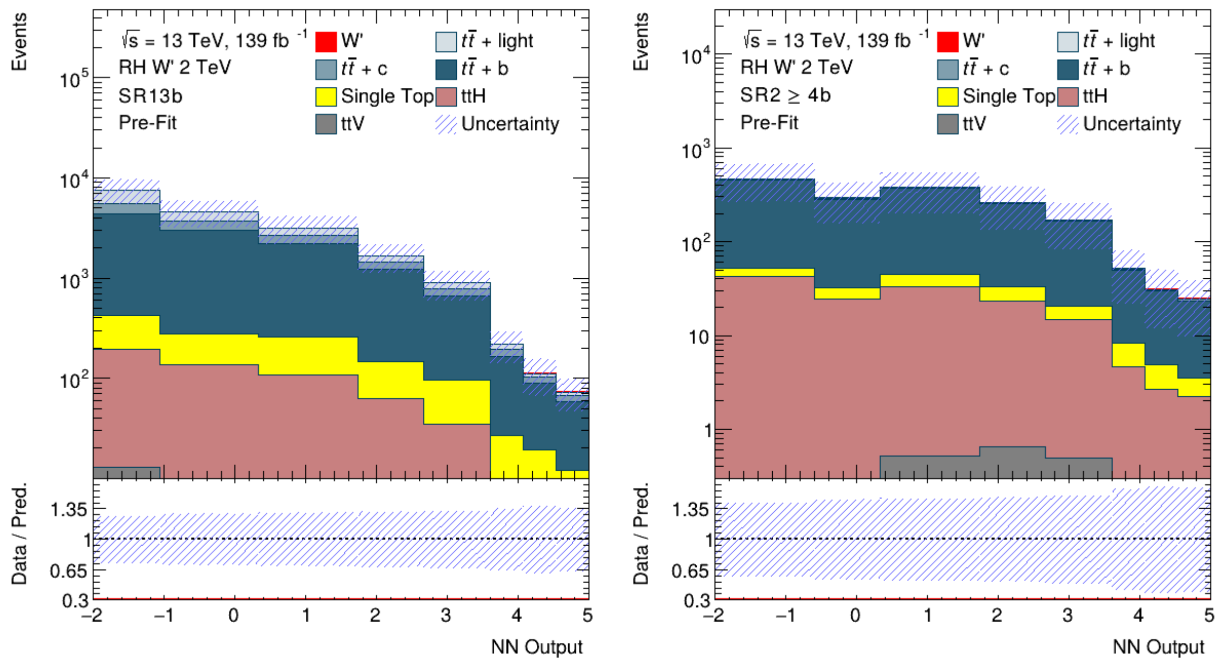

Figure B.57: Asimov pre-fit plots for RH 2 TeV W' boson signal sample where $g'/g = 2$.

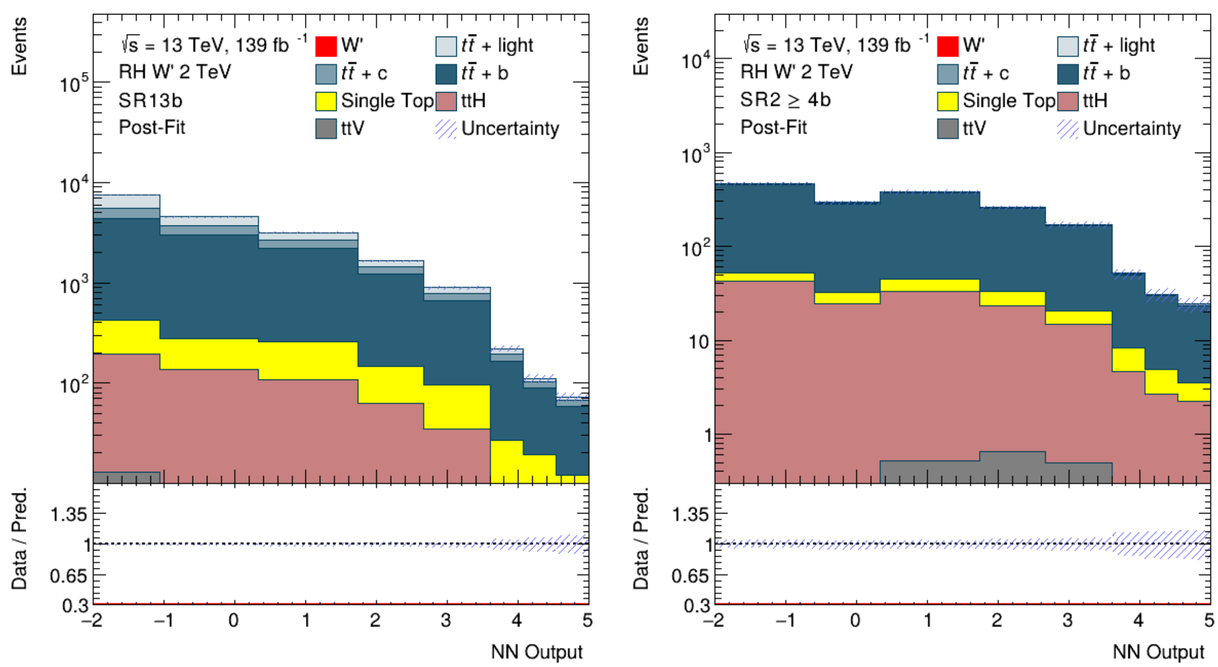

Figure B.58: Asimov post-fit plots for RH 2 TeV W' boson signal sample where $g'/g = 2$.

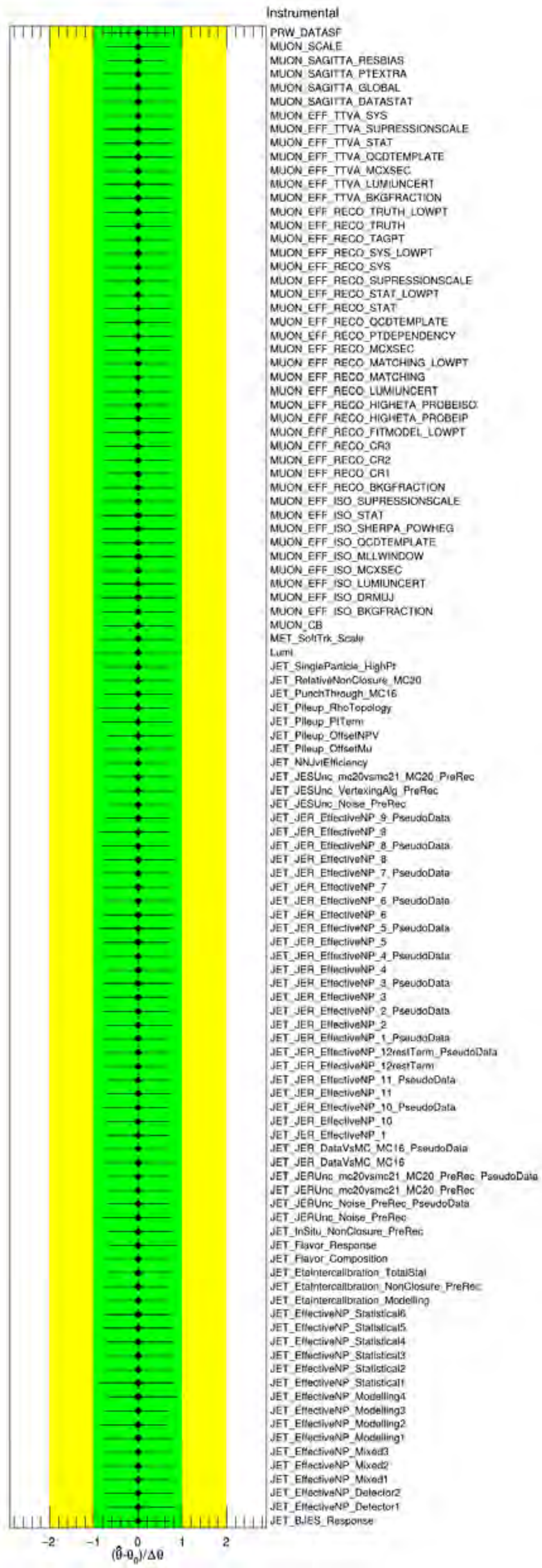

Figure B.59: Detector systematic uncertainty pull plot for Asimov fit on RH 2 TeV W' boson sample where $g'/g = 2$.

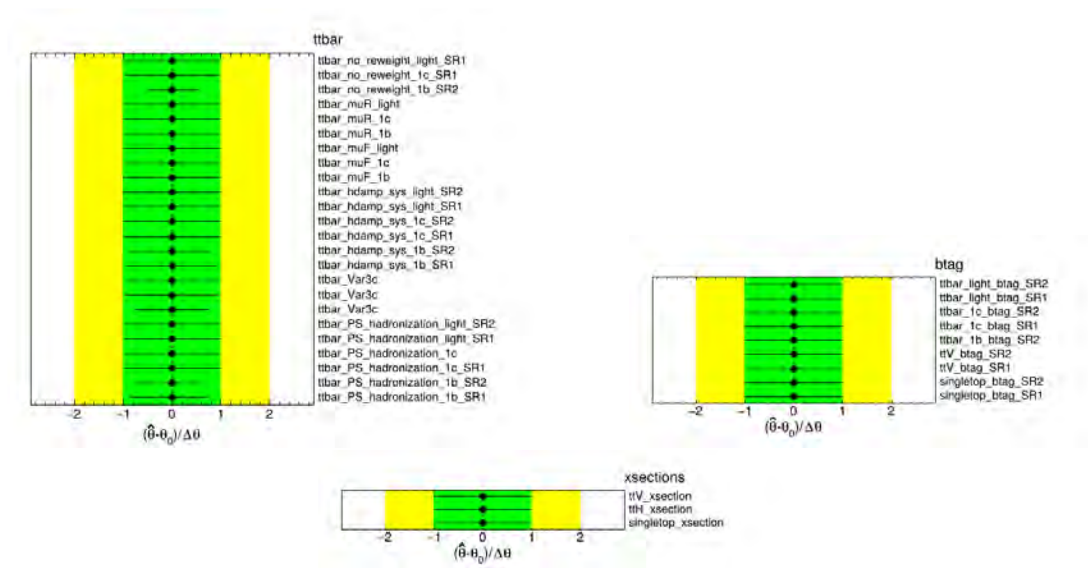

Figure B.60: $t\bar{t}$, b-tagging, and cross-section systematic uncertainty pull plot for Asimov fit on RH 2 TeV W' boson sample where $g'/g = 2$.

Appendix C

All Data Fit Results

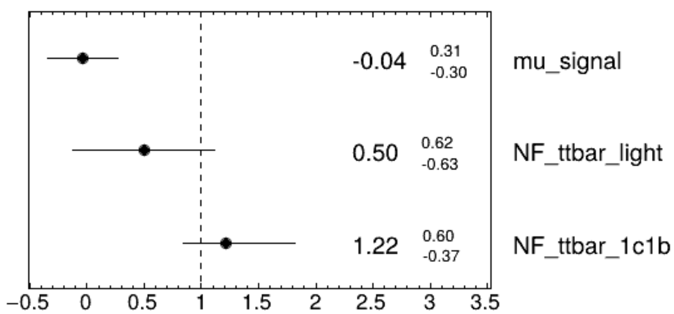

Figure C.1: Normalization factors determined by the binned maximum likelihood fit for the LH 1 TeV W' boson signal where g'/g=2.

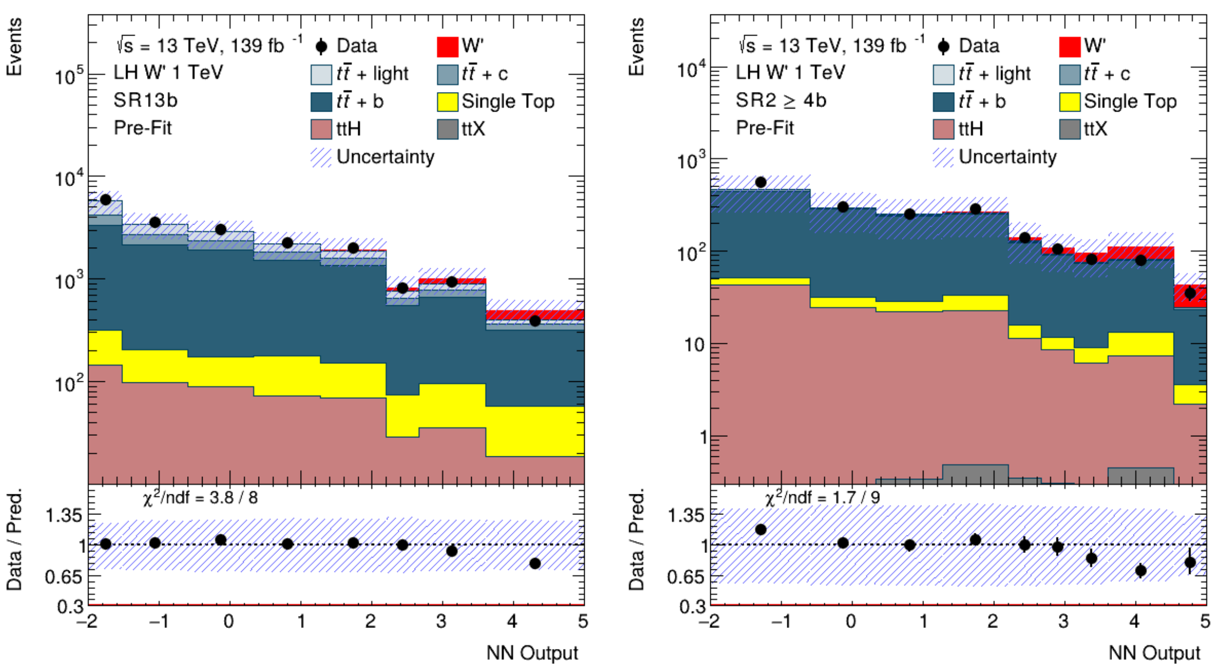

Figure C.2: Asimov pre-fit plots for LH 1 TeV W' boson signal sample where g'/g=2.

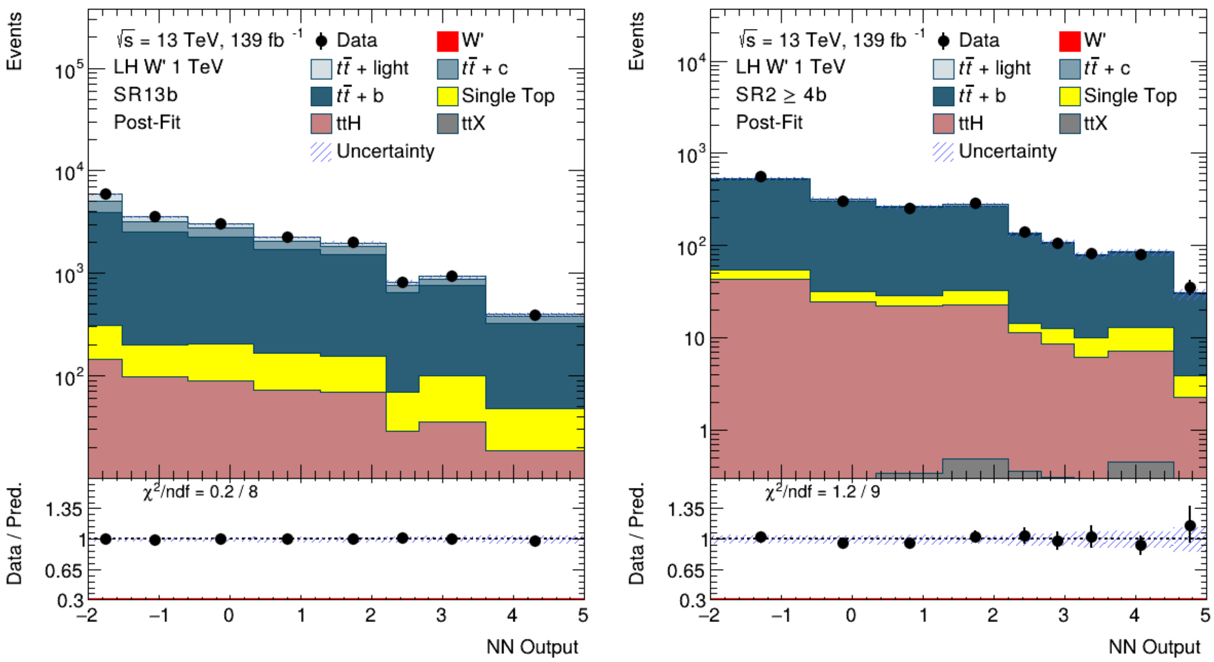

Figure C.3: Asimov post-fit plots for LH 1 TeV W' boson signal sample where g'/g=2.

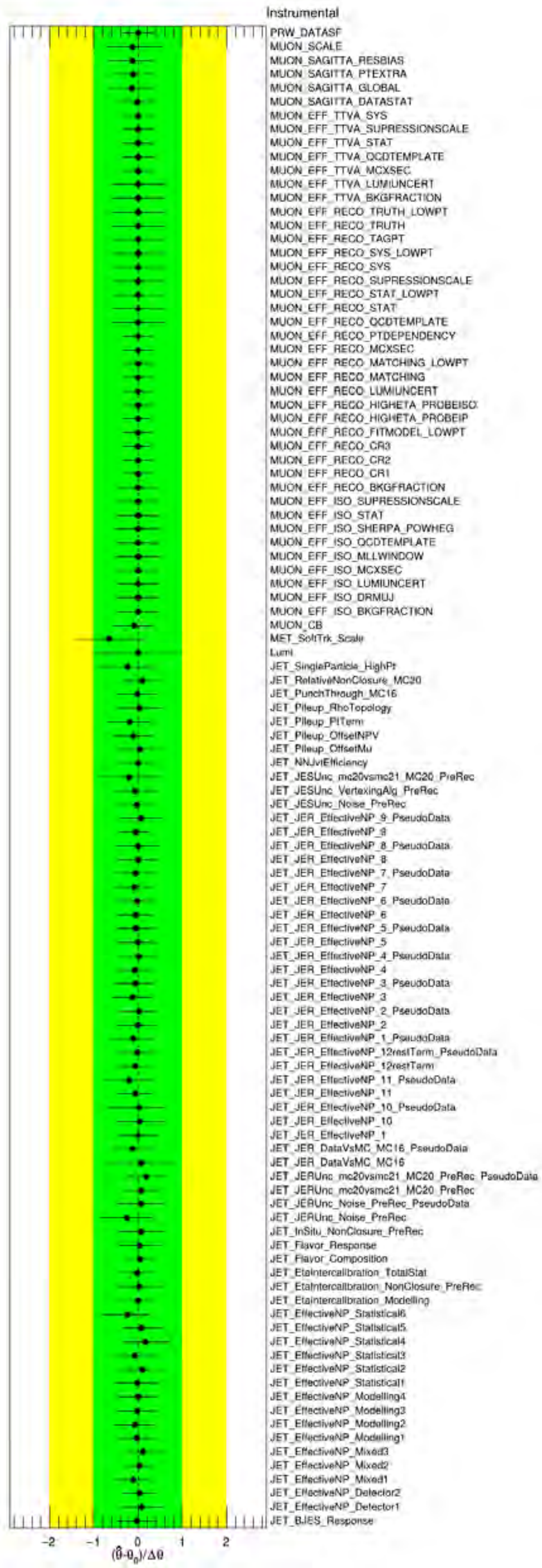

Figure C.4: Detector systematic uncertainty pull plot for Asimov fit on LH 1 TeV W' boson sample where g'/g=2.

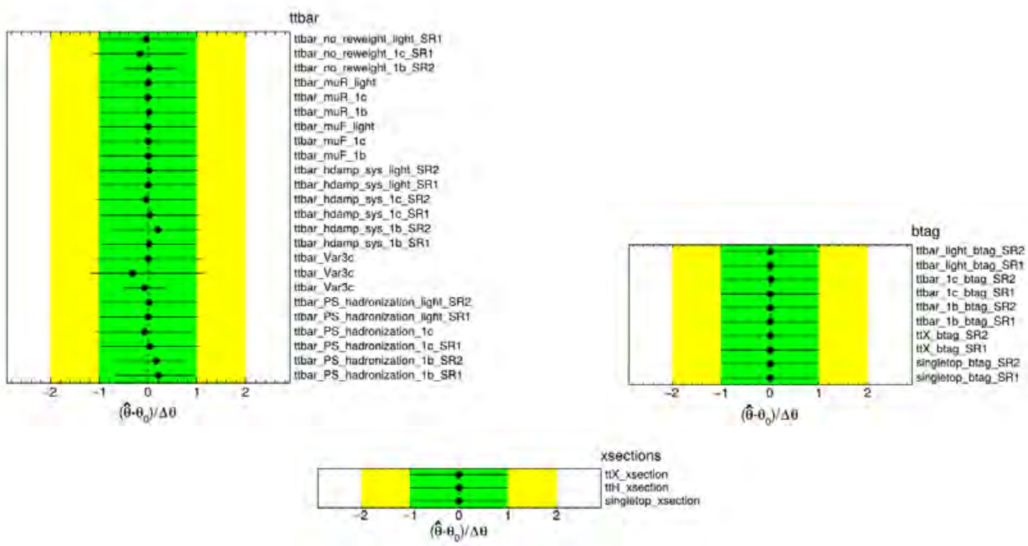

Figure C.5: $t\bar{t}$, b-tagging, and cross-section systematic uncertainty pull plot for Asimov fit on LH 1 TeV W' boson sample where g'/g=2.

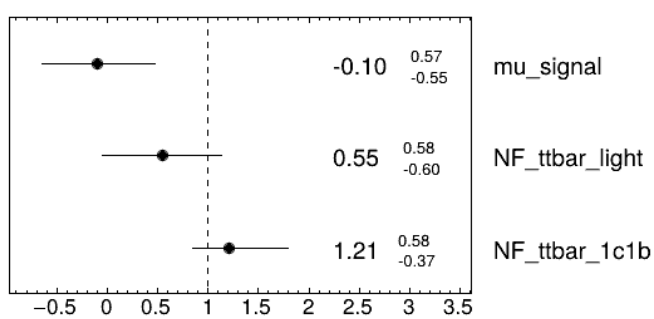

Figure C.6: Normalization factors determined by the binned maximum likelihood fit for the LH 1.2 TeV W' boson signal where $g'/g = 2$.

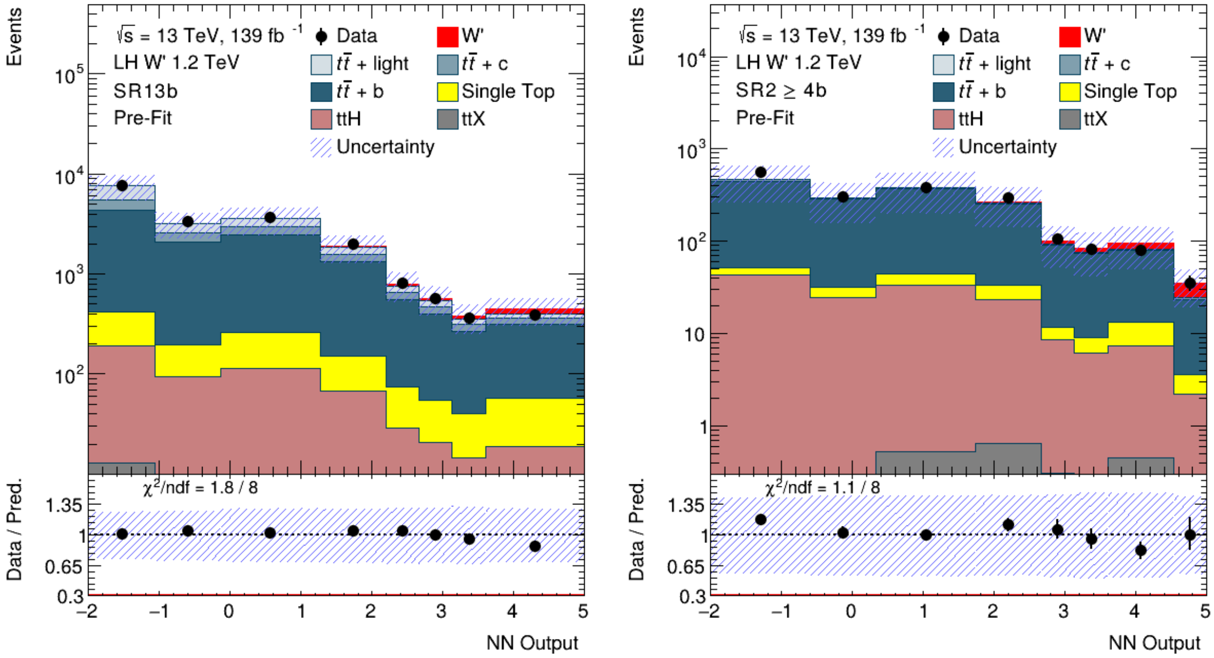

Figure C.7: Asimov pre-fit plots for LH 1.2 TeV W' boson signal sample where $g'/g = 2$.

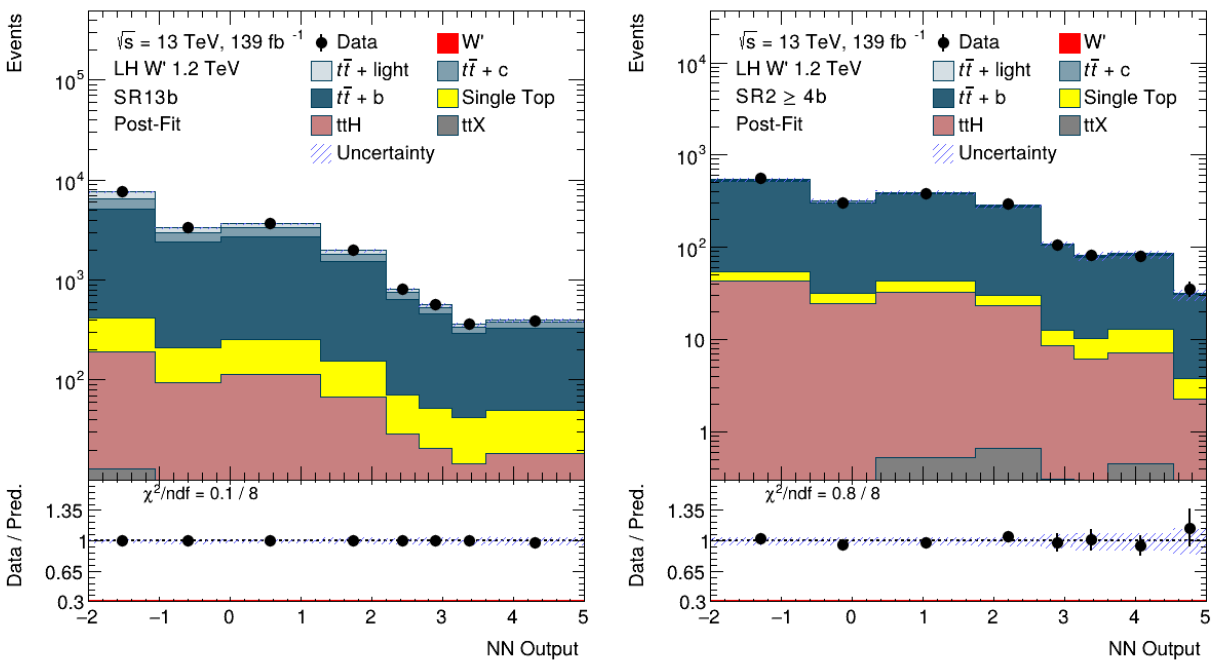

Figure C.8: Asimov post-fit plots for LH 1.2 TeV W' boson signal sample where $g'/g = 2$.

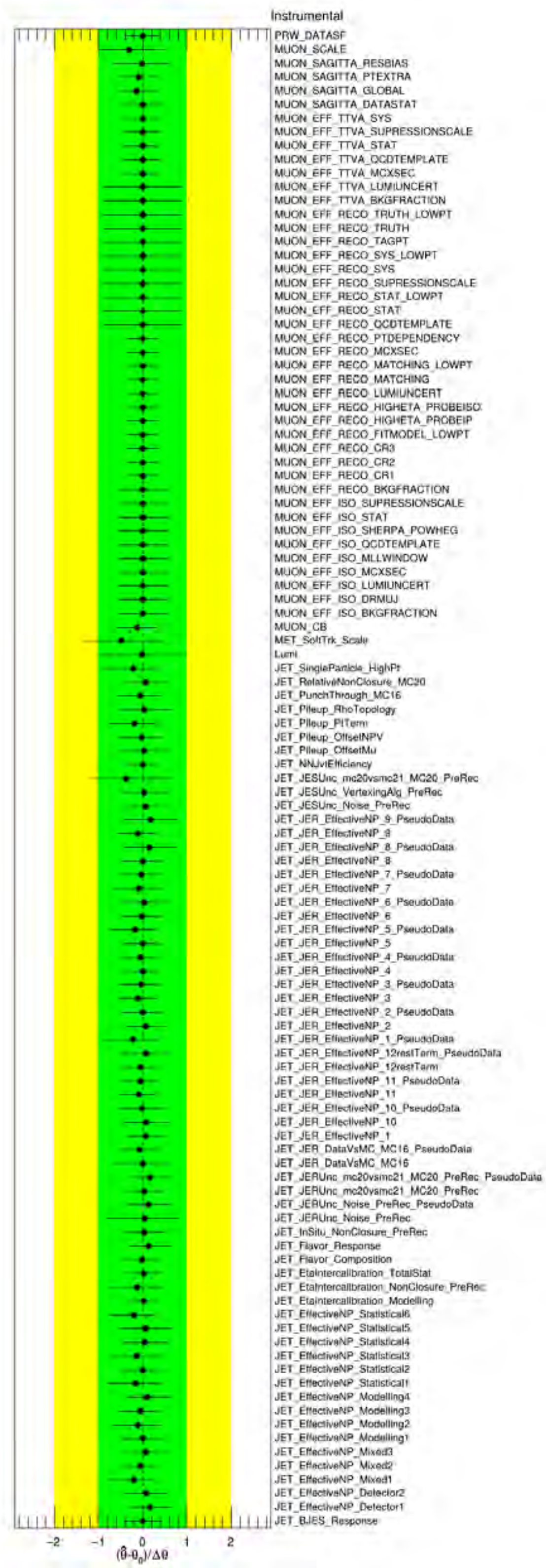

Figure C.9: Detector systematic uncertainty pull plot for Asimov fit on LH 1.2 TeV W' boson sample where $g'/g = 2$.

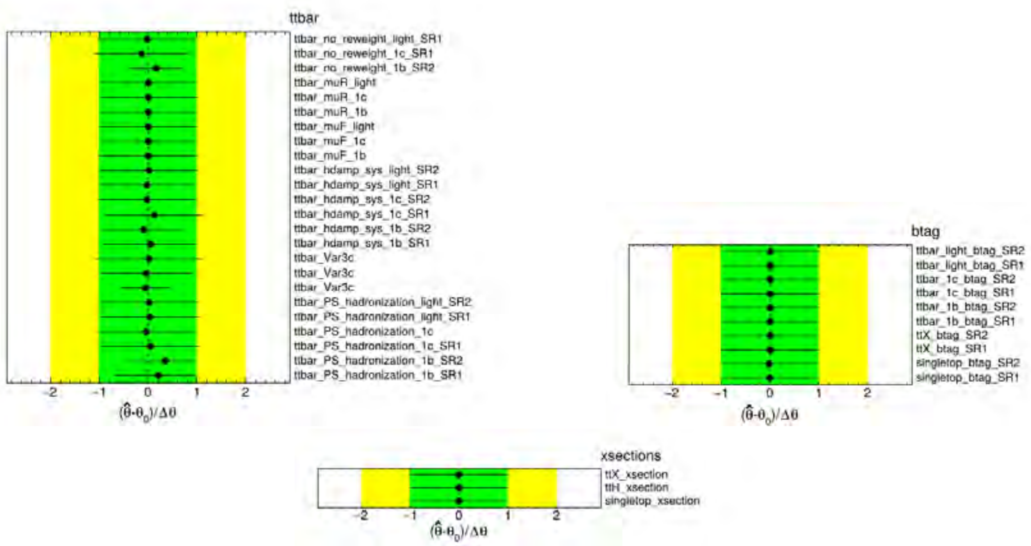

Figure C.10: $t\bar{t}$, b-tagging, and cross-section systematic uncertainty pull plot for Asimov fit on LH 1.2 TeV W' boson sample where $g'/g = 2$.

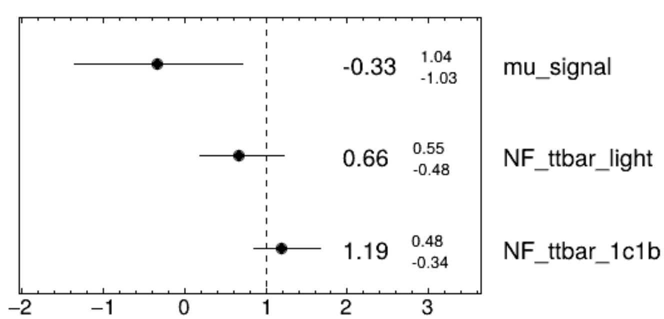

Figure C.11: Normalization factors determined by the binned maximum likelihood fit for the LH 1.4 TeV W' boson signal where $g'/g = 2$.

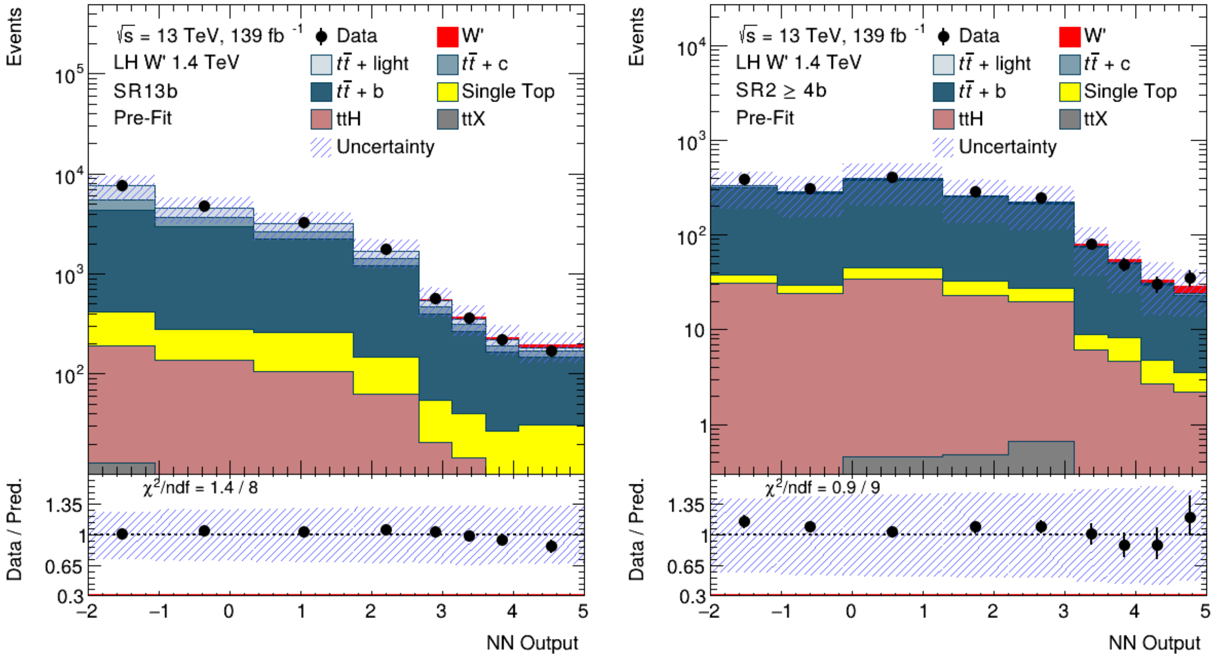

Figure C.12: Asimov pre-fit plots for LH 1.4 TeV W' boson signal sample where $g'/g = 2$.

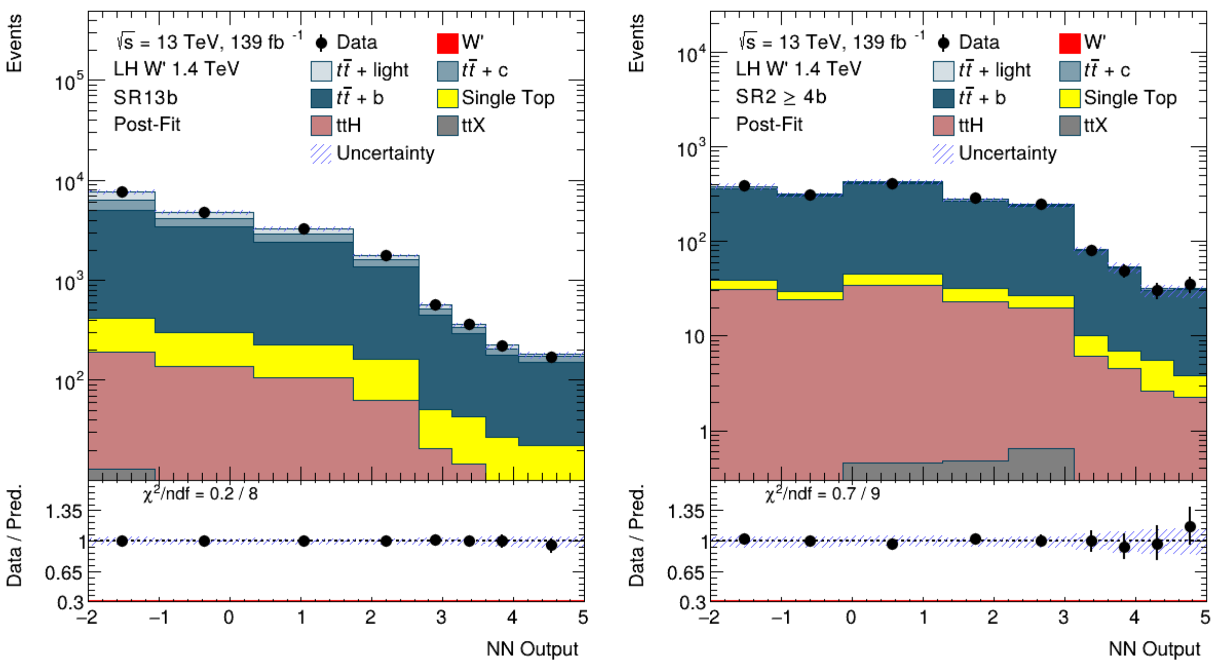

Figure C.13: Asimov post-fit plots for LH 1.4 TeV W' boson signal sample where $g'/g = 2$.

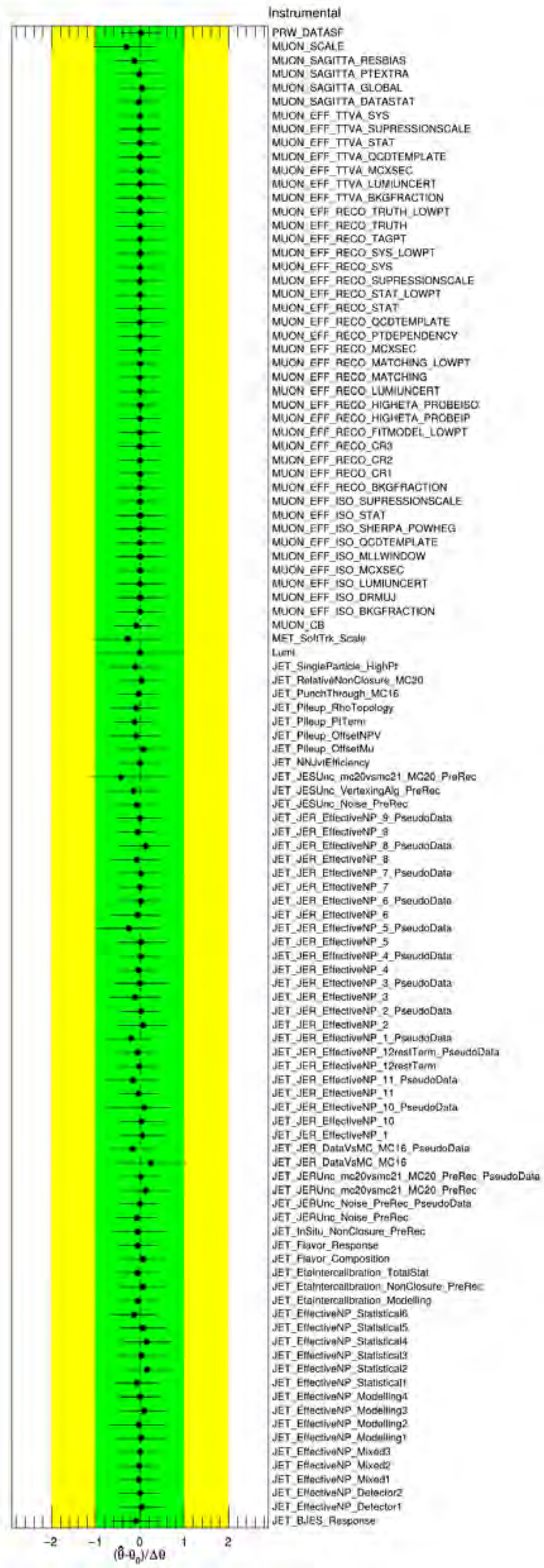

Figure C.14: Detector systematic uncertainty pull plot for Asimov fit on LH 1.4 TeV W' boson sample where $g'/g = 2$.

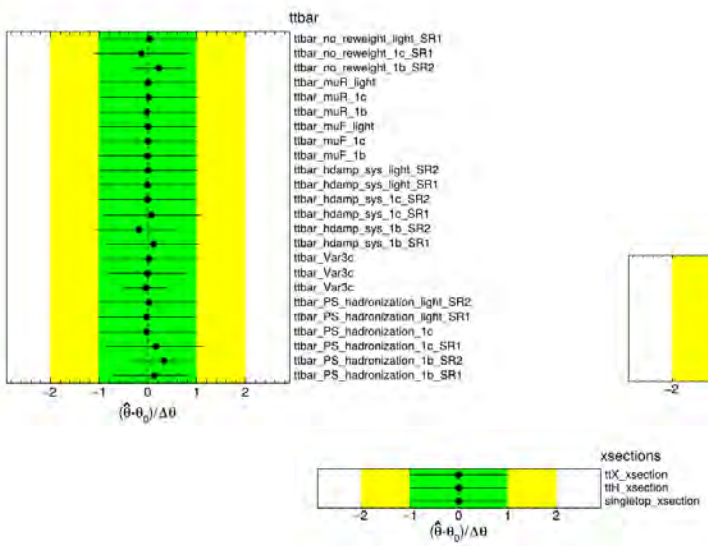

Figure C.15: $t\bar{t}$, b-tagging, and cross-section systematic uncertainty pull plot for Asimov fit on LH 1.4 TeV W' boson sample where $g'/g = 2$.

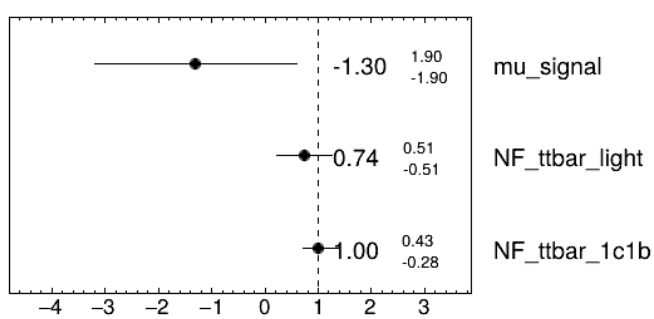

Figure C.16: Normalization factors determined by the binned maximum likelihood fit for the LH 1.6 TeV W' boson signal where $g'/g = 2$.

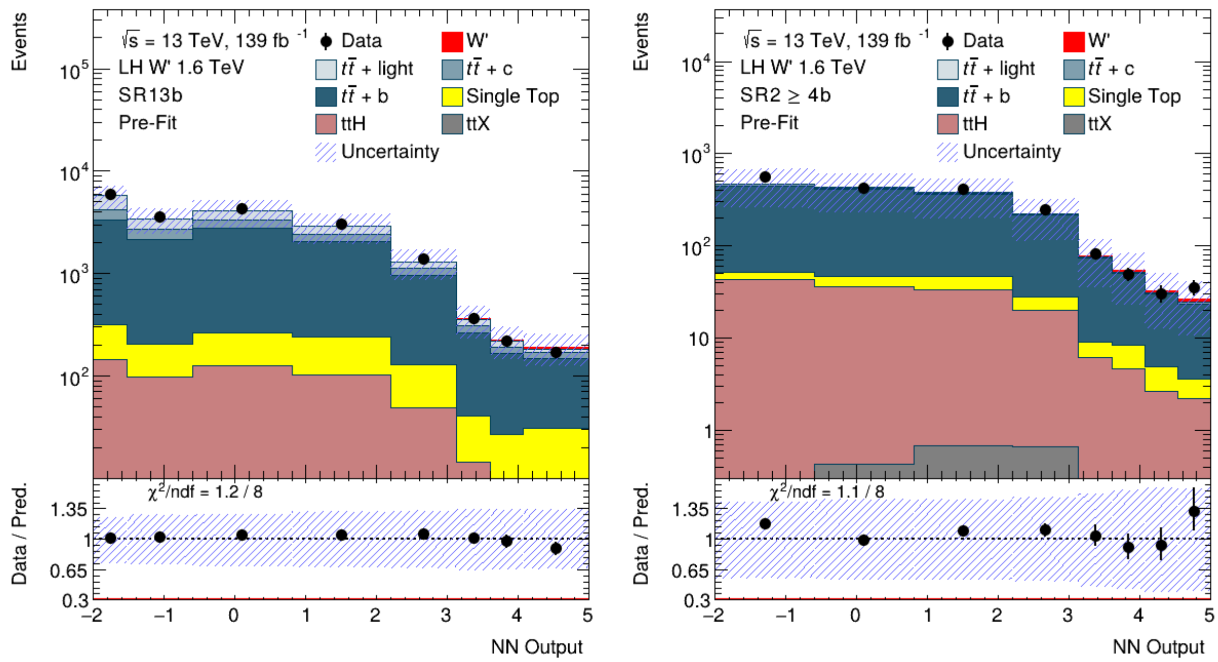

Figure C.17: Asimov pre-fit plots for LH 1.6 TeV W' boson signal sample where $g'/g = 2$.

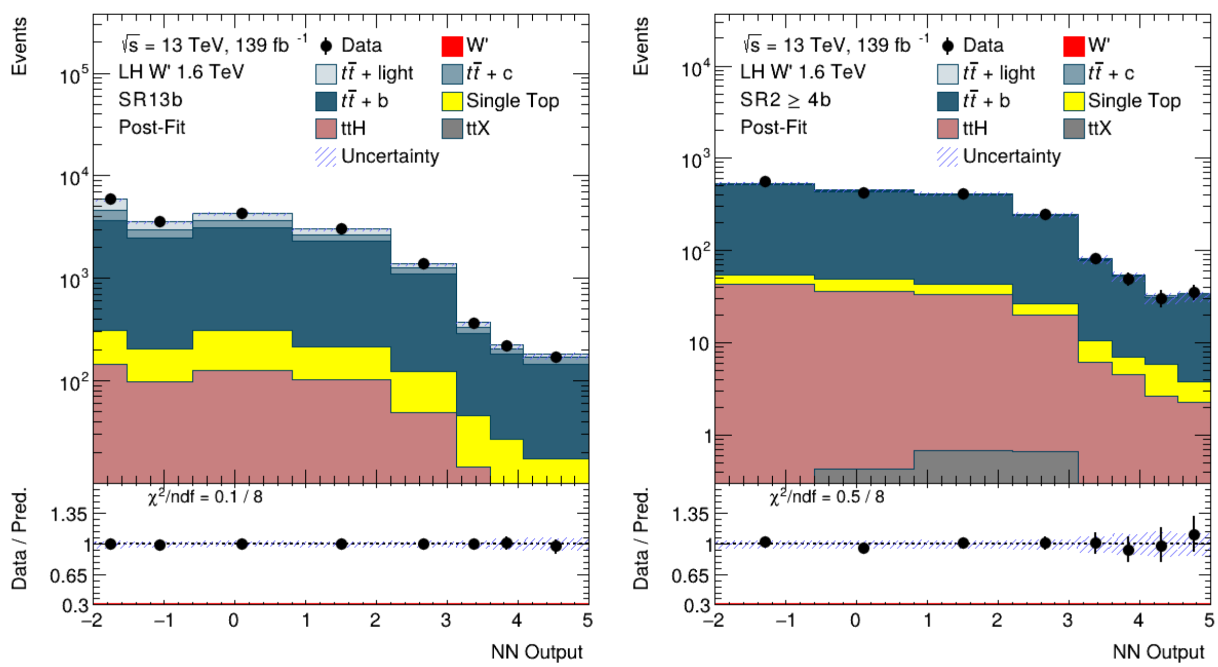

Figure C.18: Asimov post-fit plots for LH 1.6 TeV W' boson signal sample where $g'/g = 2$.

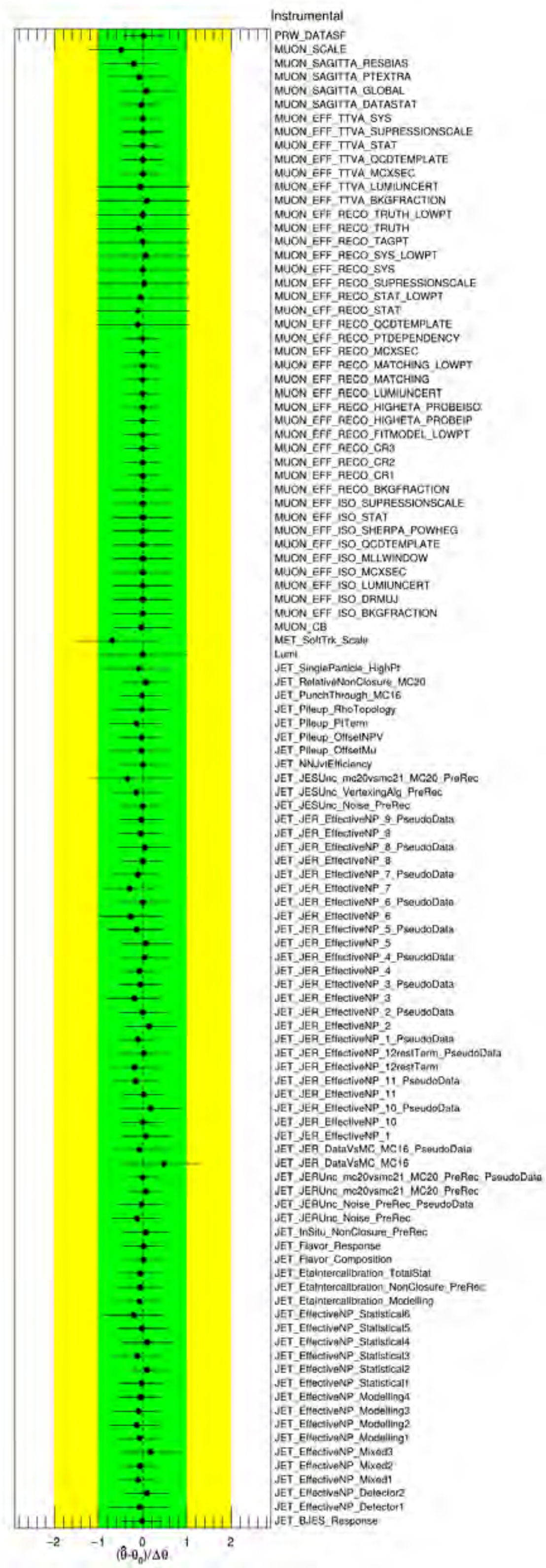

Figure C.19: Detector systematic uncertainty pull plot for Asimov fit on LH 1.6 TeV W' boson sample where $g'/g = 2$.

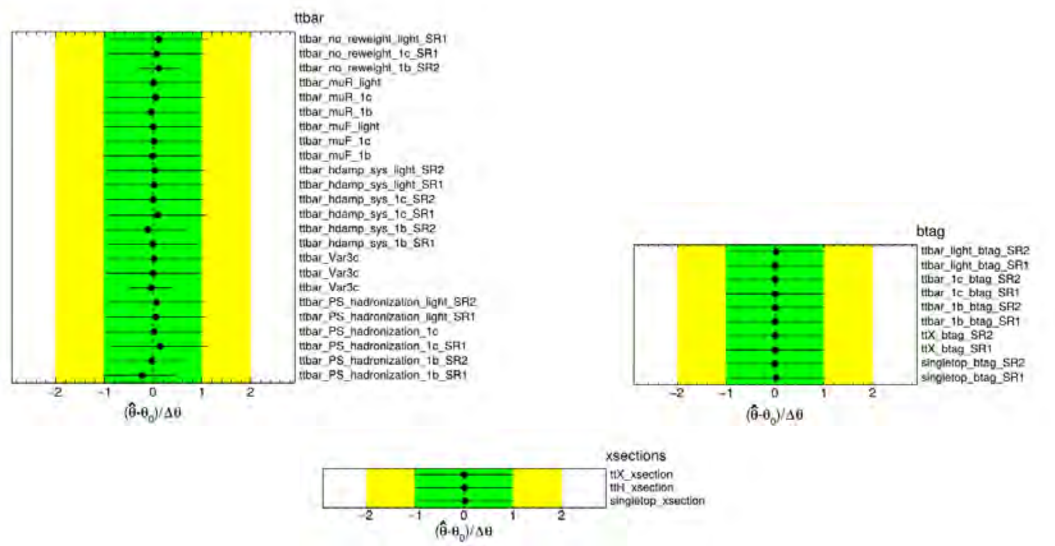

Figure C.20: $t\bar{t}$, b-tagging, and cross-section systematic uncertainty pull plot for Asimov fit on LH 1.6 TeV W' boson sample where $g'/g = 2$.

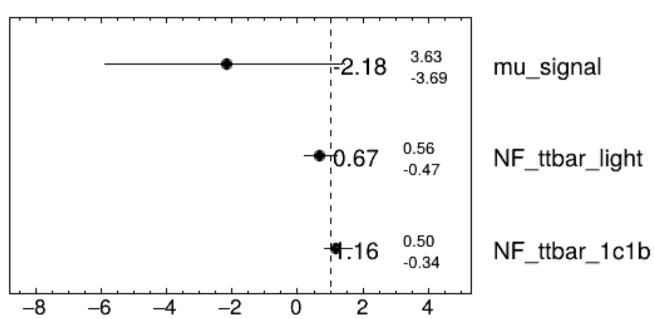

Figure C.21: Normalization factors determined by the binned maximum likelihood fit for the LH 1.8 TeV W' boson signal where $g'/g = 2$.

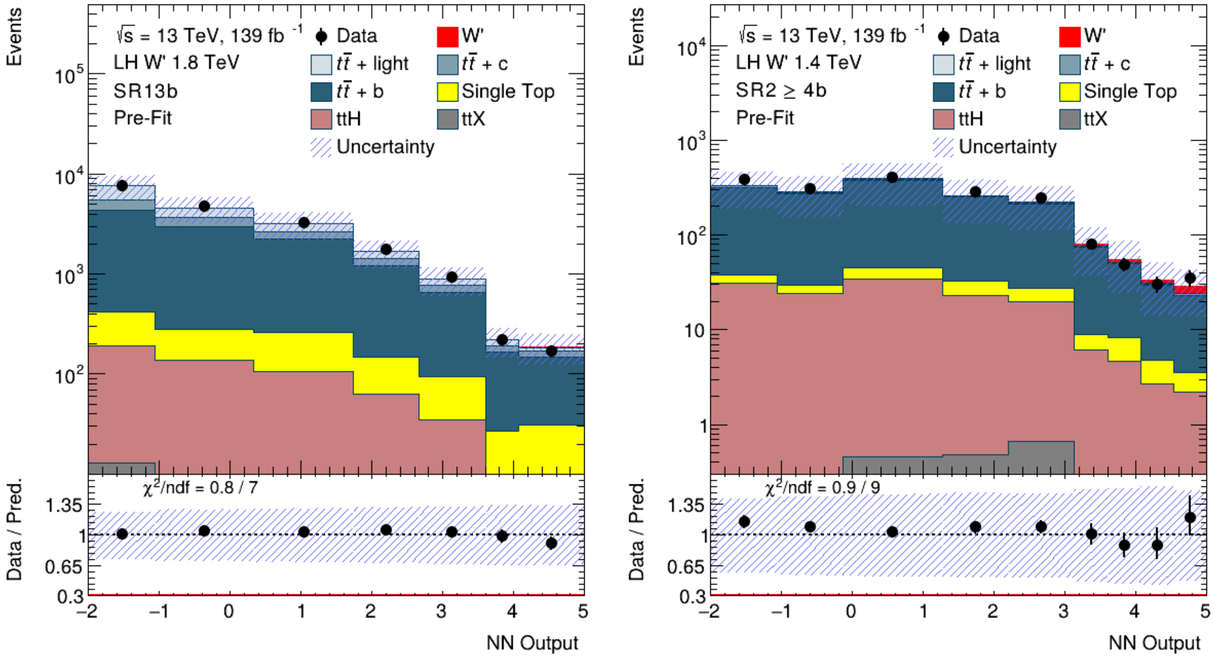

Figure C.22: Asimov pre-fit plots for LH 1.8 TeV W' boson signal sample where $g'/g = 2$.

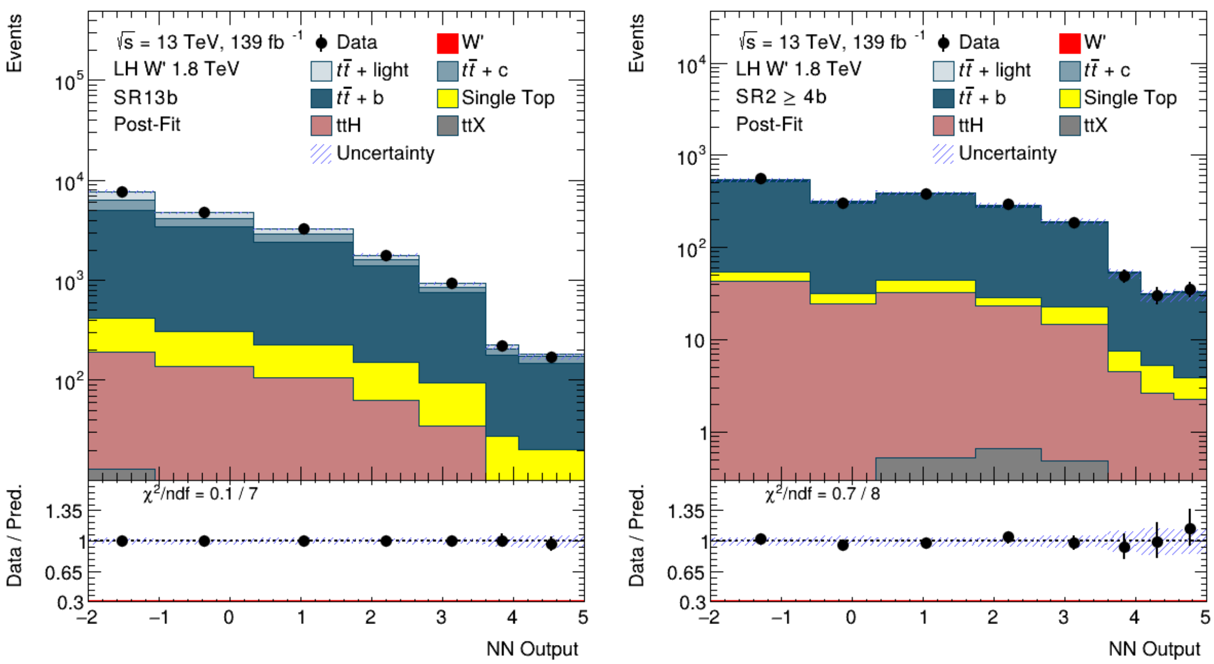

Figure C.23: Asimov post-fit plots for LH 1.8 TeV W' boson signal sample where $g'/g = 2$.

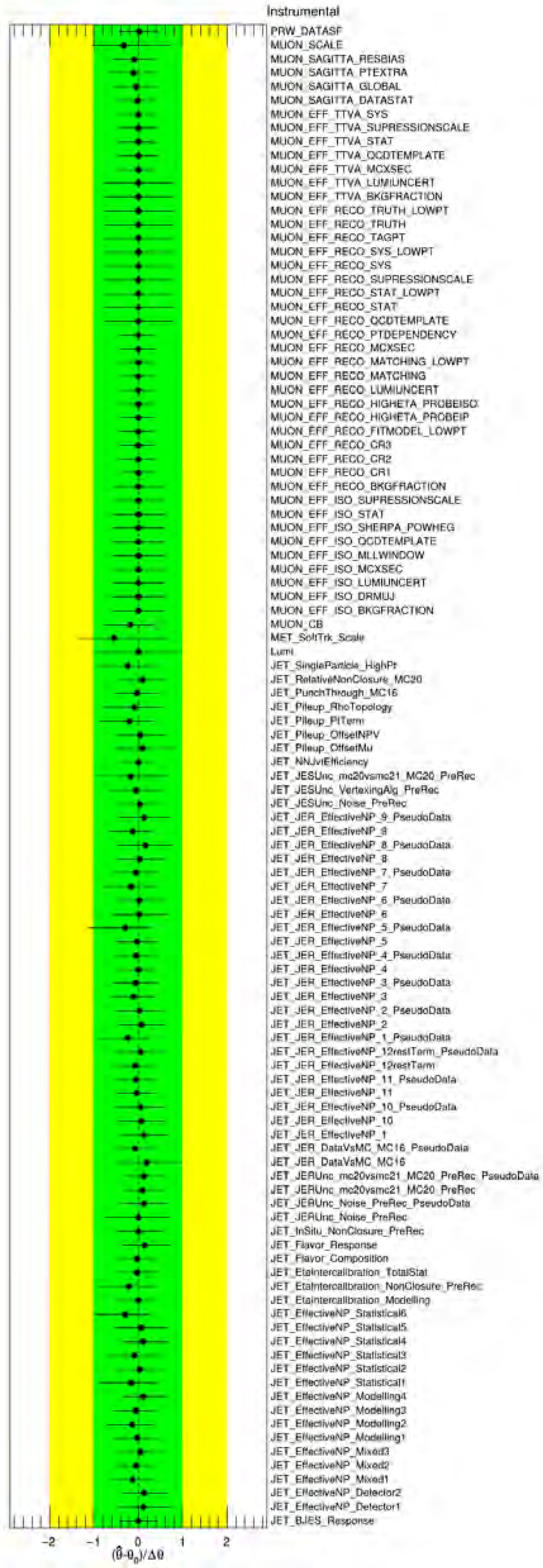

Figure C.24: Detector systematic uncertainty pull plot for Asimov fit on LH 1.8 TeV W' boson sample where $g'/g = 2$.

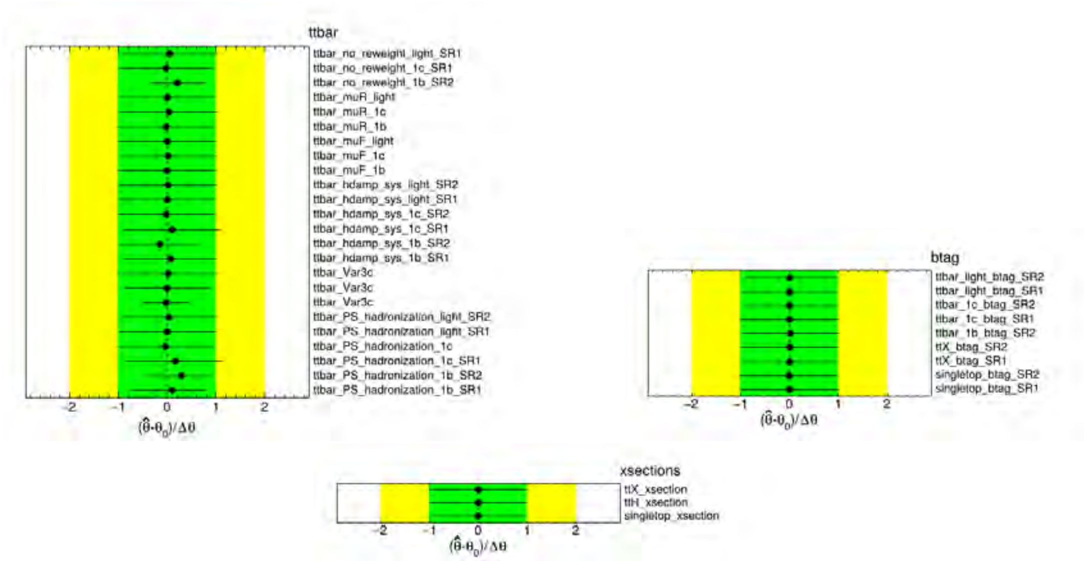

Figure C.25: $t\bar{t}$, b-tagging, and cross-section systematic uncertainty pull plot for Asimov fit on LH 1.8 TeV W' boson sample where $g'/g = 2$.

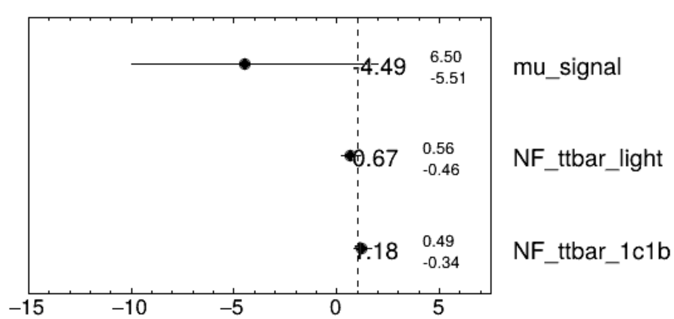

Figure C.26: Normalization factors determined by the binned maximum likelihood fit for the LH 2 TeV W' boson signal where $g'/g = 2$.

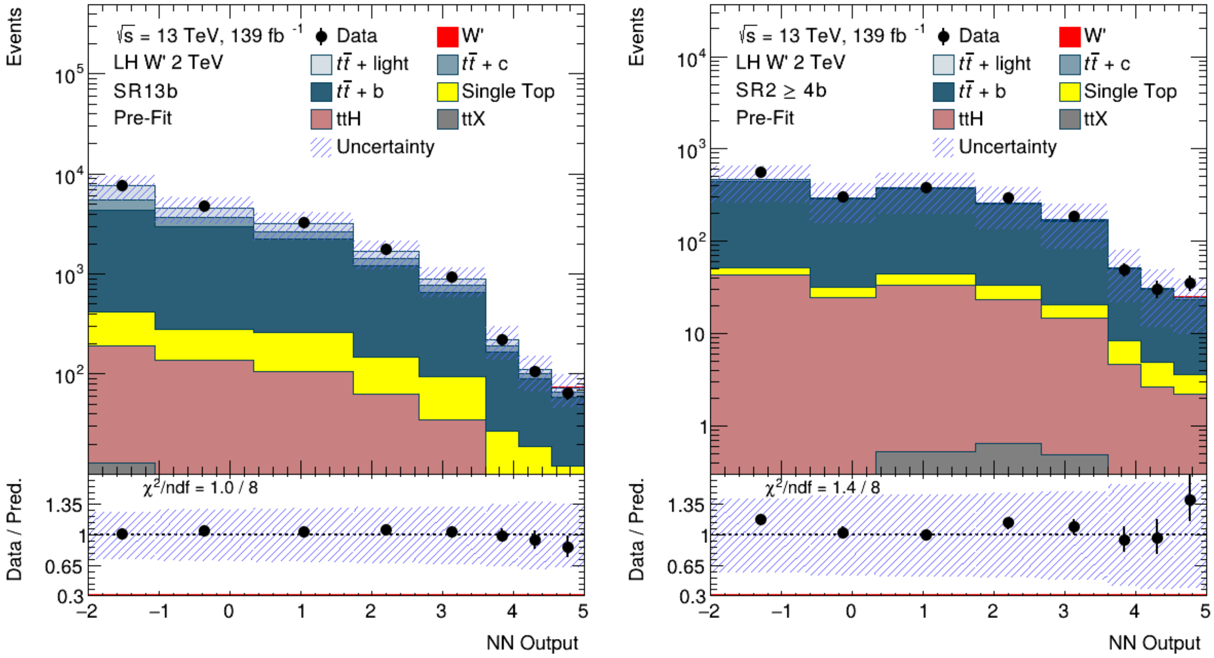

Figure C.27: Asimov pre-fit plots for LH 2 TeV W' boson signal sample where $g'/g = 2$.

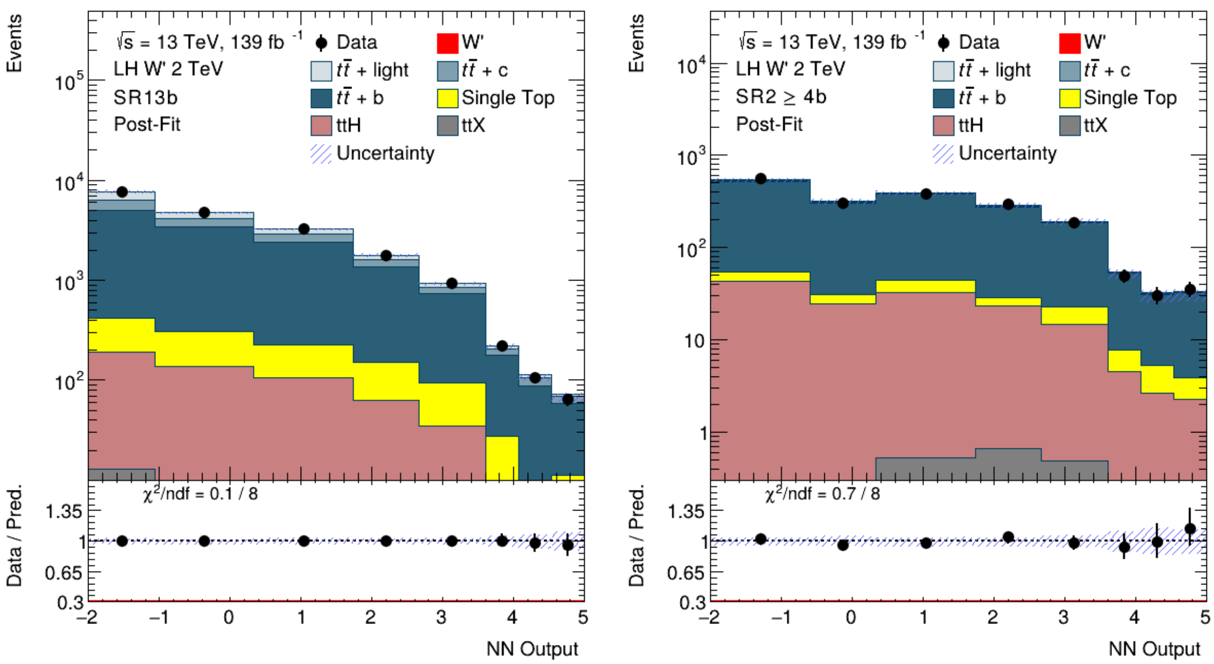

Figure C.28: Asimov post-fit plots for LH 2 TeV W' boson signal sample where $g'/g = 2$.

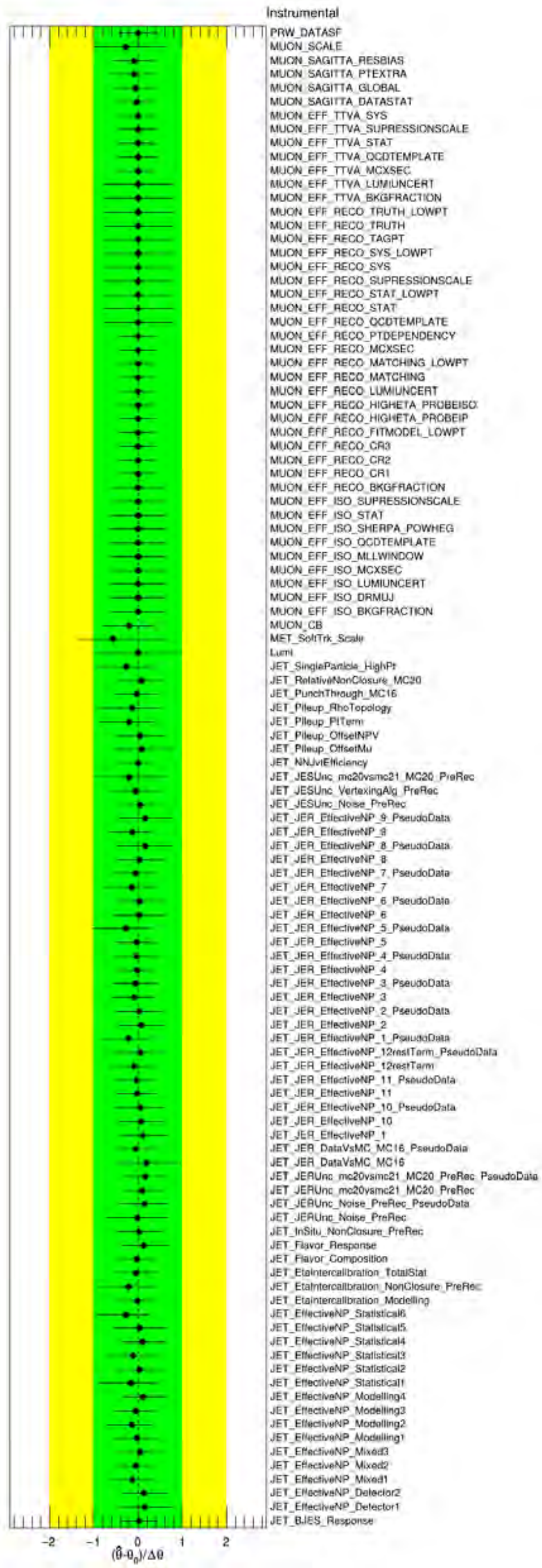

Figure C.29: Detector systematic uncertainty pull plot for Asimov fit on LH 2 TeV W' boson sample where $g'/g = 2$.

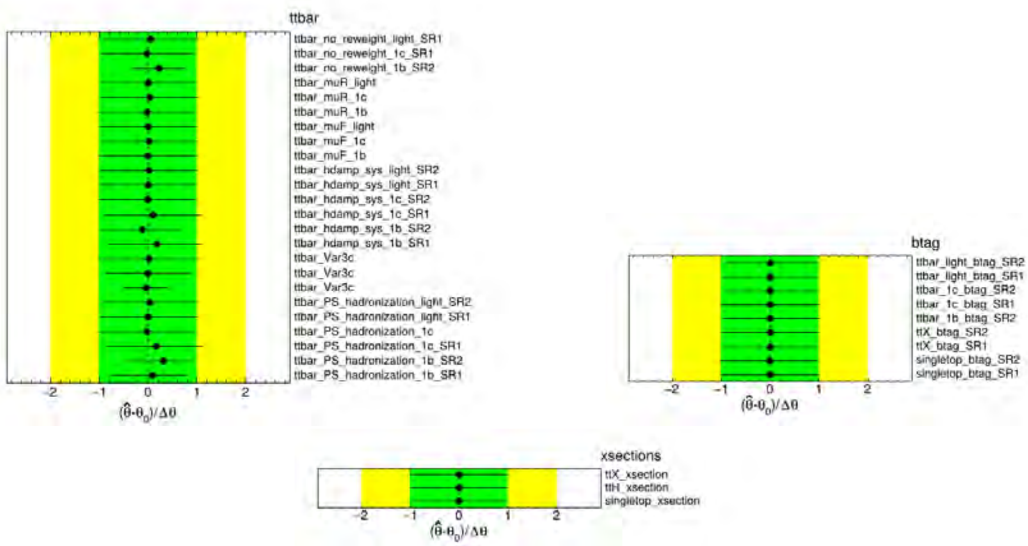

Figure C.30: $t\bar{t}$, b-tagging, and cross-section systematic uncertainty pull plot for Asimov fit on LH 2 TeV W' boson sample where $g'/g = 2$.

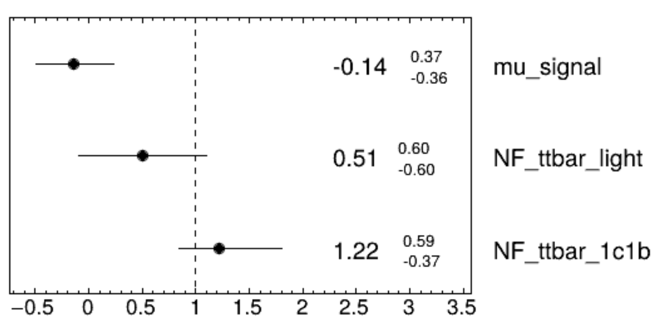

Figure C.31: Normalization factors determined by the binned maximum likelihood fit for the RH 1 TeV W' boson signal where g'/g=2.

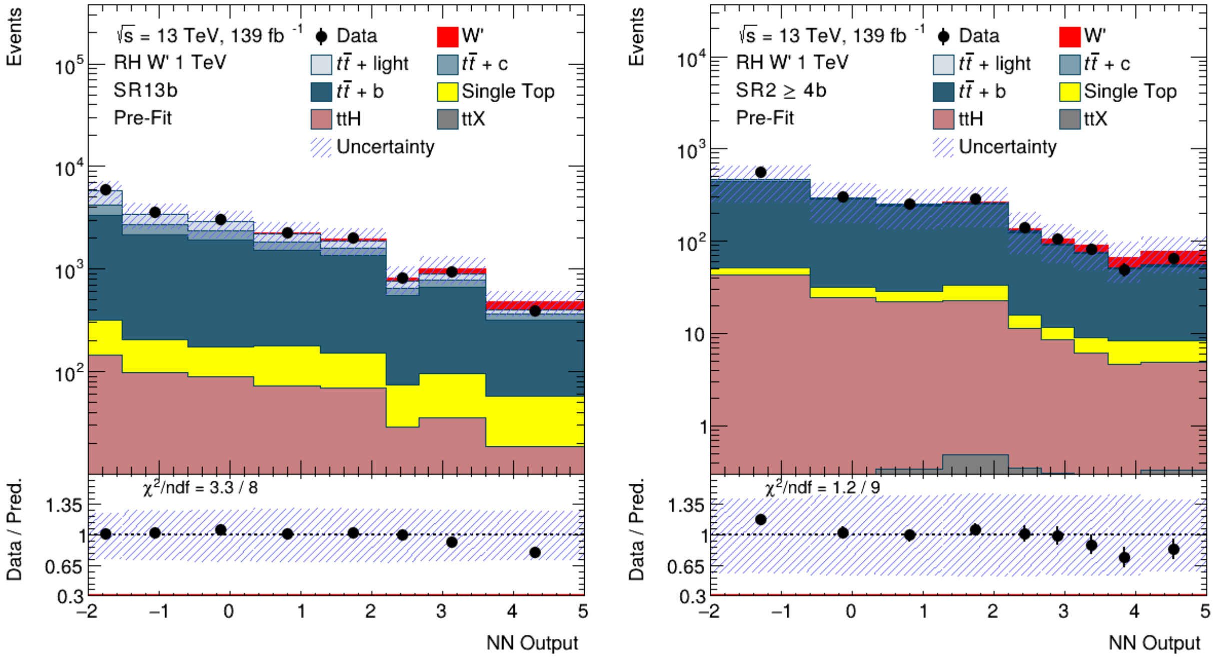

Figure C.32: Asimov pre-fit plots for RH 1 TeV W' boson signal sample where g'/g=2.

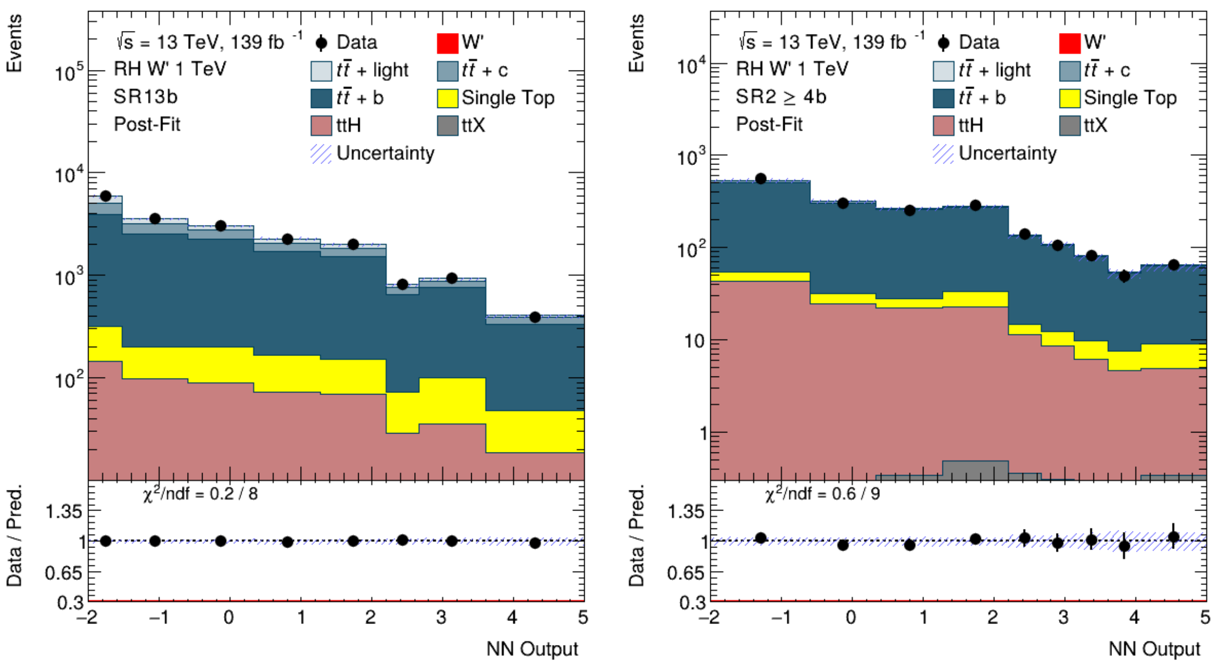

Figure C.33: Asimov post-fit plots for RH 1 TeV W' boson signal sample where g'/g=2.

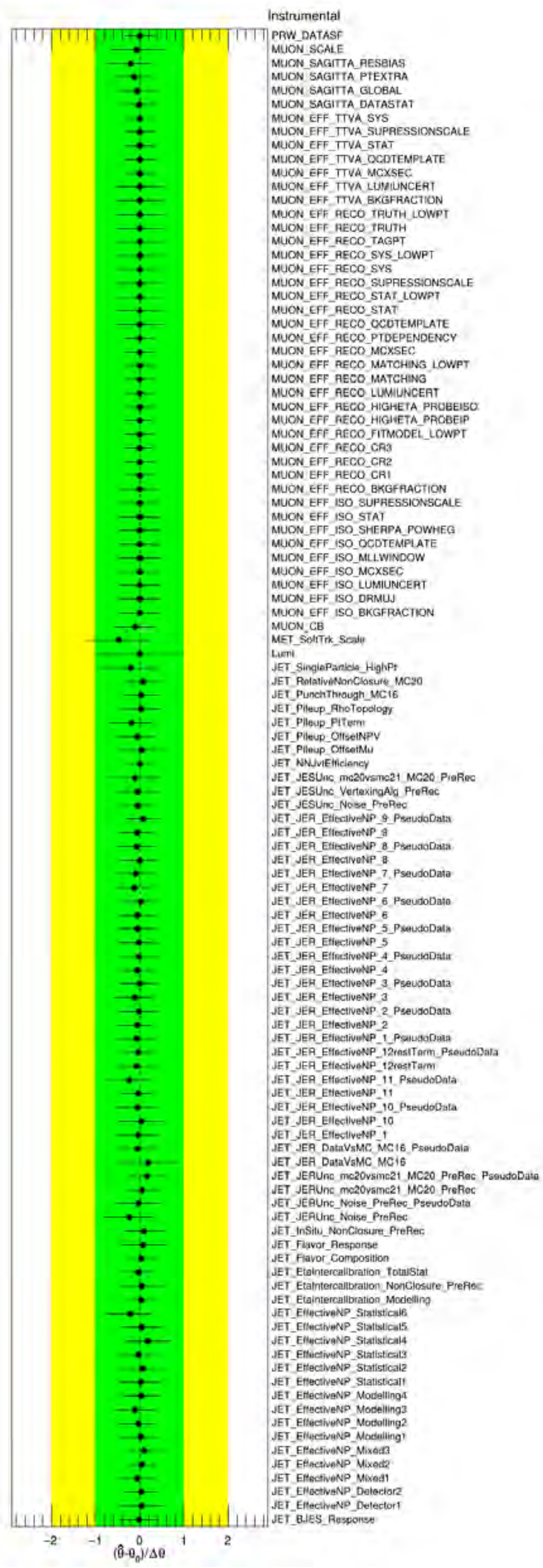

Figure C.34: Detector systematic uncertainty pull plot for Asimov fit on RH 1 TeV W' boson sample where g'/g=2.

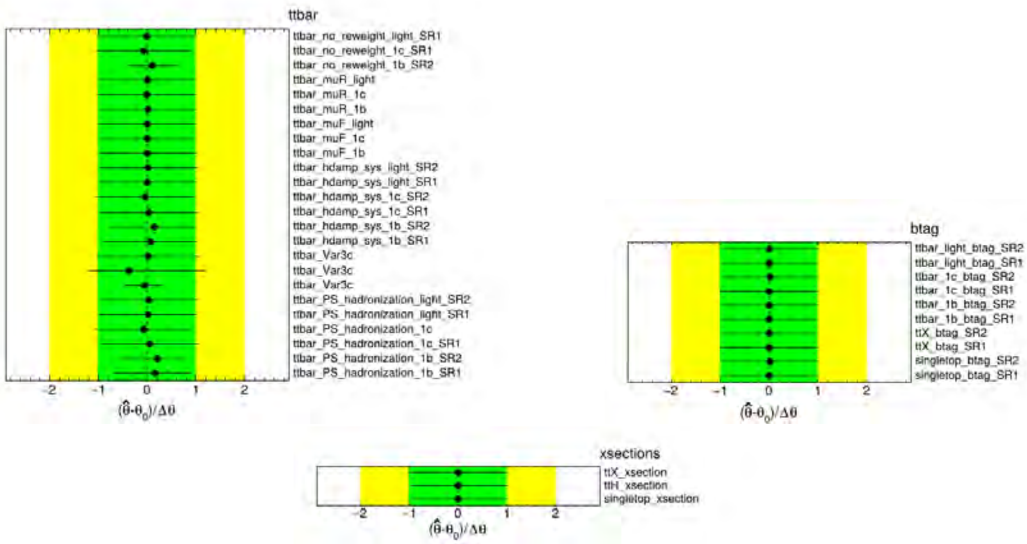

Figure C.35: $t\bar{t}$, b-tagging, and cross-section systematic uncertainty pull plot for Asimov fit on RH 1 TeV W' boson sample where g'/g=2.

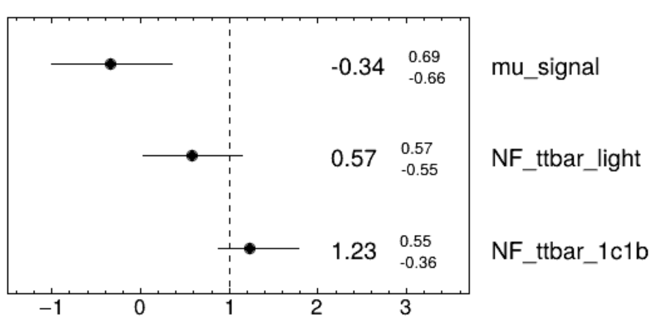

Figure C.36: Normalization factors determined by the binned maximum likelihood fit for the RH 1.2 TeV W' boson signal where $g'/g = 2$.

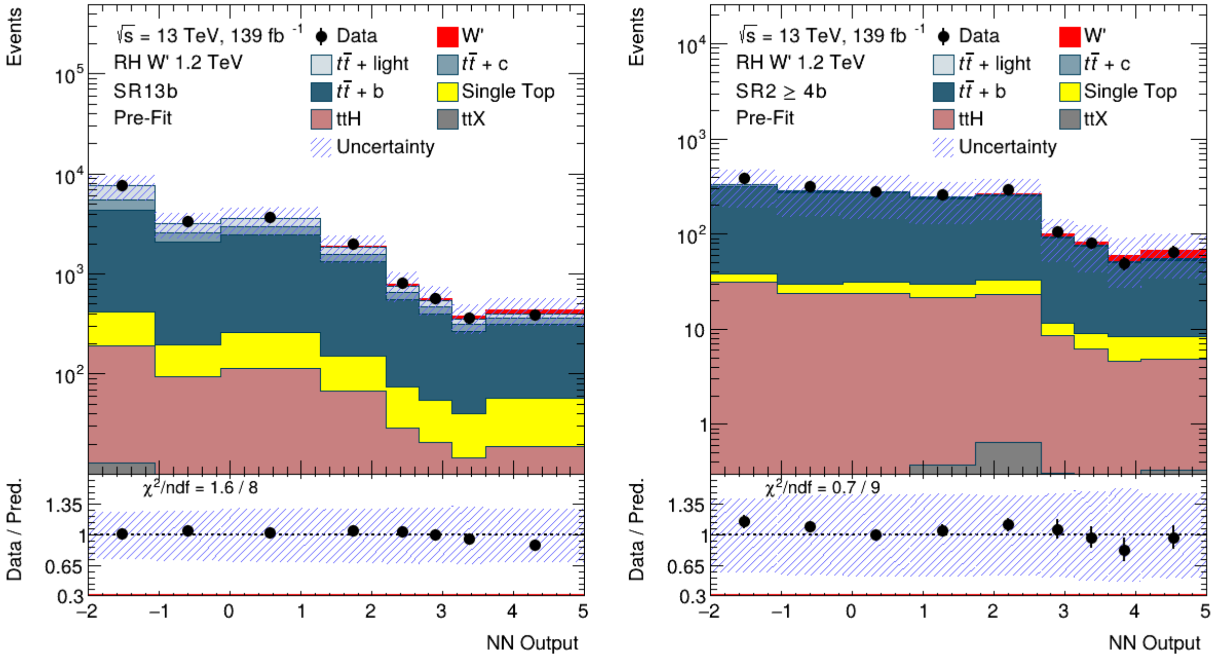

Figure C.37: Asimov pre-fit plots for RH 1.2 TeV W' boson signal sample where $g'/g = 2$.

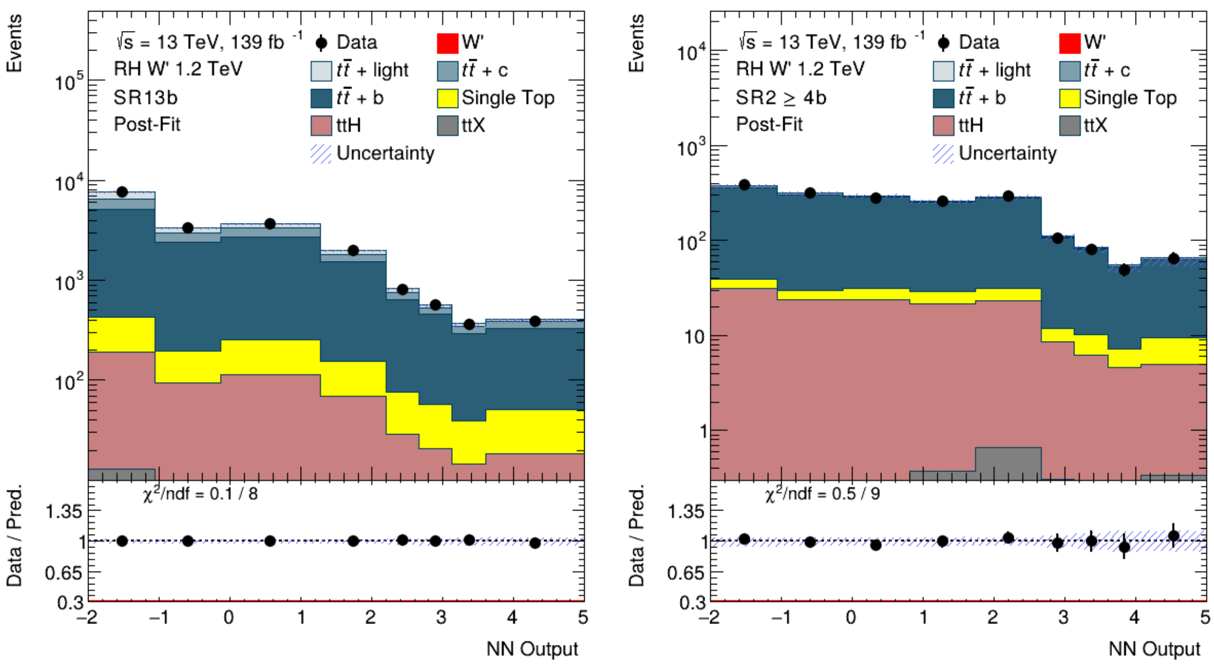

Figure C.38: Asimov post-fit plots for RH 1.2 TeV W' boson signal sample where $g'/g = 2$.

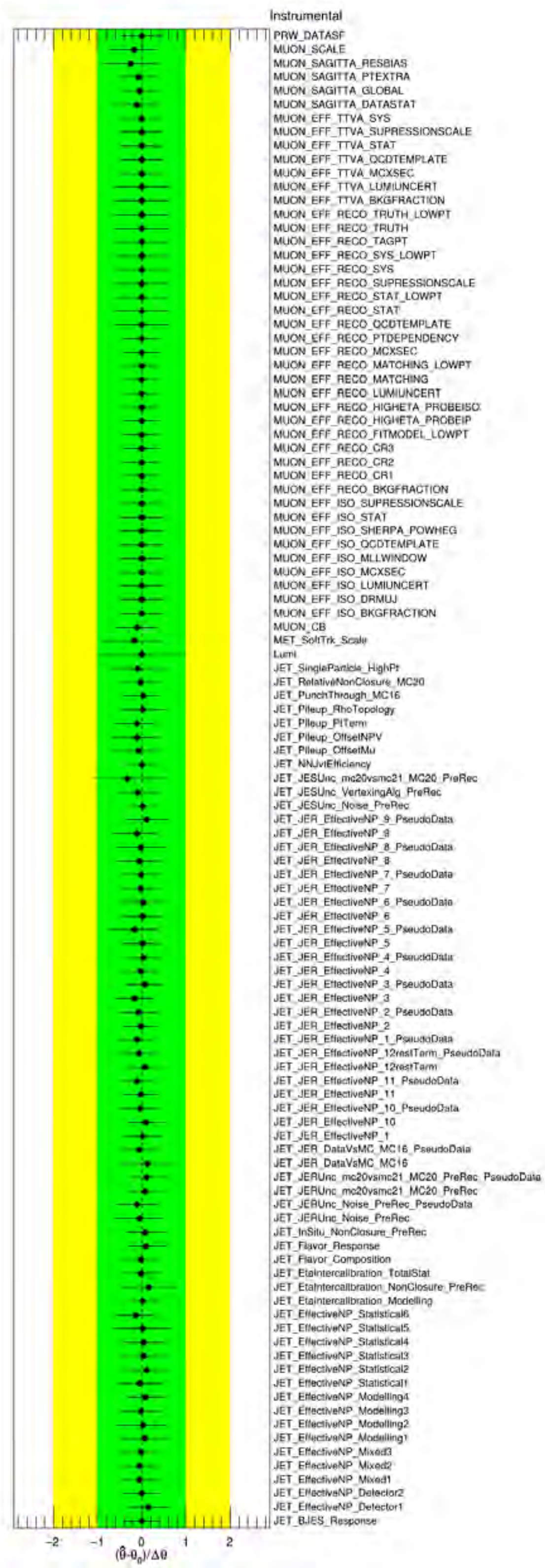

Figure C.39: Detector systematic uncertainty pull plot for Asimov fit on RH 1.2 TeV W' boson sample where $g'/g = 2$.

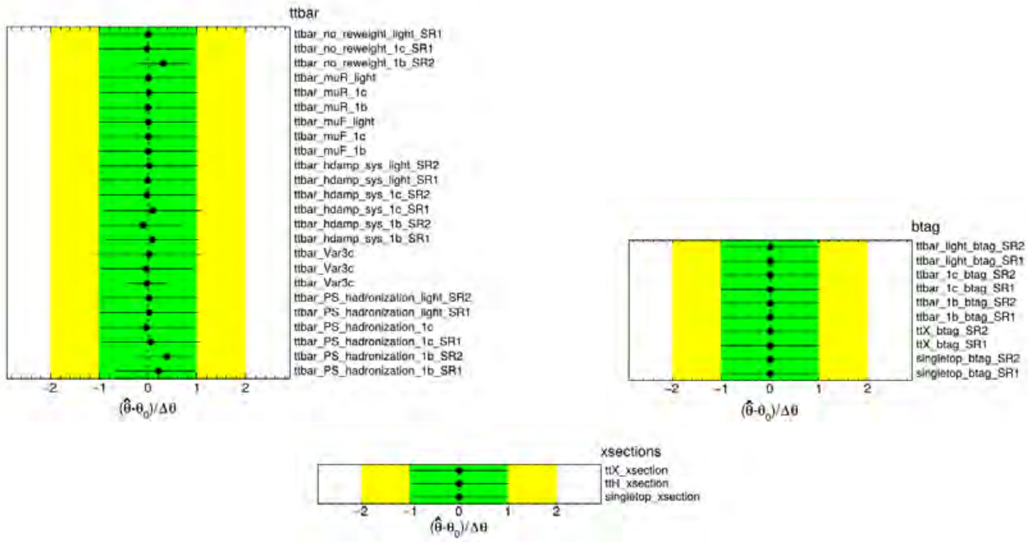

Figure C.40: $t\bar{t}$, b-tagging, and cross-section systematic uncertainty pull plot for Asimov fit on RH 1.2 TeV W' boson sample where $g'/g = 2$.

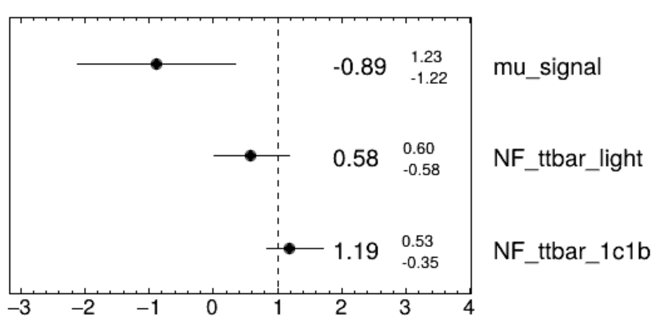

Figure C.41: Normalization factors determined by the binned maximum likelihood fit for the RH 1.4 TeV W' boson signal where $g'/g = 2$.

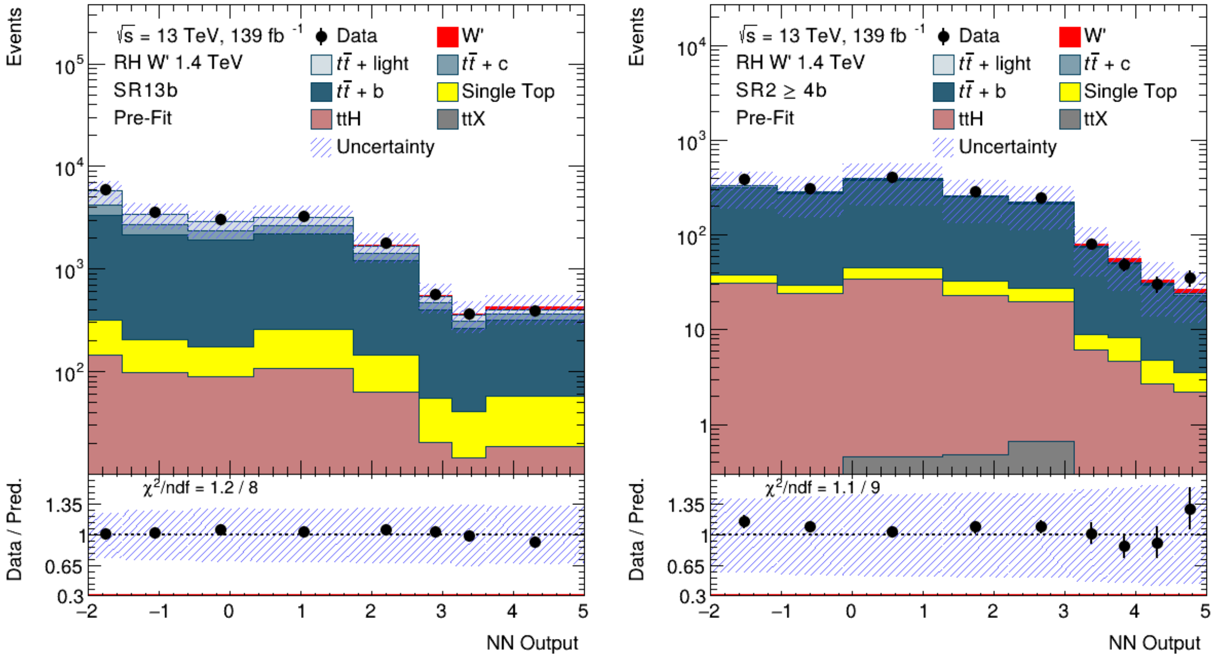

Figure C.42: Asimov pre-fit plots for RH 1.4 TeV W' boson signal sample where $g'/g = 2$.

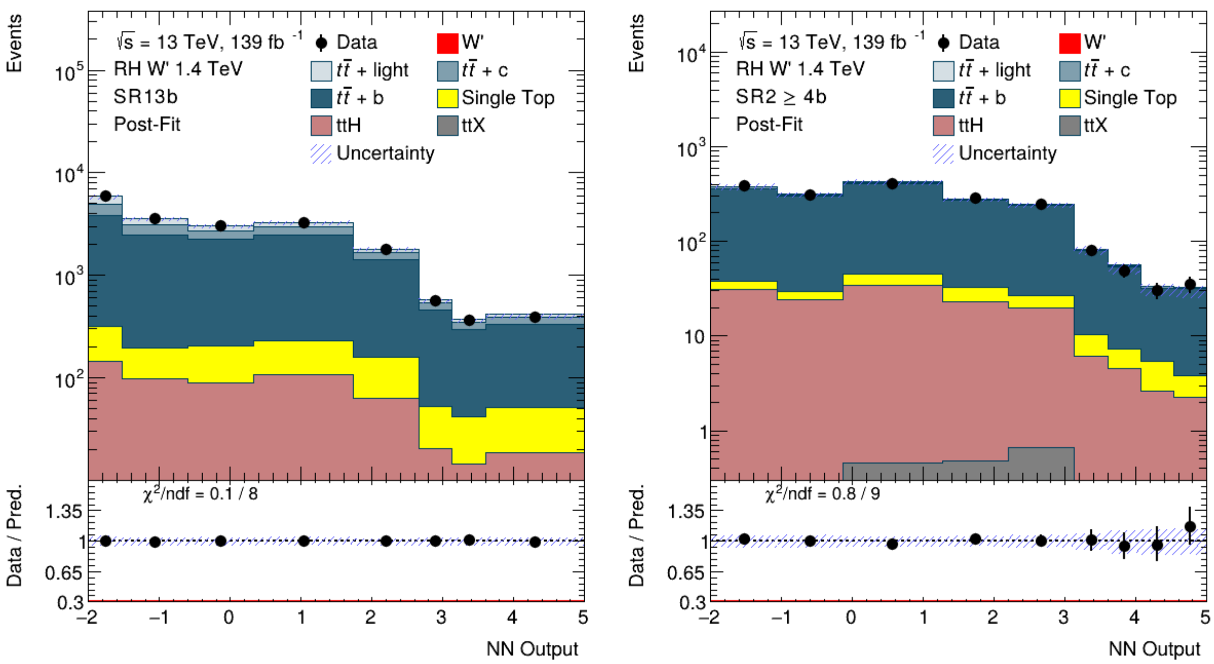

Figure C.43: Asimov post-fit plots for RH 1.4 TeV W' boson signal sample where $g'/g = 2$.

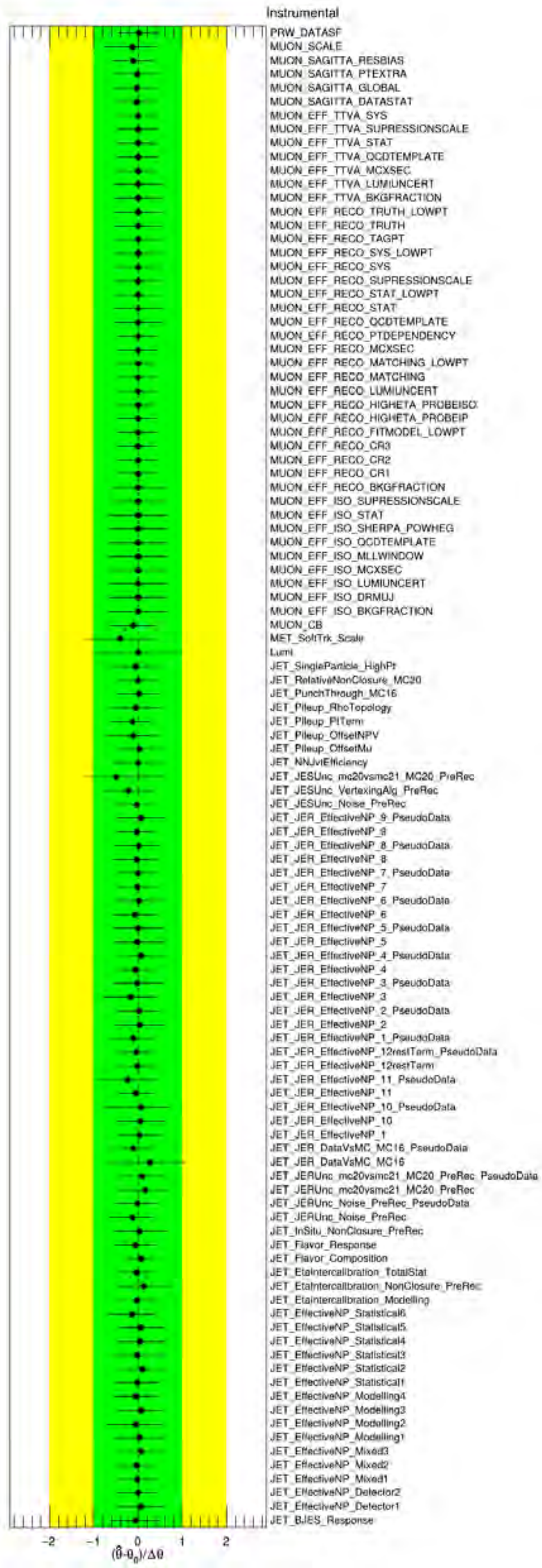

Figure C.44: Detector systematic uncertainty pull plot for Asimov fit on RH 1.4 TeV W' boson sample where $g'/g = 2$.

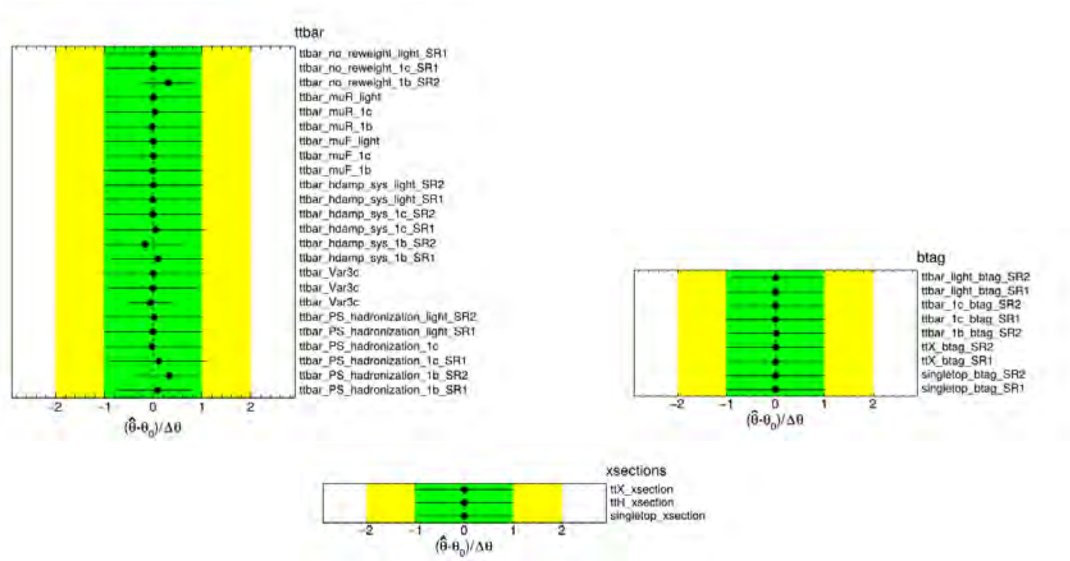

Figure C.45: $t\bar{t}$, b-tagging, and cross-section systematic uncertainty pull plot for Asimov fit on RH 1.4 TeV W' boson sample where $g'/g = 2$.

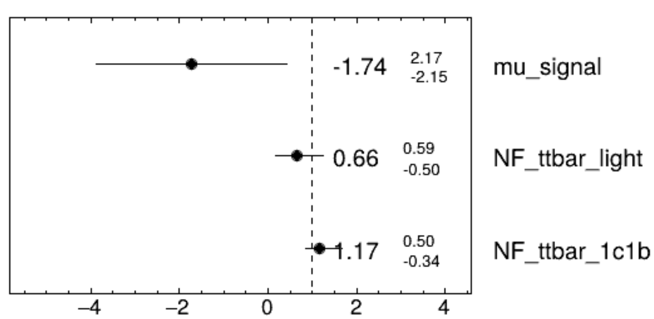

Figure C.46: Normalization factors determined by the binned maximum likelihood fit for the RH 1.6 TeV W' boson signal where $g'/g = 2$.

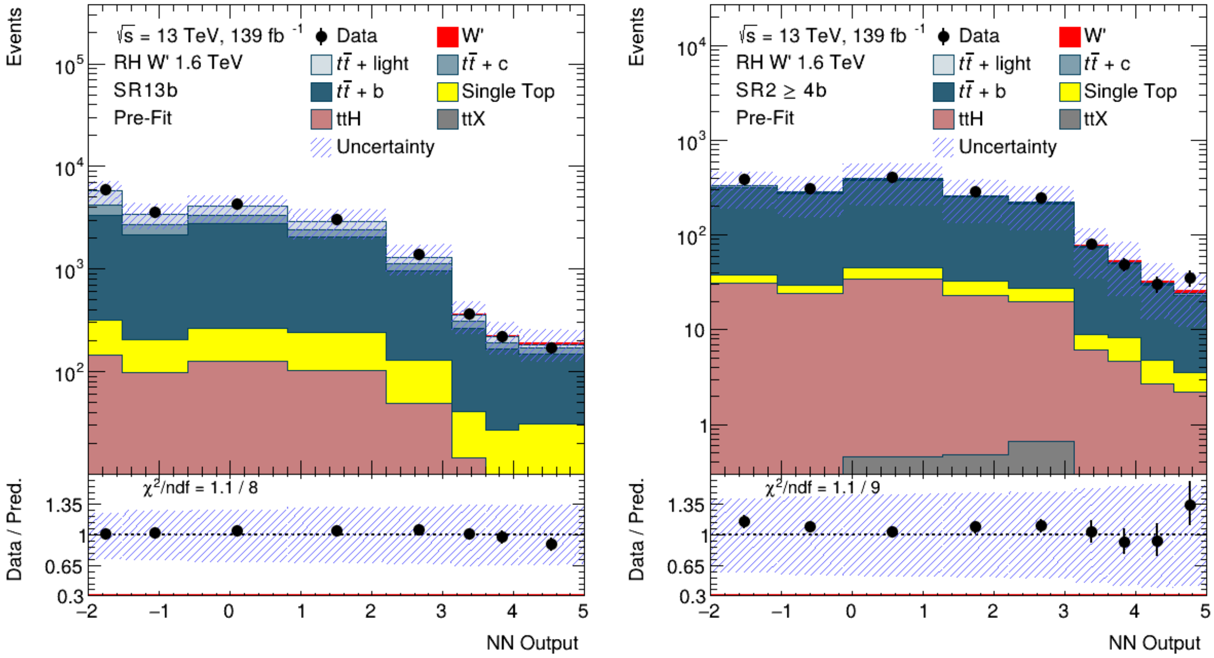

Figure C.47: Asimov pre-fit plots for RH 1.6 TeV W' boson signal sample where $g'/g = 2$.

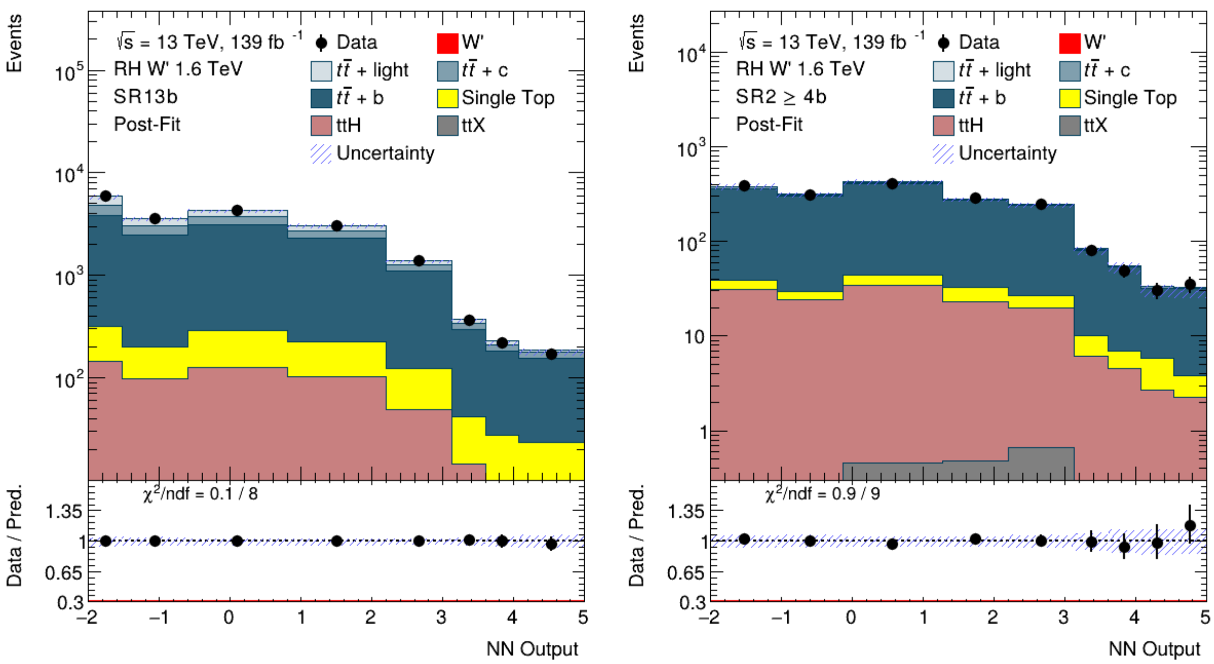

Figure C.48: Asimov post-fit plots for RH 1.6 TeV W' boson signal sample where $g'/g = 2$.

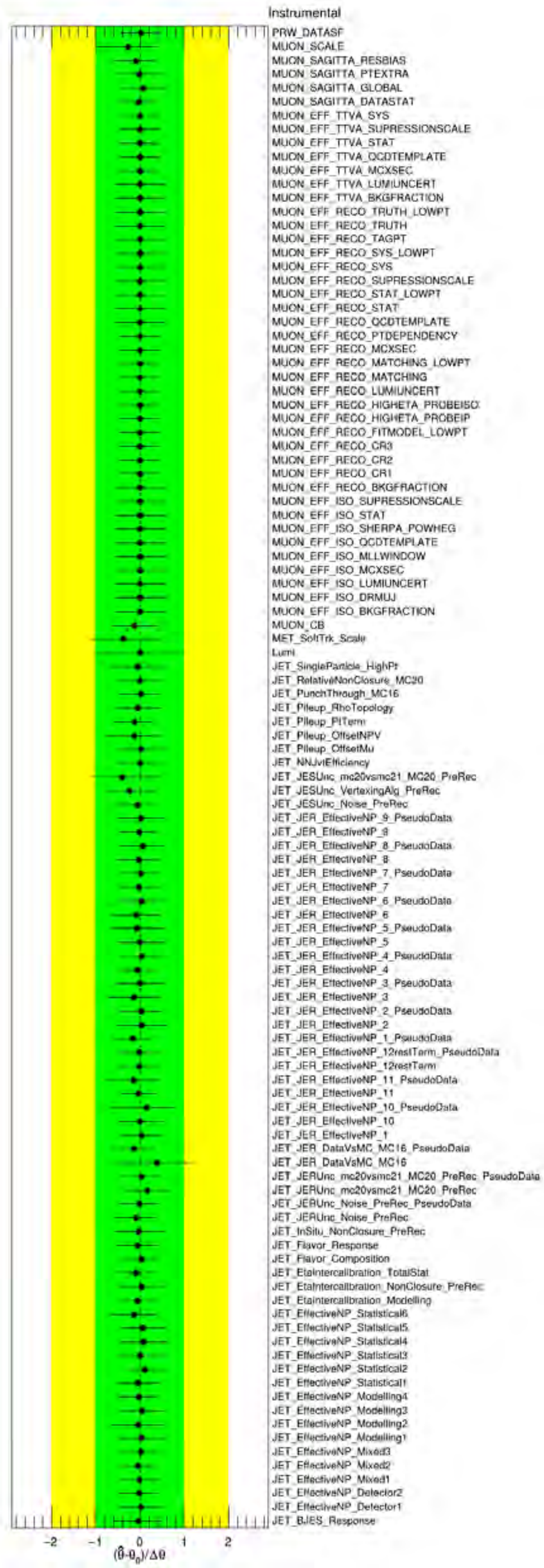

Figure C.49: Detector systematic uncertainty pull plot for Asimov fit on RH 1.6 TeV W' boson sample where $g'/g = 2$.

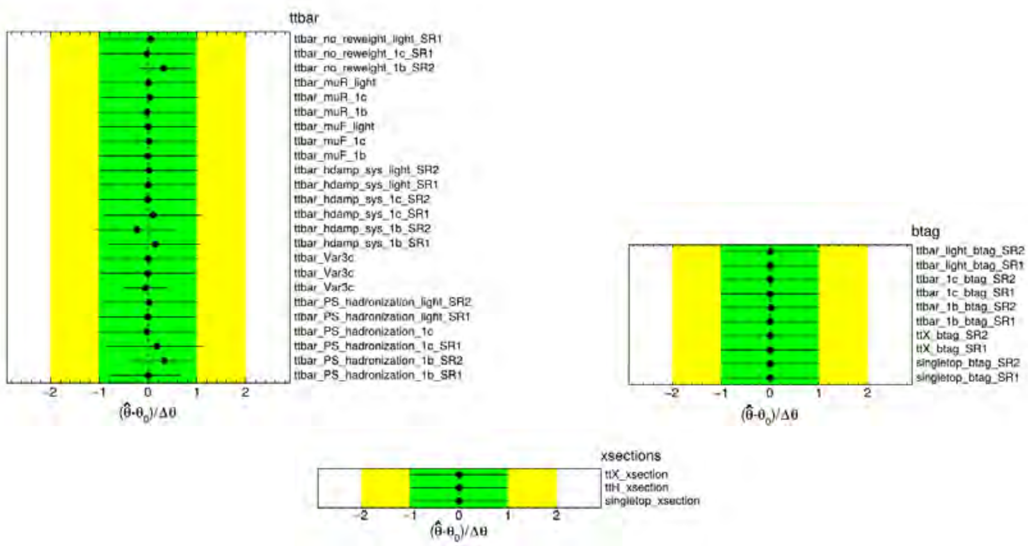

Figure C.50: $t\bar{t}$, b-tagging, and cross-section systematic uncertainty pull plot for Asimov fit on RH 1.6 TeV W' boson sample where $g'/g = 2$.

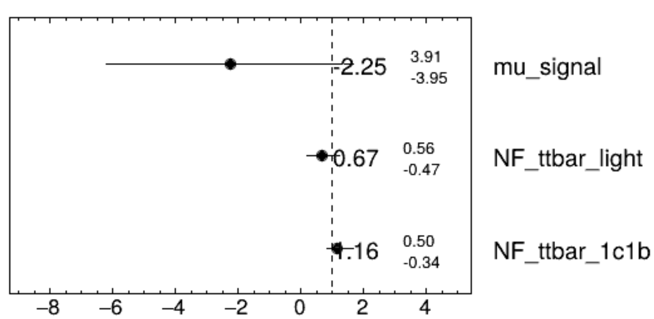

Figure C.51: Normalization factors determined by the binned maximum likelihood fit for the RH 1.8 TeV W' boson signal where $g'/g = 2$.

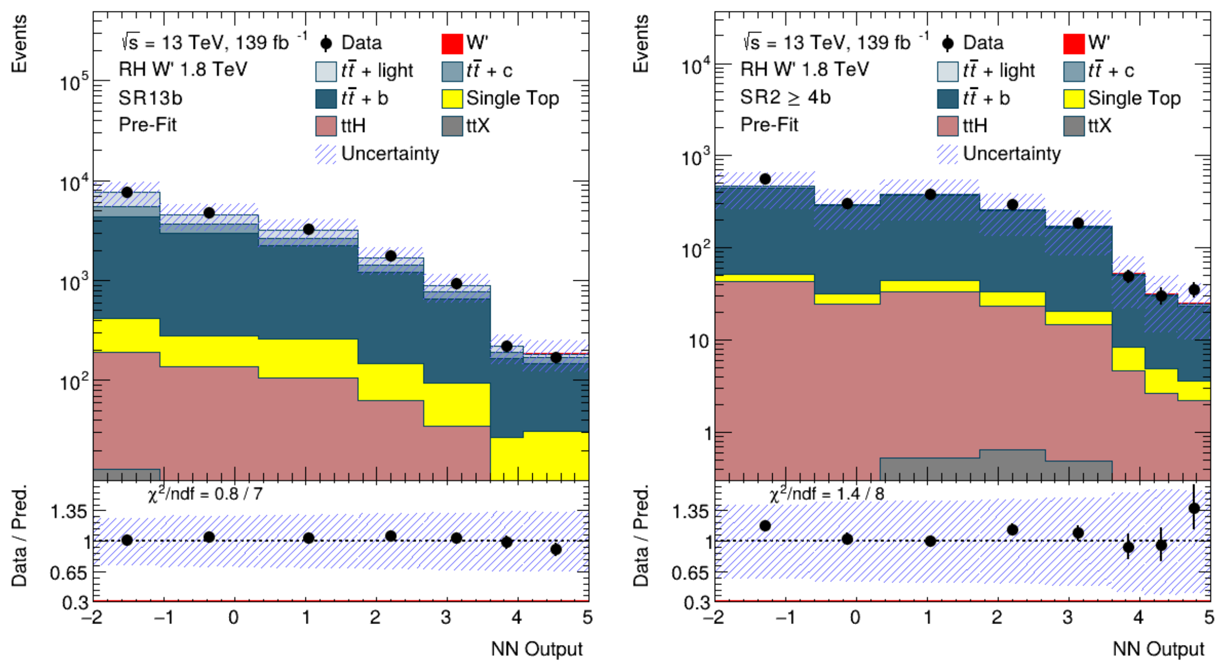

Figure C.52: Asimov pre-fit plots for RH 1.8 TeV W' boson signal sample where $g'/g = 2$.

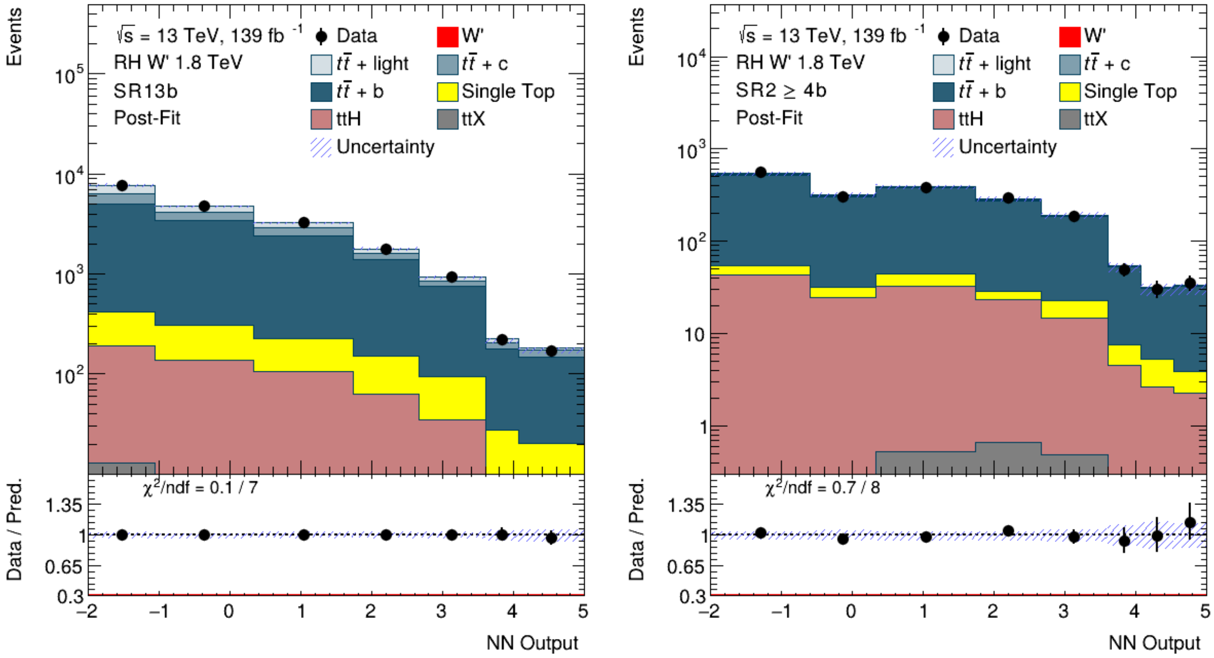

Figure C.53: Asimov post-fit plots for RH 1.8 TeV W' boson signal sample where $g'/g = 2$.

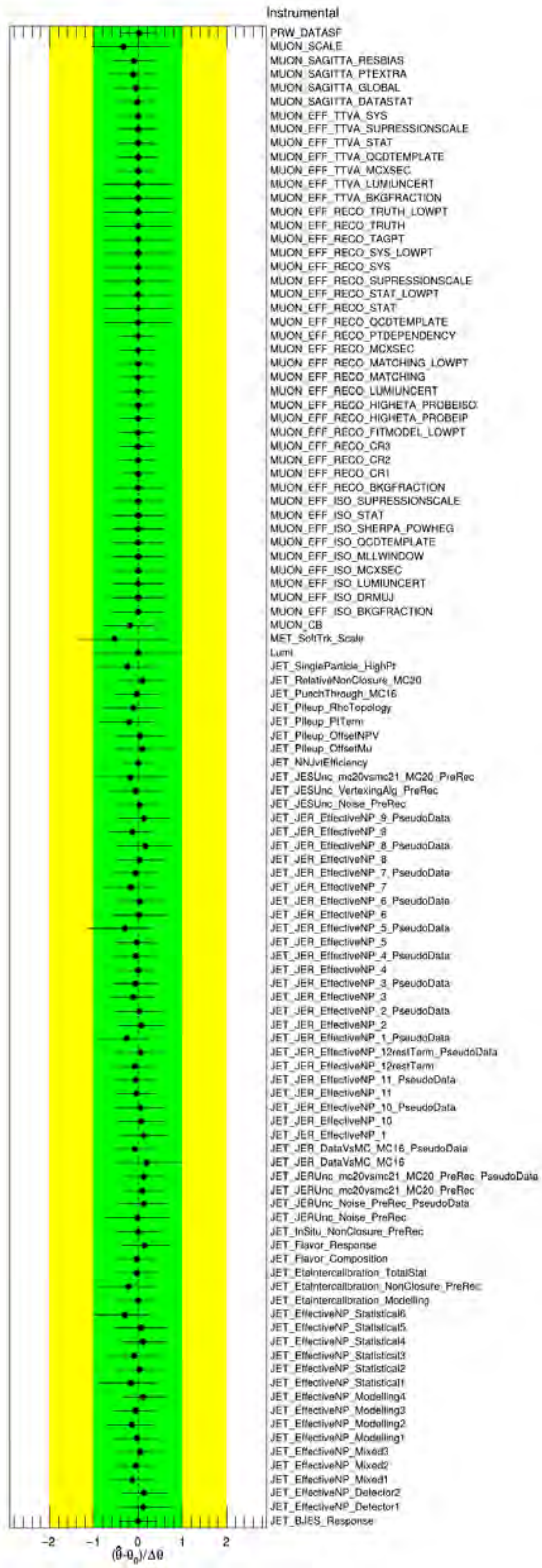

Figure C.54: Detector systematic uncertainty pull plot for Asimov fit on RH 1.8 TeV W' boson sample where $g'/g = 2$.

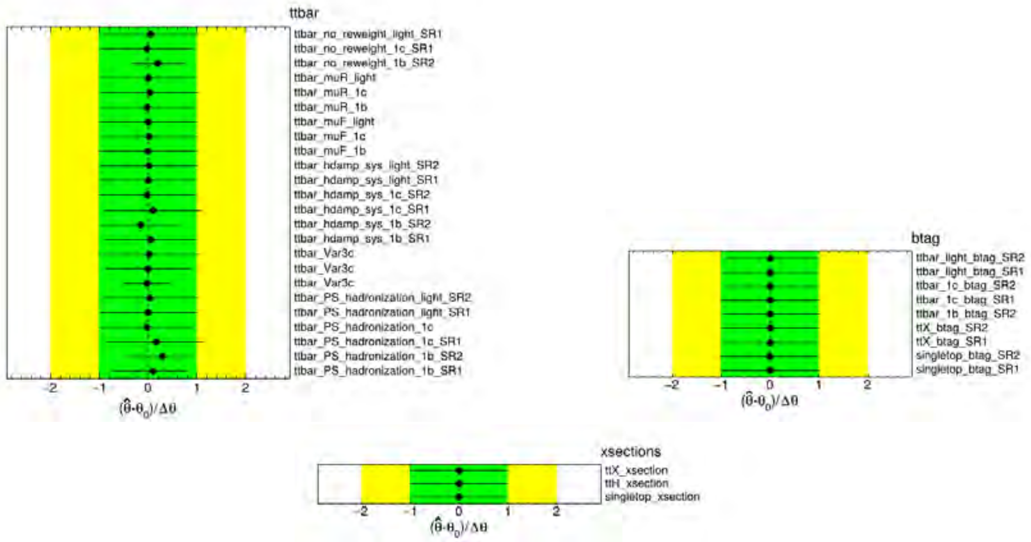

Figure C.55: $t\bar{t}$, b-tagging, and cross-section systematic uncertainty pull plot for Asimov fit on RH 1.8 TeV W' boson sample where $g'/g = 2$.

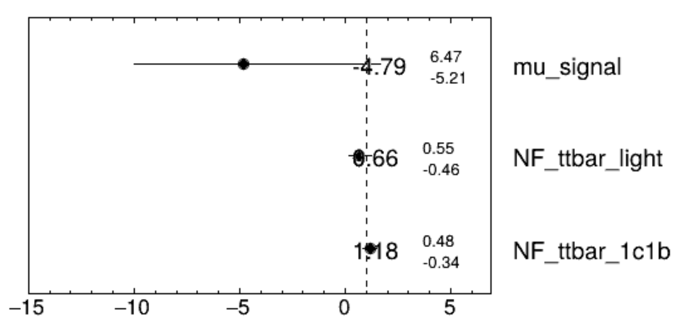

Figure C.56: Normalization factors determined by the binned maximum likelihood fit for the RH 2 TeV W' boson signal where $g'/g = 2$.

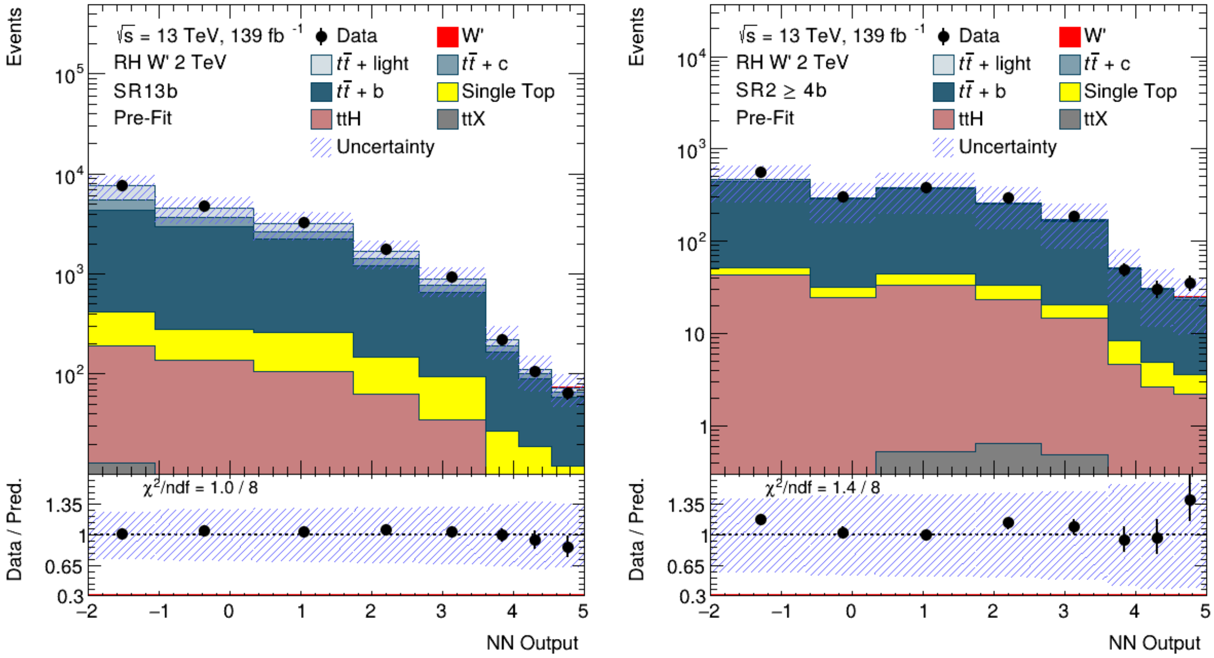

Figure C.57: Asimov pre-fit plots for RH 2 TeV W' boson signal sample where $g'/g = 2$.

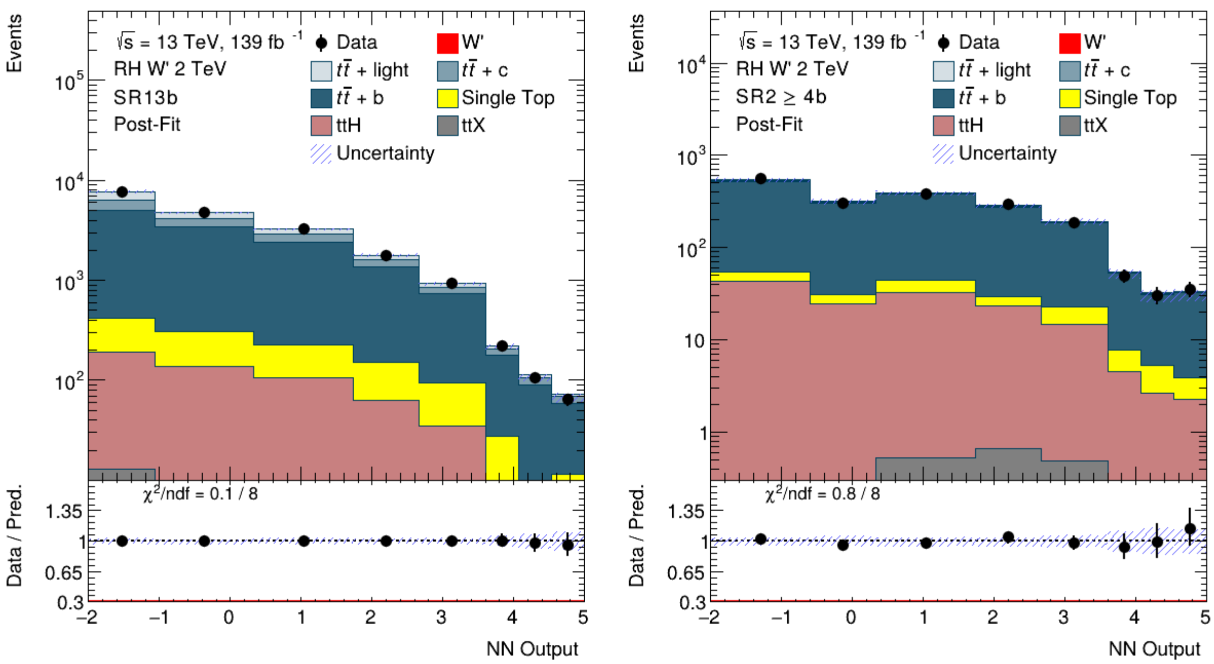

Figure C.58: Asimov post-fit plots for RH 2 TeV W' boson signal sample where $g'/g = 2$.

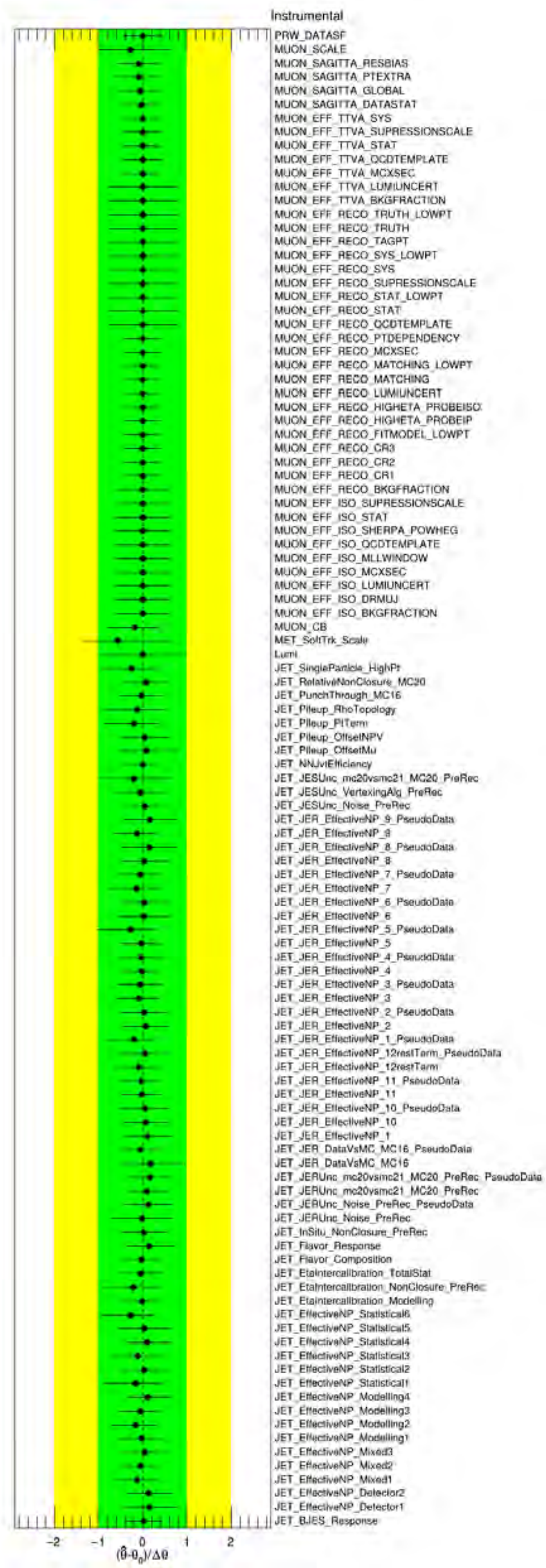

Figure C.59: Detector systematic uncertainty pull plot for Asimov fit on RH 2 TeV W' boson sample where $g'/g = 2$.

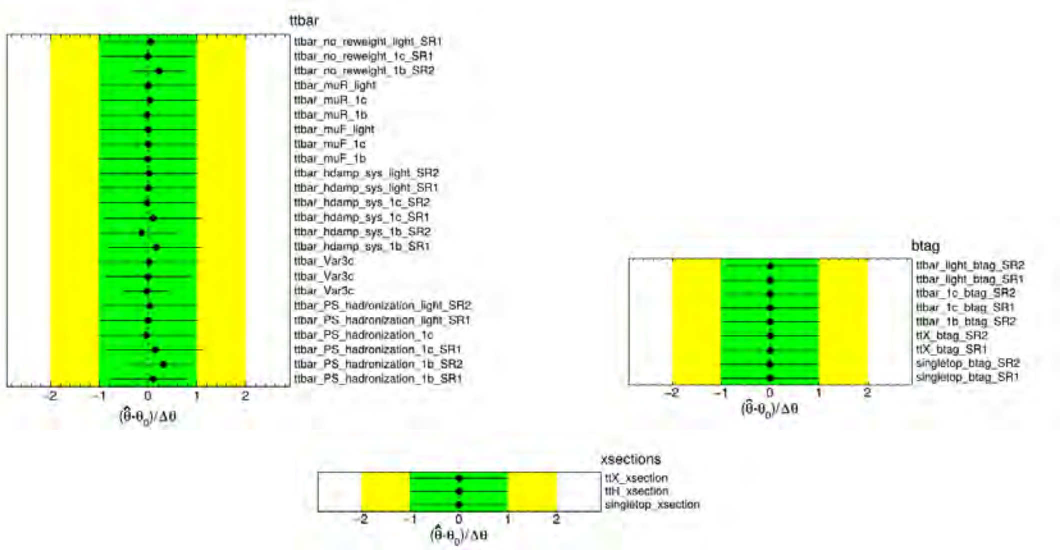

Figure C.60: $t\bar{t}$, b-tagging, and cross-section systematic uncertainty pull plot for Asimov fit on RH 2 TeV W' boson sample where $g'/g = 2$.

Appendix D

Heavy-philic W' Samples

Information on the samples that are prepared for the W' boson signal can be found in Fig. D.1

DSID	Mass (GeV)	Chirality	Cross Section (pb)	GenFiltEff	MC Events
510889	1000	LH	0.022541	5.556070E-01	0.5M
510890	1200	LH	0.0085582	5.568781E-01	0.5M
510891	1400	LH	0.0035013	5.572652E-01	0.5M
510892	1600	LH	0.0015285	5.591470E-01	0.5M
510893	1800	LH	0.00070273	5.565144E-01	0.5M
510894	2000	LH	0.00033325	5.538775E-01	0.5M
510895	2500	LH	5.9788E-05	5.528410E-01	0.5M
510896	3000	LH	1.1918E-05	5.563817E-01	0.5M
510897	4000	LH	5.5018E-07	5.535567E-01	0.5M
510898	1000	RH	0.02266	5.500035E-01	0.5M
510899	1200	RH	0.0085155	5.578584E-01	0.5M
510900	1400	RH	0.0035008	5.551680E-01	0.5M
510901	1600	RH	0.0015201	5.565374E-01	0.5M
510902	1800	RH	0.00069754	5.530268E-01	0.5M
510903	2000	RH	0.00033302	5.533983E-01	0.5M
510904	2500	RH	5.9378E-05	5.537889E-01	0.5M
510905	3000	RH	1.1875E-05	5.542597E-01	0.5M
510906	4000	RH	5.4839E-07	5.560649E-01	0.5M

Table D.1: List of the generated W' LH and RH samples. All samples are simulated with FullSim and available in the appropriate proportions of MC20a, MC20d, and MC20e.

Bibliography

[1] ATLAS Collaboration. “Observation of a new particle in the search for the Standard Model Higgs boson with the ATLAS detector at the LHC”. In: *Phys. Lett. B* 716 (2012), p. 1. DOI: 10.1016/j.physletb.2012.08.020. arXiv: 1207.7214 [hep-ex] (cit. on p. 1).

[2] S. Chatrchyan and others [CMS Collaboration]. “Observation of a new boson at a mass of 125 GeV with the CMS experiment at the LHC”. In: *Phys. Lett. B* 716.1 (2012), 30–61. ISSN: 0370-2693. DOI: {10.1016/j.physletb.2012.08.021} (cit. on p. 1).

[3] “Characterising the Higgs boson with ATLAS data from the LHC Run-2”. In: *Physics Reports* 1116 (2025). Breaking boundaries — ATLAS physics highlights and milestones from the LHC Run 2, pp. 4–56. ISSN: 0370-1573. DOI: https://doi.org/10.1016/j.physrep.2024.11.001. URL: https://www.sciencedirect.com/science/article/pii/S037015732400382X (cit. on p. 1).

[4] “Electroweak, QCD and flavour physics studies with ATLAS data from Run 2 of the LHC”. In: *Physics Reports* 1116 (2025). Breaking boundaries — ATLAS physics highlights and milestones from the LHC Run 2, pp. 57–126. ISSN: 0370-1573. DOI: https://doi.org/10.1016/j.physrep.2024.12.003. URL: https://www.sciencedirect.com/science/article/pii/S0370157324004290 (cit. on p. 1).

[5] “Climbing to the Top of the ATLAS 13 TeV data”. In: *Physics Reports* 1116 (2025). Breaking boundaries — ATLAS physics highlights and milestones from the LHC Run 2, pp. 127–183. ISSN: 0370-1573. DOI: https://doi.org/10.1016/j.physrep.2024.12.004. URL: https://www.sciencedirect.com/science/article/pii/S0370157324004307 (cit. on p. 1).

[6] “ATLAS searches for additional scalars and exotic Higgs boson decays with the LHC Run 2 dataset”. In: *Physics Reports* 1116 (2025). Breaking boundaries — ATLAS physics highlights and milestones from the LHC Run 2, pp. 184–260. ISSN: 0370-1573. DOI: https://doi.org/10.1016/j.physrep.2024.09.002. URL: https://www.sciencedirect.com/science/article/pii/S037015732400303X (cit. on p. 1).

[7] “The quest to discover supersymmetry at the ATLAS experiment”. In: *Physics Reports* 1116 (2025). Breaking boundaries — ATLAS physics highlights and milestones from the LHC Run 2, pp. 261–300. ISSN: 0370-1573. DOI: https://doi.org/10.1016/j.physrep.2024.09.010. URL: https://www.sciencedirect.com/science/article/pii/S0370157324003338 (cit. on p. 1).

[8] ATLAS Collaboration. *Exploration at the high-energy frontier: ATLAS Run 2 searches investigating the exotic jungle beyond the Standard Model*. 2024. arXiv: 2403.09292 [hep-ex]. URL: https://arxiv.org/abs/2403.09292 (cit. on pp. 1, 2).

[9] Vera C. Rubin and W. Kent Ford. "Rotation of the Andromeda Nebula from a Spectroscopic Survey of Emission Regions". In: *Astrophysical Journal* 159 (1970), p. 379. DOI: 10.1086/150317 (cit. on p. 1).

[10] Vera C. Rubin, W. Kent Ford, and Norbert Thonnard. "Rotational properties of 21 SC galaxies with a large range of luminosities and radii, from NGC 4605 (R = 4kpc) to UGC 2885 (R = 122kpc)". In: *Astrophysical Journal* 238 (1980), pp. 471–487. DOI: 10.1086/158003 (cit. on p. 1).

[11] Albert Einstein. "Physics and Reality". In: *Journal of the Franklin Institute* 221.3 (1936), pp. 349–382 (cit. on p. 2).

[12] Eugene P. Wigner. "The Unreasonable Effectiveness of Mathematics in the Natural Sciences". In: *Communications on Pure and Applied Mathematics* 13.1 (1960), pp. 1–14 (cit. on p. 2).

[13] Robert Hooke. *Micrographia*. Royal Society, 1665 (cit. on p. 2).

[14] J. J. Thomson. "Cathode Rays". In: *Philosophical Magazine* 44 (1897), pp. 293–316 (cit. on p. 2).

[15] Max Knoll and Ernst Ruska. "Das Elektronenmikroskop". In: *Zeitschrift für Physik* 78.5–6 (1932), pp. 318–339 (cit. on p. 2).

[16] David J. Griffiths. *Introduction to Elementary Particles*. Wiley-VCH, 2008 (cit. on pp. 2, 16).

[17] Murray Gell-Mann. "A Schematic Model of Baryons and Mesons". In: *Physics Letters* 8.3 (1964), pp. 214–215 (cit. on p. 2).

[18] Anne-Mazarine Lyon. *Review of searches for new physics at CMS*. 2024. arXiv: 2406.02010 [hep-ex]. URL: https://arxiv.org/abs/2406.02010 (cit. on p. 2).

[19] David J Muller and Satyanarayan Nandi. "Topflavor: a separate SU(2) for the third family". In: *Physics Letters B* 383.3 (Sept. 1996), pp. 345–350. ISSN: 0370-2693. DOI: 10.1016/0370-2693(96)00745-9. URL: http://dx.doi.org/10.1016/0370-2693(96)00745-9 (cit. on p. 3).

[20] Gustavo Burdman, Bogdan A. Dobrescu, and Eduardo Pontón. "Resonances from two universal extra dimensions". In: *Phys. Rev. D* 74 (7 Oct. 2006), p. 075008. DOI: 10.1103/PhysRevD.74.075008. URL: https://link.aps.org/doi/10.1103/PhysRevD.74.075008 (cit. on p. 3).

[21] Ehab Malkawi, Tim Tait, and C.-P. Yuan. "A model of strong flavor dynamics for the top quark". In: *Physics Letters B* 385.1 (1996), pp. 304–310. ISSN: 0370-2693. DOI: https://doi.org/10.1016/0370-2693(96)00859-3. URL: https://www.sciencedirect.com/science/article/pii/0370269396008593 (cit. on p. 3).

[22] Jogesh C. Pati and Abdus Salam. "Lepton number as the fourth "color"". In: *Physical Review D* 10.1 (1974), pp. 275–289. DOI: 10.1103/PhysRevD.10.275. URL: https://doi.org/10.1103/PhysRevD.10.275 (cit. on p. 3).

[23] Keith R. Dienes, Emilian Dudas, and Tony Gherghetta. “Grand unification at intermediate mass scales through extra dimensions”. In: *Nuclear Physics B* 537.1–3 (Jan. 1999), pp. 47–108. ISSN: 0550-3213. DOI: 10.1016/s0550-3213(98)00669-5. URL: http://dx.doi.org/10.1016/S0550-3213(98)00669-5 (cit. on p. 3).

[24] Steven Weinberg. “Implications of dynamical symmetry breaking”. In: *Phys. Rev. D* 13 (4 Feb. 1976), pp. 974–996. DOI: 10.1103/PhysRevD.13.974. URL: https://link.aps.org/doi/10.1103/PhysRevD.13.974 (cit. on p. 3).

[25] Estia Eichten and Kenneth Lane. “Dynamical breaking of weak interaction symmetries”. In: *Physics Letters B* 90.1 (1980), pp. 125–130. ISSN: 0370-2693. DOI: https://doi.org/10.1016/0370-2693(80)90065-9. URL: https://www.sciencedirect.com/science/article/pii/0370269380900659 (cit. on p. 3).

[26] ATLAS Collaboration. “Search for top-philic heavy resonances in pp collisions at $\sqrt{s} =$ 13TeV with the ATLAS detector”. In: *The European Physical Journal C* 84.2 (Feb. 2024). ISSN: 1434-6052. DOI: 10.1140/epjc/s10052-023-12318-9. URL: http://dx.doi.org/10.1140/epjc/s10052-023-12318-9 (cit. on p. 4).

[27] [ATLAS Collaboration]. “Search for vector-boson resonances decaying into a top quark and a bottom quark using pp collisions at $\sqrt{s} = 13$ TeV with the ATLAS detector”. In: *Journal of High Energy Physics* 2023.12 (Dec. 2023). ISSN: 1029-8479. DOI: 10.1007/jhep12(2023)073. URL: http://dx.doi.org/10.1007/JHEP12(2023)073 (cit. on pp. 4, 17).

[28] [ATLAS Collaboration]. “Search for resonances produced in association with or decaying to a Z boson”. In: *Physical Review D* 109.11 (June 2024). ISSN: 2470-0029. DOI: 10.1103/physrevd.109.112008. URL: http://dx.doi.org/10.1103/PhysRevD.109.112008 (cit. on pp. 4, 17).

[29] The CMS collaboration. “Search for W’ bosons decaying to a top and a bottom quark in leptonic final states in proton-proton collisions at $\sqrt{s} = 13$ TeV”. In: *Journal of High Energy Physics* 2024.5 (2024), p. 46. DOI: 10.1007/JHEP05(2024)046. URL: https://doi.org/10.1007/JHEP05(2024)046 (cit. on p. 4).

[30] Michael Edward Peskin and Daniel V. Schroeder. *An Introduction to Quantum Field Theory*. Reading, USA: Addison-Wesley (1995) 842 p. Westview Press, 1995 (cit. on p. 7).

[31] ATLAS Collaboration. “Luminosity determination in *pp* collisions at $\sqrt{s} = 13\,\mathrm{TeV}$ using the ATLAS detector at the LHC”. In: *Eur. Phys. J. C* 83 (2023), p. 982. DOI: 10.1140/epjc/s10052-023-11747-w. arXiv: 2212.09379 [hep-ex] (cit. on pp. 9, 27).

[32] Fabio Maltoni, Giovanni Ridolfi, and Maria Ubiali. “b-initiated processes at the LHC: a reappraisal”. In: *Journal of High Energy Physics* 2012.7 (July 2012). ISSN: 1029-8479. DOI: 10.1007/jhep07(2012)022. URL: http://dx.doi.org/10.1007/JHEP07(2012)022 (cit. on p. 9).

[33] S. Navas and et al. “Review of Particle Physics”. In: *Phys. Rev. D* 110 (3 Oct. 2024), p. 030001. DOI: 10.1103/PhysRevD.110.030001. URL: https://link.aps.org/doi/10.1103/PhysRevD.110.030001 (cit. on pp. 12, 14).

[34] ATLAS & CMS Collaboration. “Combination of measurements of the top quark mass from data collected by the ATLAS and CMS experiments at $\sqrt{s} = 7$ and 8 TeV”. In: *Physical Review Letters* 132.26 (2024), p. 261902. DOI: 10.1103/PhysRevLett.132.261902. arXiv: 2402.08713 [hep-ex] (cit. on p. 13).

[35] “Direct top-quark decay width measurement in the $t\bar{t}$ lepton+jets channel at $\sqrt{s} =$ 8 TeV with the ATLAS experiment”. In: *The European Physical Journal C* 78.2 (Feb. 2018). ISSN: 1434-6052. DOI: 10.1140/epjc/s10052-018-5595-5. URL: http://dx.doi.org/10.1140/epjc/s10052-018-5595-5 (cit. on p. 13).

[36] Taesoo Song and Hamza Berrehrah. “Hadronization time of heavy quarks in nuclear matter”. In: *Physical Review C* 94.3 (Sept. 2016). ISSN: 2469-9993. DOI: 10.1103/physrevc.94.034901. URL: http://dx.doi.org/10.1103/PhysRevC.94.034901 (cit. on p. 13).

[37] The CMS Collaboration. “Observation of quantum entanglement in top quark pair production in proton–proton collisions at $\sqrt{s} = 13$ TeV”. In: *Reports on Progress in Physics* 87.11 (Oct. 2024), p. 117801. DOI: 10.1088/1361-6633/ad7e4d. URL: https://dx.doi.org/10.1088/1361-6633/ad7e4d (cit. on p. 13).

[38] ATLAS Collaboration. “Inclusive and differential cross-sections for dilepton $t\bar{t}$ production measured in $\sqrt{s} = 13$ TeV pp collisions with the ATLAS detector”. In: *Journal of High Energy Physics* 2023.7 (July 2023). ISSN: 1029-8479. DOI: 10.1007/jhep07(2023)141. URL: http://dx.doi.org/10.1007/JHEP07(2023)141 (cit. on p. 13).

[39] M. Tanabashi and et al. “Review of Particle Physics”. In: *Phys. Rev. D* 98 (3 Oct. 2018), p. 030001. DOI: 10.1103/PhysRevD.98.030001. URL: https://link.aps.org/doi/10.1103/PhysRevD.98.030001 (cit. on p. 13).

[40] R Brinkmann. “HERA”. In: (1989). DOI: 10.5170/CERN-1989-001.131. URL: https://cds.cern.ch/record/366965 (cit. on p. 15).

[41] Mark Thomson. *Modern Particle Physics*. Section 8.5.1: Scaling violations. Cambridge, United Kingdom: Cambridge University Press, 2013, pp. 201–202. ISBN: 978-1-107-03426-6 (cit. on p. 15).

[42] Tie-Jiun Hou et al. “New CTEQ global analysis of quantum chromodynamics with high-precision data from the LHC”. In: *Phys. Rev. D* 103.1 (2021), p. 014013. DOI: 10.1103/PhysRevD.103.014013. arXiv: 1912.10053 [hep-ph] (cit. on pp. 15, 93).

[43] Lyndon Evans and Philip Bryant. “LHC Machine”. In: *JINST* 3 (2008), S08001. DOI: 10.1088/1748-0221/3/08/S08001 (cit. on p. 20).

[44] Glen Cowan et al. “Asymptotic formulae for likelihood-based tests of new physics”. In: *Eur. Phys. J. C* 71 (2011), p. 1554. DOI: 10.1140/epjc/s10052-011-1554-0. arXiv: 1007.1727 [physics.data-an] (cit. on pp. 20, 70–72). Erratum: in: *Eur. Phys. J. C* 73 (2013), p. 2501. DOI: 10.1140/epjc/s10052-013-2501-z.

[45] ATLAS Collaboration. “The ATLAS Experiment at the CERN Large Hadron Collider”. In: *JINST* 3 (2008), S08003. DOI: 10.1088/1748-0221/3/08/S08003 (cit. on p. 22).

[46] ATLAS Collaboration. *Introduction to the ATLAS Experiment*. https://opendata.atlas.cern/docs/documentation/introduction/introduction_ATLAS. Accessed: 2025-05-03. n.d. (Cit. on p. 22).

[47] Joao Pequenao and Paul Schaffner. "How ATLAS detects particles: diagram of particle paths in the detector". 2013. URL: https://cds.cern.ch/record/1505342 (cit. on p. 24).

[48] Mukund Gupta. *Calculation of radiation length in materials*. Tech. rep. Geneva: CERN, 2010. URL: https://cds.cern.ch/record/1279627 (cit. on p. 24).

[49] ATLAS Collaboration. "Operation and performance of the ATLAS tile calorimeter in LHC Run 2". In: (2024). arXiv: 2401.16034 [hep-ex] (cit. on p. 24).

[50] ATLAS Collaboration. *ATLAS Liquid Argon Calorimeter: Technical Design Report*. ATLAS-TDR-2; CERN-LHCC-96-041. 1996. URL: https://cds.cern.ch/record/331061 (cit. on p. 24).

[51] ATLAS Collaboration. *ATLAS Liquid Argon Calorimeter Phase-I Upgrade: Technical Design Report*. ATLAS-TDR-022; CERN-LHCC-2013-017. 2013. URL: https://cds.cern.ch/record/1602230 (cit. on p. 24).

[52] ATLAS Collaboration. "Measurement of the muon reconstruction performance of the ATLAS detector using 2011 and 2012 LHC proton–proton collision data". In: *Eur. Phys. J. C* 74 (2014), p. 3130. DOI: 10.1140/epjc/s10052-014-3130-x. arXiv: 1407.3935 [hep-ex] (cit. on p. 25).

[53] ATLAS Collaboration. *ATLAS Muon Spectrometer Phase-II Upgrade: Technical Design Report*. ATLAS-TDR-026; CERN-LHCC-2017-017. 2017. URL: https://cds.cern.ch/record/2285580 (cit. on p. 25).

[54] The ATLAS collaboration. "Operation of the ATLAS trigger system in Run 2". In: *Journal of Instrumentation* 15.10 (Oct. 2020), P10004–P10004. ISSN: 1748-0221. DOI: 10.1088/1748-0221/15/10/p10004. URL: http://dx.doi.org/10.1088/1748-0221/15/10/P10004 (cit. on p. 27).

[55] The ATLAS collaboration. "Operation of the ATLAS trigger system in Run 2". In: *Journal of Instrumentation* 15.10 (Oct. 2020), P10004–P10004. ISSN: 1748-0221. DOI: 10.1088/1748-0221/15/10/p10004. URL: http://dx.doi.org/10.1088/1748-0221/15/10/P10004 (cit. on p. 27).

[56] Markus Elsing et al. "The ATLAS Tier-0: Overview and operational experience". In: *Journal of Physics: Conference Series* 219.7 (Apr. 2010), p. 072011. DOI: 10.1088/1742-6596/219/7/072011. URL: https://dx.doi.org/10.1088/1742-6596/219/7/072011 (cit. on p. 28).

[57] J. Alwall et al. "The automated computation of tree-level and next-to-leading order differential cross sections, and their matching to parton shower simulations". In: *JHEP* 07 (2014), p. 079. DOI: 10.1007/JHEP07(2014)079. arXiv: 1405.0301 [hep-ph] (cit. on pp. 29, 45, 92).

[58] Torbjorn Sjöstrand, Stephen Mrenna, and Peter Skands. "PYTHIA 6.4 physics and manual". In: *JHEP* 05 (2006), p. 026. DOI: 10.1088/1126-6708/2006/05/026. arXiv: hep-ph/0603175 (cit. on p. 30).

[59] G. Corcella et al. "HERWIG 6: an event generator for hadron emission reactions with interfering gluons (including supersymmetric processes)". In: *JHEP* 01 (2001), p. 010. DOI: 10.1088/1126-6708/2001/01/010. arXiv: hep-ph/0011363 (cit. on p. 30).

[60] S. Agostinelli et al. "GEANT4 – a simulation toolkit". In: *Nucl. Instrum. Meth. A* 506 (2003), p. 250. DOI: 10.1016/S0168-9002(03)01368-8 (cit. on p. 30).

[61] ATLAS Collaboration. "Electron and photon efficiencies in LHC Run 2 with the ATLAS experiment". In: *JHEP* 05 (2024), p. 162. DOI: 10.1007/JHEP05(2024)162. arXiv: 2308.13362 [hep-ex] (cit. on p. 31).

[62] ATLAS Collaboration. "Electron and photon energy calibration with the ATLAS detector using LHC Run 2 data". In: *JINST* 19 (2023), P02009. DOI: 10.1088/1748-0221/19/02/P02009. arXiv: 2309.05471 [hep-ex] (cit. on p. 31).

[63] ATLAS Collaboration. "Studies of the muon momentum calibration and performance of the ATLAS detector with pp collisions at $\sqrt{s} = 13\,\text{TeV}$". In: *Eur. Phys. J. C* 83 (2023), p. 686. DOI: 10.1140/epjc/s10052-023-11584-x. arXiv: 2212.07338 [hep-ex] (cit. on p. 31).

[64] Matteo Cacciari, Gavin P. Salam, and Gregory Soyez. "The anti-k_t jet clustering algorithm". In: *JHEP* 04 (2008), p. 063. DOI: 10.1088/1126-6708/2008/04/063. arXiv: 0802.1189 [hep-ph] (cit. on p. 32).

[65] Mohammed Faraj. "Measurement of $t\bar{t}$ and single top quark production in ATLAS experiment". In: *PoS* LHCP2023 (2024), p. 013. DOI: 10.22323/1.450.0013 (cit. on p. 37).

[66] Paolo Nason. "A new method for combining NLO QCD with shower Monte Carlo algorithms". In: *JHEP* 11 (2004), p. 040. DOI: 10.1088/1126-6708/2004/11/040. arXiv: hep-ph/0409146 (cit. on p. 38).

[67] Stefano Frixione, Paolo Nason, and Carlo Oleari. "Matching NLO QCD computations with parton shower simulations: the POWHEG method". In: *JHEP* 11 (2007), p. 070. DOI: 10.1088/1126-6708/2007/11/070. arXiv: 0709.2092 [hep-ph] (cit. on p. 38).

[68] Simone Alioli et al. "A general framework for implementing NLO calculations in shower Monte Carlo programs: the POWHEG BOX". In: *JHEP* 06 (2010), p. 043. DOI: 10.1007/JHEP06(2010)043. arXiv: 1002.2581 [hep-ph] (cit. on p. 38).

[69] NNPDF Collaboration, Richard D. Ball, et al. "Parton distributions for the LHC run II". In: *JHEP* 04 (2015), p. 040. DOI: 10.1007/JHEP04(2015)040. arXiv: 1410.8849 [hep-ph] (cit. on pp. 39, 45).

[70] S. Mrenna and P. Skands. "Automated parton-shower variations in PYTHIA 8". In: *Phys. Rev. D* 94 (2016), p. 074005. DOI: 10.1103/PhysRevD.94.074005. arXiv: 1605.08352 [hep-ph] (cit. on p. 39).

[71] Johannes Bellm et al. “Herwig 7.0/Herwig++ 3.0 release note”. In: *Eur. Phys. J. C* 76.4 (2016), p. 196. DOI: 10.1140/epjc/s10052-016-4018-8. arXiv: 1512.01178 [hep-ph] (cit. on p. 39).

[72] “Search for charged Higgs bosons decaying into top and bottom quarks at $\sqrt{s} = 13$ TeV with the ATLAS detector”. In: *Journal of High Energy Physics* 2021.6 (June 2021). ISSN: 1029-8479. DOI: 10.1007/jhep06(2021)145. URL: http://dx.doi.org/10.1007/JHEP06(2021)145 (cit. on pp. 39, 77).

[73] Rikkert Frederix, Emanuele Re, and Paolo Torrielli. “Single-top t-channel hadroproduction in the four-flavour scheme with POWHEG and aMC@NLO”. In: *JHEP* 09 (2012), p. 130. DOI: 10.1007/JHEP09(2012)130. arXiv: 1207.5391 [hep-ph] (cit. on p. 45).

[74] Stefano Frixione et al. “Single-top hadroproduction in association with a W boson”. In: *JHEP* 07 (2008), p. 029. DOI: 10.1088/1126-6708/2008/07/029. arXiv: 0805.3067 [hep-ph] (cit. on p. 45).

[75] ATLAS Collaboration. *Studies on top-quark Monte Carlo modelling for Top2016*. Tech. rep. All figures including auxiliary figures are available at https://atlas.web.cern.ch/Atlas/GROUPS/I PHYS-PUB-2016-020. Geneva: CERN, 2016. URL: https://cds.cern.ch/record/2216168 (cit. on p. 45).

[76] H. B. Hartanto et al. “Higgs boson production in association with top quarks in the POWHEG BOX”. In: *Physical Review D* 91.9 (May 2015). ISSN: 1550-2368. DOI: 10.1103/physrevd.91.094003. URL: http://dx.doi.org/10.1103/PhysRevD.91.094003 (cit. on p. 46).

[77] “Search for vector-boson resonances decaying into a top quark and a bottom quark using pp collisions at $\sqrt{s} = 13$ TeV with the ATLAS detector”. In: *JHEP* 2312 (2023), p. 073. DOI: 10.1007/JHEP12(2023)073. arXiv: 2308.08521. URL: https://cds.cern.ch/record/2867730 (cit. on pp. 54, 58, 59).

[78] Alexander Shmakov et al. “SPANet: Generalized permutationless set assignment for particle physics using symmetry preserving attention”. In: *SciPost Phys.* 12 (2022), p. 178. DOI: 10.21468/SciPostPhys.12.5.178. URL: https://scipost.org/10.21468/SciPostPhys.12.5.178 (cit. on pp. 54–56).

[79] Ashish Vaswani et al. *Attention Is All You Need*. 2023. arXiv: 1706.03762 [cs.CL]. URL: https://arxiv.org/abs/1706.03762 (cit. on p. 55).

[80] Alexander L. Read. “Presentation of search results: the CL_S technique”. In: *J. Phys. G* 28 (2002), p. 2693. DOI: 10.1088/0954-3899/28/10/313 (cit. on p. 70).

[81] T. Esch et al. “TRExFitter: A framework for statistical modelling, fitting, and limit setting”. In: *Eur. Phys. J. C* 78 (2018), p. 874. DOI: 10.1140/epjc/s10052-018-6306-2. arXiv: 1806.11063 [physics.data-an] (cit. on p. 71).

[82] Thomas P. Calvet. “Search for the production of a Higgs boson in association with top quarks and decaying into a b-quark pair and b-jet identification with the ATLAS experiment at LHC”. https://hdl.handle.net/11244/50758. Ph.D. thesis. University of Oklahoma, 2017 (cit. on p. 71).

[83] Glen Cowan et al. “Asymptotic formulae for likelihood-based tests of new physics”. In: *The European Physical Journal C* 71.2 (Feb. 2011). ISSN: 1434-6052. DOI: 10.1140/epjc/s10052-011-1554-0. URL: http://dx.doi.org/10.1140/epjc/s10052-011-1554-0 (cit. on p. 74).

[84] ATLAS Collaboration. “Jet energy scale measurements and their systematic uncertainties in proton–proton collisions at $\sqrt{s} = 13\,\text{TeV}$ with the ATLAS detector”. In: *Phys. Rev. D* 96 (2017), p. 072002. DOI: 10.1103/PhysRevD.96.072002. arXiv: 1703.09665 [hep-ex] (cit. on p. 76).

[85] ATLAS Collaboration. “Using pile-up collisions as an abundant source of low-energy hadronic physics processes in ATLAS and an extraction of the jet energy resolution”. In: *JHEP* 12 (2024), p. 032. DOI: 10.1007/JHEP12(2024)032. arXiv: 2407.10819 [hep-ex] (cit. on p. 76).

[86] ATLAS Collaboration. “Muon reconstruction performance of the ATLAS detector in proton–proton collision data at $\sqrt{s} = 13$ TeV”. In: *The European Physical Journal C* 76.5 (May 2016). ISSN: 1434-6052. DOI: 10.1140/epjc/s10052-016-4120-y. URL: http://dx.doi.org/10.1140/epjc/s10052-016-4120-y (cit. on p. 76).

[87] ATLAS Collaboration. “Electron and photon performance measurements with the ATLAS detector using the 2015–2017 LHC proton–proton collision data”. In: *JINST* 14 (2019), P12006. DOI: 10.1088/1748-0221/14/12/P12006. arXiv: 1908.00005 [hep-ex] (cit. on p. 76).

[88] ATLAS Collaboration. “Performance of missing transverse momentum reconstruction with the ATLAS detector using proton–proton collisions at $\sqrt{s} = 13$ TeV”. In: *The European Physical Journal C* 78.11 (Nov. 2018). ISSN: 1434-6052. DOI: 10.1140/epjc/s10052-018-6288-9. URL: http://dx.doi.org/10.1140/epjc/s10052-018-6288-9 (cit. on p. 77).

[89] *E_T^{miss} performance in the ATLAS detector using 2015-2016 LHC p-p collisions*. Tech. rep. Geneva: CERN, 2018. URL: https://cds.cern.ch/record/2625233 (cit. on p. 77).

[90] G. Apollinari et al. “High-Luminosity Large Hadron Collider (HL-LHC)”. In: *CERN Yellow Rep. Monogr.* 4 (2017), pp. 1–516. DOI: 10.23731/CYRM-2017-004 (cit. on p. 92).

[91] R. Schwienhorst and D. Wackeroth (editors). “Report of the Topical Group on Top quark physics and heavy flavor production for Snowmass 2021”. In: (Sept. 2022). arXiv: 2209.11267 [hep-ph] (cit. on p. 92).

[92] R. Abdul Khalek et al. *Snowmass 2021 White Paper: Electron Ion Collider for High Energy Physics*. 2022. arXiv: 2203.13199 [hep-ph] (cit. on p. 92).

[93] Mengshi Yan et al. “CT18 global PDF fit at leading order in QCD”. In: *Physical Review D* 107.11 (June 2023). ISSN: 2470-0029. DOI: 10.1103/physrevd.107.116001. URL: http://dx.doi.org/10.1103/PhysRevD.107.116001 (cit. on p. 92).

[94] S. Sawford J. Gombas J. Fein and R. Schwienhorst. *Dependence of the top-quark mass measured in top-quark pair production on the parton distribution functions at the LHC and future colliders*. 2022. arXiv: 2203.08064 [hep-ph] (cit. on p. 93).

[95] Carl Schmidt, Jon Pumplin, and C.-P. Yuan. "Updating and optimizing error parton distribution function sets in the Hessian approach". In: *Phys. Rev. D* 98.9 (2018), p. 094005. DOI: 10.1103/PhysRevD.98.094005. arXiv: 1806.07950 [hep-ph] (cit. on p. 93).